

Abstract

Josephson Bifurcation Amplifier:

Amplifying quantum signals using a dynamical bifurcation

Rajamani Vijayaraghavan

2008

Quantum measurements of solid-state systems, such as the readout of superconducting quantum bits challenge conventional low-noise amplification techniques. Ideally, the amplifier for a quantum measurement should minimally perturb the measured system while maintaining sufficient sensitivity to overcome the noise of subsequent elements in the amplification chain. Additionally, the drift of materials properties in solid-state systems mandates a fast acquisition rate to permit measurements in rapid succession. In this thesis, we describe the Josephson Bifurcation Amplifier (JBA) which was developed to meet these requirements. The JBA exploits the sensitivity of a dynamical system - a non-linear oscillator tuned near a bifurcation point. In this new scheme, all available degrees of freedom in the dynamical system participate in information transfer and none contribute to unnecessary dissipation resulting in excess

noise. We have used a superconducting tunnel junction, also known as a Josephson junction to construct our non-linear oscillator. The Josephson junction is the only electronic circuit element which remains non-linear and non-dissipative at arbitrarily low temperatures. This thesis will describe the theory and experiments demonstrating bifurcation amplification in the JBA and its application to the measurement of superconducting quantum bits. By describing the JBA as a parametrically driven oscillator, we will demonstrate that the ultimate sensitivity of the JBA is limited only by quantum fluctuations. Using this treatment, we will identify the connection between the four main aspects of working with a dynamical bifurcation: parametric amplification, squeezing, quantum activation and the Dynamical Casimir Effect.

Josephson Bifurcation Amplifier:
Amplifying quantum signals using a dynamical bifurcation

A Dissertation
Presented to the Faculty of the Graduate School
of
Yale University
in Candidacy for the Degree of
Doctor of Philosophy

by
Rajamani Vijayaraghavan

Dissertation Director: Professor Michel H. Devoret

May 2008

Copyright ©2008 by Rajamani Vijayaraghavan

All rights reserved.

Acknowledgements

Numerous people have played a role in the success of the work described in this thesis and I will try my best to thank them all.

I would like to begin by thanking my advisor, Prof. Michel Devoret for giving me a chance to work in his research group - the QuLab. His willingness to devote a lot of time to his students has always been extremely beneficial to me, especially during my early days in the group. Right from the very beginning, Michel gave me the freedom to be creative in coming up with solutions to the problems we were trying to tackle in our group. The development of the Josephson Bifurcation Amplifier (JBA), the main subject of this thesis was a direct consequence. I am thankful for his continued guidance throughout the course of my PhD and for instilling in me the importance of being thorough in the research. I am also extremely grateful for his patience and support during the writing of my thesis and for reading the manuscript in great detail.

A major part of the experimental work on the JBA was done under the direct guidance of Irfan Siddiqi who was a post-doctoral researcher in the group and an experimentalist par excellence. I would like to thank him for teaching me everything I know about microwave circuit design and cryogenics. His ability to troubleshoot noise issues in the setup always amazed me. He was also a great friend and the often monotonous data taking procedure would not have been as much fun without his

company. A special thanks is also due to Etienne Boaknin, another post-doctoral associate who developed the lossy "chocolate" filters which proved critical for implementing the ultra-low noise setup. I would also like to thank Philippe Hyafil for his assistance in the quantum escape measurements.

A big thanks to the fabrication team which was led by Frederic Pierre and Chris Wilson during the early days and then taken over by Michael Metcalfe and Chad Rigetti. All the devices measured during the course of my PhD were fabricated by them. I would like to thank them for teaching me some of the nuances of the fabrication procedure as well. I would also like to thank Luigi Frunzio, the ultimate authority on device fabrication for his assistance in the various fabrication projects. A special thanks is also due to him for reading my thesis in great detail and providing suggestions for improvement.

I am extremely grateful to Prof. Daniel Prober for allowing us access to the resources in his lab. The early work on the JBA was entirely done in his lab. I would also like to thank him for his role as the Chair of the Applied Physics department in maintaining an enjoyable and productive work environment. Thanks are also due to the other members of his lab for their help and support. I would like to thank Prof. Robert Schoelkopf who along with Prof. Prober served on my thesis committee. His expertise on designing experiments at microwave frequencies has been extremely beneficial to me. I would also like to thank him for numerous discussions on amplifiers, especially concerning their noise performance. A big thanks to all the members of his lab with whom we closely collaborated. The fact that we shared the lab space with them led to an exciting working environment.

Prof. Steven Girvin and his team of theorists have been a great source of help in

understanding the physics of the JBA. I would like to thank Prof. Girvin for many useful discussions and his special ability to interface between theory and experiments. Thanks are also due to K. Sengupta for his work on quantum langevin simulations of the JBA, Alexandre Blais for his work on the back-action of the JBA on the qubit and Jay Gambetta for helping us understand the squeezing effects in the JBA. A special thanks to Vladimir Manucharyan, a member of our lab, for numerous discussions on the theory of microwave bifurcations and help with various calculations. Thanks are also due to the newer members of QuLab: Nicolas, Markus, Flavius and Nick for their help.

A special thanks to all the administrative staff - Jayne Miller, Pat Brodka, Maria Gubitosi, Theresa Evangeliste and Giselle DeVito for their hard work in ensuring the smooth functioning of the group. I would also like to thank Cara Gibilisco for her prompt assistance in various administrative matters.

Outside of Yale, I would like to thank members of the Quantronics group at Saclay for their assistance in the design of the quantronium. Thanks are also due to Prof. Mark Dykman at Michigan State University for being the external reader and also for his assistance in understanding the physics of driven, non-linear systems. I would also like to thank all my teachers, especially Dr. Bikram Phookun and Dr. Pratibha Jolly who have been instrumental in my decision to pursue a career in Physics.

Life at Yale would have been extremely dull without all my friends. I would like to thank them all for their friendship and support during the last several years. A special thanks to Dhruv, who has always been there during the good and bad times and a constant source of encouragement. I would also like to thank Sahar, Josiah, Athena and Isaac for providing me a place in their home during the last few months

at Yale.

Finally, and most importantly, I would like to thank my family - Amma, Appa, Athai, Mohan and Vasu. Without their love and support, I could have never dreamed of embarking on this journey and I dedicate this thesis to them.

Contents

1	Introduction	21
1.1	Amplification and quantum limited detection	23
1.2	Amplifying using a bifurcation	26
1.2.1	The Josephson junction	27
1.2.2	Bifurcation in a RF driven Josephson oscillator	28
1.2.3	Operating principle of the JBA	31
1.3	Superconducting quantum circuits	32
1.4	Summary of key results	40
1.4.1	JBA Measurements	40
1.4.2	Qubit measurements	42
1.4.3	Escape measurements in the quantum regime	47
1.5	Thesis overview	52
2	Josephson Bifurcation Amplifier: Theory	56
2.1	General properties of a driven non-linear oscillator	56
2.2	Josephson junction oscillator	59
2.2.1	Bistability in driven Josephson oscillator	59

<i>CONTENTS</i>	6
2.2.2 Dynamics in quadrature amplitude plane	66
2.3 Josephson Bifurcation Amplifier	69
2.3.1 Operating principle	69
2.3.2 Transition Rates	73
2.3.3 Measurement sensitivity	77
3 Josephson Bifurcation Amplifier: Experiments	81
3.1 Experimental setup	81
3.2 Frequency domain measurements	86
3.2.1 Linear resonance	86
3.2.2 Non-linear resonance	90
3.3 Time domain measurements	92
3.3.1 Hysteresis and bistability in the JBA	93
3.3.2 JBA as a readout	96
3.4 Microwave design considerations	98
4 JBA as a qubit readout	105
4.1 The Cooper pair box	105
4.1.1 Hamiltonian in charge basis	107
4.1.2 Hamiltonian in phase basis	108
4.1.3 The split Cooper pair box	110
4.2 The quantronium	112
4.2.1 Quantronium as a quantum bit	113
4.2.2 Readout strategies	117
4.3 Measuring the quantronium with the JBA	119

4.3.1	Effective Hamiltonian	119
4.3.2	Measurement protocol	122
4.3.3	Effective critical current	124
4.3.4	Qubit readout optimization	128
4.3.5	Qubit readout performance	130
4.4	Numerical simulations	132
5	Qubit coherence measurements	136
5.1	Measurement setup	136
5.2	Ground state characterization	140
5.3	Spectroscopy	142
5.4	Time domain measurements	145
5.5	Readout fidelity	150
6	Qubit readout performance	155
6.1	Quantum non-demolition readout using a JBA	156
6.2	Information flow during qubit measurement	158
6.2.1	Multiple pulse measurements	158
6.2.2	AC Stark shift of qubit	162
6.2.3	Quantifying the losses during readout	165
6.3	Characterizing the qubit environment	171
6.4	Approaching a single-shot readout	176
7	Quantum escape and parametric amplification: Theory	182
7.1	Input-Output theory	183

7.1.1	Harmonic oscillator coupled to a transmission line	184
7.1.2	Escape in current-biased Josephson junction	189
7.2	Escape dynamics in the JBA	195
7.2.1	Parametric amplifier description of the JBA	195
7.2.2	Solutions in the frequency domain	199
7.2.3	Quadrature variables	202
7.2.4	Escape rates	204
7.3	Parametric amplification in the JBA	210
7.3.1	Parametric gain	211
7.3.2	Noise temperature and the quantum limit	212
7.3.3	Squeezing	215
8	Quantum escape and parametric amplification: Experiments	218
8.1	Dynamical Casimir Effect	220
8.2	Quantum escape measurements	222
8.2.1	Switching measurements in the JBA	222
8.2.2	Combined RF and DC biasing scheme	224
8.2.3	Measuring escape rates	228
8.2.4	Temperature dependence	230
8.2.5	Detuning dependence	233
8.3	Parametric amplification in the JBA	237
8.3.1	Measurement protocol	237
8.3.2	Gain and noise temperature	239
8.3.3	Squeezing measurements	244

<i>CONTENTS</i>	9
9 Future directions	247
9.1 Evolution of the JBA	247
9.2 Back-action of the bifurcation readout on a qubit	249
9.3 Josephson Parametric Converter	250
10 Conclusions	252
Appendices	255
A JBA formulae	255
B Mathematica formulae	257
C Numerical simulations	259
C.1 Equations of motion	260

List of Figures

1.1	General amplification process	24
1.2	Josephson tunnel junction	27
1.3	Non-linear resonance curves in a driven Josephson oscillator.	30
1.4	Schematic of bifurcation amplifier	31
1.5	Different varieties of superconducting qubits.	36
1.6	The original quantronium qubit.	37
1.7	Phase response of JBA as a function of drive frequency and power	41
1.8	Quantronium qubit readout using a JBA	43
1.9	Summary of qubit coherence measurements	45
1.10	Escape temperature v.s. bath temperature for dynamical and static escape.	51
2.1	Simple pendulum as a non-linear oscillator	57
2.2	Linear v.s. non-linear resonance	58
2.3	Driven Josephson oscillator circuit	59
2.4	Steady state solutions of the driven non-linear oscillator	63
2.5	Bistability diagram	65

2.6	Poincaré sections of an RF driven Josephson junction.	68
2.7	JBA operating principle	70
2.8	Switching probability curves	72
2.9	Metapotential for the effective slow coordinate.	75
3.1	Optical image of chip capacitor and SEM image of Josephson junction	83
3.2	Pictures of microwave setup and sample box	84
3.3	Schematic of the measurement setup	85
3.4	Phase response of JBA in linear regime.	87
3.5	Extracting JBA resonator parameters	89
3.6	Phase response of JBA as a function of drive frequency and power . .	91
3.7	Hysteretic response of the JBA	93
3.8	Histograms of the reflected signal phase	95
3.9	Switching probability curves for the JBA	96
3.10	Linear resonance measurement in a JBA with stray parameters	98
3.11	Magnitude and phase response of a JBA with stray parameters. . . .	100
3.12	Audio frequency ac resistance of a non-linear oscillator as a function of drive power at a fixed frequency	102
4.1	Cooper pair box	106
4.2	Energy levels of the Cooper pair box	109
4.3	Split Cooper pair box	110
4.4	The quantronium circuit	113
4.5	Bloch sphere representation	114
4.6	Quantronium energy levels	116

4.7	Quantronium with JBA readout	119
4.8	Quantronium loop currents	126
4.9	Quantronium gate and flux modulations	127
4.10	Critical current variation in quantronium	129
4.11	Simulated S-curves for quantronium+JBA.	134
5.1	Schematic of qubit measurement setup	137
5.2	Fridge setup for qubit measurements	138
5.3	Ground state properties of the quantronium (sample A) v.s. gate and flux bias	141
5.4	Spectroscopic peaks	143
5.5	Variation of qubit transition frequency with gate charge	144
5.6	Qubit lineshape for sample A	145
5.7	Rabi oscillation data for sample B	146
5.8	T_1 data for sample B	148
5.9	Ramsey fringe data for sample B	149
5.10	Echo data for sample B	151
5.11	S-curves for sample B	153
6.1	Multiple readout of qubit state	159
6.2	Two pulse measurements of the qubit state	161
6.3	AC Stark shift of qubit frequency with driving on phase or gate port.	164
6.4	Information flow during qubit readout	166
6.5	Detuning dependence of two pulse measurements	168
6.6	Summary of readout induced relaxation as function of drive detuning.	170

6.7	Spectroscopy data revealing resonances in the qubit environment . . .	172
6.8	Unexpected variation of T_1 with gate and flux bias.	175
6.9	T_1 measured at Stark shifted frequencies	176
6.10	Exploiting second excited of qubit to enhance readout contrast. . . .	178
7.1	Harmonic oscillator coupled to a transmission line	184
7.2	Transmission line equations	185
7.3	Input-output relations for circuits	186
7.4	DC current biased Josephson junction	189
7.5	Cubic potential and its harmonic approximation	191
7.6	Non-linear resonance curves in a driven Josephson oscillator.	198
7.7	Gain functions $ A(f) ^2$ and $ B(f) ^2$	201
7.8	Noise dynamics in quadrature variable space.	203
7.9	Spectrum of the quadrature variables	206
7.10	Computed gain of a parametric amplifier	213
7.11	Squeezing spectrum of the output field of the JBA	216
8.1	Different schemes to observe the Dynamical Casimir Effect	219
8.2	Combined biasing scheme for single-ended RF and differential DC signals. 225	
8.3	A picture of the DC and RF circuitry	227
8.4	Measurements of escape rate in the JBA at different temperatures. . .	229
8.5	A plot of T_{esc}^{DC} vs T in a DC current biased Josephson junction. . . .	231
8.6	A plot of T_{esc}^{RF} vs T in the JBA	232
8.7	Frequency dependence of RF escape temperature	234
8.8	Phase diagram of the non-linear resonance in a JBA.	236

8.9	Measurement protocol for parametric amplifier	238
8.10	Gain and output noise in a PARAMP	240
8.11	PARAMP gain near critical point.	241
8.12	Gain and noise temperature in a PARAMP	243
8.13	Squeezing in the JBA	245
9.1	Optical image of a Cavity Bifurcation Amplifier	248
9.2	Schematic of Josephson Parametric Converter	250
C.1	Full circuit model of the JBA	259

List of Tables

3.1	JBA sample parameters	82
5.1	Qubit sample parameters	139

List of symbols and abbreviations

(α)	Relative detuning $\alpha = 1 - \omega_d/\omega_p$
(α_N)	Reduced noise intensity
(β)	Reduced drive power in a driven duffing oscillator
(β_B^\pm)	Upper and lower bifurcation points in reduced units
(β_c)	Critical value of β , $\beta > \beta_c$ for bistability
(δ)	Gauge invariant phase difference across Josephson junction
(δ_{\parallel})	In-phase amplitude of oscillations in the JBA
(δ_{\perp})	Quadrature-phase amplitude of oscillations in the JBA
(δ_m)	Superconducting phase drop due to magnetic flux
(δ_R)	Superconducting phase drop across readout junction
(γ)	Coefficient of first non-linear term in Josephson oscillator $\gamma = \omega_p^2/6$
(Γ)	Oscillator damping rate
(Γ_R)	Reflection coefficient
(η_c)	Readout contrast

(η_{dp})	Readout discrimination power
(η_f)	Readout fidelity
$(\hat{\theta})$	Phase operator - conjugate variable to charge operator \hat{N}
(ν_{01}, ω_{01})	Transition frequency between ground and first excited state of quantum qubit
(ν_{RF}, ω_{RF})	Frequency of microwave pulse applied to gate port of quantum
(ν_{Rabi})	Rabi frequency
$(\sigma_{X,Y,Z})$	Pauli operators for spin 1/2 system
(ϕ)	Reflected signal phase
(Φ)	Externally applied flux
(Φ_0)	Flux quantum $\Phi_0 = h/2e$
(φ_0)	Reduced flux quantum $\varphi_0 = \hbar/2e$
(Ω)	Reduced detuning $\Omega = \Delta\omega/\Gamma$
(ω_0)	Natural frequency of an oscillator
(ω_a)	Attempt frequency for escape from a metastable state in JBA
(Ω_c)	Critical value of reduced detuning
(ω_d)	JBA drive frequency
(ω_p)	Plasma frequency
$(\Delta\omega)$	Detuning frequency $\Delta\omega = \omega_p - \omega_d$
$(0\rangle)$	Charge state of CPB with 0 Cooper pairs on the island

$(1\rangle)$	Charge state of CPB with 1 Cooper pairs on the island
$(0\rangle)$	Ground state of CPB
$(1\rangle)$	First excited state of CPB
$(k\rangle)$	k^{th} excited state of CPB
(C_Σ)	Sum capacitance of the island of a CPB
(C_g)	Gate capacitance of the island of a CPB
(C_J)	Intrinsic capacitance of Josephson junction
(C_S)	Shunting capacitance to lower the plasma frequency of the Josephson junction
(E_C)	Charging energy of a CPB (single electron units)
(E_J)	Josephson energy
(E_k)	Energy of k^{th} eigenstate of a CPB
(g)	Acceleration due to gravity
(G_{JBA})	Gain of JBA in bistable mode
(I_0)	Josephson critical current
(I_B^\pm)	Upper and lower bifurcation current
(I_e)	Error current in the JBA
(I_N)	Noise current in the JBA
(I_{RF})	Amplitude of RF current drive
(k_B)	Boltzmann constant

(L_J)	Josephson inductance
(L_S)	Stray inductance in the microfabricated capacitor
(N_g)	Reduced gate polarization charge on the island of CPB
$(N\rangle)$	Charge state with N Cooper pairs on the island of a CPB
(\hat{N})	Operator for number of Cooper pairs on the island of CPB
(O_H)	High amplitude state of the JBA
(O_L)	High amplitude state of the JBA
(O_S)	Unstable state (saddle point) of the JBA
(P_{switch})	Probability of switching from O_L to O_H
(Q)	Quality factor of a resonator
(R)	Source resistance of current source driving the JBA
(R_S)	Stray resistance in the microfabricated capacitor
(S_{I_0})	Critical current sensitivity of JBA in $\text{A} / \sqrt{\text{Hz}}$
(T)	Temperature
(T_{echo})	Echo time for a qubit
(T_φ)	Pure dephasing time for a qubit
(T_1)	Relaxation time for a qubit
(T_2)	Total dephasing time for a qubit
(T_N)	Noise temperature of an amplifier
(u)	Slow, complex amplitude of oscillator response

(U_{RF})	Amplitude of RF voltage applied the gate port
(ΔU)	Energy barrier height for escape
(Z)	Complex impedance
(Z_0)	Characteristic impedance
(CPB)	Cooper pair box
(IOT)	Input Output Theory
(HEMT)	High Electron Mobility Transistor
(JBA)	Josephson Bifurcation Amplifier
(qubit)	A quantum two level system used a quantum bit

Chapter 1

Introduction

Amplification using a laser, a maser or a transistor is based on energizing many microscopic systems. Atoms in a cavity or conduction electrons in a channel are some typical examples. Each microscopic degree of freedom is weakly coupled to the input signal. The overall power gain of the system, which is determined by the product of the number of active microscopic systems and their individual response to the input parameter, can be quite substantial. However, noise can result from the lack of control of each individual microscopic system. In this thesis, we explore another strategy for amplification. We utilize a system with only one, well controlled degree of freedom, which is driven to a high level of excitation. The input signal is coupled parametrically to the system and influences its dynamics leading to amplification. The superconducting quantum interference device (SQUID) [1] and the radio frequency single electron transistor (RF-SET) [2] are two well known devices which use this strategy. The system we have chosen is a driven, non-linear oscillator biased near a dynamical bifurcation. We call this device the Josephson Bifurcation Amplifier (JBA) since the non-linear oscillator is constructed using a Josephson junction [3].

The main advantage of the JBA over the SQUID and the RF-SET is that there is no intrinsic dissipation resulting in minimum noise and back-action.

In this dissertation, we exploit the non-linearity of a Josephson junction [3], which is a superconducting tunnel junction and therefore the only electronic circuit element which remains non-linear and non-dissipative at arbitrary low temperatures. The primary goal of the JBA was to readout the quantum state of superconducting quantum bits (qubits). Superconducting qubits are electronic circuits made to behave like artificial atoms [4, 5, 6, 7]. We map the two quantum states of the qubit to two different driven states of the non-linear oscillator which is bistable under appropriate driving conditions. Bistability has been extensively studied in non-linear optical systems too, but they have always been plagued by dissipation in the non-linear medium (see [8] for a review). We have also explored the possibility of using the JBA as a linear, phase preserving, parametric amplifier [9] operating at the quantum limit [10].

This work brings together ideas from different areas of physics like non-linear dynamics, non-equilibrium statistical mechanics, quantum measurements, quantum limited amplification and experimental techniques like cryogenics, ultra-low noise measurements and microwave engineering. In this introduction, we will first discuss the amplification process and the restrictions placed on it by quantum mechanics. This will be followed by a discussion on the use of bifurcations for amplification. We will then briefly talk about superconducting quantum circuits and highlight the challenges in reading out their quantum state. Finally, we will summarize the key experimental results of the work carried out for this dissertation.

1.1 Amplification and quantum limited detection

Amplifiers are an important part of any experiment carrying out high precision measurements. In particular, cryogenic, low noise amplifiers working in the microwave domain have recently found a growing number of applications in mesoscopic physics, astrophysics and particle detector physics [11, 12]. An amplifier is needed in order to raise the level of a weak input signal to a macroscopic level so that it can overcome the noise of conventional signal processing circuitry. The room temperature signal processing electronics are generally quite noisy and cannot be directly used to measure very weak signals from typical cryogenic, mesoscopic physics experiments. A sensitive, low noise amplifier is required to interface the extremely weak signals coming from an experiment to the noisy room temperature electronics.

A linear amplifier is one whose output is linearly related to its input signal. This definition is quite broad and includes both frequency-converting amplifiers, whose output is at a frequency different from the input frequency, and phase-sensitive amplifiers, whose response depends on the phase of the input signal. We will be mostly considering phase-insensitive linear amplifiers which preserve the phase of the input signal.

An amplifier must have two important properties. Firstly, the output power of the amplifier should be large enough, so that any further processing of the signal does not degrade the signal to noise ratio. At the same time, the amplifier must add the minimum possible noise to the signal during the amplification process. The amplification process in general degrades the signal-to-noise ratio. This is shown schematically in Fig. 1.1. Quantum mechanics places a restriction on this added noise. When this is quantum minimum is achieved, the amplifier is labeled quan-

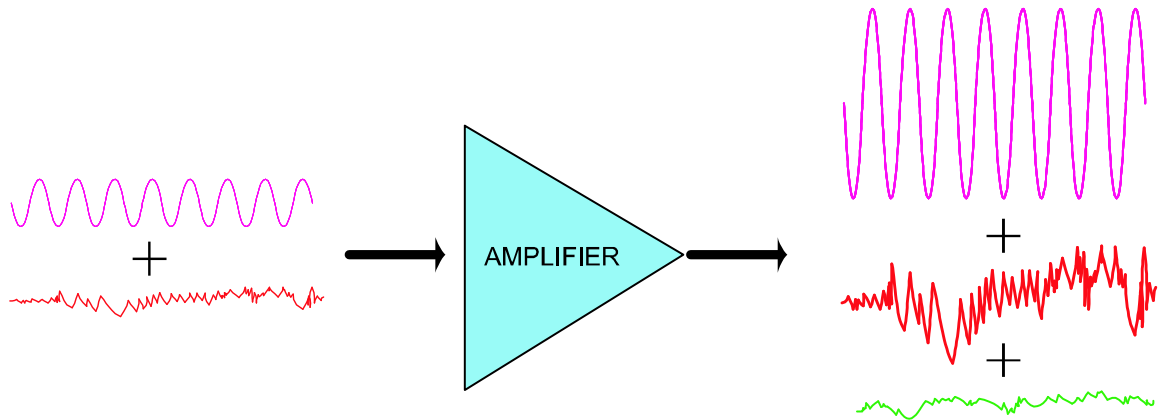


Figure 1.1: General amplification process. An amplifier in general degrades the signal to noise ratio. At the input of an amplifier, there is the signal to be amplified (a sine wave here) and some noise associated with the impedance of the signal source. The amplifier amplifies both these components but also adds a certain amount of noise (shown in green) associated with the amplification process. Quantum mechanics places a restriction on the minimum amount of this added noise and when this is achieved, the amplifier is labelled 'quantum limited'.

tum limited. The development of quantum limited amplifiers has gained considerable popularity in recent times. Apart from the detectors required to measure the state of quantum bits necessary for quantum computation, there are many other areas of research which require quantum limited detectors. Detection of gravitational radiation [13] using mechanically resonant detectors and measuring the zero point displacements of nano-mechanical resonators [14] are some examples. Presently, amplifiers based on superconducting quantum interferences devices (SQUIDs) [15] and the radio frequency single electron transistor (RF-SET) [16] are two systems which can operate close to the quantum limit.

The quantum noise associated with amplification has been discussed by many authors [17, 18, 10]. General thermodynamic constraints impose the existence of fluctu-

ations not only for dissipation but for amplification processes as well. In the limit of zero temperature, these thermal fluctuations reduce to quantum fluctuations which are governed by the Heisenberg's uncertainty principle. These quantum fluctuations determine the ultimate performance of any amplifier and hence play an important role in high precision measurements. The exact manifestation of this quantum limit depends on the kind of measurement being performed [18]. Quantum mechanics does not impose any restriction on the ultimate precision of a single measurement of a single quantity (say, position of a particle), but only on the combined precision of two conjugate variables (for example, position and momentum). For the typical case of continuous measurement of the amplitude and phase of a sinusoidal signal, the minimum noise energy (E_N) an amplifier must add to a signal at frequency ω_s is given by

$$E_N = k_B T_N = \hbar\omega_s/2. \quad (1.1)$$

Here E_N is referred to the input. This is often called the standard quantum limit and applies to phase-preserving amplifiers. The minimum noise energy (E_N) can also be expressed as a noise temperature (T_N) as shown in equation 1.1. The above limit has been derived in various ways by different authors [17, 18, 10]. A more recent analysis incorporates ideas from quantum network theory where amplification is described as an effective scattering process [19, 20]. In this treatment, signals travel to and from the amplifier via semi-infinite transmission lines. The current and voltage along the line are treated as propagating quantum fields. The incoming fields represent the input signal and fluctuations while the outgoing fields describe dissipation and output signals. The commutation properties of the input and output field operators lead to the fact that the amplifier must add a minimum amount of noise given by equation

1.1. We will use this field representation to study the quantum behavior of the JBA in chapter 7.

1.2 Amplifying using a bifurcation

The idea of amplifying signals using a bifurcation has been around for a long time [21, 22]. Any of the different types of bifurcation could be used, and only the details of the small signal sensitivity are determined by the type of bifurcation [22]. Bifurcations are quite common and have been observed in electrical, optical, chemical and biological systems (see [21] for references). An example of bifurcation amplification in nature is the ear. It turns out that the cochlea, the hearing organ in our ear, is biased close to a Hopf bifurcation [23]. This leads to several remarkable properties in our hearing like compression of dynamic range, infinitely sharp tuning at zero input and generation of combination tones. The ear is essentially a non-linear amplifier, i.e., the response depends quite strongly on the strength of the input signal. Researchers in robotics and medical sciences are currently in the process of constructing a hearing sensor which can mimic the non-linear properties of the cochlea [24].

Bifurcation amplification is also not new to the field of superconducting device physics. The well known Josephson parametric amplifiers [9] also exploit the nearness to a bifurcation. These devices are capable of achieving large gain and can show interesting quantum effects like squeezing of noise below the vacuum floor [25]. Traditionally, they have always been plagued by the "noise rise" problem where the noise tends to grow with the gain. It has been suggested that this is due to instabilities in dynamical systems operating near a bifurcation point [26]. In the JBA, we use this instability to our advantage to make a highly sensitive threshold detector. The

main application of this mode of operation of the JBA is to measure the state of superconducting quantum bits (see section 1.3). We should point out that the JBA can also be operated as a parametric amplifier (see chapter 7). We now discuss how we can access a bifurcation in a non-linear oscillator made with a Josephson junction.

1.2.1 The Josephson junction

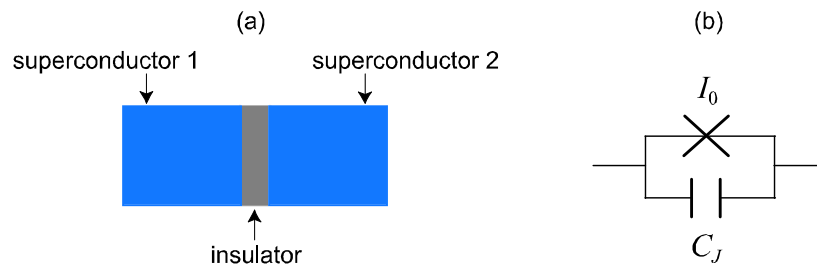


Figure 1.2: a) A simplified representation of a Josephson tunnel junction- two superconductors separated by a small insulating barrier. b) The circuit representation of a Josephson junction showing the ideal tunnel element (X) with critical current I_0 and a capacitor C_J in parallel.

The Josephson junction is made of two superconducting electrodes separated by a small insulating barrier (Fig.1.2(a)). As first understood by Josephson, the junction can be viewed as a non-linear, non-dissipative electrodynamic oscillator[3]. The tunneling of Cooper pairs in the junction manifests itself as a non-linear inductor (L_J) shunting the geometric capacitance (C_J) formed by the two electrodes and the insulating layer. The constitutive relation of the non-linear inductor also known as

the Josephson relations, can be written as

$$\begin{aligned} I(t) &= I_0 \sin \delta(t) \\ \delta(t) &= \int_{-\infty}^t dt' V(t') / \varphi_0 \end{aligned} \quad (1.2)$$

where $I(t)$, $\delta(t)$ and $V(t)$ are the current, gauge-invariant phase-difference and voltage across the junction respectively. The parameter I_0 is the junction critical current and is the maximum current that can be passed through the junction in its superconducting state. Here, $\varphi_0 = \hbar/2e$ is the reduced flux quantum. For small oscillation amplitude ($|\delta| \ll 1$), the frequency of oscillation for zero bias current is given by the so-called plasma frequency

$$\omega_p = \frac{1}{\sqrt{L_J C_J}} \quad (1.3)$$

where

$$L_J = \frac{\varphi_0}{I_0} \quad (1.4)$$

is effective junction inductance.

1.2.2 Bifurcation in a RF driven Josephson oscillator

The differential equation describing the dynamics of a Josephson junction oscillator driven with a RF current is given by

$$C_S \varphi_0 \frac{d^2 \delta(t)}{dt^2} + \frac{\varphi_0}{R} \frac{d\delta(t)}{dt} + I_0 \sin(\delta(t)) = I_{RF} \cos(\omega_d t) \quad (1.5)$$

Here δ is the gauge-invariant phase difference across the junction, I_0 is the critical current of the junction, C_S is the shunt capacitance, R is the source impedance of the

current drive and provides damping, ω_d is the drive frequency and $\varphi_0 = \hbar/2e$ is the reduced flux quantum. In our experiments, we always shunt the Josephson junction with an additional capacitance ($C_S \gg C_J$) to reduce the plasma frequency (see section 2.2). The sine term, whose origin is the current-phase relation of the Josephson junction (1.2), is the source of non-linearity in the oscillator. Under appropriate driving conditions, this non-linear oscillator can have two steady driven states differing in amplitude and phase[27, 28]. We will call these two states as the low amplitude state (O_L) and the high amplitude state (O_H) respectively. Fig. 1.3 shows the non-linear resonance curves for such a system. The figure shows a plot of the normalized oscillation amplitude ($\delta_{\max}/2\pi$) as a function of detuning ($1 - \omega_d/\omega_p$) for different drive current amplitudes.

We note that for small drive amplitudes, the response is the familiar Lorentzian response of a linear oscillator. As the drive current is increased, the resonance curves start to bend towards lower frequencies, a signature of the non-linear behavior. The direction of bending of the resonance curves is determined by the sign of the non-linear term. In the Josephson oscillator, the non-linear term is negative ($\sin(\delta) \simeq \delta - \delta^3/6$) and hence the resonance curves bend towards lower frequencies¹. For larger drive amplitudes, the solution becomes multi-valued. The two stable solutions are indicated with crosses for the curve with the largest drive amplitude (red) while the unstable solution is marked with a circle. For a given drive frequency, the systems displays bistability within a certain range of drive amplitude such that

$$I_B^- < I_{RF} < I_B^+ \quad (1.6)$$

¹The resonance curves in a system where the non-linear term is positive will bend towards higher frequencies, e.g. a mechanical reed

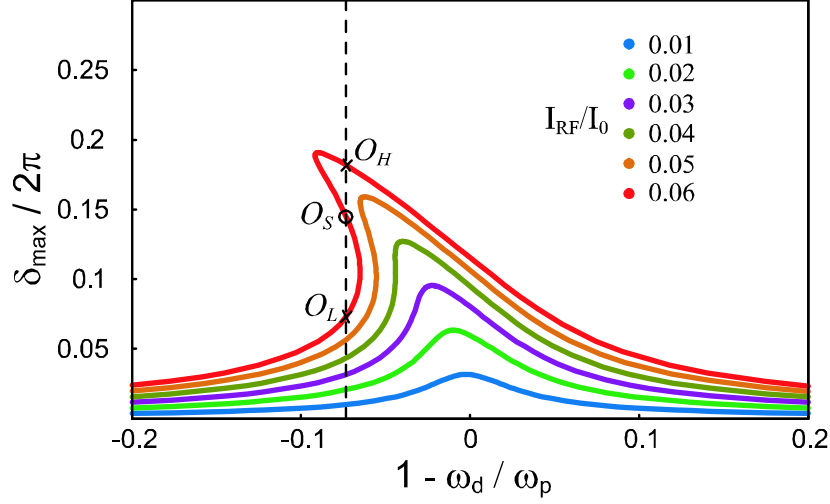


Figure 1.3: Non-linear resonance curves in a driven Josephson oscillator as a function of relative detuning $1 - \omega_d/\omega_p$ and drive amplitude I_{RF}/I_0 . ω_p is known as the plasma frequency and is the frequency for small oscillations. The resonance curves bend over as the drive amplitude is increased and become multi-valued for certain parameters. In this regime, for a given drive frequency and amplitude, there are two stable solutions (O_L and O_H) and an unstable solution (O_S). Maximum response for small amplitude oscillations occurs at $\omega_d = \omega_p$. For higher drive amplitudes, maximum response occurs at frequencies below ω_p . The sign of the first non-linear term, which is negative in our case, determines the direction of this shift.

where I_B^- and I_B^+ are called the lower and upper bifurcation currents respectively. For $I_{RF} < I_B^-$, only the low amplitude state exists while for $I_{RF} > I_B^+$, only the high amplitude exists. The saddle-node bifurcation is found in the vicinity of the upper bifurcation current I_B^+ and this where the JBA is biased. In what follows, whenever we mention bifurcation point/current, we mean the upper bifurcation point/current. This bifurcation point is extremely sensitive to the system parameters, for example the critical current I_0 .

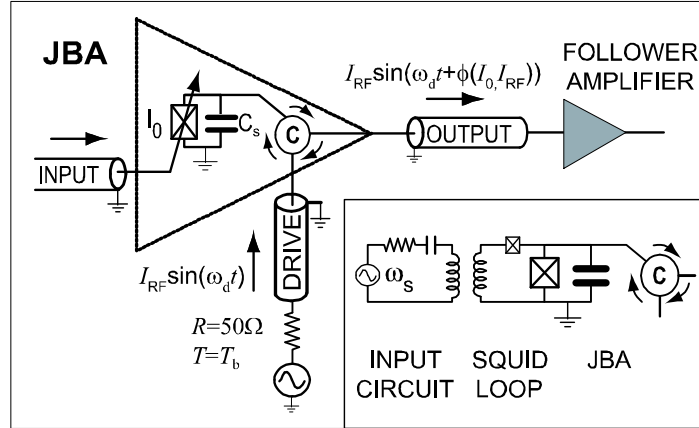


Figure 1.4: Schematic diagram of the Josephson bifurcation amplifier (JBA). A junction with critical current I_0 , parametrically coupled to the input port, is driven by an RF signal which provides the power for amplification. In the vicinity of the dynamical bifurcation point $I_{RF} = I_B$, the phase of the reflected signal ϕ depends critically on the input signal. The circulator **C** prevents the noise of the following amplifier from reaching the oscillator ensuring that the fluctuations felt by the oscillator corresponds to the noise of a 50Ω resistor at the bath temperature T_b . Inset: Example of a parametric input coupling circuit using a SQUID.

1.2.3 Operating principle of the JBA

We now describe the principle of operation of the JBA which is represented schematically in Fig. 1.4. The central element is a Josephson junction whose critical current I_0 is modulated by the input signal using an application-specific coupling scheme, such as a SQUID loop (see inset of Fig. 1.4) or a superconducting single electron transistor like in superconducting charge qubits [29]. This has been labelled as the input port. The junction is driven with a sinusoidal signal $I_{RF} \sin(\omega_d t)$ fed from a transmission line through a circulator. This is called the drive port. As explained above, when the drive frequency ω_d is detuned from the plasma frequency ω_p , the system can have two possible oscillation states which differ in amplitude and phase.

Starting in the lower amplitude state, at the bifurcation point $I_{RF} = I_B^+ \ll I_0$, the system becomes infinitely sensitive, in absence of thermal and quantum fluctuations, to variations in I_0 . In general, thermal or quantum fluctuations broaden this transition and at finite temperature T , sensitivity scales as $T^{2/3}$ (see chapter 2). The reflected component of the drive signal, measured through another transmission line connected to the circulator, is a convenient signature of the junction oscillation state which carries with it information about the input signal. This is the output port of the JBA. This arrangement minimizes the back-action of the amplifier since the only fluctuations felt at its input port arise from the load impedance of the circulator, which is physically separated from the junction via a transmission line of arbitrary length and can therefore be thermalized efficiently to base temperature². The JBA maps the tiny changes in the effective critical current of the junction (via the input signal) to changes in occupation probability of the two oscillation states which can be easily measured. This is the essence of the operation of the JBA and can be used to detect any signal which can be coupled to oscillator parameters. The main application of the JBA was to readout the quantum state of a superconducting qubit which is discussed next.

1.3 Superconducting quantum circuits

Nano-fabrication technology has enabled the fabrication of various kinds of nanoscale devices which have been shown to behave quantum mechanically. An example is superconducting quantum bits which are electronic circuits made to behave like ar-

²A common problem with DC SQUID amplifiers is the inability to cool the shunt resistors effectively [15].

tificial atoms [30]. These devices are promising candidates for building a scalable quantum computer, which relies on the coherent manipulation and entanglement of these quantum bits. In order that these systems behave quantum mechanically, they have to be well isolated from the environment but at the same time one must be able to manipulate and detect the quantum state of these systems with relative ease.

Quantum systems like atoms, ions etc. are inherently well protected from the environment and show good quantum coherence. It would seem like a natural choice to use these systems for implementing quantum bits and at present trapped ion systems are the most advanced in terms of progress towards multi-qubit systems [31, 32]. However, the small size scale, and their inherent decoupling from the environment makes it quite difficult to manipulate and detect their state, though a lot of progress has been made recently in this regard. Another major issue is the scalability of these systems. A successful implementation of a quantum computer requires thousands of such quantum bits and the ability to entangle them - a major challenge for systems based on trapped atoms/ions. This is where the solid state implementation of quantum bits may have a significant advantage, especially superconducting quantum circuits. Since these circuits are made using standard lithography techniques, it is possible to make thousands of quantum bits with relative ease. The challenge lies in a different area, namely their coherence properties which are typically much worse than their atomic counterparts. These nanoscale circuits are still much more macroscopic than their atomic counterparts, containing billions of atoms. Their macroscopic nature makes it easy to couple to them using wires, but at the same time makes them much more susceptible to sources of noise and decoherence. A lot of clever circuit design and optimal choice of fabrication material and techniques is required to pro-

tect them from environmental noise. Nevertheless, a lot of progress has been made in improving the coherence properties of superconducting quantum bits and several flavors of qubit designs with different readout schemes have emerged [6, 7, 33, 34, 28].

Superconductors are a good choice for making quantum circuits for several reasons. First, billions of electrons in a small piece of superconductor, pair up as Cooper pairs and settle down in a ground state which can be described as one collective degree of freedom [35]. This collective degree of freedom can then be used as our quantum variable to implement our "artificial atom", i.e., a superconducting circuit containing billions of atoms behaves like an effective single atom. Also, superconductors are practically dissipationless since the Cooper pairs can flow without any resistance³. Dissipation in quantum circuits can lead to decoherence. But how does one build a circuit which has energy levels like an atom? The most simple implementation of a quantum multi-level system is a quantum harmonic oscillator which in circuit representation would be a superconducting LC oscillator. At low enough temperature T such that $k_B T \ll \hbar\omega_p$, where $\omega_p = \sqrt{1/LC}$ is the plasma frequency of the oscillator, the different energy levels can be resolved. The problem with a harmonic oscillator is that all the levels have the same spacing ($\hbar\omega_p$) between them. This prevents one from isolating two levels which can then be used as an effective quantum two level system. A non-linear circuit element is required to achieve an anharmonic level structure. As discussed in the previous section, a Josephson junction behaves like a non-linear inductor and is the element of choice for building these quantum anharmonic oscillators for implementing quantum bits.

³In practice, there is always a finite amount of dissipation due to quasiparticles (unpaired electrons), but their population is suppressed exponentially at low temperatures. Also, the frequencies used must be below the gap frequency of the superconductor.

Various kinds of qubits have been implemented using superconducting tunnel junctions [30]. At the start of this thesis work, the superconducting qubit system with the longest coherence time (~ 500 ns), was the "quantronium" design developed at CEA-Saclay, France [6]. The "quantronium", also known as the charge-phase qubit, is a slight modification to the charge qubit which is based on the Cooper pair box circuit [36, 37] and was the first superconducting qubit system to demonstrate coherent oscillations [4]. One can also use superconducting loops interrupted with Josephson junctions to form what is known as the flux qubit [5]. Another design, called the phase qubit [7] uses the plasma mode of a current biased Josephson junction to implement the quantum two level system. Fig. 1.5 shows SEM images of these different types of qubits.

We have chosen the quantronium design as our qubit for the work described in this thesis. The quantronium design uses a split Cooper pair box⁴ as shown in Fig. 1.6a. In this circuit, there are two small junctions with Josephson energy $E_J/2$ and a large readout junction with a Josephson energy $E_J^R \sim 50E_J$, all in a superconducting loop. There are two control parameters which controls the energy spectrum of the quantronium— the gate charge $N_g = C_g U/2e$, and the superconducting phase δ across the two junctions which can be set by a flux ($\delta_m = \Phi/\varphi_0$) through the loop or by applying a current bias ($\delta_R = \arcsin(I\varphi_0/E_J^R)$) to the readout junction. The quantronium has a special property when biased at the so called "sweet spot" ($N_g = 0.5, \delta = 0$). At this bias point, the transition frequency between the first two qubit states is stationary with respect to both control variables N_g and δ , i.e., the system becomes immune to charge and flux noise to first order. The quantum states of the

⁴See chapter 4 and ref. [38] for more details about the quantronium circuit

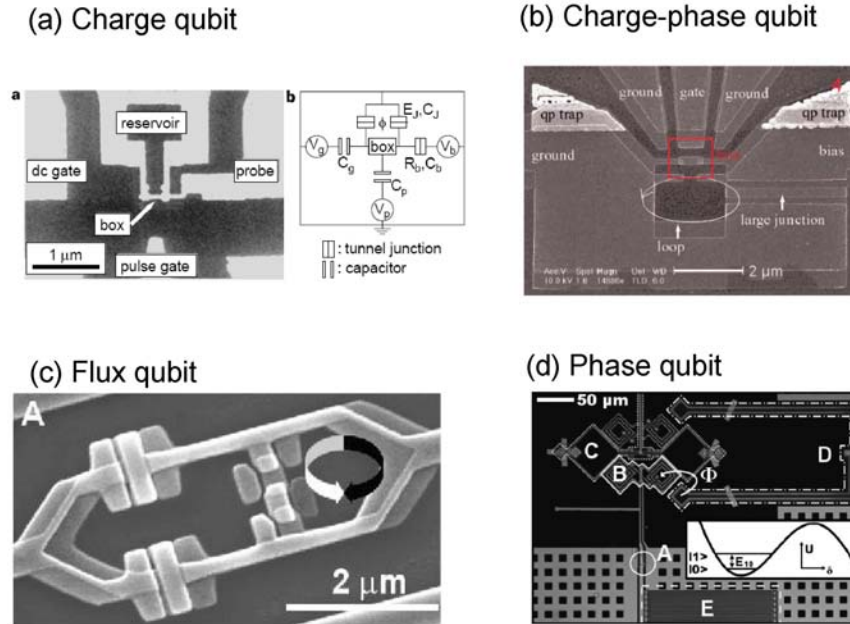


Figure 1.5: Different varieties of superconducting qubits. (a) The original charge qubit based on the Cooper-pair box and readout using a probe junction [4]. (b) The charge-phase qubit based on the split Cooper pair box. The quantum states are manipulated via the charge port while the readout is done via the phase port [6]. (c) The different quantum states of the flux qubit correspond to a different direction of the circulating current in the loop. Readout is carried out by measuring the associated flux using a SQUID [5]. (d) A phase qubit uses the two lowest levels in a current-biased Josephson junction as the quantum states. The inherent metastability is exploited for the readout [7].

qubit are now the symmetric and anti-symmetric superposition of 0 and 1 Cooper pair on the island, the average charge in both states being the same. In order to measure the qubit state, we now move in phase (δ) and measure the persistent current which flows in the loop with a qubit state dependent magnitude. This way, we avoid moving away from $N_g = 0.5$, where the qubit is protected from $1/f$ charge fluctuations which are the dominant source of decoherence in charge qubits.

The original quantum design used the switching of the readout junction from

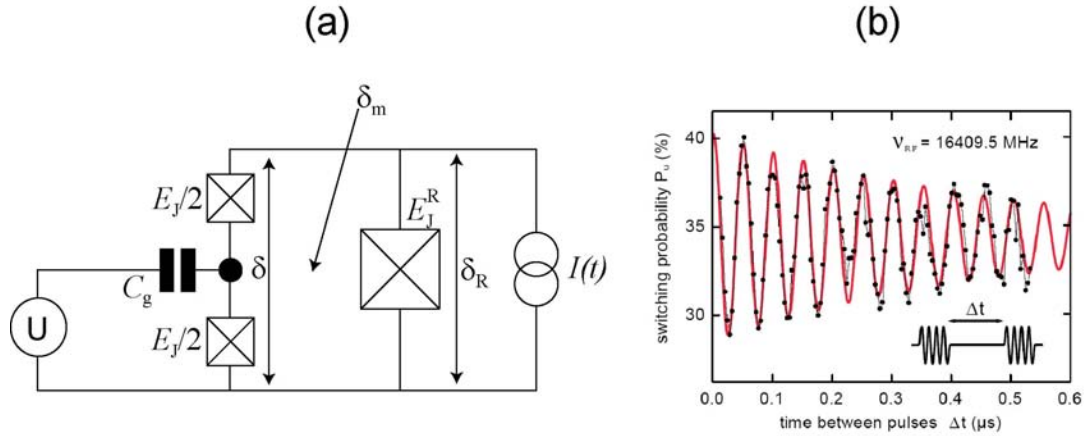


Figure 1.6: (a) The original quantronium circuit with DC readout. The quantronium is based on the split Cooper pair box which comprises of two small ($E_J/2$) Josephson junctions in a superconducting loop. A large Josephson junction (E_J^R) is inserted in the loop and used to readout the quantum state. There are two control parameters which controls the energy spectrum of the quantronium— the gate charge $N_g = C_g U/2e$, and the superconducting phase δ across the two junctions which can be set by a flux ($\delta_m = \Phi/\varphi_0$) through the loop or by applying a current bias ($\delta_R \simeq \arcsin(I\varphi_0/E_J^R)$) to the readout junction. The effective critical current of the quantronium depends on the quantum state of the qubit. The readout junction is current biased with an appropriate pulse and the switching of the junction from its superconducting state to its voltage state is monitored by measuring the voltage across the junction. The switching probability varies with the qubit state, hence providing the readout mechanism. (b) Ramsey fringe data measured in a quantronium qubit with DC readout at CEA-Saclay obtained from ref. [6]. The Ramsey decay time is about 500 ns, the longest value measured in superconducting qubits at that time. But, the readout contrast is only 10%. The improvement of the readout contrast was one of the main motivations behind the development of the JBA.

its superconducting state to the voltage state to discriminate between the qubit states. In the absence of an external current bias, the system remains at the ‘magic’ point and one can carry out quantum manipulations by applying microwave pulses to the gate port. The measurement process is initiated by passing a current through the big junction, which in turn imposes a phase across the split Cooper pair box. The loop currents thus generated, modify the amount of current flowing through the readout junction. By carefully biasing the system with a current pulse of the right amplitude and length, one can make the readout junction switch into its voltage state with high probability when the qubit is in state $|1\rangle$ and very low probability when it is in state $|0\rangle$. This way one could discriminate between the two qubit states. Fig. 1.6b shows the result of a Ramsey fringe experiment [6] yielding a coherence time $T_2 \sim 500\text{ns}$. At the start of this thesis work, this was the best result in the superconducting qubit community and an important reason for choosing this system for our work. The quantronium design also allows the separation between the read (phase) and write (charge) ports which prevents complications due to cross-talk between the read and write operation.

Nevertheless, there were still a few problems in the original design which needed to be rectified in order to achieve better operation. A major issue was the generation of quasi-particles when the readout junction switched into its voltage state. It is now widely accepted that the presence of quasi-particles near the qubit is very harmful. It leads to heating, poisoning of the qubit states and limits the repetition rate of the experiment because one has to wait long enough to make sure that all the quasi-particles have diffused out (which can be quite long at the extremely low temperatures at which the experiments are performed $\sim 10\text{ mK}$). Moreover, the recombination

process can itself produce excess noise for the adjacent circuitry[39]. The observed contrast of Rabi oscillations and Ramsey fringes was also quite low ($\sim 10\%$) [6] though it was subsequently improved to about 40% using a clever combination of flux and current bias [40]. It was clear that a better readout was needed which would address all these problems. This was the main motivation behind the development of the Josephson Bifurcation Amplifier.

Instead of probing the loop currents by biasing with a DC current and measuring the probability of switching into the voltage state, we decided to bias the junction with an AC current (microwaves) and probe the inductance of the quntronium. The readout junction was shunted with a capacitor to form a non-linear oscillator and energized with microwave pulses to bias it near a saddle-node bifurcation. The qubit state modified the bifurcation point of the non-linear oscillator which resulted in the JBA ending up in either the low amplitude state or the high amplitude state depending on whether qubit was in state $|0\rangle$ or $|1\rangle$. Analogous to the previous measurement scheme one can now measure the probability of switching from one oscillation state to another to discriminate between the qubit states. This purely dispersive method has the advantage of high speed and high fidelity, with no on-chip dissipation. This method avoids generation of quasi-particles since the readout junction remains in the superconducting state at all times.

The next section briefly summarizes the key results obtained in this thesis.

1.4 Summary of key results

1.4.1 JBA Measurements

The existence of a plasma like mode of oscillation in Josephson junctions was first predicted by Josephson himself [3]. Several experiments followed which probed the microwave power absorption at the plasma resonance [41, 42]. In our experiment, we directly measure the plasma resonance in a coherent microwave reflection experiment, measuring both the magnitude and the phase of reflected microwave signal. Typical junction fabrication parameters limit the plasma frequency to the 20 - 100 GHz range where techniques for addressing junction dynamics are inconvenient. We have chosen to shunt the junction by a capacitive admittance to lower the plasma frequency by more than an order of magnitude and attain a frequency in 1-2 GHz range (microwave L-band). In this frequency range, a simple on-chip electrodynamic environment with minimum parasitic elements can be implemented, and the hardware for precise signal generation and processing is readily available. Since there is no intrinsic dissipation in the oscillator in principle⁵, the phase of the reflected signal contains all the information about the resonance characteristics. The response of the system was studied in both the linear and non-linear regime by varying the drive power and the result is shown in Fig. 1.7.

The normalized reflected signal phase as a function of drive frequency and power is presented in the right panel of Fig. 1.7 as a two dimensional color plot. For small excitation power, we recover the linear plasma resonance at 1.54 GHz, shown in yellow corresponding to $\phi = 0$. As the power is increased above -115 dBm, the

⁵In practice, the on-chip capacitive admittance always provides some dissipation but it is usually very small.

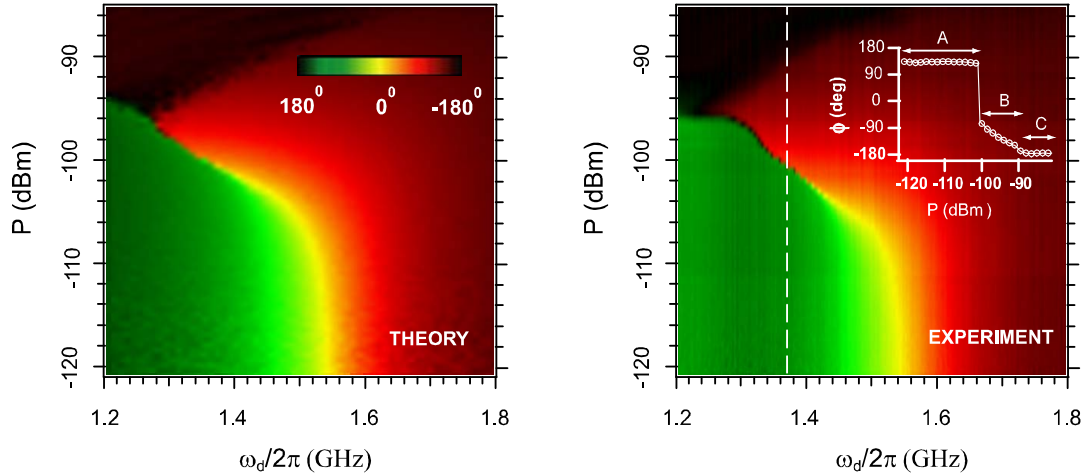


Figure 1.7: Normalized reflected signal phase ϕ (wrap-around color scheme) as a function of excitation frequency $\omega_d/2\pi$ and excitation power P . Experimental data is shown in the right panel. A vertical slice taken at $\omega_d/2\pi = 1.375$ GHz (dashed line in the inset) shows the abrupt transition between two oscillation states of the system. The left panel is the result of numerical simulations of the full circuit including stray elements, and shows very good agreement with the experimental results.

plasma frequency decreases as expected for the non-linear oscillator. The boundary between the leading-phase region (green) and the lagging-phase region (red) therefore curves for high powers. When we increase the drive power at a constant frequency slightly below the plasma frequency, the phase as a function of power undergoes an abrupt step (dashed line), as predicted. This represents the transition from the low amplitude state to the high amplitude state. For yet greater powers (> -90 dBm), we encounter a new dynamical regime (black region in Fig. 1.7) where δ appears to diffuse between the wells of the cosine potential. This was confirmed by the presence of an unambiguous audio frequency AC resistance in the black region (see section 3.4). In the inset of right panel of Fig. 1.7, we illustrate the sequence of dynamical transitions by plotting ϕ as a function of incident power at $\omega_d/2\pi = 1.375$ GHz. For

$P < -102$ dBm, the phase is independent of power (δ oscillates in a single well in the harmonic-like, phase-leading state, letter A). For -102 dBm $< P < -90$ dBm, the phase evolves with power and δ still remains within the same well, but oscillates in the anharmonic phase-lagging state (letter B). Finally, for $P > -90$ dBm, the average phase of the reflected signal saturates to -180 degrees, corresponding to a capacitive short circuit. This last value is expected if δ hops randomly between wells, the effect of which is to neutralize the Josephson inductive admittance.

The above measurements were taken using a network analyzer which only allows for slow frequency sweeps. In other measurements (see Chapter 3), where the power is ramped in less than 100 ns, we verified that the transition between dynamical states is hysteretic, another prediction of the theory. To explain the complete frequency and power dependence of the transitions shown in the right panel of Fig. 1.7, we have performed numerical simulations by solving the full circuit model (equation 1.5 + stray elements). The result of this calculation is shown in the left panel of Fig. 1.7. It correctly predicts the variation of the plasma frequency with excitation power, and the boundaries of the phase diffusion region. The agreement between theory and experiment is remarkable in view of the simplicity of the model which uses only measured parameters, and only small differences in the exact shape of region boundaries are observed.

1.4.2 Qubit measurements

As discussed in section 1.2, the transition from the low amplitude state to the high amplitude state of the JBA depends sensitively on the critical current of the junction. This is exploited to make a readout for superconducting qubits using the JBA. The

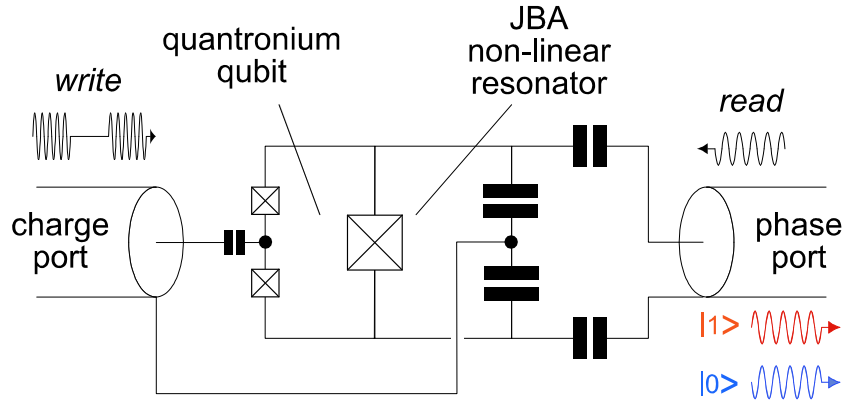


Figure 1.8: Schematic showing the measurement setup of a quantronium with JBA readout. The big readout junction along with the shunt capacitors forms the non-linear oscillator which is the central element of the JBA. The quantronium and the non-linear oscillator are coupled via the shared readout junction. Qubit manipulations are carried out by sending microwave pulses to the charge (write) port while the state of the qubit can be measured by sending microwave pulses to the phase (read) port.

general idea of the readout is depicted in Fig. 1.8.

The quantronium qubit and the JBA are coupled via the shared big junction. The quantum state of the qubit affects the critical current of the readout junction and hence the state of the qubit can be readout by measuring the state of the JBA. The qubit state is prepared by sending microwave pulses to the charge port (chapter 4) while the readout operation is performed by sending microwave pulses to the phase port and analyzing the phase of the reflected signal. This way, the state of the qubit is encoded in the phase of the signal reflected from the JBA. A typical qubit measurement sequence starts with qubit preparation and manipulation by sending appropriate microwave pulses to the charge port. This is followed by a readout operation where a microwave pulse is sent to the phase port which energizes the JBA and biases it near its bifurcation point. The signal reflected from the JBA is

then analyzed to determine whether the JBA is in the low amplitude state or the high amplitude state. The process is then repeated thousands of times and the probability of switching from the low amplitude to the high amplitude state is determined (output signal). The measurement is arranged so that the switching probability is close to zero when the qubit is in its ground state while the switching probability is close to one when the qubit is in its first excited state. Ideally, we would like the switching probability to be zero for qubit ground state and one for qubit excited state. The optimization of the qubit readout performance is discussed in chapter 6.

The coherence properties of different qubit samples were measured and typical results are shown in Fig. 1.9. Panel (a) shows the Rabi oscillation data. The Rabi decay time \tilde{T}_2 was found to be in the range $0.8 - 1.7 \mu\text{s}$ depending on the sample and precise biasing conditions. A linear dependence of the Rabi oscillation frequency ν_{Rabi} with the microwave drive amplitude U_{RF}^{max} was observed (see Fig. 5.7b), in agreement with the theory of driven two level quantum systems. We can now calibrate the π pulse required to prepare the qubit in the excited state. Panel (b) shows the decay of the excited state lifetime (T_1) with typical lifetimes being in the range of $1 - 5 \mu\text{s}$. The values of T_1 obtained with our dispersive readout are comparable with the results of Vion *et. al.* [6], but are significantly shorter than the values expected from coupling to a well thermalized 50Ω microwave environment shunting the qubit. The loss mechanisms giving rise to the observed energy relaxation are not understood at this time. Panel (c) shows the Ramsey oscillation data which allows one to measure the decay time of qubit phase coherence during free evolution of the qubit state. Typical Ramsey decay times observed were $T_2 \sim 300 \text{ ns}$. The Ramsey fringes decay time T_2 has a component due to energy relaxation and one due to

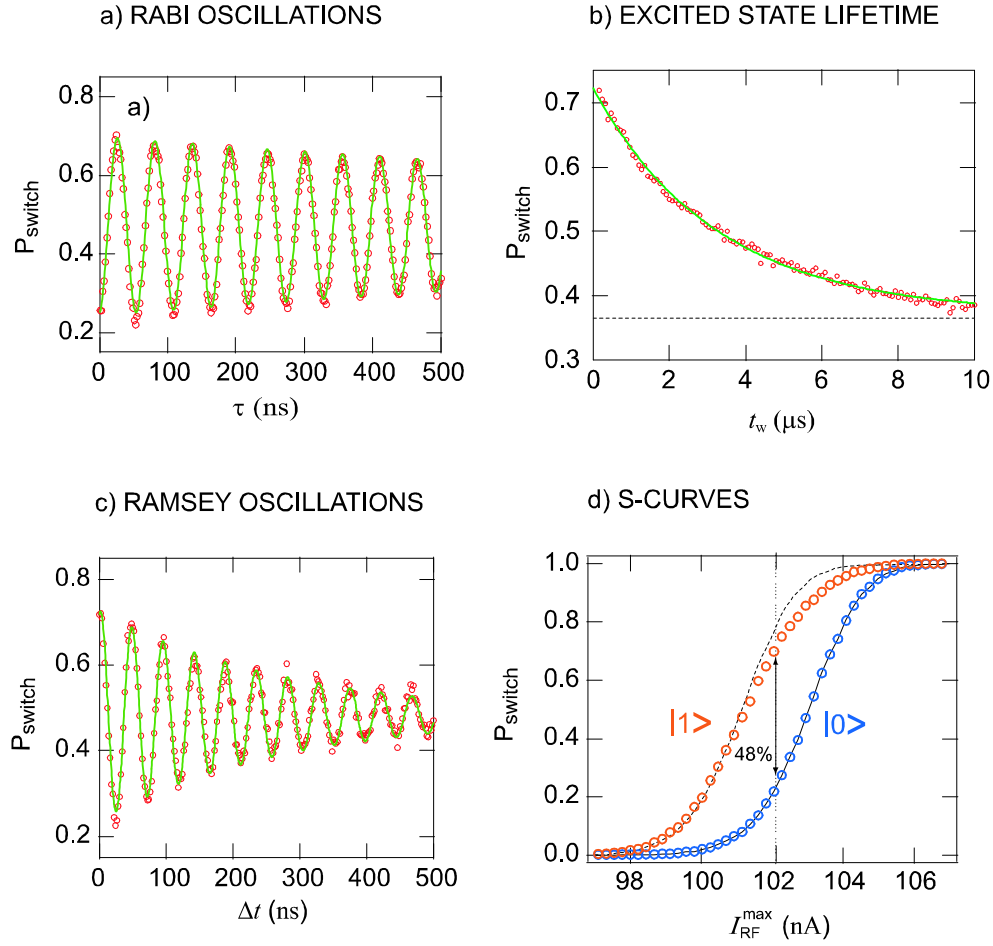


Figure 1.9: Summary of qubit coherence measurement. (a) Rabi oscillations of the switching probability as a function of the duration τ of a square pulse applied on the gate. Solid green curve is an exponentially decaying sinusoidal fit with $T_2 = 1.6 \mu\text{s}$. (b) Decay of the excited state switching probability after preparing the qubit in the excited state by a π pulse, as a function of the waiting time t_w between the preparation pulse and the readout pulse. Solid green curve is an exponential fit with a decay constant $T_1 = 3.2 \mu\text{s}$. The dashed line indicates the value of P_{switch} in the absence of a π pulse. (c) Ramsey fringes obtained with two $\pi/2$ pulses separated by the time interval Δt . The pulse frequency was detuned from the Larmor frequency by 20 MHz. The green curve is an exponentially decaying sinusoid fit. The decay time T_2 is 320 ns. (d) Switching probability as a function of maximum drive current and qubit state. The vertical dotted line represents value of drive current at which maximal difference in P_{switch} is observed. The solid line connects the observed data points in the $|0\rangle$ state and the dashed line is a copy of the solid line horizontally shifted to overlap the $|1\rangle$ state data at low values of P_{switch} .

pure dephasing: $1/T_2 = 1/(2T_1) + 1/T_\varphi$, where T_φ represents pure dephasing. In our measurements, T_2 is usually dominated by pure dephasing which is due to fluctuations in the qubit transition frequency originating from $1/f$ offset charge noise. Recent qubit measurements using the cavity version of the JBA show that the dephasing times are compatible with the magnitude of the typical $1/f$ offset noise seen in these systems [43]. Immunity to $1/f$ charge noise can be achieved by increasing the E_J/E_C ratio in these qubits and we observed some improvement in the pure dephasing time for such samples (see chapter 5). This strategy is now being implemented in some new qubit implementations which use very large E_J/E_C ratios to almost eliminate the gate charge dependence of the transition frequency [44, 45].

Panel (d) shows the S-curves corresponding to the qubit being in the ground and excited state. The open circle points in blue and red correspond to data for the qubit ground and excited states respectively while the solid black line is the best fit through the ground state data. The dashed black line is the same as the solid black line but shifted to match the excited state data for low switching probabilities. This was done to indicate the small difference in the shape of the excited state S-curve resulting in the reduction of readout contrast. The observed contrast for this data is about 15 – 30 % smaller than expected. In a set of experiments described in chapter 6, we used two readout pulses in succession to determine that a 15 – 30 % loss of qubit population occurs, even before the resonator is energized to its operating point. We attribute this loss to spurious on-chip defects [46]. As photons are injected into the resonator, the effective qubit frequency is lowered due to a Stark shift via the phase port [47]. When the Stark shifted frequency coincides with the frequency of an on-chip defect, a relaxation of the qubit can occur. Typically, the qubit frequency

spans 200 – 300 MHz before the state of the qubit is registered by the readout, and 3 – 4 spurious resonances are encountered in this range. Chapter 6 discusses these issues in more detail.

1.4.3 Escape measurements in the quantum regime

The ultimate sensitivity of the JBA depends on the effective intensity of fluctuations felt by it at the operating temperature (chapter 2). As the operating temperature approaches zero, quantum fluctuations start becoming important. In the classical regime, the transitions are governed by some kind of activation process and thermal noise activates the system over an effective barrier [27]. But what mechanism governs the transition as $T \rightarrow 0$? More importantly, what sets the classical to quantum crossover temperature? Borrowing ideas from the theory of macroscopic quantum tunnelling (MQT) in current biased Josephson junctions (see [48] and references therein), we can make an educated guess that the crossover temperature must be related to the plasma frequency of the oscillator. It turns out that for this driven, non-linear system, the transition between the metastable states is predominantly due to an activation process even as $T \rightarrow 0$ [49, 50, 51], but the origin of fluctuations is the zero-point fluctuations of the oscillator. There has also been some recent work on the signatures of quantum behavior in driven non-linear systems and its dependence on system parameters [52].

The escape in the quantum regime is closely connected to the Dynamical Casimir Effect (DCE)—an elusively weak phenomenon predicted about 40 years ago [53, 54] but whose theory remains essentially experimentally unverified. In perhaps the most promising opto-mechanical realization of the DCE [55], one of the mirrors of a Fabry-

Perot cavity is driven by a force that periodically varies the cavity's geometric length at a frequency Ω which is a multiple of the lowest cavity mode frequency ω_0 . According to prediction, even when the cavity is at a low temperature T such that it is initially void of all real electromagnetic radiation ($\hbar\omega_0 \gg k_B T$) and contains only virtual zero-point quantum fluctuations, the mirror motion should spontaneously create thermal radiation inside the cavity. Our experiment implements a fully electrical version of the DCE where we have periodically varied the frequency of an electromagnetic resonator not by mechanical means, but through an element whose reactance can be modulated by an electrical signal. This element is the Josephson tunnel junction in the JBA which can be modelled as an inductor which is both non-linear and purely dispersive. The non-linearity enables electrical modulation of the resonator inductance while the absence of dissipation eliminates parasitic channels of heat production.

Our implementation can be classified as a pumped, doubly degenerate parametric resonator operating in the quantum regime. Its operation can be described as the parametric conversion of positive frequency components at the idler and signal frequencies into their negative counterparts. Josephson parametric amplifiers[9] which essentially perform the same function are also potential candidates for observing the DCE, but a major experimental challenge is to detect the small effective temperature of the output photon field produced by the DCE, and requires a detector with minimal coupling loss and quantum-noise limited sensitivity. In our experiment, we use a unique approach by operating the non-linear resonator close to a saddle-node bifurcation which can then also function as a detector. Thermal noise that, according to the DCE, should be generated from the amplification of quantum fluctuations inside

the resonator, here provokes the switching of the system from the initially prepared low amplitude state into the high amplitude state. By performing a calibration in the high temperature regime where the switching process is dominated solely by ordinary black-body thermal radiation, we can infer the temperature of the spontaneously created noise in the quantum regime and compare it to theory.

The theory of quantum escape [49, 50, 51] predicts⁶ that the effective temperature is given by

$$T_{eff}(T) = \frac{\hbar\omega_d}{2k_B} \coth\left(\frac{\hbar\omega_d}{2k_B T}\right) \quad (1.7)$$

From the above equation, we can see that in the classical regime ($k_B T \gg \hbar\omega_d$), the effective temperature T_{eff} tends to the physical temperature T . On the other hand, as $T \rightarrow 0$, $T_{eff} \rightarrow \hbar\omega_d/2k_B$. We note that this result is different from the MQT results where the saturation temperature is given by $\hbar\omega_d/7.2k_B$ [48]. This is due to the fact the escape from the metastable state in the JBA takes place via quantum activation and not via tunneling.

The experimental procedure is similar to the MQT experiment [48]. We bias the JBA near the bifurcation point and monitor the rate of escape as a function of the distance to the bifurcation point. Since we know this expected dependence from theory [27], we can infer the effective escape temperature. This experiment is then repeated for different temperatures and the corresponding escape temperatures are recorded (see chapter 8 and [56]). Since we expect the escape temperature to be equal to the physical temperature in the classical regime, we normalize the data so that the measured escape temperature matches the physical temperature in the classical regime. This can only be done if we are sure that the only source of fluctuations

⁶This result is derived in Chapter 7 using a different approach based on Input-Output theory.

felt by the system in the classical regime is the thermal noise corresponding to that temperature. In order to verify this, we also measured at every temperature point, the escape from the DC current biased junction which provides an independent calibration of the noise intensity in the system. We then observe how the escape temperature in the RF case varies as the physical temperature is lowered. The experiment was performed on two samples with different plasma frequency and the result is shown in Fig. 1.10.

The blue square points correspond to the sample with the $\omega_p/2\pi = 1.67$ GHz while the red circles correspond to the sample with $\omega_p/2\pi = 4.69$ GHz. The corresponding drive frequencies are $\omega_d/2\pi = 1.525$ GHz and $\omega_d/2\pi = 4.450$ GHz. The solid colored lines are a plot of equation 1.7 as a function of physical temperature for the corresponding values of drive frequency. We note that the solid lines fit the data quite well. The dashed black line represents the equation $T_{esc} = T$ for comparison. In the inset, we show the data for the escape temperature inferred from DC switching measurements and the DC saturation temperatures are indicated with colored arrows on the main plot. For our system parameters, we should have measured $T_{eff}^{MQT} = T$ over the entire temperature range. We believe that the small residual deviations are due to improperly thermalized filters and noise in the dual biasing configuration. Another possibility is the contribution of higher frequency plasma dynamics due to residual inductance in series with the shunting capacitor. Nevertheless, we note that the data for escape in the quantum regime agrees well with the theoretical predictions and the saturation temperatures corresponds to $\hbar\omega_d/2k_B$. This experiment provides evidence for the existence of the electrical version of DCE at microwave frequencies involving a Josephson junction RF driven near its dynamic bifurcation point. From the point of

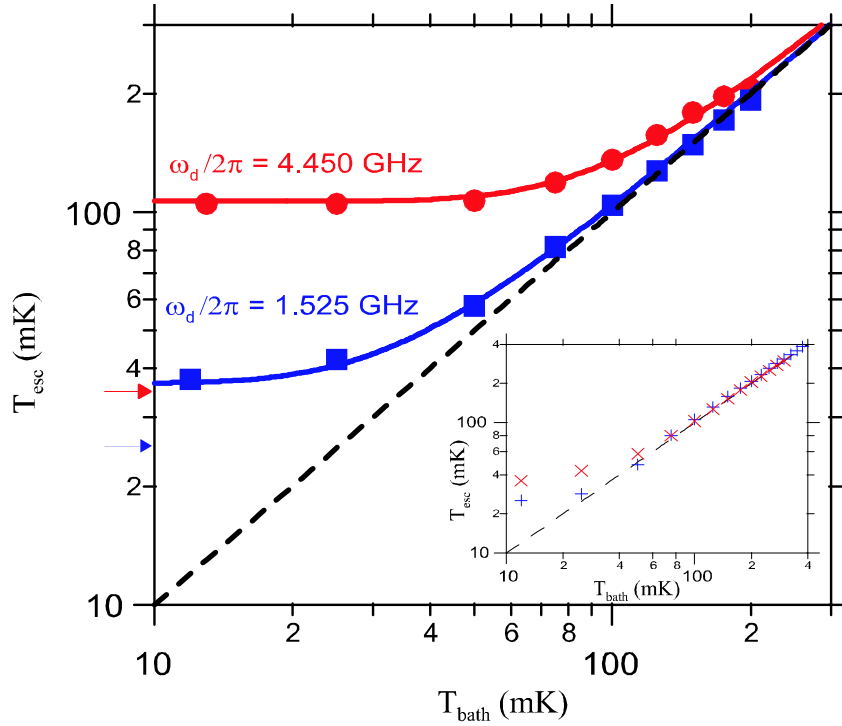


Figure 1.10: Escape temperature v.s. bath temperature for an RF driven Josephson oscillator biased near a bifurcation point. The escape temperature is inferred by monitoring the transition rates from the low amplitude to the high amplitude state of the Josephson oscillator. The blue square points correspond to the sample with the $\omega_p/2\pi = 1.67$ GHz while the red circles correspond to the sample with $\omega_p/2\pi = 4.69$ GHz. The corresponding drive frequencies are $\omega_d/2\pi = 1.525$ GHz and $\omega_d/2\pi = 4.450$ GHz. The solid colored lines are a plot of equation 1.7 as a function of physical temperature for the corresponding values of ω_d . We note that solid lines fit the data quite well. The dashed black line represents the equation $T_{esc} = T$ for comparison. The errors in the measurement of escape temperature are set by the amount of statistics obtained and the stability of the drive power. It is usually less than 5%. In the inset, we show the data for the escape temperature inferred from DC switching measurements and the DC saturation temperatures are indicated with colored arrows on main plot.

view of signals coming from the load impedance, the RF biased junction behaves as a parametric amplifier and, in the quantum regime, converts quantum fluctuations into thermal noise. In other experiments described in chapter 8, we have characterized the performance of the JBA as a parametric amplifier for amplifying small signals coupled via the drive port. Data indicates that performance near the quantum limit is possible.

1.5 Thesis overview

Quantum measurements of solid-state systems, such as the readout of superconducting quantum bits challenge conventional low-noise amplification techniques. Ideally, the amplifier for a quantum measurement should minimally perturb the measured system while maintaining sufficient sensitivity to overcome the noise of subsequent elements in the amplification chain. Additionally, the drift of materials properties in solid-state systems mandates a fast acquisition rate to permit measurements in rapid succession. In this thesis, we harness the sensitivity of a dynamical system - a non-linear oscillator tuned near a bifurcation point to meet these requirements. In this new scheme, all available degrees of freedom in the dynamical system participate in information transfer and none contribute to unnecessary dissipation resulting in excess noise. We have used a superconducting tunnel junction which can be viewed as a non-linear inductor to construct our non-linear oscillator. The superconducting tunnel junction is the only electronic circuit element which remains non-linear and non-dissipative at arbitrary low temperatures. As the key component of present superconducting amplifiers, it is known to exhibit a high degree of stability.

We have performed a novel, phase-sensitive, microwave experiment demonstrat-

ing that the Josephson plasma oscillation can transition between the two dynamical states predicted for a driven non-linear system[28]. Using different samples, we have shown that this dynamical phenomenon is stable, reproducible and can be precisely controlled, thus opening the possibility for practical applications like amplification which we call the Josephson Bifurcation Amplifier. A signal coupled to the critical current of the junction can be detected by monitoring the changes in the dynamical state of the non-linear oscillator[57]. This approach was used to develop a non-linear, dispersive readout for superconducting qubits by coupling a Cooper-pair box with the JBA[29]. In order to perform a readout, the resonator is RF-energized to a level where its oscillation state now acts as a sensitive pointer of the qubit state. This technique does not generate any dissipation on chip since the resonator is only damped by circuitry outside the chip, i.e., a $50\ \Omega$ transmission line with a matched circulator and amplifier, and enables a high-fidelity qubit readout with a MHz repetition rate. We have measured Rabi oscillations and Ramsey fringes with sufficient speed that real time filtering to correct for drifts in the charge and flux bias becomes possible. Also, several successive readouts may be performed within the energy relaxation time of the qubit (T_1). This gives valuable information on the readout-induced interaction between the qubit and its environment, and accounts for the observed contrast. The JBA was also used as a parametric amplifier to amplify small signals coupled via the drive port (as opposed to parametric coupling of signals in the qubit readout) achieving signal gain of about 20 dB and near quantum limited noise temperature. The parametric amplifier model of the JBA also helps us understand its behavior in the quantum regime. The dynamical transition between the metastable states of the JBA takes place via an activation process even in the limit $T \rightarrow 0$ as opposed to a tunnel-

ing process for escape in static systems. The JBA acts as a parametric amplifier for the quantum fluctuations and converts them into thermal fluctuations which in turn leads to the activation process which causes transitions. Theory predicts that the effective temperature of the amplified quantum noise is given by $\hbar\omega_d/2k_B$ where ω_d is the drive frequency. Experimental data shows good agreement with this prediction.

The material in this thesis is arranged as follows. Chapter 2 describes the theoretical aspects of the JBA, discussing the properties of the driven, non-linear oscillator and how it is used to build an amplifier. Chapter 3 deals with the experiments conducted to characterize the performance of the JBA and also discusses some practical aspects of implementing a JBA. Chapter 4 talks about the implementation of the qubit readout using the JBA. The properties of the basic Cooper-pair box is discussed followed by the implementation of the quantronium qubit and how to measure it using the JBA. The expected readout performance is characterized with the help of numerical simulations. Chapter 5 discusses the experiments which characterize the coherence properties of the quantronium qubit with a JBA readout. Both frequency domain and time domain measurements are discussed. Chapter 6 deals with the issue of qubit readout performance. It describes experiments with multiple readout pulses to determine the information flow during a qubit readout and to account for any losses in qubit population. Experiments which characterize the losses in the environment coupled to the qubit are also discussed. We move on to discuss the JBA as a doubly degenerate parametric amplifier in Chapter 7. This chapter uses Input-Output theory to describe the physics of escape from metastable states. This technique is applied to the JBA which provides useful insights into its behavior in the quantum regime. Chapter 8 then describes experiments which explore the behavior of the JBA as it

goes from the classical to the quantum regime. In particular, measurements of the transition rates from the low amplitude to the high amplitude states as a function of temperature, are described. Data describing the performance of the JBA as a parametric amplifier are also presented. Finally, we provide some directions for future experiments in chapter 9 and conclusions of this thesis in chapter 10.

Chapter 2

Josephson Bifurcation Amplifier: Theory

In this chapter we will introduce the Josephson Bifurcation Amplifier (JBA), the main subject of research in this thesis. We will begin by describing a driven, non-linear oscillator and its properties. We will then describe how one can use such a system to make a sensitive detector/amplifier. Finally, we will discuss the various properties of the JBA and derive formulae to compute its performance.

2.1 General properties of a driven non-linear oscillator

Periodically driven non-linear oscillators often have several stable states, that correspond to steady state oscillations differing in their amplitude and phase. A well known example of a non-linear oscillator is a simple pendulum(Fig. 2.1 (a)).

In a linear oscillator, the restoring force is proportional to the displacement. But the restoring force in a pendulum is proportional to the sine of the angle θ_v with respect to the vertical, which makes it non-linear. In other words, the frequency of oscillations depends on its amplitude or energy. As the oscillation energy increases,

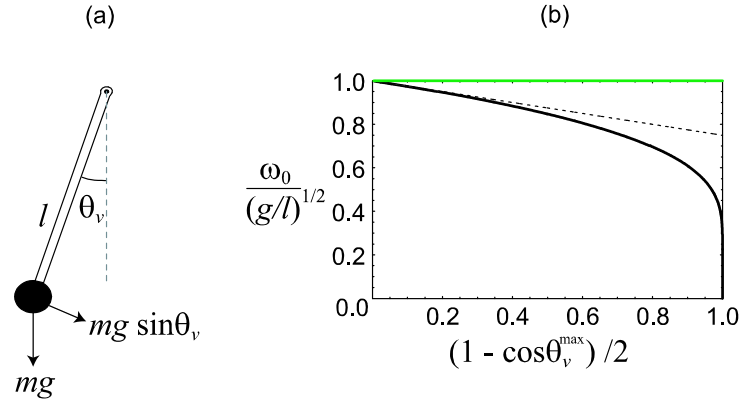


Figure 2.1: a) Simple pendulum as a non-linear oscillator. The restoring force is proportional to the sine of the angular displacement which is the origin of the non-linearity. The frequency for small oscillations is given by $(g/l)^{1/2}$. b) A plot of the normalized angular frequency ($\omega_0/(g/l)^{1/2}$) as a function of the normalized oscillation energy of the pendulum. θ_v^{\max} now refers to the amplitude of oscillation. The energy of oscillation is given by the potential energy at maximum displacement i.e. $mgl(1 - \cos \theta_v^{\max})$ with the maximum value mgl at $\theta_v^{\max} = \pi$. We note how the frequency first decreases linearly with energy. The slope at the origin is $-1/4$ as indicated by the dashed line. The green line is the expected behavior for a linear oscillator. We have assumed that there is no damping in the pendulum

the frequency of oscillation decreases ($\sin \theta_v^{\max} \leq \theta_v^{\max}$). This behavior is illustrated in Fig. 2.1(b). The frequency of small oscillations ($\sin \theta_v \simeq \theta_v$) is given by $\omega_0 = \sqrt{g/l}$, where g is the acceleration due to gravity and l is the length of the pendulum. Now consider the situation where the pendulum is subject to periodic driving at a frequency $\omega_d < \omega_0$. If the pendulum has finite damping, this driving frequency has to satisfy¹ $\omega_0 - \omega_d > \sqrt{3}\Gamma$ where Γ is the amplitude damping coefficient. For a large enough strength of driving, the pendulum can respond in two different ways [58]. It can either respond by oscillating with a small amplitude at frequency ω_d where its natural frequency ($\sim \omega_0$) is different than the driving frequency. This is the

¹This condition is derived in the next section

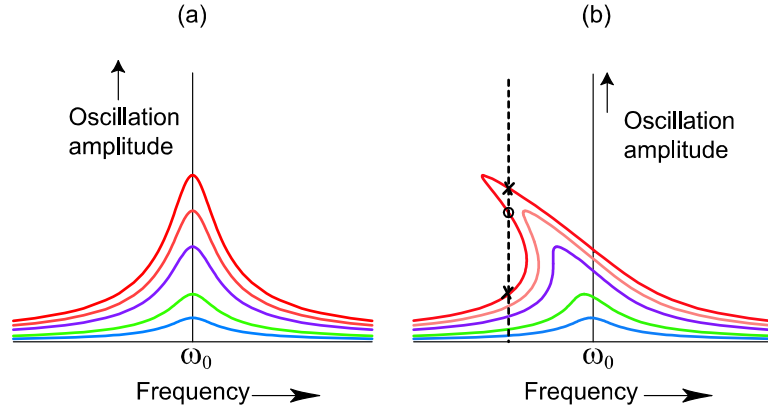


Figure 2.2: Oscillation amplitude of a linear and non-linear oscillator as a function of frequency for increasing drive amplitudes. a) Linear oscillator: the shape of the resonance curve doesn't change with drive amplitude. Maximum response occurs at the natural frequency ω_0 . b) Non-linear oscillator: the resonance curves bends over as the drive amplitude is increased and becomes multi-valued for certain parameters. Maximum response for small amplitude oscillations occurs at ω_0 . For higher drive amplitudes, maximum response occurs at frequencies below ω_0 . The sign of the first non-linear term which is negative for the pendulum, determines the direction of this shift. The intersection of the dashed line with the red curve shows the two possible oscillation states (x). The intersection marked with a circle corresponds to an unstable state. This is discussed in the next section.

off-resonant behavior. Or, it can oscillate with a larger amplitude thereby lowering its natural frequency and bringing it closer to the driving frequency. This is the resonant behavior. These two modes of oscillation are possible for the same driving condition, i.e., the system is bistable. In contrast to a linear oscillator, it is possible to drive a non-linear oscillator into resonance by changing either the frequency or amplitude. An example of resonance curves in a linear and non-linear oscillator is shown schematically in Fig. 2.2. This phenomenon is quite generic in non-linear oscillators provided certain conditions are satisfied. We will discuss these conditions in detail in the next section.

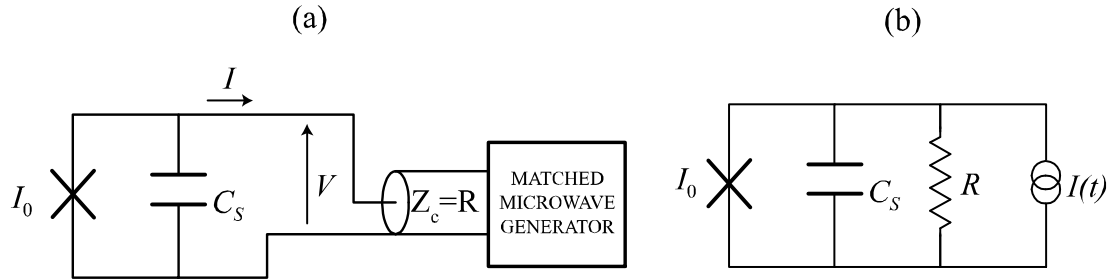


Figure 2.3: Circuit diagram of a capacitively (C_S) shunted Josephson junction biased with a current source $I(t)$ with source impedance R .

2.2 Josephson junction oscillator

In this section, we will describe how to use a Josephson junction to make a non-linear oscillator. This will be our prototypical system from now on and we will use this example to discuss the properties of a driven non-linear oscillator.

2.2.1 Bistability in driven Josephson oscillator

The Josephson junction was introduced in section 1.2.1 and can be viewed as a non-linear inductor. In our experiments, we always shunt the Josephson junction with an additional capacitor (C_S) to bring down the plasma frequency from around 20 GHz to about 1.5 GHz so that the microwave circuit design is easier to implement. Since $C_S \gg C_J$, we will ignore the junction capacitance C_J from now on. The effective circuit in our experiments can be reduced to that a capacitively shunted junction driven by a current source $I(t)$ with source impedance R . The circuit is shown in Fig.2.3b and the equation describing its dynamics is given by

$$C_S \varphi_0 \frac{d^2 \delta(t)}{dt^2} + \frac{\varphi_0}{R} \frac{d\delta(t)}{dt} + I_0 \sin(\delta(t)) = I(t). \quad (2.1)$$

Note that the above equation is identical to the well known RCSJ equation (resistively and capacitively shunted junction). The resistance R is often used in literature to describe the quasi-particle resistance of the junction. It is also used to describe a shunt resistance whose function is to damp the plasma oscillations of the junction. This is not the case here. In our experiments, we use microwave signals, propagating on a transmission line to bias the Josephson oscillator (Fig.2.3a). Here, the resistance R describes the characteristic impedance (which is real) of the transmission line or equivalently, the source impedance of the matched, microwave signal generator. At microwave frequencies, there are no ideal current or voltage sources and they usually have a finite source impedance $R = 50 \Omega$. We have chosen to represent the microwave source as an ideal current source shunted with a resistance R . Since we always work with the junction in its superconducting state, the Josephson oscillator has no intrinsic dissipation². Dissipation enters equation 2.1 only due to the fact that the oscillator is connected to a transmission line which provides a mechanism for energy to leak out of the oscillator. See section 7.1 for a more detailed discussion of these ideas.

In equation 2.1, the non-linear term is given by the sine of the phase difference across the junction - just like in the pendulum. Similarly, the frequency of natural oscillations decreases with increasing amplitude. We will now derive the condition for bistability when this non-linear oscillator is subject to harmonic driving, i.e., $I(t) = I_{RF} \cos(\omega_d t)$. Rewriting the above equation for a harmonic drive at frequency ω_d , and retaining only the first non-linear term in the expansion of the sine term, we

²This is true provided the operating temperature (~ 10 mK) is much lower than the critical temperature of the superconductor (~ 1 K). Also the frequencies used (~ 1 GHz) are much below the gap frequency (~ 100 GHz) of the superconductor.

get:

$$\frac{d^2\delta(t)}{dt^2} + 2\Gamma\frac{d\delta(t)}{dt} + \omega_p^2\left(\delta(t) - \frac{\delta(t)^3}{6}\right) = \omega_p^2\frac{I_{RF}}{I_0}\cos(\omega_d t) \quad (2.2)$$

where $\Gamma = 1/2RC_S$ is the damping rate of the oscillation amplitude and $\omega_p = \sqrt{I_0/(\varphi_0 C_S)}$ is the plasma frequency. We expect that the oscillator will respond predominantly at the frequency of driving (ω_d). Therefore, it is convenient to describe the dynamics by using dimensionless, slow complex amplitudes [27] as below:

$$\delta(t) = \sqrt{\frac{2\omega_d\Delta\omega}{3\gamma}} (u(\tau)\exp(i\omega_d t) + u^*(\tau)\exp(-i\omega_d t)) \quad (2.3)$$

where

$$\gamma = \omega_p^2/6 \quad (2.4)$$

is the magnitude of the coefficient of the non-linear term ($\propto \delta(t)^3$),

$$\Delta\omega = \omega_p - \omega_d \quad (2.5)$$

is the detuning of the drive from the plasma frequency, and

$$\tau = \Delta\omega t \quad (2.6)$$

is the new dimensionless, slow time variable. Substituting 2.3 into 2.2, we get:

$$\frac{\Delta\omega}{\omega_d}\frac{d^2u}{d\tau^2} + \left(\frac{2\Gamma}{\omega_d} + 2i\right)\frac{du}{d\tau} + \left(2\left(\frac{\omega_p^2 - \omega_d^2}{2\omega_d\Delta\omega}\right) + \frac{i2\Gamma}{\Delta\omega} - 2|u|^2\right)u(\tau) = 2\sqrt{\beta} \quad (2.7)$$

where

$$\beta = \frac{3\gamma\omega_p^4 I_{RF}^2}{32I_0^2\omega_d^3(\Delta\omega)^3} \quad (2.8)$$

is the reduced drive strength. We will now make some approximations. We only consider under-damped oscillators, i.e., $2\Gamma/\omega_p \ll 1$. Also $\omega_d \sim \omega_p$, i.e., $\Delta\omega/\omega_d \ll 1$. Making these approximations, equation 2.7 reduces to

$$\frac{du}{d\tau} = -\frac{u}{\Omega} - iu(|u|^2 - 1) - i\sqrt{\beta} \quad (2.9)$$

where

$$\Omega = |\Delta\omega|/\Gamma \quad (2.10)$$

is the reduced detuning.

In order to find the steady state solutions, we set $du/d\tau = 0$ and we get a complex algebraic equation

$$-\frac{u}{\Omega} - u(|u|^2 - 1) = i\sqrt{\beta} \quad (2.11)$$

Multiplying equation 2.11 by its complex conjugate, we get a cubic equation for the modulus square of the complex amplitude $|u|^2$:

$$\frac{|u|^2}{\Omega^2} + |u|^2(|u|^2 - 1)^2 = \beta \quad (2.12)$$

Provided $\Omega > \sqrt{3}$, the above equation has three real roots for a certain range of β . The extreme points of this range are called the bifurcation points and are given by

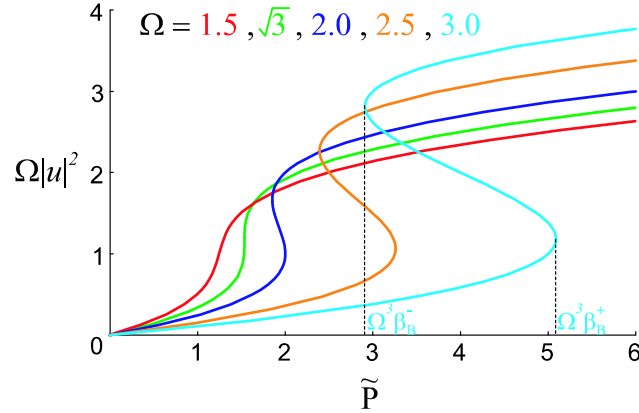


Figure 2.4: Steady state solutions of the driven non-linear oscillator for different values of reduced detuning Ω . The magnitude square of reduced oscillation amplitude is plotted as a function of reduced drive power $\tilde{P} = \Omega^3\beta$. The x and y axes have been scaled to clearly depict the variation with Ω . We observe multi-valued solutions for $\Omega > \sqrt{3}$. The turning points of the curves for $\Omega > \sqrt{3}$ are the bifurcation points (β_B^\pm) and are indicated for the curve with $\Omega = 3.0$

the solution to the equation $d\beta/d(|u|^2) = 0$:

$$\beta_B^\pm(\Omega) = \frac{2}{27} \left(1 + \frac{9}{\Omega^2} \pm \left(1 - \frac{3}{\Omega^2} \right)^{3/2} \right) \quad (2.13)$$

The smallest and largest roots of equation 2.12 correspond to the small and large amplitude mode of oscillation while the third root represents an unstable solution. The complex amplitude corresponding to the three solutions can be obtained by plugging the solution of equation 2.12 into equation 2.11. Fig. 2.4 shows a plot of equation 2.12 for different values of Ω .

The plotted quantities have been scaled to clearly indicate the variation in the steady state amplitudes and bifurcation points as Ω changes. The turning points of each curve correspond to the bifurcation points β_B^\pm . β_B^+ (upper bifurcation point)

corresponds to the drive amplitude above which the low amplitude state no longer exists, while β_B^- (lower bifurcation point) corresponds to the drive amplitude below which the high amplitude state vanishes. If the oscillator is driven at a certain detuning Ω , and the drive amplitude is slowly increased from zero, the amplitude of oscillation will follow one of the curves shown above until the amplitude β_B^+ is reached, at which point the oscillator will make a transition from the low amplitude state to the high amplitude state. If the drive amplitude is now slowly decreased, the oscillator will continue to stay in the high amplitude state until β_B^- is reached and the oscillator transitions back to the low amplitude state. This implies that the response of the oscillator is hysteretic.

We can now identify two conditions for bistability of a driven non-linear oscillator:

$$\Omega > \sqrt{3} \quad (2.14a)$$

$$\beta_B^-(\Omega) < \beta < \beta_B^+(\Omega) \quad (2.14b)$$

The first condition places a restriction on the minimum detuning for the drive frequency from the plasma frequency for a given damping, i.e., $\omega_p - \omega_d > \sqrt{3}\Gamma$. We will call this value the critical detuning Ω_c and the corresponding critical drive strength β_c :

$$\begin{aligned} \Omega_c &= \sqrt{3} \\ \beta_c &= \frac{8}{27} \end{aligned} \quad (2.15)$$

The bistability diagram shown in Fig. 2.5 is a plot of equation 2.13. For values

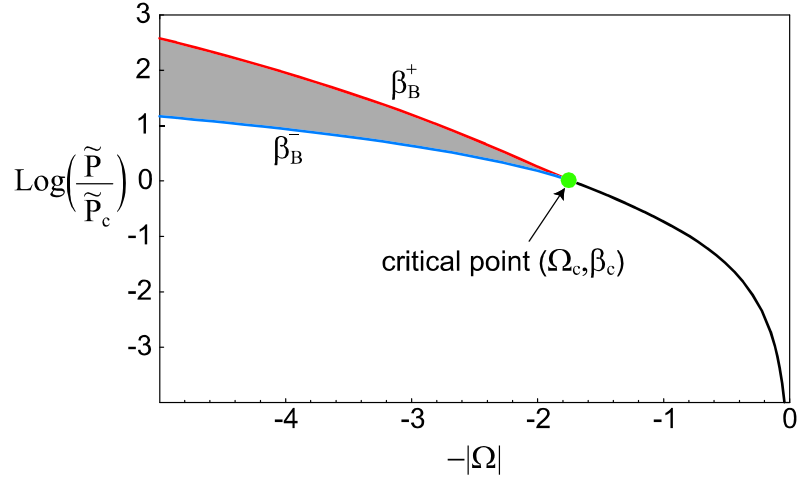


Figure 2.5: Bistability diagram in the plane of reduced drive power ($\tilde{P}/\tilde{P}_c = (\Omega^3\beta_B^\pm)/(\Omega_c^3\beta_c^\pm)$) and detuning (Ω). The power is plotted on log units to enable easy comparison with experimental plots. The x-axis has been plotted as a negative quantity to emphasize that for the Josephson oscillator, we need $\omega_d - \omega_p < 0$ to observe bistability. The red and blue curves represent the upper (β_B^+) and lower (β_B^-) bifurcation points as a function of Ω for $\Omega > \sqrt{3}$. The area between these two curves (shaded in gray) is the bistable region. The black curve ($\Omega \leq \sqrt{3}$) represents the value of β for which $d(|u|^2)/d\beta$ is maximum. The green dot represents the critical point (Ω_c, β_c) and marks the onset of bistability. Note that this plot is universal and does not depend on the particular parameters of the system.

of $\Omega > \Omega_c$, the red and blue curves correspond to the upper (β_B^+) and lower (β_B^-) bifurcation points respectively. For values of $\Omega \leq \Omega_c$, the black curve depicts the real part of equation 2.13, which is the value of β at which $d(|u|^2)/d\beta$ is maximum. The green dot identifies the critical point which marks the onset of the bistable region (shaded in gray). We will use these ideas in the next section for making a sensitive detector.

We can now write down the expressions for the bifurcation points in terms of the

drive current by using equation 2.8 in equation 2.13:

$$I_B^\pm = 8I_0 \sqrt{\alpha^3 \beta_B^\pm} \quad (2.16)$$

where we have approximated³ $\omega_p \sim \omega_d$. Here, α is the relative detuning given by

$$\alpha = \frac{\Delta\omega}{\omega_p} \quad (2.17)$$

Equation 2.16 is useful for getting numerical estimates for the bifurcation current in a real experiment. We will see in section 2.3 how changes in the critical current affect the bifurcation current and hence provide a way for detecting small changes in critical current.

In this analysis, we have assumed that the oscillator is damped via a frequency independent impedance R . This can be extended to the general case where this impedance $Z(\omega)$ can be a function of frequency. It turns out that bistability can still be observed provided constraints similar to equations 2.14 are satisfied. See reference [59] for more details. The experiments are engineered to minimize the variation of this impedance, especially near the plasma frequency of the oscillator.

2.2.2 Dynamics in quadrature amplitude plane

The driven states of the non-linear oscillator can be visualized in the plane of in-phase (δ_{\parallel}) and quadrature phase (δ_{\perp}) components of the oscillations amplitude δ , i.e.,

$$\delta(t) = \delta_{\parallel} \cos \omega_d t + \delta_{\perp} \sin \omega_d t \quad (2.18)$$

³See Appendix A for expressions without this approximation

The quadrature variables are just another way of parameterizing the solution and are related to the complex amplitude u defined earlier in equation 2.3 ($\delta_{\parallel} \propto u + u^*$, $\delta_{\perp} \propto u - u^*$). In this plane, the steady state solution can be represented as points $(\delta_{\parallel}, \delta_{\perp})$ and we can also draw trajectories to show dynamics. Fig. 2.6 shows four such plots. The color code depicts the magnitude of the error current $|I_e|$ [60], which can be thought of as the restoring force in this plane driving the system to steady state. The error current $|I_e|(\delta_{\parallel}, \delta_{\perp})$ is computed by substituting equation 2.18 into equation 2.2 and averaging over one period of the drive

$$\frac{|I_e|(\delta_{\parallel}, \delta_{\perp})}{I_0} = \left\langle \frac{d^2\delta(t)}{dt^2} + 2\Gamma \frac{d\delta(t)}{dt} + \omega_p^2 \left(\delta(t) - \frac{\delta(t)^3}{6} \right) - \omega_p^2 \frac{I_{RF}}{I_0} \cos(\omega_d t) \right\rangle \quad (2.19)$$

The above equation illustrates why this quantity is called the error current. The steady state solutions correspond to the points where the error current goes to zero (O_L, O_H and O_S). At all other points $(\delta_{\parallel}, \delta_{\perp})$, equation 2.2 is not satisfied for a given value of I_{RF} . The error current can be thought of as the additional drive current required to satisfy equation 2.2. The first three panels (a,b,c) in Fig. 2.6 are computed for the parameters $Q = 20$, $\alpha = 0.129$ and three different drive amplitudes as indicated in the plots. Panel (d) shows the case when the system is driven at the plasma frequency with a power corresponding to the bifurcation power for $\alpha = 0.129$, but we note that there is only one steady state as condition 2.14a is not satisfied. Panel (b) also shows some trajectories like the separatrix (red dashed line) which separates the basins of attraction of the two steady states labelled as O_L (low amplitude) and O_H (high amplitude). The black dashed line is the escape trajectory from the low

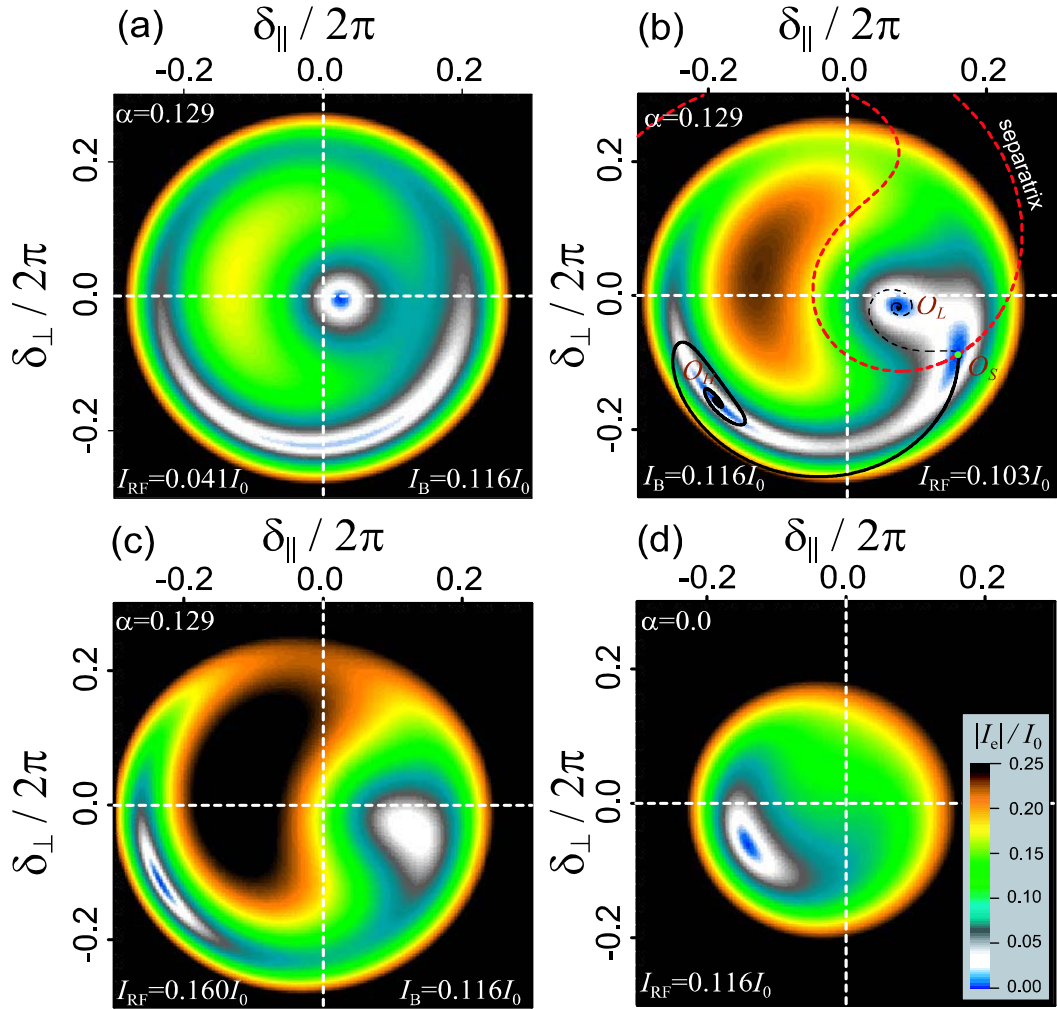


Figure 2.6: Poincaré sections of an RF-driven Josephson junction with $Q = 20$. Panels (a), (b) and (c) have $\alpha = 0.129$ and different drive strengths corresponding to the system being below bifurcation point, near bifurcation point and above the bifurcation point respectively. The coordinates δ_{\parallel} and δ_{\perp} are the in-phase and quadrature-phase components of the junction gauge-invariant phase difference δ . The color code gives the magnitude of the error current I_e [60] which describes the “force” on δ . In panel (b), where the system is near the upper bifurcation point, the two stable oscillation states are labeled by O_L and O_H . The basins of attraction corresponding to the two states are separated by the red dashed line (separatrix). Point O_S which lies on the separatrix is the saddle point at which the escape trajectory from state O_L (black, dashed line) meets the retrapping trajectory into state O_H (black, solid line). Panel (d) has $\alpha = 0$ and $I_{RF}/I_B^+ = 1$ and does not display bistability since it doesn’t satisfy $\Omega = 2\alpha Q > \sqrt{3}$.

amplitude and intersects the retrapping trajectory (black solid line) at the saddle point (O_S). The escape trajectory is the path of least action [61] which takes the system, in the presence of fluctuations, from the low amplitude state to the high amplitude state via the saddle point. More about escape rates will be discussed in section 2.3.2

2.3 Josephson Bifurcation Amplifier

2.3.1 Operating principle

We will now describe how to use the driven Josephson oscillator as a sensitive detector. The idea is based on the fact that the driven oscillation state of the Josephson oscillator depends very sensitively on the parameters of the oscillator when operated in the vicinity of the bifurcation points. This is the origin of the name Josephson Bifurcation Amplifier (JBA). Small changes in a parameter of the oscillator (e.g. critical current) are amplified into large changes in the oscillation state which can be measured in an experiment. There are two possible modes of operation.

The first one is in the hysteretic regime ($\Omega > \sqrt{3}$) where the oscillator is bistable. If we bias the oscillator near its upper bifurcation point (β_B^+), a small change in a parameter of the oscillator can make the oscillator transition from the low amplitude state to the high amplitude state. In this mode, the JBA acts as a two state amplifier or a threshold detector. Fig. 2.7 schematically illustrates the bistable mode of operation. The oscillator response is plotted as a function of the RF drive amplitude (non reduced). The two curves correspond to the oscillator response for a small change in a parameter of the oscillator e.g. the critical current of the Josephson junction. The

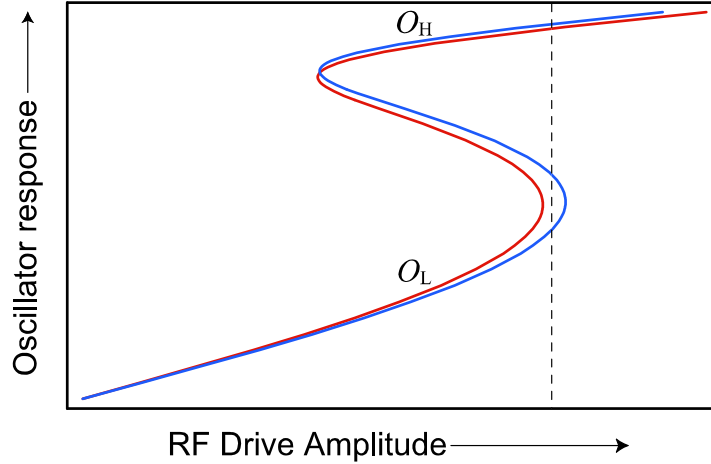


Figure 2.7: Operating principle of the JBA in the bistable mode. The oscillator response is plotted as a function of the RF drive amplitude (non reduced). The two curves correspond to the oscillator response for two different values of the critical current of the Josephson junction. The dashed line is the optimal bias point for detecting this difference in critical current. At this bias point, the oscillator will end up in the low (O_L) or high (O_H) amplitude state depending on whether the critical current is lower (red curve) or higher (blue curve).

dashed line is the optimal bias point for discriminating this change. At this bias point, the oscillator will end up in the low amplitude or the high amplitude state, depending on whether the critical current is smaller (red curve) or larger (blue curve). This forms the basis of detection. This mode of operation results in an extremely non-linear amplifier, though it is possible to implement an effective linear amplifier using the bistable mode as explained later in this section. The second mode of operation is in the non-hysteretic regime ($\Omega \leq \sqrt{3}$), where the oscillator has only one stable state and the oscillation state is a smooth function of the properties of the oscillator. We will be primarily interested in the bistable mode of operation.

The procedure for coupling input signals to change the oscillator properties will depend on the particular application. One of the properties of the Josephson oscillator

that can be changed easily is the critical current (I_0) or equivalently the Josephson inductance ($L_J = \varphi_0/I_0$). From now on, we will consider small changes in the critical current of the Josephson junction as our input signal. We will see in later chapters how one can couple to the critical current of the Josephson junction in various ways for different applications.

Till now, we have completely ignored the effect of fluctuations. In practice there are always fluctuations present in the system. The most important source of fluctuations is the Johnson noise of the shunt impedance (R , see Fig. 2.3 (b)) which also provides damping. In a carefully designed experiment, this should be the only source of fluctuations and the only way to lower this noise is by lowering the operating temperature. The presence of fluctuations makes the two oscillation states metastable, i.e., the oscillator can make transitions between the two states (with a certain probability) even when it is biased away from the bifurcation points. The transition curves are no longer infinitely sharp and acquire a finite width which depends on the intensity of fluctuations. It is now convenient to talk in terms of occupation probabilities of the two metastable states. The measurement protocol now works like this. We slowly ramp the drive current amplitude (I_{RF}) and bias near the bifurcation point (I_B^+) with the JBA in the low amplitude state. After a fixed amount of time (t_w), we probe the state of the oscillator. By repeating this many times, we can compute the probability of switching from the low amplitude state to the high amplitude state for different bias amplitudes. We call this quantity the 'switching probability' (P_{switch}). Fig. 2.8 shows such switching probability curves or S curves for two junction critical currents and two different intensity of fluctuations. The red curves correspond to a lower critical current than the blue curves. The dashed lines correspond to the higher

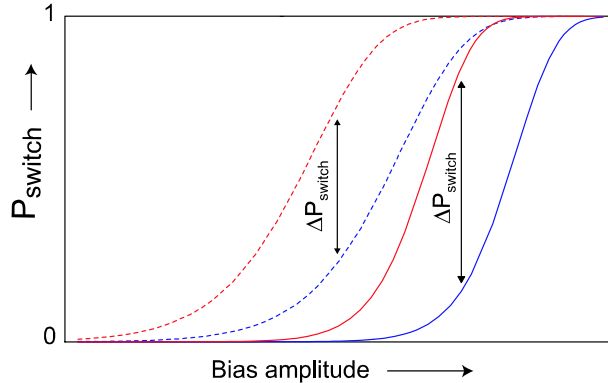


Figure 2.8: Switching probability or S curves indicate the probability of the JBA switching from the low amplitude state to the high amplitude when biased near the upper bifurcation point (β_B^+). S curves are plotted as a function of the bias amplitude. Solid lines correspond to lower intensity of fluctuations while the dashed lines correspond to higher intensity of fluctuations. The red and blue curves correspond to different critical currents of the junction with the red one being lower than the blue one. The change in switching probability (ΔP_{switch}) for a given change in critical current is smaller for larger intensity of fluctuations.

intensity of fluctuations. We note that the change in switching probability (ΔP_{switch}) for a given change in critical current gets smaller when the intensity of fluctuations gets larger.

Small changes in critical current now result in small changes in switching probability. This mapping is linear for small changes and can be the basis of building an effective linear amplifier. Note that the switching probability is an average quantity and requires several measurements of the state of the oscillator. So the JBA can act as a linear amplifier for small, slow changes in critical current permitting several preparations and measurements of the oscillator state before the critical current changes significantly. For detecting changes in a single measurement without too much uncertainty, the shift in the S curve due that change in critical current must be

comparable to its width. In order to compute S curves and measurement sensitivity, we need to compute the fluctuation induced transition rates between the metastable states. This will be the subject of the next section.

2.3.2 Transition Rates

The theory of fluctuation induced transitions between metastable states in a driven non-linear oscillator has been the subject of several papers [61, 27, 62] and the transition rates have been computed by different techniques. We will present results based on the method followed in reference [27] because it provides easy to use formulae.

The starting point is the equation of motion for the driven Josephson junction (2.1), but now we will include a noise term which is responsible for the transitions between the metastable states

$$C_S \varphi_0 \frac{d^2 \delta(t)}{dt^2} + \frac{\varphi_0}{R} \frac{d\delta(t)}{dt} + I_0 \sin(\delta(t)) = I(t) + I_N(t). \quad (2.20)$$

Here $I_N(t)$ is the noise current corresponding to the Johnson noise in the resistor R at temperature T . The noise current is white with a correlation function given by

$$\langle I_N(t) I_N(0) \rangle = \frac{2k_B T}{R} \delta(t) \quad (2.21)$$

where T is the temperature of the resistor R and $\delta(t)$ is the Dirac delta function [60]. Using the procedure outlined in section 2.2.1 we can arrive at the following equation of motion for the complex amplitude u

$$\frac{du}{d\tau} = -\frac{u}{\Omega} - u (|u|^2 - 1) - i\sqrt{\beta} + \tilde{i}_N(\tau) \quad (2.22)$$

where $\tilde{i}_N(\tau)$ is the reduced noise current in the new notation and is related to $I_N(t)$ by

$$\tilde{i}_N(\tau) = -i \frac{\sqrt{3}\gamma\omega_p^2}{(2\omega_d\Delta\omega)^{3/2}} \frac{I_N(t)}{I_0} \exp(-i\omega_d t). \quad (2.23)$$

Its correlation function is given by

$$\langle \tilde{i}_N(\tau) \tilde{i}_N^*(0) \rangle = \frac{3\gamma\omega_p^4}{4(\omega_d\Delta\omega)^3} \frac{k_B T \Delta\omega}{R I_0^2} \delta(\tau), \quad \langle \tilde{i}_N(\tau) \tilde{i}_N(\tau') \rangle = 0 \quad (2.24)$$

Using $\omega_d/\omega_p \sim 1$, we can simplify the above equation to

$$\langle \tilde{i}_N(\tau) \tilde{i}_N^*(0) \rangle = \frac{k_B T}{E_J} \frac{Q}{2\Omega^2} \delta(\tau) = 4\alpha_N \delta(t) \quad (2.25)$$

where α_N characterizes the reduced current noise. Using the procedure described in ref. [27], the complex equation 2.22 when expanded⁴ near β_B^+ can be reduced to a Langevin equation for an effective coordinate $y(\tau)$ given by

$$\frac{dy}{d\tau} = -\frac{dV}{dy} + \tilde{i}_N(\tau) \quad (2.26a)$$

$$V(y) = -\frac{b}{3}y^3 + \zeta y \quad (2.26b)$$

The above equation describes the motion of a particle diffusing in a cubic potential $V(y)$ where

$$b(\Omega) = \frac{1}{27\sqrt{\beta_B^+}} \left(\Omega^2 \left(1 + \sqrt{1 - 3/\Omega^2} \right) + 9\sqrt{1 - 3/\Omega^2} + 9/\Omega^2 - 6 \right) \quad (2.27)$$

⁴A similar equation can also be derived for expansion around the other bifurcation point β_B^- .

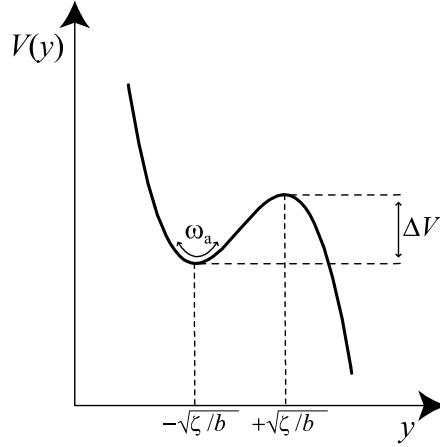


Figure 2.9: Metapotential for the effective slow coordinate. Its form is cubic when $\beta \rightarrow \beta_B^+$. The minima at $-\sqrt{\zeta/b}$ corresponds to the low amplitude state while the maxima at $+\sqrt{\zeta/b}$ corresponds to the unstable solution also known as the saddle point (in phase space).

$$\zeta(\Omega, \beta) = \frac{1}{2} \frac{\beta_B^+ - \beta}{\sqrt{\beta_B^+}} \quad (2.28)$$

When the system is biased near a bifurcation point, its motion becomes overdamped and one of the coordinates becomes much slower than all the other time scales in the problem [27]. Consequently, the equation describing the dynamics can be simplified and the multidimensional equation 2.22 can be reduced to a simple 1-D motion of an effective slow coordinate 2.26a. This separation of time scales is discussed using a different approach in chapter 7.

For bias points such that $\zeta > 0$, i.e., $\beta < \beta_B^+$, the potential $V(y)$ has a local minima and a saddle point at $\mp\sqrt{\zeta/b}$ respectively (see Fig. 2.9). The local minima corresponds to the low amplitude state of the JBA while the saddle point is the unstable solution (see section 2.2.1). The escape problem has now been reduced to a

standard Kramer's [63, 64] problem for escape over barrier. It is now straightforward to write down the escape rate from the low amplitude state of the JBA and it has an Arrhenius like form given by

$$\Gamma_{esc}^{RF} = \frac{\omega_a^{RF}}{2\pi} \exp\left(\frac{-\Delta U_{esc}^{RF}}{k_B T}\right) \quad (2.29)$$

where the exponent has been written as the ratio of an effective barrier energy (ΔU_{esc}^{RF}) over thermal energy ($k_B T$). ω_a^{RF} is called the attempt frequency (or inverse equilibration time) and is given by

$$\omega_a^{RF} = 2\sqrt{b\zeta} \quad (2.30)$$

while the expression for the barrier height is given by

$$\Delta U_{esc}^{RF} = k_B T \frac{\Delta V}{\alpha_N} = \frac{4}{3} \frac{\zeta^{3/2}}{b^{1/2}} \frac{1}{\alpha_N}. \quad (2.31)$$

Using equations 2.25, 2.27 and 2.28 in equations 2.30 and 2.31, and simplifying⁵ in the limit of large detuning $\Omega \gg 1$, we arrive at the following expressions

$$\omega_a^{RF} = \omega_{a0}^{RF} \left(1 - (I_{RF}/I_B^+)^2\right)^{1/2} \quad (2.32a)$$

$$\Delta U = U_{esc}^{RF} \left(1 - (I_{RF}/I_B^+)^2\right)^{3/2} \quad (2.32b)$$

⁵See Appendix A for expressions without this approximation

where

$$\omega_{a0}^{RF} = \frac{2}{3\sqrt{3}} \frac{\Delta\omega^2}{\Gamma} \quad (2.33a)$$

$$U_{esc}^{RF} = \frac{32}{9\sqrt{3}} E_J \frac{\Omega}{Q}. \quad (2.33b)$$

As expected for a cubic potential, the barrier height goes to zero with a $3/2$ power law as one approaches the bifurcation point. It is important to note that the Kramer's escape rate given by equation 2.29 is valid when $\Delta U_{esc}^{RF}/k_B T \gg 1$, i.e., only in the limit of small escape rate [63].

The above expressions illustrate the dependence of the escape rate on various parameters of the experiment. The dominant effect comes due to changes in the barrier height as it is inside the exponential. The drive amplitude I_{RF} is one obvious way of controlling the escape rate but we also see its dependence on the critical current of the junction via various parameters ($E_J = \varphi_0 I_0$, $\omega_p = (I_0/\varphi_0 C_S)^{1/2}$, $I_B^+(I_0)$). This provides for a mechanism to detect changes in critical current via changes in switching probability. We will discuss the sensitivity of the JBA to changes in critical current in the next section.

2.3.3 Measurement sensitivity

There are two important quantities which go into determining the sensitivity of the JBA to changes in critical current. The first quantity is the variation of the bifurcation current I_B^+ with critical current I_0 . This quantity for $\Omega \gg 1$ can be written as follows

$$\frac{\partial I_B^+}{\partial I_0} = \frac{I_B^+}{I_0} \frac{3}{4\alpha}. \quad (2.34)$$

We can reorder the above equation in the following way

$$\frac{\partial I_B^+/I_B^+}{\partial I_0/I_0} = \frac{3}{4\alpha} \quad (2.35)$$

and note that the fractional variation in the bifurcation current ($\partial I_B^+/I_B^+$) is always bigger than the fractional variation in critical current ($\partial I_0/I_0$) since $3/4\alpha > 1$.

We introduced the idea of a switching probability curve or an S-curve in section 2.3.1. The width of the S-curve which depends on the intensity of fluctuations (given by temperature T) is the second quantity which determines the sensitivity of the JBA. We will now define this mathematically. Since we know the escape rate from the low amplitude state to the high amplitude state of the JBA, we can define the probability of switching in a given time t_w

$$P_{\text{switch}}(I_{RF}, I_0) = 1 - \exp(-t_w \Gamma_{\text{esc}}^{RF}(I_{RF}, I_0)) \quad (2.36)$$

where $P_{\text{switch}}(I_{RF}, I_0)$ has been defined as function of two parameters - the drive amplitude I_{RF} and the critical current I_0 as we are interested in the variation of P_{switch} with respect to these two parameters. The S-curve is basically the plot of P_{switch} v.s. I_{RF} for a given I_0 (Fig. 5.11). In order to compute the sensitivity, we need to calculate $\partial P_{\text{switch}}/\partial I_0$, which is given by

$$\frac{\partial P_{\text{switch}}}{\partial I_0} = \eta_s \frac{1}{I_0} \left(\frac{U_{\text{esc}}^{RF}}{k_B T} \right)^{2/3} \left(\frac{I_0}{I_B^+} \frac{\partial I_B^+}{\partial I_0} \right) \quad (2.37)$$

where $\eta_s \sim 1$ is a scaling factor which depends weakly on the operating parameters.

We can now compute the smallest change in critical current ΔI_0 that can be resolved

($\Delta P_{\text{switch}} \sim 1$) in a single measurement

$$\Delta I_0 = \left(\frac{\partial P_{\text{switch}}}{\partial I_0} \right)^{-1} \quad (2.38)$$

This is can be expressed in terms of a current sensitivity S_{I_0} (in A/ $\sqrt{\text{Hz}}$) given a time t_{pulse} by the following equation

$$S_{I_0} = \Delta I_0 \sqrt{t_{\text{pulse}}} = \left(\frac{\partial P_{\text{switch}}}{\partial I_0} \right)^{-1} \sqrt{t_{\text{pulse}}} \quad (2.39)$$

The time t_{pulse} is the total time of a single measurement which includes the time to energize the JBA, the wait time t_w , the time to record the oscillation state and the time to ramp down the JBA. This time scale is set by the inverse damping rate Γ of the JBA and we can write

$$t_{\text{pulse}} = \eta_{po} \frac{1}{2\Gamma} \quad (2.40)$$

where $\eta_{po} \sim 10$ is the pulse overhead factor. We can now write down the full expression for the sensitivity as

$$S_{I_0} = \frac{3^{2/3}}{4\sqrt{2}} \frac{\sqrt{\eta_{po}}}{\eta_s} \frac{1}{\sqrt{\Gamma}} I_0^{1/3} \left(\frac{k_B T}{\varphi_0} \right)^{2/3} \alpha^{1/3} \quad (2.41)$$

We note that the sensitivity depends quite weakly on most parameters, the strongest being the temperature ($T^{2/3}$). The dependence on I_0 is quite weak ($I_0^{1/3}$) which means that there is flexibility in choosing the value of junction critical current. An important point to be noted is that the above analysis involves many approximations which have been used to simplify calculations and see trends clearly. Often, many of these approximations become too crude in real experiments and the only way to get

accurate predictions is to do full numerical simulations (Appendix C). Nevertheless, the above formulae serve as a guide to the phenomena and provide quick estimates.

Chapter 3

Josephson Bifurcation Amplifier: Experiments

In this chapter, we will discuss the experiments that were carried out to characterize the performance of the Josephson Bifurcation Amplifier. We will begin by discussing the experimental setup and then go on to describe the measurement of the Josephson oscillator resonance in the linear and non-linear regime. The hysteresis and bistability measurements of the JBA will then be discussed. We will then describe the experiments implementing the JBA as a sensitive detector and also discuss the noise and sensitivity issues. Finally, we will discuss some practical issues concerning the successful implementation of the JBA.

3.1 Experimental setup

The basic experiment that was carried out to probe the properties of the Josephson oscillator was a phase-sensitive microwave reflection experiment. A microwave signal is sent via a transmission line to the oscillator, and the signal which is reflected from the oscillator is amplified and its relative magnitude and phase recorded. For an ideal

electrical oscillator made with dissipationless inductors and capacitors, the magnitude of the reflected signal is the same as the incident magnitude, and all the information is contained in the relative phase of the reflected signal.

The Josephson junction is the only known electrical element which remains non-linear and non-dissipative at arbitrarily low temperatures. Typical junction fabrication parameters limit the plasma frequency of the Josephson oscillator to the 20 - 100 GHz range where techniques for addressing junction dynamics are inconvenient. We have chosen to shunt the junction by a capacitive admittance to lower the plasma frequency by more than an order of magnitude and attain a frequency in 1-2 GHz range (microwave L-band). In this frequency range, a simple on-chip electrodynamic environment with minimum parasitic elements can be implemented, and the hardware for precise signal generation and processing is readily available.

Sample	L_J (nH)	$\omega_p/2\pi$ (GHz)	C_S (pF)	L_S (nH)	R_S (Ω)
1	0.28	1.18	39 ± 1	$0.20 \pm .02$	0.8
2	0.18	1.25	30 ± 4	$0.34 \pm .04$	0.8
2a	0.17	1.66	18 ± 1	$0.32 \pm .02$	0.8
3	0.32	1.64	16 ± 1	$0.27 \pm .02$	~ 0.0
4	0.38	1.81	19 ± 1	$0.03 \pm .02$	~ 0.02
5	0.40	1.54	19 ± 1	$0.15 \pm .02$	~ 0.0
6	0.28	1.80	27 ± 1	$0.01 \pm .02$	~ 0.0

Table 3.1: Sample parameters. $L_J = \varphi_0/I_0$ and ω_p are measured values. C_S and L_S are fit values to the data. Samples 1,2 and 2a have a 100 nm thick Au underlayer, sample 3 has a 50 nm thick Nb underlayer, sample 4 has a 1 μ m thick Cu underlayer, and sample 5 has a 200 nm thick Nb underlayer.

In the first step of sample fabrication, a metallic underlayer – either a normal metal (Au, Cu) or a superconductor (Nb) – was deposited on a silicon substrate to form one plate of the shunting capacitor, followed by the deposition of an insulating Si_3N_4 layer which is the dielectric material in the capacitor. Using e-beam lithography and

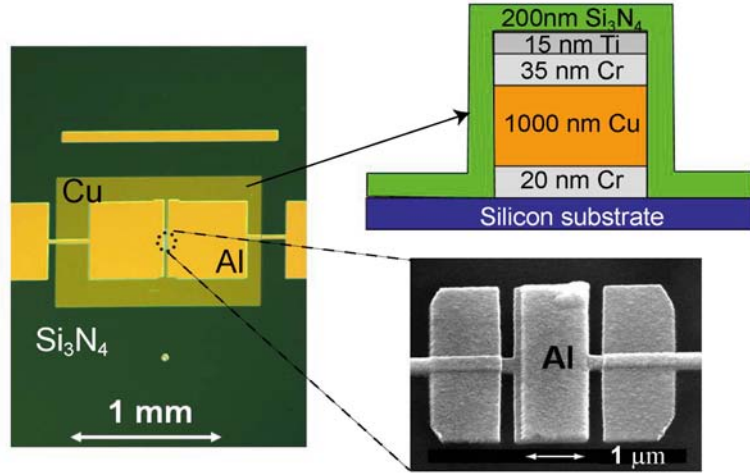


Figure 3.1: Optical image (false color) of the microfabricated on chip capacitor is shown in the left panel. Top right panel shows the actual profile of the different layers in the ground plane. The additional layers (Ti and Cr) sandwiching the Cu layer are there to protect the Cu layer during the deposition of Si_3N_4 . The bottom right panel shows a SEM image of a Josephson junction.

double-angle shadow mask evaporation, we subsequently fabricated the top capacitor plates along with a micron sized Al/Al₂O₃/Al tunnel junction. Fig. 3.1 shows an optical image of the chip capacitor along with the actual profile of the ground plane layer. The other metallic layers (Ti and Cr) were employed for protecting the Cu layer during the deposition of the dielectric layer. It also ensured that the Cu layer would stick properly to the silicon substrate. Also shown in the bottom right corner is a SEM image of the Josephson tunnel junction. The critical current of the junction was in the range $I_0 = 1 - 2 \mu\text{A}$ corresponding to a Josephson inductance in the range $L_J = 0.15 - 0.3 \text{ nH}$. By varying both the dielectric layer thickness and the pad area, the capacitance C_S was varied between 16 and 40 pF. Sample parameters are listed

in Table 3.1.

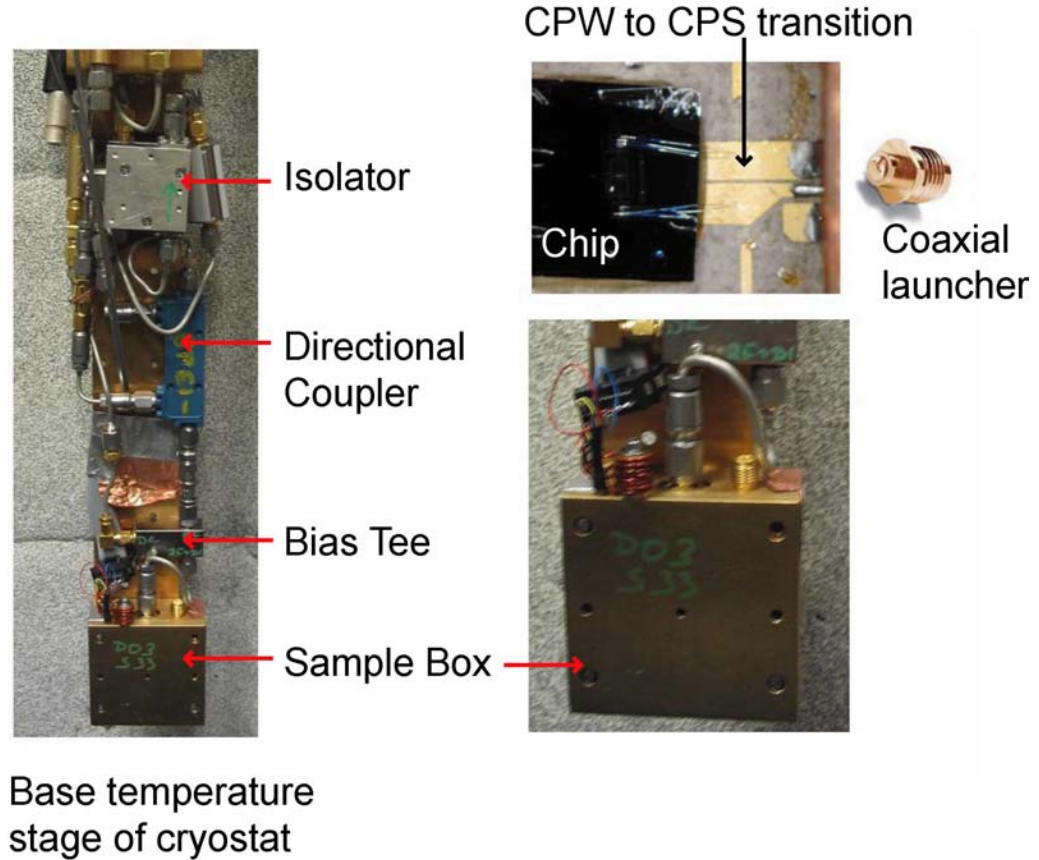


Figure 3.2: Optical image of the base temperature stage of the cryostat is shown in the left and the lower right panel. The top right panel shows the microwave launch circuit.

The junction + capacitor chip is placed on a microwave circuit-board and is wire-bonded to the end of a coplanar stripline which is soldered to a coaxial launcher affixed to the side wall of the copper sample box (Fig. 3.2). We anchor the RF leak-tight sample box to the cold stage of a ^3He refrigerator with base temperature $T = 280\text{ mK}$. The measurement setup is schematically shown in Fig. 3.3 while Fig. 3.2 shows a photograph of the base temperature stage with the layout of the various

microwave components.

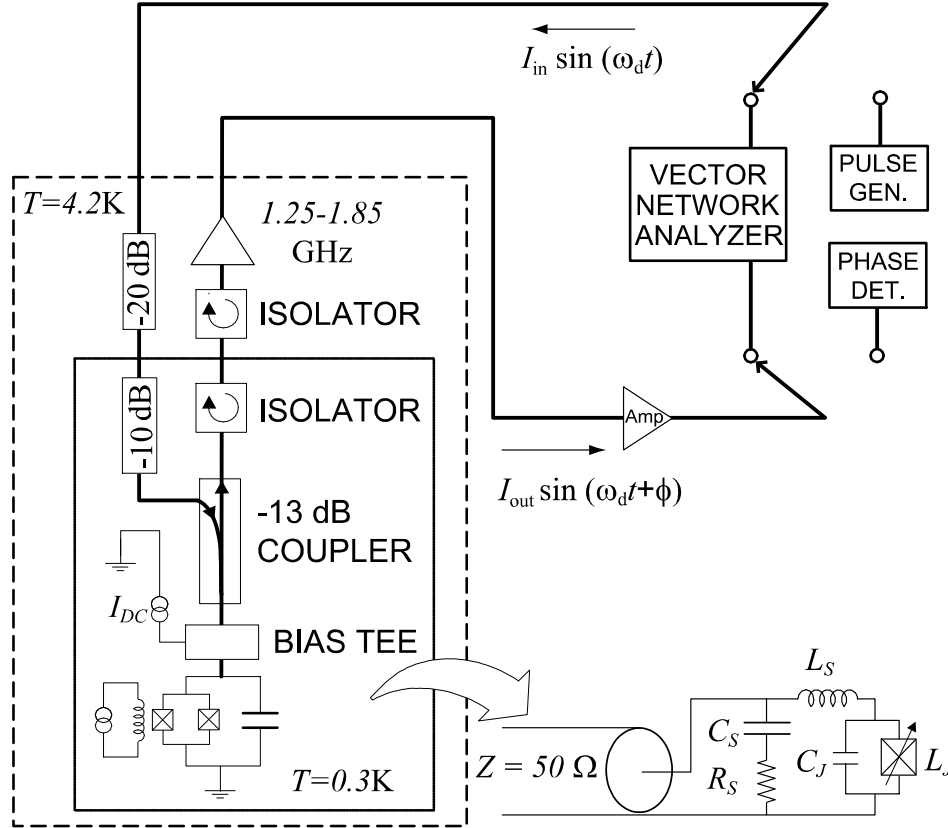


Figure 3.3: Schematic of the measurement setup. Thick lines correspond to $50\ \Omega$ coaxial transmission lines. The network analyzer is used for CW measurements. For probing the dynamics (section 3.3), the pulse generator and phase detector were used. A lumped element model for the junction chip and measurement line is shown. The two ideal current sources actually represent external sources.

Microwave excitation signals are generated by a HP 8722D vector network analyzer or a pulse generator and are coupled to the sample via the $-13\ \text{dB}$ side port of a directional coupler after passing through cryogenic attenuators. The reflected microwave signal passes through the direct port of the coupler, and is amplified first using a cryogenic $1.20 - 1.85\ \text{GHz}$ HEMT amplifier with noise temperature $T_N = 4\ \text{K}$

before returning to the network analyzer or a phase detector¹. The isolators allow microwave signals to propagate only in one direction, preventing the HEMT amplifier noise from reaching the sample. The attenuators on the input line carry out a similar function by attenuating the thermal noise from higher temperature stages. In later experiments we have also used various kinds of microwave filters to prevent spurious noise from reaching the sample. All this ensures that the fluctuations felt by the sample correspond to the temperature of the cold stage to which it is anchored. This is important for maximizing the sensitivity of the JBA when implemented as a readout. A DC bias current can also be applied to the junction by way of a bias tee and a passive filter network.

3.2 Frequency domain measurements

3.2.1 Linear resonance

We locate the linear plasma resonance by sweeping the excitation frequency from 1 to 2 GHz and measuring the reflection coefficient

$$\Gamma_R(\omega_d) = I_{in}/I_{out} e^{j\phi} = (Z(\omega_d) - Z_0)/(Z(\omega_d) + Z_0) \quad (3.1)$$

where $Z_0 = 50 \Omega$ is the characteristic impedance of our transmission lines and $Z(\omega_d)$ is the impedance presented to the analyzer by the chip and the measurement lines. For an ideal LC resonator without intrinsic dissipation, we expect a phase shift $\Delta\phi = \phi_{\omega_d \gg \omega_p} - \phi_{\omega_d \ll \omega_p} = 2\pi$, which we verified by placing a chip capacitor and an inductive

¹A pulse generator and a phase detector were used for the time domain measurements described section 3.3.

wire bond in place of the junction chip. An important aspect of our experiment is that Q is now determined by the ratio $Z_0/Z_J \sim 10$, where $Z_J = \sqrt{L_J/C_S}$ and not by the intrinsic junction losses which are negligible. An excitation power (at the level of the sample) $P = I_{RF}^2 Z_0/4 \approx -120$ dBm (1 fW) corresponding to a drive current amplitude of $I_{RF} = 9$ nA $\ll I_0$ keeps the junction in the linear regime.

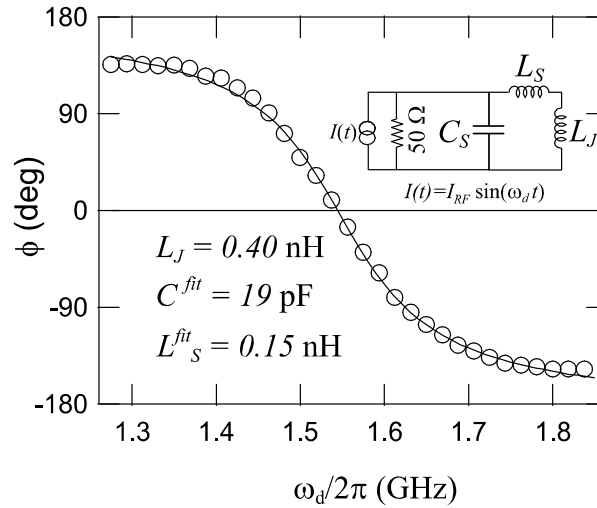


Figure 3.4: Normalized reflected signal phase ϕ as a function of excitation frequency for sample 5. The open circles are measured data for $L_J = 0.40$ nH. The solid line is calculated from the equivalent circuit model shown in the inset. The magnitude of the reflected signal is unity within experimental uncertainty.

In Fig. 3.4, we present the reflected signal phase ϕ as a function of excitation frequency for sample 5. In order to remove the linear phase evolution associated with the finite length of the measurement lines, we have subtracted from our measurement in the superconducting state, the reflection coefficient measured with the junction in the normal state. The point where $\phi = 0$ is the linear-regime plasma frequency. For sample 5, $\omega_p/2\pi = 1.54$ GHz.

The precise frequency and critical current dependence of the reflected signal phase

of our samples can be accounted for by a 3-element model for the electrodynamic environment seen by the junction. This lumped element model is shown in the lower right corner of Fig. 3.3. The parasitic inductance L_S and resistance R_S model the non-ideality of the shunting capacitor C_S . They arise from the imperfect screening of currents flowing in the capacitor plates and the finite conductivity of these plates. The plasma frequency in the linear regime is determined by the total inductance $L_J + L_S$ and capacitance $C_{eff} = C_J + C_S \simeq C_S$, and is given by the following relation:

$$\left(\frac{1}{\omega_p}\right)^2 = C_S(L_J + L_S) = \frac{\varphi_0 C_S}{I_0} + C_S L_S. \quad (3.2)$$

We thus plot $(2\pi/\omega_p)^2$ versus $1/I_0 = L_J/\varphi_0$ in Fig. 3.5 for samples 1, 2, 2a, 4 and 5. As the critical current is decreased by applying a magnetic field, the junction inductance increases, and the plasma frequency is reduced. For each sample, a linear fit to the data of Fig. 3.5 yields the values of C_S and L_S (see table 3.1). The fit values for C_S agree well with simple estimates made from the sample geometry. Samples 1 and 2 have nominally the same capacitance but different critical current, and hence lie approximately on the same line in Fig. 3.5.

A total of four capacitive pads were used to make the shunting capacitor in samples 1 and 2, and after initial measurements, we scratched off two of the pads from sample 2 to obtain sample 2a, and the resulting capacitance is indeed halved. For samples with a thin underlayer (1,2 and 3), a stray inductance in the range $L_S = 0.20 - 0.34$ nH is observed. For samples 4 and 5 with a significantly thicker underlayer, L_S was reduced to 0.026 nH and 0.15 nH respectively. This behavior is consistent with the calculated screening properties of our thin films. To verify that the values of C_S and

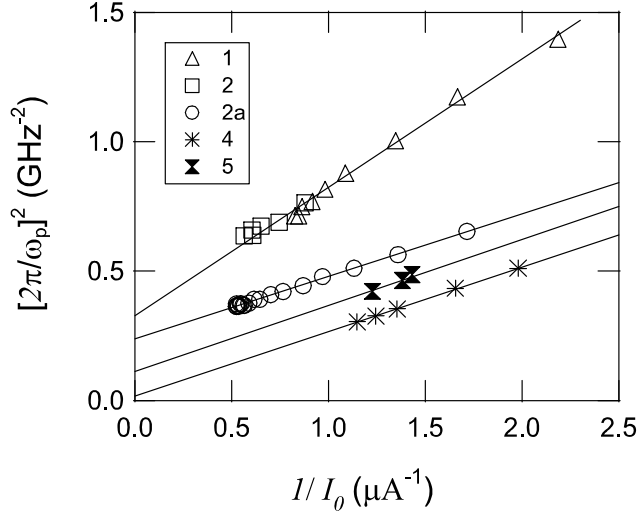


Figure 3.5: Inverse square of the plasma frequency $(2\pi/\omega_p)^2$ as a function of the inverse critical current $1/I_0$ for samples 1, 2, 2a, 4 and 5. Solid lines are linear fits to the data corresponding to the model of Fig. 3.4, with a single best fit line drawn for samples 1 and 2 which nominally differ only in I_0 .

L_S were not affected by the magnetic field used to vary I_0 , we varied L_J by applying a bias current [42] at zero magnetic field. The parameters extracted using the DC bias current method agreed with the ones extracted using the magnetic field method. Using L_S and C_S we can accurately predict the observed resonant lineshape of Fig. 3.4, in which $R_S \sim 0$. For samples with a normal underlayer, we find the data is accurately fit by $R_S = 0.8 \Omega$ for sample 1 and 2 while $R_S = 0.02 \Omega$ for sample 4. Finally, we have independently verified the effect of the shunting capacitor on the plasma resonance by performing resonant activation experiments [65]. The escape rate from the zero voltage state of the DC current biased junction was enhanced when the applied microwave frequency equalled the reduced plasma frequency.

3.2.2 Non-linear resonance

We now address the measurement of the non-linear regime of the plasma resonance. The reflection coefficient as a function of frequency for increasing power for sample 5 is presented in the right panel of Fig. 3.6 as a two dimensional color plot, in which each row is a single frequency sweep, similar to Fig. 3.4. For small excitation power, we recover the linear plasma resonance at 1.54 GHz, shown in yellow corresponding to $\phi = 0$. As the power is increased above -115 dBm, the plasma frequency decreases, as is expected for a junction driven with large amplitude [65]. The boundary between the leading-phase region (green) and the lagging-phase region (red) therefore curves for high powers. This curvature has an interesting consequence. When we increase the drive power at a constant frequency slightly below the plasma frequency, the phase as a function of power undergoes an abrupt step, as predicted. This represents the transition from the low amplitude state to the high amplitude state. From now on we will call these states as state O_L and state O_H respectively. For yet greater powers (> -90 dBm), we encounter a new dynamical regime (black region in Fig. 3.6) where δ appears to diffuse between the wells of the cosine potential. This was confirmed by the presence of an unambiguous audiofrequency ac resistance in the black region (see 3.4). In the right panel of Fig. 3.6 (inset), we illustrate the sequence of dynamical transitions by plotting ϕ as a function of incident power at $\omega_d/2\pi = 1.375$ GHz. For $P < -102$ dBm, the phase is independent of power (δ oscillates in a single well in the harmonic-like, phase-leading state, letter A). For -102 dBm $< P < -90$ dBm, the phase evolves with power and δ still remains within the same well, but oscillates in the anharmonic phase-lagging state (letter B). Finally, for $P > -90$ dBm, the average phase of the reflected signal saturates to -180 degrees, corresponding to a capacitive

short circuit. This last value is expected if δ hops randomly between wells, the effect of which is to neutralize the Josephson inductive admittance.

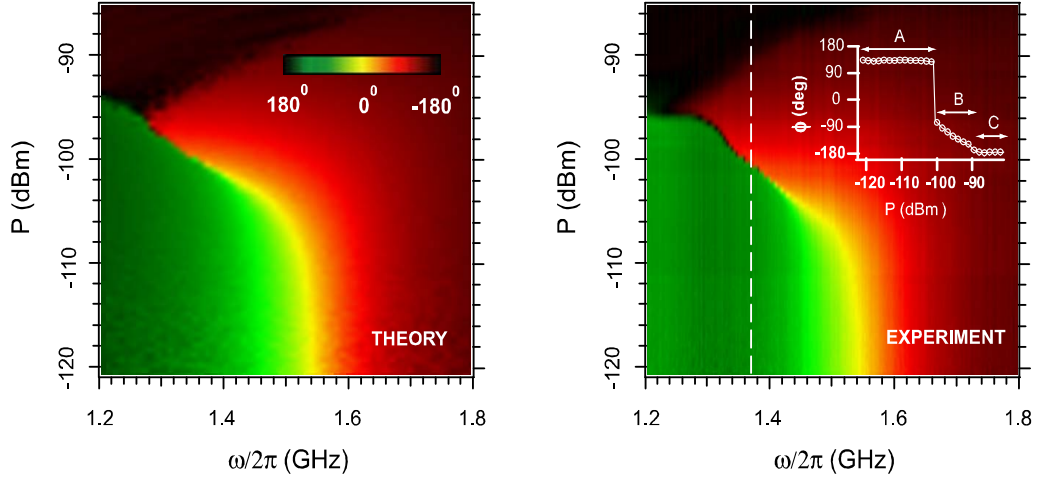


Figure 3.6: Normalized reflected signal phase ϕ (wrap-around color scheme) as a function of excitation frequency $\omega_d/2\pi$ and excitation power P is shown for sample 5. Experimental data is shown in the right panel while the left panel is the result of numerical simulations. A vertical slice taken at $\omega_d/2\pi = 1.375$ GHz (dashed line) shows the abrupt transition between two oscillation states of the system.

The value of the current I_B for the A-B transition, which is a function of both the relative detuning $\alpha = 1 - \omega_d/\omega_p$ and power P , is in good agreement with the analytical theory which retains only the first anharmonic term in the cosine potential (see chapter 2). For instance, the slope of the A-B transition line (equation 2.8 and 2.13) at the linecut in Fig. 3.6, $dP(\text{dBm})/d\alpha(\%) = 0.8$ for the experiment while we calculate its value to be 0.7. Furthermore, in measurements in which the power is ramped in less than 100 ns, we verified that the transition between dynamical states is hysteretic, another prediction of the theory. To explain the complete frequency and power dependence of the transitions shown in the right panel of Fig. 3.6, we have

performed numerical simulations by solving the full circuit model of the lower right corner of Fig. 3.3, including the exact junction non-linear constitutive relation. The result of this calculation is shown in the left panel of Fig. 3.6. It correctly predicts the variation of the plasma frequency with excitation power, and the boundaries of the phase diffusion region. The agreement between theory and experiment is remarkable in view of the simplicity of the model which uses only measured parameters, and only small differences in the exact shape of region boundaries are observed².

3.3 Time domain measurements

The measurements described so far characterized the time averaged response of the Josephson oscillator under continuous microwave excitation. We will now describe the experiments which probed the response of the JBA at short time scales (~ 10 ns) under pulsed microwave excitation. Sample 6 was used for this experiment and had a Josephson junction with critical current $I_0 = 1.17 \mu\text{A}$, an on-chip lithographic capacitance $C_S = 27$ pF resulting in a reduced plasma frequency $\omega_p/2\pi = 1.80$ GHz. The stray elements L_S and R_S were negligible for this sample. The dynamics of the transition between the two oscillation states were probed using microwave pulses, generated by the amplitude modulation of a CW source with a phase-locked arbitrary waveform generator with 1 ns resolution. As described in the previous section, the reflected signal from the sample was passed through a circulator at base temperature $T = 0.25$ K to a matched HEMT amplifier at $T = 4.2$ K. At room temperature, the reflected signal was further amplified, mixed down to 100 MHz and finally digitally

²It is important to mention that the overall topology of Fig. 3.6 is not significantly affected by changes in the parameter values within the bounds of Table 3.1

demodulated using a 2 GS/s digitizer to extract the signal phase ϕ .

3.3.1 Hysteresis and bistability in the JBA

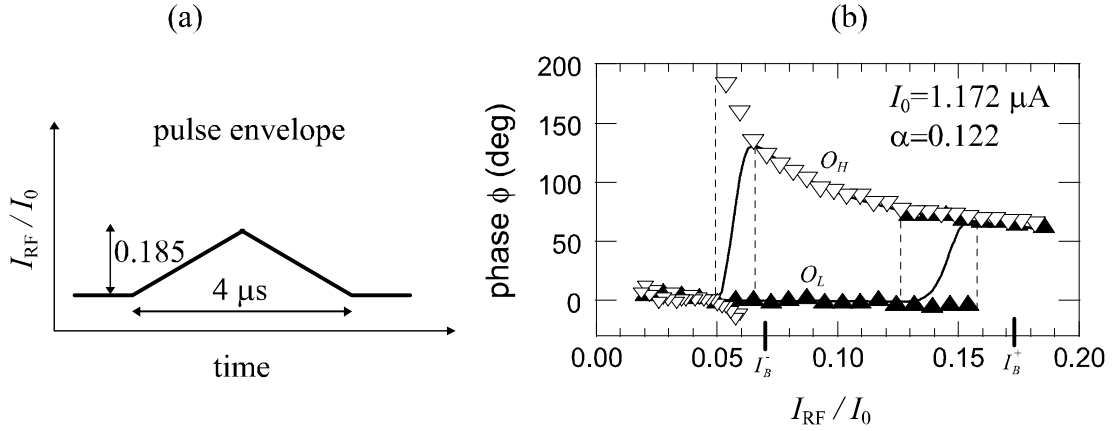


Figure 3.7: (a) Triangular waveform envelope used for measuring hysteresis. (b) Hysteretic variation of the reflected signal phase with drive current I_{RF}/I_0 . Symbols denote the mode of ϕ , with up and down triangles corresponding to increasing and decreasing I_{RF} , respectively. The dotted line is $\langle \phi \rangle$. The calculated bifurcation points, I_B^+ and I_B^- , are marked on the horizontal axis. The low amplitude and high amplitude states are marked as O_L and O_H .

We first probed the drive current dependence of the reflected signal phase $\phi(I_{RF})$ by applying a 4 μs long symmetric triangular shaped pulse with a peak value 0.185 I_0 . The demodulated reflected signal was divided into 20 ns sections, each yielding one measurement of ϕ for a corresponding value of I_{RF} . The measurement was repeated 6×10^5 times to obtain a distribution of $\phi(I_{RF})$. In Fig. 3.7, the mode of the distribution is plotted as a function of I_{RF}/I_0 . For $I_{RF}/I_0 < 0.125$, the bifurcation amplifier is always in state O_L , ϕ is constant and assigned a value of 0 deg. As the drive current is increased above $I_{RF}/I_0 = 0.125$, thermal fluctuations are sufficiently large to cause transitions to the O_H state. In the region between the two dashed

lines at $I_{RF}/I_0 = 0.125$ and $I_{RF}/I_0 = 0.160$, ϕ displays a bimodal distribution with peaks centered at 0 and 74 deg with the latter corresponding to the amplifier in the O_H state. The dotted line in Fig. 3.7 is the average reflected signal phase $\langle\phi\rangle$. When I_{RF}/I_0 is increased above 0.160, the system is only found in state O_H . In the decreasing part of the I_{RF} ramp, the system does not start to switch back to state O_L until $I_{RF}/I_0 = 0.065$. The critical switching currents I_B^+ for the $O_L \rightarrow O_H$ transition and I_B^- for the $O_H \rightarrow O_L$ transition, calculated from numerical simulations to treat the inductance of wire bonds, are denoted with ticks in Fig. 3.7, and are in good agreement with experiment. The hysteresis $I_B^- < I_B^+$ is a consequence of the asymmetry in the escape barrier height for the two states. Thus, the $O_L \rightarrow O_H$ transition at $I_{RF} = I_B^+$ is nearly irreversible, allowing the bifurcation amplifier to latch and store its output during the integration time set by the sensitivity of the follower amplifier.

We then characterized in detail the switching in the vicinity of the $O_L \rightarrow O_H$ transition. We excited the system with two different readout pulse protocols. In the first protocol, the drive current was ramped from 0 to its maximum value in 40 ns and was then held constant for 40 ns before returning to 0. Only the final 20 ns of the constant drive period were used to determine the oscillation phase with the first 20 ns allotted for settling of the phase. Histograms taken with a 10 MHz acquisition rate are shown in Fig. 3.8. In the upper panel, the two peaks corresponding to states O_L and O_H can easily be resolved with a small relative overlap of 10^{-2} . The finite width of each peak is due to the output noise and is consistent with the noise temperature of our HEMT amplifier. In this first method, the latching property of the system has not been exploited. In our second protocol for the readout pulse, we again ramp

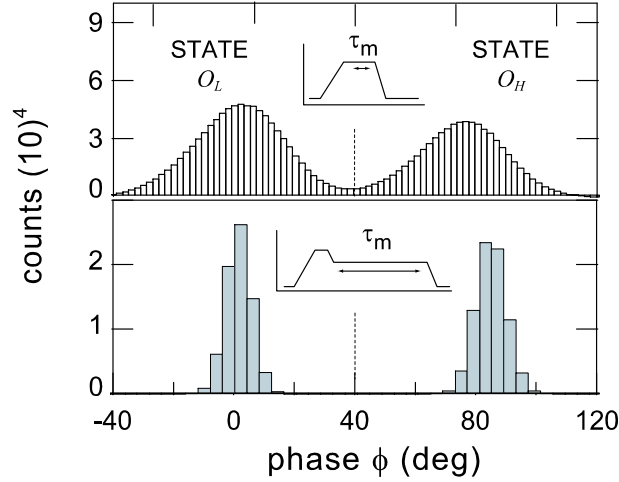


Figure 3.8: Histograms of the reflected signal phase at $i_{RF}/I_0 = 0.145$. The upper histogram contains 1.6×10^6 counts with a measurement time $\tau_m = 20$ ns. The lower panel, taken with the latching technique, has 1.5×10^5 counts with a measurement time $\tau_m = 300$ ns. Data here has been taken under the same operating conditions as in Fig 3.7. The dashed line represents the discrimination threshold between the O_L and O_H state.

for 40 ns and allow a settling time of 20 ns, but we then reduce the drive current by 20% and measure the reflected signal for 300 ns. In that latter period, whatever state was reached at the end of the initial 60 ns period is "latched" and time is spent just increasing the signal/noise ratio of the reflected phase measurement. As shown in the lower panel of Fig. 3.8, the two peaks are now fully separated, with a relative overlap of 6×10^{-5} allowing a determination of the state O_H probability with an accuracy better than 10^{-3} . This second protocol would be preferred only for very precise time-resolved measurements of I_0 or for applications where a low-noise follower amplifier is impractical.

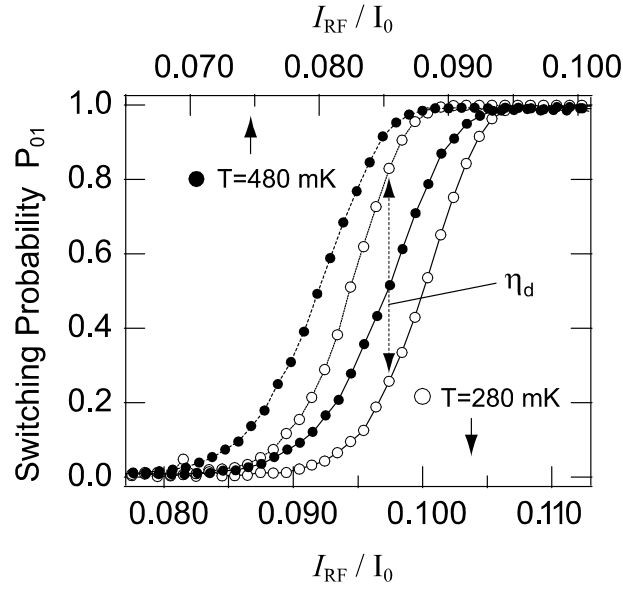


Figure 3.9: Switching probability curves at $T = 280$ mK (open circles) and $T = 480$ mK (closed circles) as a function of the normalized drive current I_{RF}/I_0 . The discrimination power η_d is the maximum difference between the two curves at the same temperature. The two curves differ by approximately 1% in I_0 with the curve corresponding to the higher critical current lies at higher values of I_{RF}/I_0 .

3.3.2 JBA as a readout

A third experiment was performed to study the switching probability $P_{\text{switch}}(I_{RF})$ from state O_L to O_H for different values of the temperature T and critical current I_0 , the latter being varied with a magnetic field applied parallel to the junction plane. Using the readout protocol and the discrimination threshold shown in Fig. 3.8, we obtain the switching probability curves shown in Fig. 3.9. Defining the discrimination power η_d as the maximum difference between two switching probability curves which differ in I_0 (see sections 2.3.3 and 4.3.5), we find that at $T = 280$ mK, $\eta_d = 57\%$ for $\Delta I_0/I_0 = 1\%$ – the typical variation observed in a superconducting

charge-phase qubit [6]. The switching probability curves should shift according to $(\Delta I_B/I_B)/(\Delta I_0/I_0) = 3/4\alpha$ (equation 2.35), which for our case takes the value 6.1. In Fig. 3.9, the curves are shifted by 6%, which agrees well with this prediction. For the case of the DC current biased junction, similar curves would shift only by 1%. Comparable discrimination power using DC switching has only been achieved in these devices at $T \leq 60$ mK. As the temperature is increased, the switching probability curves broaden due to increased thermal fluctuations and the discriminating power decreases: at $T = 480$ mK, $\eta_d = 49\%$. Correspondingly, the discrimination increases as the temperature is lowered. The experimentally achieved values of discrimination power were in good agreement with the theoretical predictions and numerical simulations. Numerical simulations of the combined JBA+qubit system will be discussed in the next chapter.

As discussed in section 2.3.3, the sensitivity of the JBA as a detector of critical current variations is determined by the width of the S-curves, which in turn is determined by the effective intensity of fluctuations felt by the JBA. A well designed experimental setup will ensure that this intensity of fluctuations is set by the thermal/quantum fluctuations corresponding to the operating temperature of the JBA. It is possible to determine the effective temperature felt by the JBA by carefully measuring the escape rates from state O_L to O_H as a function of the various bias parameters. The classical theory of escape was briefly described in section 2.3.2. Chapter 7 describes a theory of escape which is applicable both the classical ($k_B T \gg \hbar\omega_p$) and quantum ($k_B T \ll \hbar\omega_p$) regimes. The escape measurements are described in chapter 8. These measurements will help in determining the ultimate sensitivity of the JBA.

3.4 Microwave design considerations

In this section, we will discuss some important considerations to ensure that a well controlled bifurcation can be observed. In particular, we will discuss the microwave characteristics of the shunting capacitor which reduces the bare plasma frequency of the Josephson junction. A more detailed and generalized discussion on this topic can be found in reference [59].

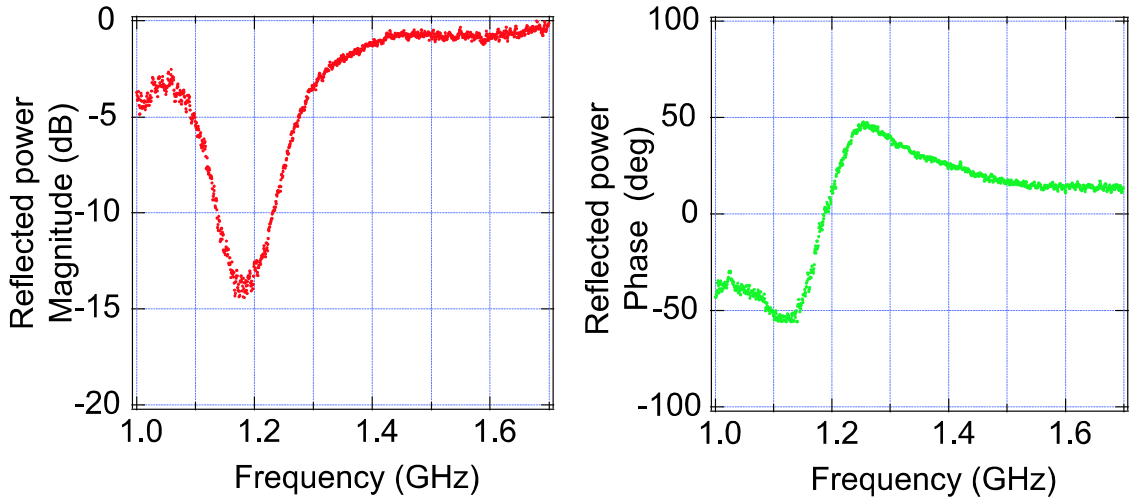


Figure 3.10: Magnitude and phase of the reflected power. Data shown is for sample 1 with a 100 nm Au ground plane. The stray parameters $R_S = 0.8 \Omega$ and $L_S = 0.2$ nH. The strong dip in the magnitude response and the smaller phase shift at resonance is a consequence of the dissipation in the oscillator due to the stray resistance.

A driven, non-linear oscillator of any type can undergo some kind of transition at a critical power/frequency and even show sensitivity to system parameters. But that does not always mean that it can be used as a detector; e.g., a transition into a chaotic regime might be very hard to control and hence not be practically implemented. In other cases, the back-action of the detector/amplifier on the system being measured

might become uncontrolled. The kind of bifurcation described theoretically in the previous chapter and experimentally in this one, is controllable and well behaved as a function of bias parameters (frequency and power). In order to observe this bifurcation phenomena and use it effectively as a detector/amplifier, we need to ensure that the non-linear system is constructed correctly.

During the initial stages of this experiment, we realized that the design of the shunting capacitor had to be implemented carefully to ensure that it behaved as a capacitor at the relevant frequencies. Fabricating ideal, lumped circuit elements operable at microwave frequencies is non-trivial. Typically, the lumped element will have capacitance, inductance and resistance depending on how it is fabricated and the frequencies at which it is being used. As we go to higher frequencies (> 5 GHz), it is much easier and practical to use distributed circuit elements like transmission line resonators. This was one of the reasons for the development of the Cavity Bifurcation Amplifier (CBA) which uses transmission line resonators with an embedded Josephson junction to implement the non-linear oscillator [66].

The first generation of our microwave capacitors were made using a thin (100 nm) Au ground plane. This was followed by Nb ground planes (50 and 200 nm) and then thick (1 μ m) Cu. As discussed in section 3.1, imperfect screening currents in the capacitor plates due to the finite conductivity (Au and Cu) and thickness of the ground planes, results in a stray inductance (L_S) and a stray resistance (R_S). The inset shown in Fig. 3.3 depicts a model which accounts for the stray inductance and resistance. The samples made with superconducting Nb ground planes did not have any stray resistance while the data for samples with Au and Cu ground planes lead to a value of $R_S = 0.8 \Omega$ and 0.02Ω respectively. The best results were obtained with

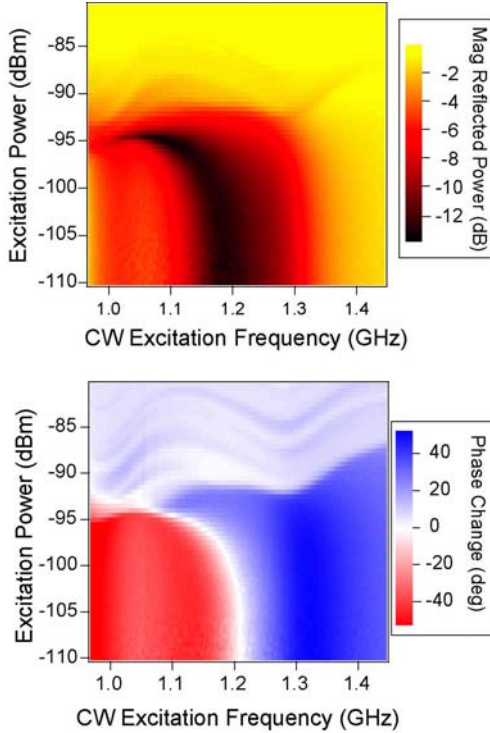


Figure 3.11: Magnitude (a) and phase (b) of the reflected power as a function of drive power and frequency. Data is shown for sample 1 which has a Au ground plane and shows strong absorption near resonance in the magnitude response. The phase response shows a diminished phase shift at resonance and a different behavior as a function of power. Note that a different color scheme (as compared to Fig. 3.6) is used here for the phase plot to depict the features more clearly.

the 1 μm Cu ground planes with the value of $L_S = 0.026$ nH while the other samples had a value in the range of 0.15 – 0.34 nH.

The samples with Au ground planes and a large stray resistance (0.8Ω) did not show the correct bifurcation phenomena. The line shape of the linear resonance was also significantly affected as shown in Fig. 3.10. The presence of the stray resistance results in dissipation in the oscillator, and the phase shift in the reflected signal as one goes through resonance, is much less than 360 degrees. The direction of the phase

shift can also get reversed. The full non-linear response for this sample is shown Fig. 3.11. Note that a different color scheme (as compared to Fig. 3.6) is used here for the phase plot to depict the features more clearly.

As before, the resonant frequency starts to decrease with increasing power but one encounters the well-hopping regime (the wavy region in the top half of the plot) before the bistable regime can be reached. A simple explanation of this phenomena is that the presence of the stray inductance and resistance dilutes the effective non-linearity of the oscillator. This leads to a higher critical power to enter the bistable regime. As the value of the RF current flowing through the Josephson junction approaches the critical current (I_0), the system tends to become unstable. A more detailed theoretical discussion on the exact condition can be found in reference [59]. Numerical simulations of the full system including all the stray parameters showed that the phase particle is not confined to one well of the washboard potential of the Josephson junction but hops randomly between different wells. On average, this new dynamic state has a reflected phase value of zero but does not correspond to the high oscillation state of the JBA as described in the previous chapter. The diffusive motion of the phase particle in this regime results in a finite audio frequency ac resistance which was measured with a lock-in amplifier. The lock-in output voltage was monitored as the drive power at a fixed frequency was swept through the transition region. The resulting curves are shown in Fig. 3.12.

The upper panel shows the data for a sample 1 with a 100 nm thick Au ground plane. We note that the lock-in voltage starts to rise exactly at the same power at which the reflected phase starts to change sharply signifying a transition to a different state. In the lower panel, data is shown for a sample 6 with a 1 μm thick Cu ground

plane with negligible stray resistance and a L_J/L_S ratio of about 28. The lock-in voltage remains at zero as the power is swept through the transition and the phase changes sharply. This is the signature of a clean transition from the low amplitude to the high amplitude state of the JBA.

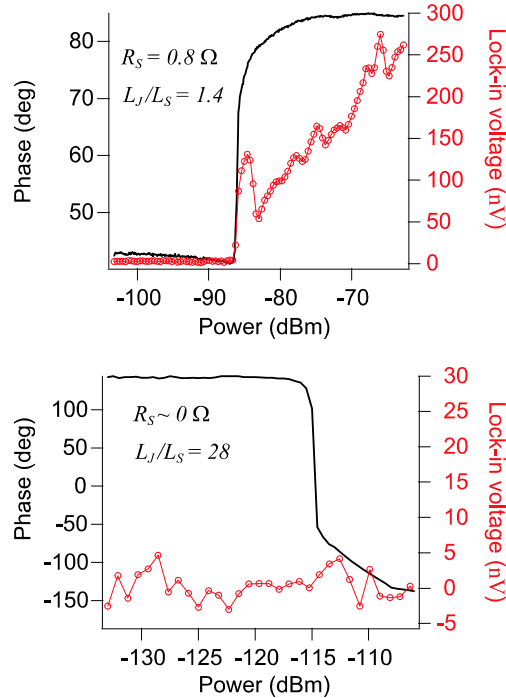


Figure 3.12: Audio frequency ac resistance of a non-linear oscillator as a function of drive power at a fixed frequency. The upper panel shows data for sample 1 with non-negligible values for stray inductance and resistance. The systems undergoes a transition into a state where the phase particle hops randomly between the wells of the washboard potential. This results in a finite audio frequency resistance which is depicted by the rising lock-in voltage at the transition point. The lower panel shows data for a sample 6 with negligible stray parameters. The sharp phase shift here, signifies a transition from the low amplitude to the high amplitude of the JBA. The lock-in voltage remains at zero, signifying a clean transition.

It is clear from the above discussion that the bifurcation phenomena is very sensitive to the stray elements in the circuit and one should ensure that they are kept to

a minimum. Irrespective of the stray parameters, the well-hopping regime is always encountered at high enough drive power (the black region in Fig. 3.6 and the white region in Fig. 3.11). The stray parameters determine whether one can approach the critical power required for observing the bifurcation phenomena before running into the well-hopping regime. For future experiments, we decided on using a 500 nm thick Cu ground plane for the capacitors. This provided us with a small stray resistance ($< 0.05 \Omega$) and L_J/L_S ratio greater than 20. The thickness of the ground plane was reduced from 1 μm to make the fabrication procedure easier. These parameters provided us with a clean bifurcation and sufficient room to vary drive frequency and power without running into the well-hopping regime. Furthermore, we noted that the transition into the well-hopping state showed sufficient sensitivity to system parameters and could in principle be used for making a detector. But the diffusive nature of the phase particle in this regime can lead to strong back-action effects. This rules out its application for measuring delicate systems like superconducting qubits. We will discuss these back-action effects on qubits in chapter 6.

In conclusion, we have performed a novel, phase-sensitive, microwave experiment demonstrating that the Josephson plasma oscillation can transition between the two dynamical states predicted for a driven non-linear system. Using different samples, we have shown that this dynamical phenomenon is stable, reproducible and can be precisely controlled, thus opening the possibility for practical applications like amplification. We have also studied its response in the time domain and successfully implemented a readout protocol to discriminate small changes in critical current of the Josephson junction. With the JBA operating at $T = 280 \text{ mK}$, it is possible to resolve with a signal/noise ratio of 1 a 10 nA variation in I_0 in a total time ≤ 80

ns, corresponding to a critical current sensitivity of $S_{I_0}^{1/2} = 3.3 \times 10^{-12} \text{ A} \cdot \text{Hz}^{-1/2}$ (see section 2.3.3). The critical current (I_0) of typical junctions is about $1 - 2 \mu\text{A}$ leading to a fractional sensitivity of $S_{I_0}^{1/2}/I_0 \simeq 10^{-6} \text{ Hz}^{-1/2}$. If we replace the junction with a SQUID, this would correspond to a flux sensitivity of approximately $S_{\phi}^{1/2}/\Phi_0 = 10^{-6} \text{ Hz}^{-1/2}$. This is comparable to the flux sensitivity obtained in typical DC SQUIDS [67] though the best DC SQUIDS have a flux sensitivity of $10^{-8} \Phi_0 \text{ Hz}^{-1/2}$. The flux sensitivity in the SQUID-JBA device could be enhanced by increasing the critical current of the junction and going to lower temperatures. The advantage of the JBA over DC SQUIDS [15] resides in its extremely low back-action. Since there is no on-chip dissipation, the only source of back-action is the matched isolator load, which is efficiently thermalized at $T = 280 \text{ mK}$. An important point is that in the JBA, only fluctuations from the load that occur in a narrow band centered about the plasma frequency contribute to the back-action, whereas in the SQUID noise from many high frequency bands is also significant. Finally, the bifurcation amplifier does not suffer from quasiparticle generation associated with hysteretic SQUIDS [68] and DC current-biased junctions [38] which switch into the voltage state. Long quasiparticle recombination times at low temperatures limit the acquisition rate of these devices while the recombination process itself produces excess noise for adjacent circuitry [39].

We will discuss the implementation of JBA as a readout for superconducting qubits in the next three chapters.

Chapter 4

JBA as a qubit readout

In this chapter, we will describe the implementation of the JBA as a qubit readout. Specifically, we will use the so-called quantronium qubit which was developed at CEA-Saclay [6]. We will first describe the Cooper pair box (CPB) circuit [36, 69, 37] and then go on to discuss the split Cooper pair box circuit on which the quantronium qubit is based. The material presented on the Cooper pair box and the quantronium is based on the Cottet thesis [38]. This will be followed by a description of the combined quantronium and JBA system. We will discuss how the properties of the quantronium affect the JBA and the principle of the qubit readout. We will finally look at some numerical simulations which will provide us with an idea of the performance of the JBA as a qubit readout.

4.1 The Cooper pair box

The Cooper pair box circuit (Fig. 4.1) consists of a superconducting island which is connected to a superconducting reservoir via a Josephson junction. The island is

biased by an external voltage source U via a gate capacitance C_g . The Josephson junction has a Josephson energy E_J and capacitance C_J . The two energy scales in the description of the circuit are the Josephson energy E_J and the electrostatic energy E_C . E_C is the electrostatic energy required to put one extra electron on the superconducting island and is given by

$$E_C = \frac{e^2}{2C_\Sigma}$$

where e is the electron charge and C_Σ is the total capacitance of the island given by

$$C_\Sigma = C_J + C_g \quad (4.1)$$

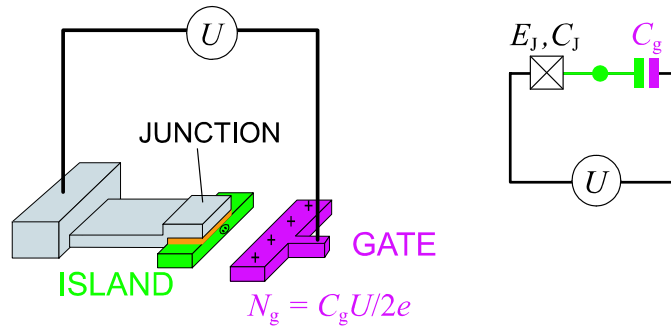


Figure 4.1: Physical layout and circuit diagram of a Cooper pair box. It consists of a superconducting island coupled to a superconducting reservoir by a Josephson junction. The island is biased with an external voltage source U via a gate capacitor C_g .

4.1.1 Hamiltonian in charge basis

The operator describing the number of excess Cooper pairs on the island is written in dimensionless form

$$\hat{N} = \frac{\hat{q}_{island}}{2e} \quad (4.2)$$

where \hat{q}_{island} is the excess charge on the island. Similarly, the external bias voltage U can be written in dimensionless form in units of excess Cooper pairs as

$$N_g = \frac{C_g U}{2e} \quad (4.3)$$

where N_g is called the reduced gate charge and is a continuous variable. In terms of these dimensionless variables, we can write the electrostatic part of the Hamiltonian of the Cooper pair box as

$$\hat{H}_{el} = 4E_C \left(\hat{N} - N_g \right)^2 \quad (4.4)$$

The Josephson part of the Hamiltonian allows for coupling between different charge states. Using a set of charge states $|N\rangle$ such $\hat{N}|N\rangle = N|N\rangle$, we can write

$$\hat{H}_J = \frac{E_J}{2} \sum_N (|N\rangle\langle N+1| + |N+1\rangle\langle N|) \quad (4.5)$$

The total Hamiltonian of the CPB is given by

$$\hat{H}(N_g) = \sum_N \left(4E_C \left(\hat{N} - N_g \right)^2 |N\rangle\langle N| + \frac{E_J}{2} (|N\rangle\langle N+1| + |N+1\rangle\langle N|) \right) \quad (4.6)$$

Denoting the energy eigenstates of the above Hamiltonian as $|\mathbf{k}\rangle$ ¹, we can write

$$\hat{H}(N_g)|\mathbf{k}\rangle = E_k|\mathbf{k}\rangle \quad (4.7)$$

where E_k is the energy of the eigenstate $|\mathbf{k}\rangle$. Fig. 4.2 shows the discrete energy levels² associated with the eigenstates of the above Hamiltonian. The energy levels are periodic in the external gate charge N_g with a period of 1. We note that the Josephson coupling term lifts the degeneracy between the ground and first excited state at $N_g = m + 1/2$, where m is an integer. The dotted lines represent the energy levels in the absence of the Josephson term.

4.1.2 Hamiltonian in phase basis

It is often convenient to represent the CPB Hamiltonian in terms of superconducting phase operator $\hat{\theta}$ of the island. $\hat{\theta}$ and \hat{N} are like the position and momentum operators and the relation between the canonically conjugate variables is given by

$$\hat{N} = \frac{1}{i} \frac{\partial}{\partial \hat{\theta}} \quad (4.8)$$

The operator $\exp(\pm i\hat{\theta})$ acting on the charge states $|N\rangle$ produces the following effect

$$\exp(\pm i\hat{\theta})|N\rangle = |N \pm 1\rangle \quad (4.9)$$

¹ $|\mathbf{k}\rangle$ which is an energy eigenstate is written in bold to distinguish it from $|N\rangle$ which represents a state with N excess Cooper pairs on the island e.g. $|\mathbf{1}\rangle$ represents the first excited state of the hamiltonian while $|1\rangle$ is the state with one excess Cooper pair.

²These plots were created using calculations based on the phase representation as discussed in the next section.

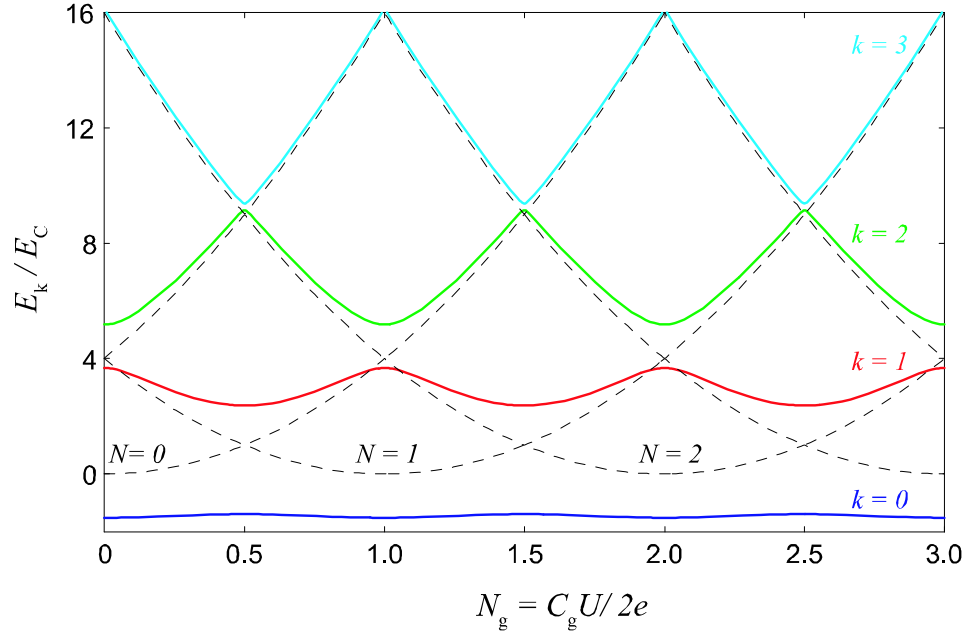


Figure 4.2: Energy levels of the Cooper pair box with $E_J/E_C = 4.0$ as a function of gate charge N_g . The ground state and the first three excited states are shown. The dotted lines correspond to the case where the Josephson coupling term is absent.

Using equations 4.8 and 4.9 we can rewrite the CPB Hamiltonian (4.6) in phase representation as

$$\hat{H}(N_g) = 4E_C \left(\frac{1}{i} \frac{\partial}{\partial \theta} - N_g \right)^2 - E_J \cos(\hat{\theta}) \quad (4.10)$$

The advantage of using the phase representation is that the Schrödinger equation associated with the above Hamiltonian can be solved analytically in terms of the Mathieu functions. The Mathieu functions which are the solutions to the Mathieu equation can be computed easily using the software package *Mathematica* (see [38] for more details and Appendix B for a *Mathematica* notebook demonstrating the calculations)

4.1.3 The split Cooper pair box

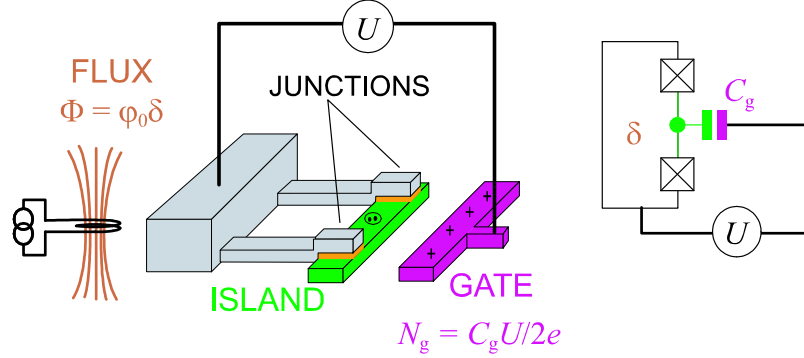


Figure 4.3: Physical layout and circuit diagram of a split Cooper pair box. This circuit is similar to the CPB except that the single junction has been replaced by two junctions in a loop. Now we have two parameters (n_g and δ) which control the properties of the split CPB.

The split Cooper pair box circuit is shown in Fig. 4.3 and is a small modification to the basic CPB circuit. The single Josephson junction is replaced by two nominally equal junctions in a loop. This leads to two control parameters with which we can tune the properties of the split CPB - the gate charge N_g and the loop flux $\delta/2\pi = \Phi/\Phi_0$. Let d describe the asymmetry in the two junctions so that the Josephson energy of the two junctions can be written as

$$E_{J1} = \frac{E_J}{2}(1 + d) \quad (4.11a)$$

$$E_{J2} = \frac{E_J}{2}(1 - d) \quad (4.11b)$$

where $E_J = E_{J1} + E_{J2}$. Now, the total capacitance $C_\Sigma = C_g + C_{J1} + C_{J2}$ where C_{J1} and C_{J2} are the individual junction capacitances. The superconducting phase $\hat{\theta}$ of

the island is now equal to the difference in the phase across the individual junctions

$$\hat{\theta} = \frac{\hat{\delta}_1 - \hat{\delta}_2}{2} \quad (4.12)$$

while the net phase across the two junctions is given by their sum

$$\hat{\delta} = \hat{\delta}_1 + \hat{\delta}_2 \quad (4.13)$$

where $\hat{\delta}_1$ and $\hat{\delta}_2$ are the individual phases across the two junctions. We will treat $\hat{\delta}$ as a classical parameter δ since in our measurements, the impedance across the split junction is always kept lower than the resistance quantum h/e^2 (see chapter 2 in [38]). The external flux Φ imposes a phase³ δ such that $\Phi = \varphi_0 \delta$ where $\varphi_0 = \Phi_0/2\pi$ is the reduced flux quantum. So N_g and δ are the two external control parameters.

The electrostatic part of the Hamiltonian remains the same as before (4.4) while the Josephson part of the Hamiltonian can be written as

$$\hat{H}_J = -E_{J1} \cos(\hat{\delta}_1) - E_{J2} \cos(\hat{\delta}_2) \quad (4.14)$$

Using equations 4.11,4.12,4.13, and after carrying out some trigonometric manipulations, we write the Josephson Hamiltonian as

$$\hat{H}_J(\delta) = -E_J \cos\left(\frac{\delta}{2}\right) \cos(\hat{\theta}) + dE_J \sin\left(\frac{\delta}{2}\right) \sin(\hat{\theta}) \quad (4.15)$$

The above Hamiltonian reduces to the CPB Hamiltonian for $d = 0$ and $\delta = 0$. For $d = 0$, the split Cooper pair box can be considered as a CPB with a tunable

³Assuming that the loop inductance is much smaller than Josephson inductance of the junctions

Josephson energy as $\hat{H}(\delta) = -E_J \cos(\delta/2) \cos(\hat{\theta})$. The full Hamiltonian in the phase representation for the split CPB can now be written as

$$\hat{H}(N_g, \delta) = 4E_C \left(\frac{1}{i} \frac{\partial}{\partial \theta} - N_g \right)^2 - E_J^*(d, \delta) \cos \left(\hat{\theta} + \Lambda(d, \delta) \right) \quad (4.16)$$

where

$$E_J^*(d, \delta) = E_J \sqrt{\frac{1 + d^2 + (1 - d^2) \cos(\delta)}{2}} \quad (4.17a)$$

$$\tan \Lambda(d, \delta) = -d \tan\left(\frac{\delta}{2}\right) \quad (4.17b)$$

The properties of the split CPB are periodic in both N_g (period 1) and δ (period 2π). In what follows, whenever a particular value of N_g or δ is specified, it is assumed that the same would be true for other values which are separated by integer number of periods e.g. $N_g = N_0$ is the same as $N_g = N_0 + m$ where m is any integer. Similarly $\delta = \delta_0$ is the same as $\delta = \delta_0 + 2\pi m$.

4.2 The quantronium

If we take the split CPB circuit and insert a large Josephson junction (with Josephson energy E_J^R such that $E_J^R \gg E_J$) in the loop, we get the circuit shown in Fig. 4.4. This circuit has been nicknamed quantronium to illustrate the fact that this circuit behaves like an artificial atom with the big junction being equivalent to the nucleus and the small junctions being equivalent to electrons. This modification allows one to impose a phase difference δ across the split CPB junctions by means of passing a current through the large Josephson junction, which we will call the readout junction.

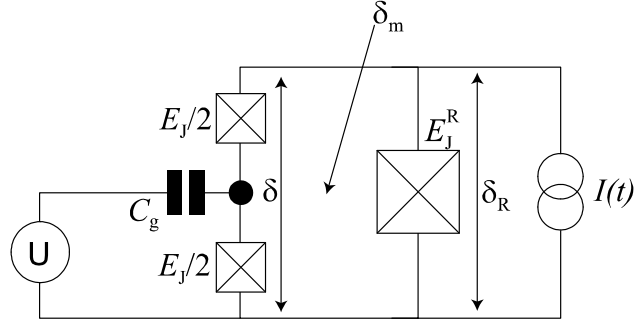


Figure 4.4: Circuit diagram of the quantronium. It consists of three junctions in a superconducting loop. The large readout junction (E_J^R) is about 100 times bigger than the two small junctions ($E_J/2$). Like the split CPB there are two control parameters ($N_g = C_g U/2e$ and δ). The phase δ can now be controlled via an external flux (δ_m) or with a current bias.

Since $E_J^R \gg E_J$, most of the current will pass through the large junction and the phase δ_R developed across the readout junction can be written as

$$\delta_R(t) \approx \arcsin \frac{I(t)}{I_0} \quad (4.18)$$

where $I_0 = E_J^R/\varphi_0$ is the critical current of the large Josephson junction and $I(t)$ is the applied current bias. The net phase developed across the CPB junctions is equal to the sum of the phases imposed due to an external flux ($\delta_m = \Phi/\varphi_0$) and the phase across the readout junction

$$\delta = \delta_m + \delta_R \quad (4.19)$$

4.2.1 Quantronium as a quantum bit

When the external control parameters N_g and δ are tuned appropriately, the lowest two energy levels are sufficiently separated from the other levels. These two lowest

levels form an effective two level system and can then be used as a quantum bit or qubit. We will represent these two states as $|0\rangle$ and $|1\rangle$. The quantum states of a two level system can be conveniently depicted using fictitious spin 1/2 or the Bloch sphere representation [70]. In this representation, $|0\rangle$ and $|1\rangle$ correspond to the north and south pole of a unit sphere. Any normalized superposition of $|0\rangle$ and $|1\rangle$ can then be represented as a point on this sphere with a unit Bloch vector connecting the origin to this point. Fig. 4.5 illustrates this idea. This representation is also quite useful in illustrating quantum manipulations on the two level systems.

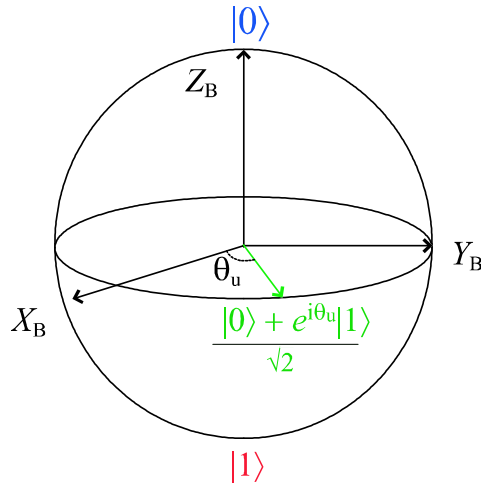


Figure 4.5: Bloch sphere representation of a two level system. The ground state $|0\rangle$ corresponds to the North pole while excited state $|1\rangle$ corresponds to the South pole. Any other point on the sphere corresponds to a superposition of $|0\rangle$ and $|1\rangle$.

The energy surfaces corresponding to the lowest two states is shown in Fig. 4.6 as a function of N_g and δ . We note that for $N_g = 0.5$ and $\delta = 0$, the gradient of the energy surfaces w.r.t. N_g and δ is zero. This implies, that at this bias point, the energy difference between the two levels is insensitive to fluctuations in the external control parameters N_g and δ to first order. In other words, the transition frequency

$\nu_{01}(N_g = 0.5, \delta = 0) = [E_1 - E_0]_{(N_g=0.5, \delta=0)}$ at this operating point is protected from noise in N_g and δ to first order:

$$\left[\frac{\partial \nu_{01}}{\partial N_g} \right]_{N_g=0.5, \delta=0} = 0 \quad (4.20)$$

$$\left[\frac{\partial \nu_{01}}{\partial \delta} \right]_{N_g=0.5, \delta=0} = 0 \quad (4.21)$$

This point has been nicknamed the "sweet spot" and is the optimal point to operate the quantum qubit. Note that, other operating points where $\partial \nu_{01} / \partial (N_g, \delta) = 0$ exist e.g. $N_g = 0$ and $\delta = 0$. But, the second derivative⁴ in charge $\partial_{01}^2 \nu / \partial N_g^2$ has a larger value at $N_g = 0$ when compared to its value at $N_g = 0.5$. Hence the best protection from noise in N_g and δ is achieved at the "sweet spot". This is important because low frequency noise in the control parameters can cause dephasing of the qubit [6, 40]. Unless specified otherwise, all qubit manipulations are carried out at the "sweet spot", i.e., $N_g = 0.5$ and $\delta = 0$.

The qubit state manipulations are carried out using techniques borrowed from Nuclear Magnetic Resonance (NMR) experiments [71]. This involves applying a microwave frequency signal of amplitude U_{RF} and frequency ν_{RF} to the gate electrode. This results in an additional time dependent term in the Hamiltonian 4.16 of the split CPB

$$\hat{H}_{RF} = -8E_C \Delta N_g \cos(2\pi \nu_{RF} t) \hat{N}$$

where $\Delta N_g = C_g U_{RF} / 2e$ is the reduced gate voltage amplitude. Under the influence of this drive, the qubit state vector precesses in a frame rotating at ν_{RF} at a frequency

⁴The second and higher derivatives at the sweet spot depend on the ratio E_J/E_C and can be tuned by adjusting sample parameters.

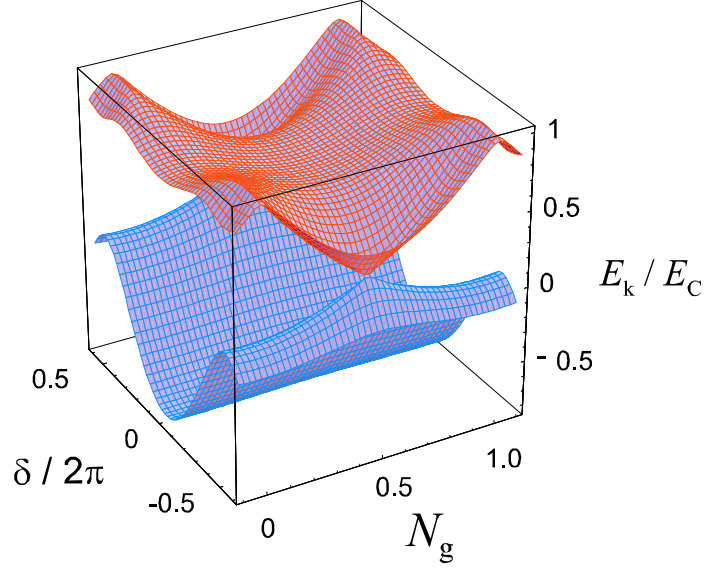


Figure 4.6: Ground and first excited energy level of the qubit as a function of the control parameters N_g and δ . Data is shown for an E_J/E_C ratio of 4. The bias point $N_g = 0.5$, $\delta = 0$ is nicknamed the sweet spot because the transition frequency ν_{01} , to first order, is insensitive to noise in the control parameters (N_g , δ).

[38] given by

$$\nu_p = \sqrt{\nu_{Rabi}^2 + (\nu_{01} - \nu_{RF})^2} \quad (4.22)$$

When this driving field is resonant with the qubit transition frequency, i.e., $\nu_{RF} = \nu_{01}$, the system undergoes Rabi oscillations [72] at a rate given by

$$\nu_{Rabi} = \frac{8E_C \Delta N_g \langle \mathbf{1} | \hat{N} | \mathbf{0} \rangle}{h} \quad (4.23)$$

We note that ν_{Rabi} is proportional to the drive amplitude U_{RF} and to the matrix element between the ground and first excited state. In the Bloch sphere representation, this corresponds to the Bloch vector rotating from the North pole to the South pole around the x_B axis. When the qubit evolves freely ($\nu_{Rabi} = 0$) e.g. between successive

Rabi pulse, the Bloch vector precesses around the z_B axis in a frame rotating at ν_{RF} , at a rate given by the Ramsey [73] frequency

$$\nu_{Ramsey} = |\nu_{01} - \nu_{RF}| \quad (4.24)$$

Thus, a combination of driven and free evolution allows one to prepare any qubit state on the Bloch sphere.

4.2.2 Readout strategies

We now discuss the various strategies that can be used to measure the state of the qubit. We need to exploit some property of the qubit which depends on its quantum state. The control ports (gate and flux/phase) also allow us to couple to the qubit and measure its properties. For the qubit, there are four quantities that can be conveniently measured to determine the state of the qubit. These are the island charge ($Q_k \propto \partial E_k / \partial N_g$), the loop current ($I_k \propto \partial E_k / \partial \delta$), the island capacitance ($C_k \propto \partial^2 E_k / \partial N_g^2$) and the loop inductance ($L_k \propto (\partial^2 E_k / \partial \delta^2)^{-1}$). The first CPB based qubits employed a charge measurement technique to readout the qubit state [4]. Measuring the charge requires an electrometer coupled to the island of the CPB [74], but the ground and the excited state have the same average charge when operated at the sweet spot. Hence, one has to move away from the sweet spot (in gate charge) at the time of measurement which can lead to rapid decoherence [40].

The original qubit readout [6] was based on measuring the current in the loop. The loop currents modified the effective critical current of the readout junction. This change was detected by measuring the switching of the readout junction

from the superconducting state to the voltage state. This measurement also involved moving away from the sweet spot (in phase/flux) during the readout, because the average current at the sweet spot was zero for both qubit states. Furthermore, the switching of the readout junction into the voltage state led to the generation of quasiparticles which take a long time to recombine at low temperatures resulting in a slow repetition rate of the experiment. The presence of quasiparticles near the qubit can cause dissipation and lead to decoherence.

It is now well understood that dispersive measurements of the qubit state [75, 76, 77, 33], which probe the reactive part of the response of the circuit, perform better as qubit readouts. For the CPB based qubits, this amounts to measuring the capacitance or inductance of the qubit. This can be done by coupling the qubit to a resonator and measuring its response under AC excitation. The measurement can now be performed at the sweet spot as the technique probes the second derivative (w.r.t. charge or phase) of the energy surface which has a different value for the two qubit states even at the sweet spot. In fact, the difference is maximum at this operating point, making it ideal for measurement. Our measurement technique using the JBA involves the measurement of the inductance by coupling the quantum qubit to a non-linear resonator via the phase port. Using the phase port offers the additional advantage of separating the write port (charge) from the readout port (phase). Experiments probing the effective capacitance of the CPB have also been successfully implemented [33, 78]. It should be pointed out that the idea of an effective capacitance or inductance is valid only when the readout frequency is much smaller than the qubit transition frequency. This condition is satisfied for the JBA readout. In general, one should characterize the qubit by a state dependent effective impedance.

We discuss the JBA readout in more detail in the next section.

4.3 Measuring the qantronium with the JBA

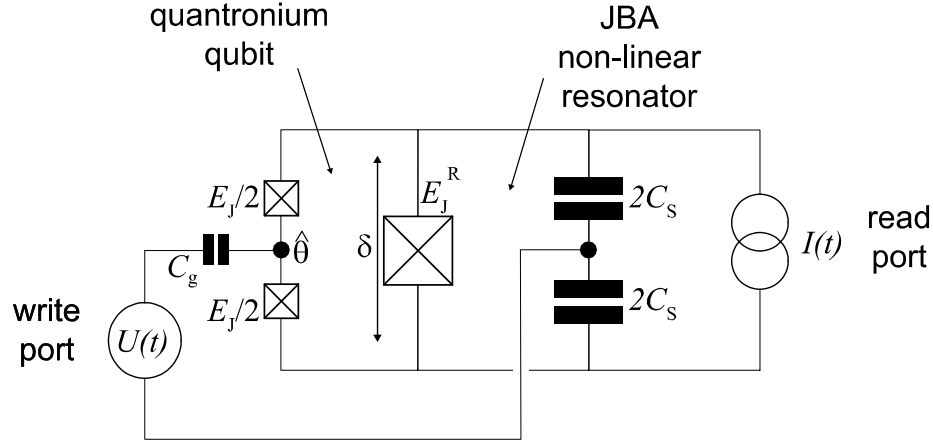


Figure 4.7: Circuit diagram of a qantronium with a JBA readout. The big readout junction along with the shunt capacitors forms the non-linear oscillator which is the central element of the JBA. The qantronium and the non-linear oscillator are coupled via the shared readout junction. The control parameters $U(t) = U_{RF}(t) \cos \omega_{RF}t$ and $I(t) = I_{RF}(t) \cos \omega_d t$ are analogous to electromagnetic probe fields in an atomic system and induce a charge excitation of the write port and a phase excitation of the read port, respectively. Under appropriate driving conditions, the two qubit states are mapped to the two driven states of the non-linear oscillator forming the basis of the readout.

4.3.1 Effective Hamiltonian

The combined qantronium with JBA circuit is schematically depicted in Fig. 4.7. The set of three junctions consists of two small junctions, which we assume to be identical⁵ and have a Josephson energy ($E_J/2$) comparable to the charging energy

⁵The small asymmetry ($< 10\%$) in the two junctions of the split CPB does not affect its properties significantly at $\delta = 0$, where the qubit is operated.

(E_C) of the island between them, and a large readout junction, whose Josephson energy (E_J^R) is approximately 100 times larger than that of each small junction. The readout junction is shunted with capacitors (C_S) to reduce its plasma frequency to the 1 – 2 GHz range. The readout junction together with the shunt capacitors form the non-linear resonator which is the central element of the JBA readout. The quantronium qubit and the non-linear resonator are phase coupled via the shared readout junction. The gauge-invariant phase difference $\hat{\theta}$ of the island with respect to the mid-point of the capacitance shunting the large junction is analogous to the position of the electron relative to the nucleus of the atom, while the gauge-invariant phase difference $\hat{\delta}$ across the large junction is the absolute position of the nucleus. Neglecting the dissipation induced in the transmission lines, the total Hamiltonian of the split Cooper pair box biased at the sweet spot and coupled to a JBA resonator is $\hat{H}(t) = \hat{H}_{box}(t) + \hat{H}_{res}(t)$ with

$$\begin{aligned}\hat{H}_{box}(t) &= 4E_C \left(\hat{N} - \frac{1}{2} + \frac{C_g U(t)}{2e} \right)^2 - \left(E_J \cos \frac{\hat{\delta}}{2} \right) \cos \hat{\theta} \\ \hat{H}_{res}(t) &= \frac{\hat{q}^2}{2C_s} - E_J^R \cos \hat{\delta} - \varphi_0 I(t) \hat{\delta}\end{aligned}\quad (4.25)$$

This Hamiltonian has been written supposing that the asymmetry between the two small junctions is zero⁵, and the DC values of the offset gate charge and loop flux have been compensated to operate at the sweet spot, i.e., $N_g = 1/2$ and $\delta_m = 0$ and hence $\delta_R = \delta$ (see 4.19). Here, \hat{N} and $\hat{q}/2e$ are the momenta conjugate to the generalized positions $\hat{\theta}$ and $\hat{\delta}$, respectively. The control parameters $U(t) = U_{RF}(t) \cos \omega_{RF} t$ and $I(t) = I_{RF}(t) \cos \omega_d t$ are analogous to electromagnetic probe fields in an atomic system and induce a charge excitation of the write port and a phase excitation of the

read port, respectively.

If we keep these two lowest states in the Hilbert space of \hat{H}_{box} [40] and we express \hat{H}_{res} in terms of the photon creation and annihilation operators, we obtain an effective Hamiltonian

$$\begin{aligned} \hat{H}_{eff} = & \frac{2C_g U(t)}{e} E_C \sigma_X - \frac{E_J}{2} \sigma_Z + \hbar \omega_p (1 + \lambda \sigma_Z) a^\dagger a \\ & - \mu \left(1 + \frac{\lambda}{4} \sigma_Z \right) (a + a^\dagger)^4 - f (a + a^\dagger) I(t) \end{aligned} \quad (4.26)$$

where

$$\omega_p = \sqrt{\frac{E_J^R}{\varphi_0^2 C_S}} \quad (4.27a)$$

$$\lambda = \frac{E_J}{4E_J^R} \quad (4.27b)$$

$$\mu = \frac{E_C^R}{12} = \frac{1}{12} \frac{(e)^2}{2C_S} \quad (4.27c)$$

$$f = \varphi_0 \left(\frac{2E_C^R}{E_J^R} \right)^{1/4} \quad (4.27d)$$

The photon annihilation operator a is related to $\hat{\delta}$ by

$$\hat{\delta} = \frac{a + a^\dagger}{(E_J^R/2E_C^R)^{1/4}} \quad (4.28)$$

which represents the decomposition of the gauge-invariant phase difference into annihilation and creation operators of the “plasma” mode whose bare frequency is ω_p . The operators σ_X and σ_Z are the Pauli spin operators and $E_C^R = e^2/(2C_S)$ is the single electron charging energy of the readout junction. In this effective Hamiltonian, the expansion of $\cos \hat{\delta}$ is carried out only to the first anharmonic term, which describes

the non-linear resonator dynamics with sufficient accuracy for a bifurcation readout (see chapter 2).

Let us describe the role of each term in equation 4.26. The first term describes the influence on the qubit of the charge port drive which is used to manipulate its state. The second term describes the free evolution of the qubit at the Larmor frequency $\omega_{01} = E_J/\hbar$. We have supposed here that the ratio E_J/E_C is sufficiently small that corrections to the Larmor frequency involving E_C are small. To model the behavior of qubit samples with an appreciable E_J/E_C ratio, we would keep higher order terms, yielding renormalized values of the coefficients in equation 4.26. The third term describes the dominant coupling between the qubit and the resonator. Note that this term commutes with the Hamiltonian of the qubit when $U = 0$, offering the possibility of quantum non-demolition measurements⁶ (see chapter 6 for more details). The fourth term describes a decrease in the frequency of the resonator when its photon population increases (chapter 2). Finally, the fifth term describes the excitation of the resonator by the drive current applied through the phase port. When the drive current is increased while its frequency is sufficiently below ω_p the system becomes metastable with two possible dynamical states with different oscillation amplitudes (chapter 2). We exploit this bistability for our readout, which we describe in the next section.

4.3.2 Measurement protocol

It is clear from the Hamiltonian (4.26) above that the dynamics of the non-linear resonator depend on the value $\sigma_Z = \pm 1$ corresponding to the state of the qubit.

⁶This is strictly true in the limit of zero asymmetry $d = 0$. For finite values of d , corrections to the QND fraction of order d^2 exists [79].

In particular, the small oscillation “plasma” frequency $\omega_p^{\text{eff}} = \omega_p (1 \pm \lambda)$ varies with the qubit state. We probe the nonlinear resonator by sending down the phase port transmission line a microwave pulse with carrier frequency $\omega_d = \omega_p - \Delta\omega$, such that the detuning $\Delta\omega > \frac{\sqrt{3}}{2Q}\omega_p$ where Q is the quality factor of the plasma resonance (chapter 2). In our circuit, the damping of the plasma resonance arises from the characteristic transmission line impedance $Z_c = 50 \Omega$ and thus $Q = Z_c C \omega_p \simeq 10 - 20$. For this value of detuning, when ramping up the drive current I_{RF} the resonator switches from one dynamical state to another when

$$I_{RF} > I_B^+(\omega_d, \omega_p^{\text{eff}}) \quad (4.29)$$

where I_B^+ is the bifurcation current (equation 2.16). Therefore, by choosing the maximum pulse amplitude

$$I_B^+[\omega_d, \omega_p(1 - \lambda)] < I_{RF}^{\text{max}} < I_B^+[\omega_d, \omega_p(1 + \lambda)] \quad (4.30)$$

we can determine, by measuring if the resonator has switched or not, whether the qubit was in state $|0\rangle$ or $|1\rangle$.

The dynamical states of the resonator differ in both the amplitude and phase of the forced oscillations at frequency ω_d . In this work, we have chosen to use a reflectometry setup in which all the information about the resonator state is carried by the reflected drive signal phase ϕ . This last property occurs because the probed circuit is not intrinsically dissipative (in absence of quasi-particles, which is very well realized in our measurements) and the power reflected from the chip is equal to the incident power in steady state.

As explained in chapter 2, a further advantage of the non-linear resonator is that the switching is strongly hysteretic. Once a switching event has occurred we can decrease the drive current I_{RF} to a value which, while much smaller than $I_B^+ [\omega_d, \omega_p (1 - \lambda)]$, is still higher than the reverse bifurcation “retrapping” current I_B^- . This latching property conserves the information about the qubit state acquired during a small time interval τ_m in the resonator and allows us to probe the reflected phase ϕ during a time typically longer than τ_m . This helps in determining the reflected signal phase with much higher accuracy (see section 3.3) without being affected by any subsequent evolution of the qubit.

4.3.3 Effective critical current

The last two subsections gave us a simple picture to understand the coupling between the qubit and the JBA. The calculation was carried out in the limit $E_J/E_C \ll 1$. But in order to make accurate predictions for the performance of the JBA as a qubit readout, we will use the full expressions for the loop currents computed in the phase representation. We saw in chapter 2 that the JBA converts changes in the critical current of the Josephson junction to changes in switching probability, i.e., the JBA amplifies changes in critical current. Hence, it is convenient to consider the changes in effective critical current of the qubit+JBA system as the main signal of interest⁷. This can then be converted to changes in switching probability once the parameters of the JBA are known (see section 2.3.3).

We need to compute the loop currents of the quantronium as a function of δ in order to determine its effect on the critical current of the Josephson junction, i.e., we

⁷This is equivalent to considering the changes in effective inductance ($L_J \propto I_0^{-1}$) but is computationally more convenient.

need to calculate the current-phase relationship for the quantronium. For the readout junction, this is given by the standard Josephson relationship $I(\delta) = I_0 \sin \delta$. For DC experiments, the critical current is the maximum current that can be passed before the junction switches into its voltage state and is given by $I(\delta = \pi/2) = I_0$. Here, we will define the effective critical current as the slope of the current-phase relationship at $\delta = 0$.

$$I_0^{eff} = \left| \frac{\partial I(\delta)}{\partial \delta} \right|_{\delta=0} \quad (4.31)$$

This is related to the fact that we are essentially probing the inductance of the quantronium which is proportional to the inverse of this slope.

$$L_J^{eff} = \varphi_0 \left(\left| \frac{\partial I(\delta)}{\partial \delta} \right|_{\delta=0} \right)^{-1} \quad (4.32)$$

For the bare readout junction, $I_0^{eff} = I_0$, but this not true for the quantronium which typically has a non-sinusoidal current-phase relationship. The loop currents in the quantronium are given by [38]

$$i_k(N_g, \delta) = \frac{1}{\varphi_0} \frac{\partial E_k(N_g, \delta)}{\partial \delta} \quad (4.33)$$

Then from equation 4.31, we can write the effective critical current for the quantronium as

$$i_k^{eff}(N_g, \delta_m) = \frac{1}{\varphi_0} \frac{\partial^2 E_k(N_g, \delta = \delta_m)}{\partial \delta^2} \quad (4.34)$$

where δ_m takes into account an external flux bias. The above expression can be computed in terms of the Mathieu functions (Appendix B). Fig. 4.8 shows a plot of the loop currents in the ground and excited state at $N_g = 0.5$. The parameters used

correspond to the four qubit samples whose data is presented in chapters 5 and 6.

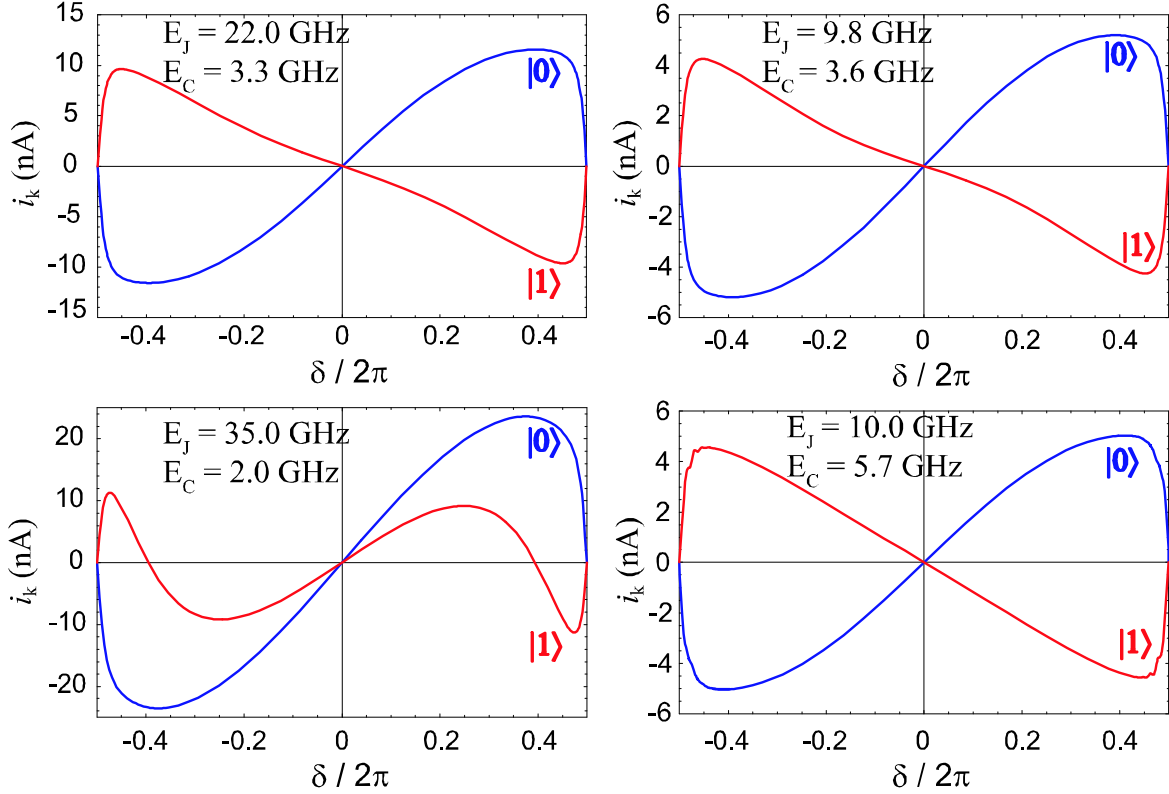


Figure 4.8: Loop currents for the ground and first excited state of the quantonium qubit are plotted as a function of phase δ (for $N_g = 0.5$). Theoretical curves are shown for four different qubit samples. One can observe how the shape of the loop currents depends on the E_J/E_C ratio.

We note that the current-phase relationship for the quantonium depends on the E_J/E_C ratio quite strongly. For small values of E_J/E_C , the loop currents have opposite signs for the ground and excited states, but for larger values, they have the same sign. However, the slopes at $\delta = 0$ are always different allowing one to discriminate between the two states. The ground state properties of the quantonium are often the first quantities to be measured in an experiment. We plot in Fig. 4.9 the variation

of the effective critical current in the ground state $i_0^{eff}(N_g, \delta_m)$ as a function of gate charge (N_g) for a few different values of external flux (δ_m). We note that the effective critical current varies periodically with N_g with period 1. It has a maximum value at $N_g = 0.5$. It also varies periodically with δ_m with period 2π with a maximum value at $\delta_m = 0$.

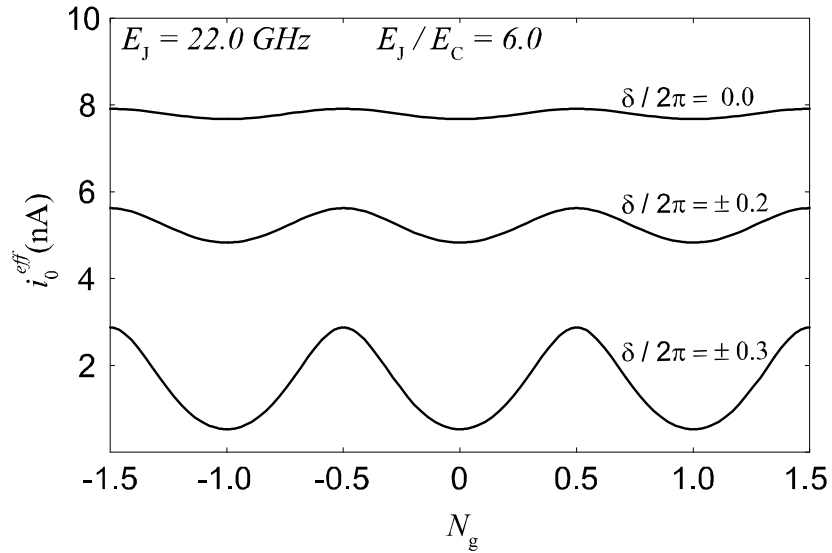


Figure 4.9: Variation in effective critical current of the quantronium in its ground state with N_g for three different values of applied flux (δ_m). Qubit parameters correspond to sample A (chapter 5). The signal is periodic in N_g with period 1. It is also periodic in δ with period 2π (not shown here).

The conversion from changes in effective critical current to the switching probability of the JBA is linear only for small changes (see section 2.3.3). This can lead to significant variations from the above predictions when the quantronium properties are measured in a real experiment. Also, when the JBA is energized, it imposes a significant deviation in δ around the mean value. When operating at values of δ_m significantly different from zero, the observed variation in switching probability in an

experiment can vary significantly from the above prediction. The qubit can also Zener tunnel between the ground and excited state during measurements near $\delta_m = 0.5$, which can affect the switching probability. In order to fully understand the effect of the quantronium on the JBA, we carried out classical numerical simulations of the JBA but used the modified current-phase relations to fully incorporate the effect of the quantronium. This is discussed in more detail in the next section. Nevertheless, the effective critical current discussed above provides a convenient way to predict the expected signal in a qubit measurement using simple analytical formulae and without resorting to time consuming numerical simulations.

4.3.4 Qubit readout optimization

We now consider the problem of choosing the parameters for the quantronium and JBA to achieve the best possible qubit readout. As discussed in chapter 3, the JBA parameters are dictated by the requirement that $\omega_p/2\pi \sim 1 - 2$ GHz⁸, $Q \sim 20$ and $R = 50 \Omega$. This leads to a junction critical current $I_0 \sim 1 \mu\text{A}$ and shunt capacitance $C_S \sim 30$ pF. For the quantronium, we are looking to maximize the change in effective critical current (Δi_{01}^{eff}) between the two qubit states. This is entirely determined by the choice of E_J and E_C . In order to achieve robust microwave design and signal manipulation, it is better to keep the qubit Larmor frequency $\nu_{01} < 20$ GHz. The qubit Larmor frequency also depends on E_J and E_C . Once ν_{01} is fixed, the other free parameter is the ratio E_J/E_C . It can be shown that the critical current variation $\Delta i_{01}^{eff} \propto \nu_{01}$. Fig. 4.10 shows the variation of $\Delta i_{01}^{eff}/\nu_{01}$ with E_J/E_C .

⁸This is not a fundamental requirement but only constrained by our choice of experimental setup. We have successfully operated the JBA up to 4.5 GHz and to about 10 GHz with geometric resonators (CBA).

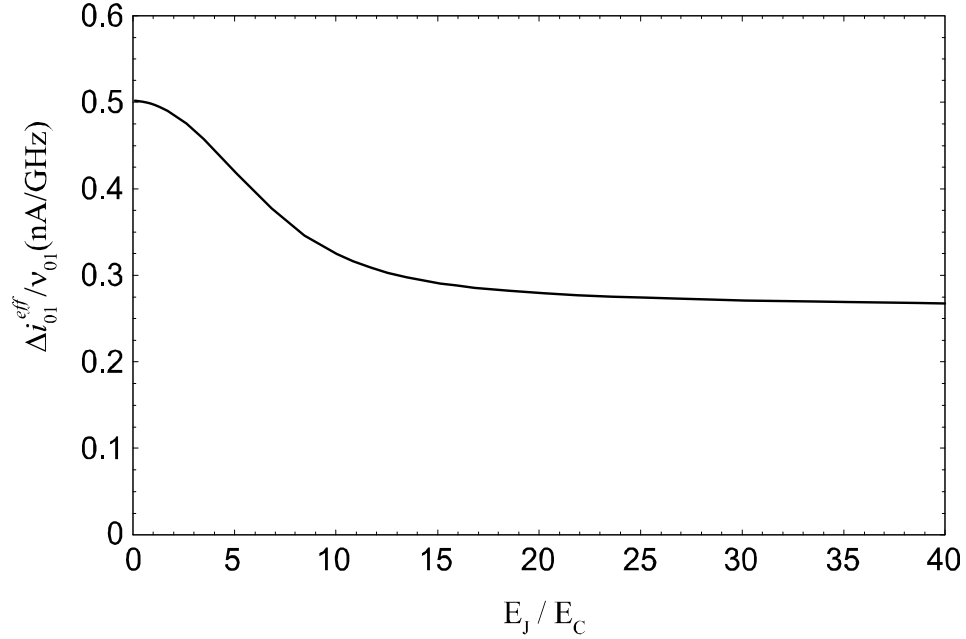


Figure 4.10: Difference in effective critical current (Δi_{01}^{eff}) between the ground and excited state of the quantonium as a function of E_J/E_C . Δi_{01}^{eff} is larger for larger values of ν_{01} . As E_J/E_C ratio increases beyond a value of 10, Δi_{01}^{eff} tends to saturate.

We note that $\Delta i_{01}^{eff}/\nu_{01}$ has two asymptotic values for small and large values of E_J/E_C . It starts out with a value of around 0.5 at low values of E_J/E_C . It then decreases with increasing values of E_J/E_C but tends to saturate to value of around 0.3 for $E_J/E_C > 10$. This is related to the fact that the Larmor frequency $\nu_{01} \rightarrow E_J$ for $E_J/E_C \ll 1$ while $\nu_{01} \rightarrow \sqrt{8E_J E_C}$ for $E_J/E_C \gg 1$. Also, the loop currents have opposite signs for $E_J/E_C \ll 1$ resulting in a bigger signal while the loop currents tend to have the same sign for $E_J/E_C \gg 1$. As discussed earlier in this chapter, the sensitivity to low frequency charge noise decreases dramatically with increasing E_J/E_C and typically $E_J/E_C > 4$ is used. The experiments presented in the next two chapter were carried out on four samples with E_J/E_C ratios of 6, 2.7, 17.5, and

1.8. From the above plot, we can estimate that for values of $E_J/E_C > 10$, we get a critical current variation (Δi_{01}^{eff}) of about 0.3 nA per GHz for the Larmor frequency. If we have $\nu_{01} = 20$ GHz, we can get a critical current variation between 6 and 10 nA depending on the E_J/E_C ratio. In section 4.4, we will use these numbers to predict the performance of the JBA as a qubit readout.

As discussed above, the value of Δi_{01}^{eff} is limited to a certain range due to experimental constraints. In order to enhance this signal, we developed a new circuit which uses two readout junction in series to increase the coupling between the JBA and the qubit. The two readout junctions now have twice the original value of E_J^R which results in the double junction JBA (DJBA) having the same plasma frequency as the single junction JBA. This circuit effectively doubles the coupling and hence the effective change in critical current (Δi_{01}^{eff}). Numerical simulations with the DJBA confirm this effect (section 4.4).

4.3.5 Qubit readout performance

We now define a few quantities which are useful for gauging the performance of a qubit readout. The first quantity is the gain or transfer function of the detector. In the case of JBA, the relevant quantity is the change in switching probability (ΔP_{switch}) per unit change in critical current of the junction (ΔI_0). We will denote this quantity by

$$G_{JBA} = \frac{\Delta P_{\text{switch}}}{\Delta I_0}. \quad (4.35)$$

This quantity only depends on the parameters of the JBA (including pulse parameters and temperature) and does not depend on the qubit parameters. It characterizes the sensitivity of the detector. As mentioned earlier in this section, equation 4.35 is valid

only for small changes in critical current and the gain drops as ΔI_0 increases. For a qubit readout, the qubit parameters set the value of ΔI_0 . So the gain can be computed for the given value of ΔI_0 .

The next quantity characterizes a given qubit readout system. Once the parameters of the qubit are known, we can calculate $\Delta I_0 = \Delta i_{01}^{eff}$ and hence the expected ΔP_{switch} . We call this quantity the *discrimination power* and is given by

$$\eta_{dp} = \Delta i_{01}^{eff} G_{JBA} \left(\Delta i_{01}^{eff} \right) \quad (4.36)$$

where we have written gain G_{JBA} as a function of Δi_{01}^{eff} to emphasize that the gain has been calculated for a particular value of Δi_{01}^{eff} . This quantity tells us the expected performance of the given qubit readout system. While setting up an experiment, we will try to adjust the parameters so that the value of η_{dp} is as close to 1.0 as possible. We will compute this number for a few systems in the next section.

The next quantity called contrast (η_c) is the actual ΔP_{switch} observed in a qubit readout experiment. This is the actual performance of the qubit readout achieved in a given experiment. This incorporates all possible problems in the qubit as well as the readout.

The three quantities G_{JBA} , η_{dp} , and η_c allow us to gauge the anticipated and the actual performance of the qubit readout system. There are two more quantities which are sometimes useful to characterize a qubit readout. The first one is called the *readout fidelity* (η_f) and takes into account imperfections in the qubit e.g. finite qubit lifetime and state preparation of the qubit. These imperfections can reduce the contrast in an experiment and the readout fidelity allows us to isolate the qubit/technical problems

from the detector performance. Note that the readout fidelity still includes any back-action effects which could be present during a measurement. The last quantity is called *visibility* and is given by

$$\eta_v = \frac{\eta_c}{\eta_{dp}} \quad (4.37)$$

This quantity compares the achieved performance (η_c) to the anticipated performance (η_{dp}) of a qubit readout system. In a typical experiment, the quantities η_{dp}, η_f and η_c line up as follows

$$\eta_{dp} \geq \eta_f \geq \eta_c \quad (4.38)$$

though ideally we would like $\eta_{dp} = \eta_f = \eta_c = 1.0$. Chapter 6 discusses experimental results which help us identify some of the problems which results in a reduced contrast.

4.4 Numerical simulations

We will now briefly describe the numerical simulations that were carried out to characterize the performance of the JBA as a qubit readout. The equation of motion for the JBA was given in equation 2.1. In order to incorporate the effect of the quantonium, we just add a term corresponding to the current-phase relationship of the quantonium (4.33)

$$C_J \varphi_0 \frac{d^2 \delta(t)}{dt^2} + \frac{\varphi_0}{R} \frac{d\delta(t)}{dt} + I_0 \sin \delta(t) + i_k (N_g, \delta_m + \delta) = I(t) + I_N(t) \quad (4.39)$$

where k , N_g and δ_m are constants for a given problem and determine the qubit state, gate bias and flux bias respectively. The loop current function $i_k(N_g, \delta_m + \delta)$, is incorporated in the numerical simulation by storing a sampled version (calculated in

Mathematica) in an array for given values of k , N_g and δ_m . $I(t)$ is the RF current drive and $I_N(t)$ is the Johnson noise current corresponding to a given temperature. A *C++* code solves the above equation (in reduced units) using the 4th order *Runge-Kutta* method. The details of the implementation are given in Appendix C.

Each numerical experiment involves simulating the above equation for a given set of parameters. The simulator outputs $\delta(t)$ from which we can determine the state of the JBA at the end of a particular numerical experiment. By repeating the experiment many times one can compute the switching probability P_{switch} . One can then study the variation of P_{switch} as a function of the control parameters like drive amplitude and temperature. In Fig. 4.11 we show plots of the switching probability curves or S-curves which plot the variation of P_{switch} with drive amplitude. Numerically simulated S-curve data⁹ is shown for typical qubit parameters with $\Delta i_{01}^{\text{eff}} = 4.5$ nA (corresponds to Sample B, see chapter 5) for both the ground and the excited state. A simulation temperature of $T = 80$ mK was used, while $\omega_p/2\pi = 1.7$ GHz and $\omega_d/2\pi = 1.55$ GHz for the JBA. The value of temperature (T) used for this simulation is our best guess for the effective temperature¹⁰ which was determined through other measurements (not described here). This allows us to determine the expected discrimination power (η_{dp}) which is computed by taking the maximum of the difference between the S-curves corresponding to the two qubit states. The discrimination power tells us how good the JBA will perform as a qubit readout e.g. $\eta_{dp} = 0.7$ implies that the JBA should measure the qubit state correctly 70% of the times. The panels (a) and (b) compare

⁹The actual equation used in the numerical simulation is slightly different from equation 4.39 to incorporate effects of stray parameters in the circuit. See section 3.2.1 and Appendix C for more details.

¹⁰The effective temperature of the JBA when $T \ll \hbar\omega_p$, is given by $T_{\text{eff}} = \hbar\omega_p/(2k_B)$ (chapter 7&8). It could be higher if the microwave lines connected to the JBA are not sufficiently filtered.

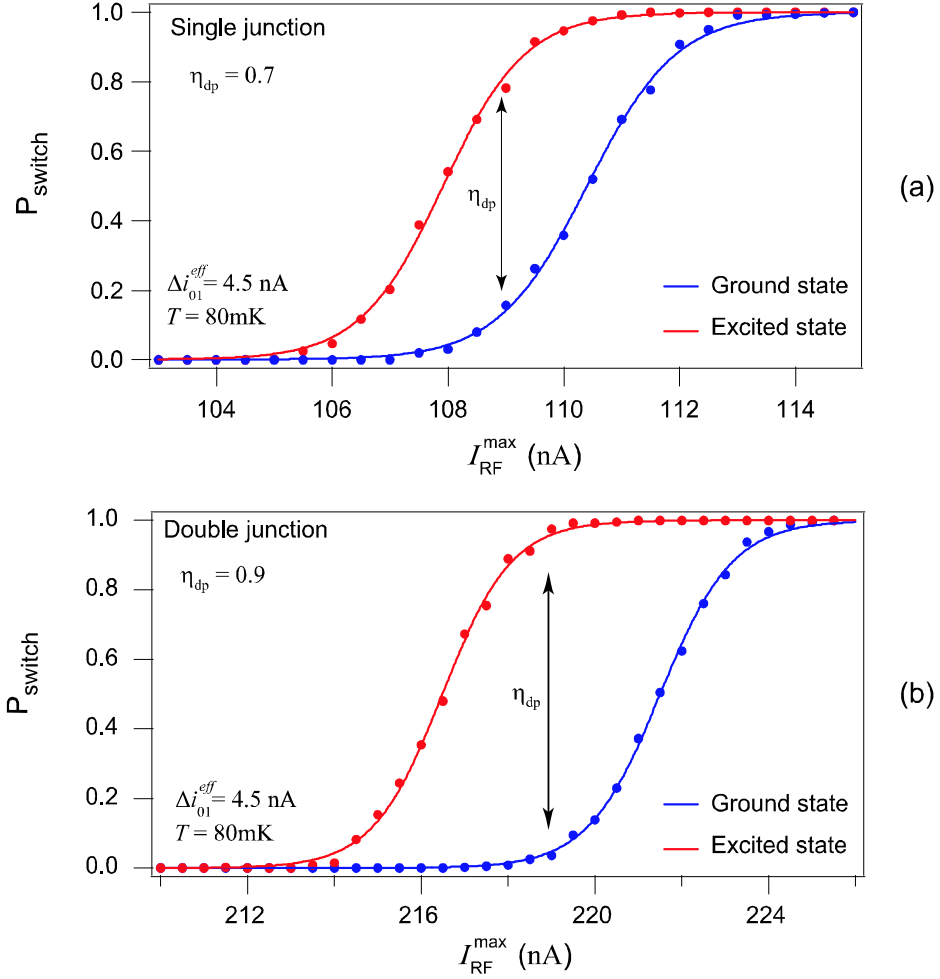


Figure 4.11: Switching probability curves computed using numerical simulations of the quantonium+JBA circuit. The effect of the quantonium was incorporated by including the current-phase relation of the quantonium. Data is shown for typical qubit parameters with $\Delta i_{01}^{\text{eff}} = 4.5$ nA (corresponds to Sample B, see chapter 5). A simulation temperature of $T = 80$ mK was used, while $\omega_p/2\pi = 1.7$ GHz and $\omega_d/2\pi = 1.55$ GHz for the JBA. Panel (a) shows the case for a single junction JBA while panel (b) is for the double junction JBA and we see an improvement in η_{dp} from 0.7 to 0.9. An interesting feature to note is that the width of the S-curves (in units of current) is roughly the same for the two cases but the shift is double in panel (b). This is a consequence of enhanced (roughly double) coupling to the quantonium in the double junction JBA. Also note that the typical values of $I_{\text{RF}}^{\text{max}}$ are also double in panel (b) due to the fact that the critical currents of the individual junctions are doubled to keep the same ω_p .

results for the single junction JBA with the double junction JBA which provides enhanced coupling to the quntronium and hence higher discrimination power.

The ultimate goal is to get $\eta_{dp} = 1.0$ (and $\eta_c = 1.0$), but a readout with $\eta_{dp} < 1$ is still usable. It just means that the experiment has to be repeated several times in order to determine the qubit state accurately. As discussed in the previous section, discrimination power mainly depends on two quantities. The first is the effective change in critical current (Δi_{01}^{eff}) when the qubit state changes. Δi_{01}^{eff} depends on E_J and E_C and determines the shift in the S-curves. The second is the effective temperature of the JBA which determines the width of the S-curves (sections 2.3.3 and 3.3.2). We will see in chapters 7 and 8 that the effective temperature of the JBA has a lower bound and is given by $T_{eff} = \hbar\omega_p / (2k_B)$. In order to get closer to $\eta_{dp}, \eta_c = 1.0$, one can use tricks like enhanced coupling using the DJBA. In certain cases, it is possible to access the second excited state ($|2\rangle$) by sending a microwave pulse at frequency ν_{12} to the gate port, just before the measurement. For certain range of parameters, Δi_{02}^{eff} is bigger than Δi_{01}^{eff} and can provide an improvement in contrast. The next two chapters discuss experimental results of measurements carried out on the quntronium qubit using the JBA.

Chapter 5

Qubit coherence measurements

In this chapter, we will describe the measurements that were carried out on the quantronium qubit (see chapter 4) using the JBA, to probe its coherence properties. The experiments were carried out in a dilution refrigerator with a base temperature of 12 mK. We will first discuss the new experimental setup for the qubit measurements. The measurements characterizing the ground state of the split Cooper pair box will then be discussed. This will be followed by the discussion of the spectroscopic measurements of the excited state. We will then describe the time domain measurements which characterize the coherence properties of the qubit. Finally, we will talk about the fidelity of the JBA readout.

5.1 Measurement setup

The principle of our experiment is schematically depicted in Fig. 5.1 and is based, as discussed in the previous chapter, on the quantronium qubit, a three junction circuit which is analogous to a one-dimensional atom. The set of three junctions consists of

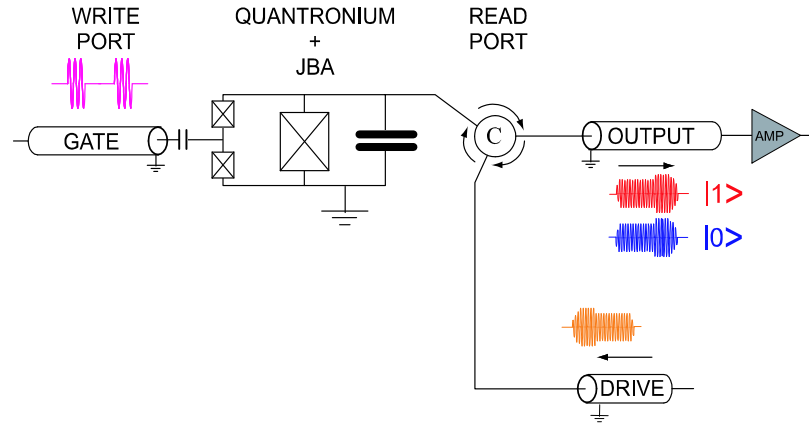


Figure 5.1: Schematic of the measurement setup. The quantronium qubit is a split Cooper pair box with two small Josephson junctions in which a large junction is inserted for readout. This latter junction is shunted by a capacitor and forms the non-linear oscillator of the JBA readout. The qubit state is manipulated by sending pulses to the gate (write port), while readout operation is performed by sending a pulse to the non-linear resonator via the read port. The circulator (C) is used to separate the incident and reflected signals. The phase of the reflected signal which carries information about the qubit state is amplified and measured.

two small junctions, and a large junction, whose Josephson energy is approximately 100 times larger than that of each small junction. The capacitors shunting the big junction reduce the plasma frequency of the big junction to the 1 – 2 GHz range and form the non-linear oscillator. As discussed in chapters 2 and 3, the non-linear oscillator is the heart of the JBA readout. The quantronium qubit and the JBA are coupled via the shared big junction. The quantum state of the qubit affects the properties of the JBA and hence the state of the qubit can be readout by measuring the state of the JBA. The qubit state can be prepared by sending microwave pulses to the gate (chapter 4) while the readout operation is performed by sending microwave pulses to the non-linear oscillator via the read port and analyzing the phase of the reflected signal.

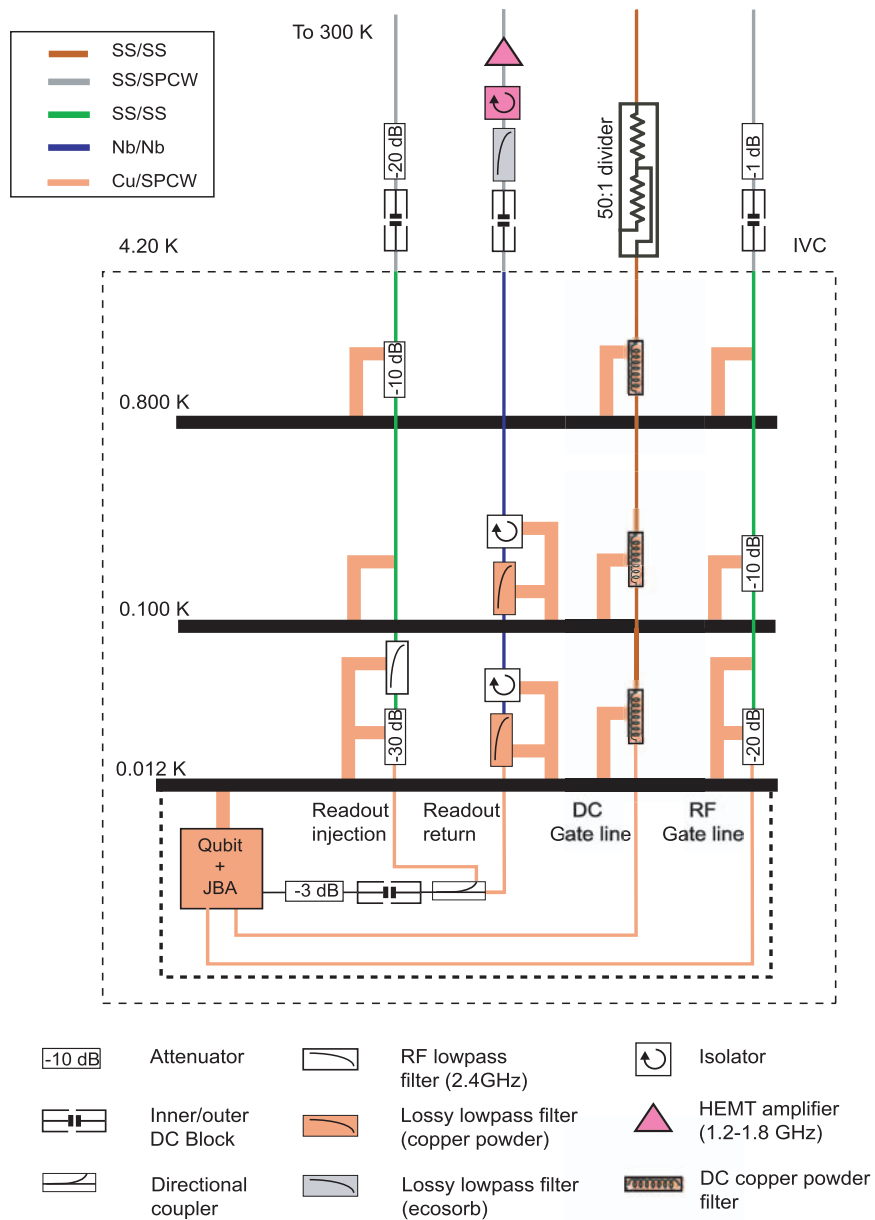


Figure 5.2: Fridge setup for qubit measurements. There are three microwave lines and one DC line. The readout injection and the RF gate line are attenuated and filtered while the readout return line has isolators and lossy filters. The DC gate line has a voltage divider and copper powder filters. Typical values of attenuators used are indicated. They were varied between different experiments depending on the parameters being optimized.

The detailed setup of the fridge with the various microwave lines is shown in Fig. 5.2. There are three microwave lines - readout injection, readout return and qubit injection. The injection lines as before (chapter 3) have attenuators and filters while the return line has circulators and lossy filters. All this ensures that the only noise felt by the qubit and the JBA corresponds to the fluctuations from a 50Ω resistor at the base temperature. The qubit and readout pulses are created using similar techniques as discussed in chapter 3. The measurements described in the next few sections were carried out on three different samples (A-C) whose parameters are described in Table 5.1.

Sample	$\omega_{01}/2\pi(\text{GHz})$	E_J/E_C	$T_{1,\text{typical}}(\mu\text{s})$	$T_2(\text{ns})$	$T_{\text{echo}}(\text{ns})$	η_c	η_{dp}
A	18.989	6.0	1.0	300	300	0.61	0.70
B	9.513	2.7	4.0	320	400 – 500	0.48	0.70
C	20.344	17.5	0.07	110	X	0.68	0.95
D	9.910	1.8	$(0.1, 1.0)^*$	120	X	0.30	0.90

Table 5.1: Qubit samples and their parameters. The parameter η_{dp} is the discrimination power of the readout while η_c is the actual contrast achieved in the experiment. Samples A and B had one large Josephson junction while samples C and D had two large Josephson junctions in series for the JBA readout in order to increase the discrimination power. (* - data could only be fit with a double exponential with a short and long time scale as indicated, X - T_1 was too short to carry out echo measurements).

Samples A and B had a single large junction for the JBA readout while samples C and D had two large junctions in series. This modified design was introduced to enhance the readout fidelity. More details will be discussed in the last section and the next chapter. In this chapter, we will mostly present data from samples A and B. In the next three sections, we will present measurements which will characterize the ground state and coherence properties of the qubit. The measurements are presented roughly in the order in which they would be typically carried out while characterizing

a qubit. This gives us a flavour of the sequence of operations involved during a typical experiment.

5.2 Ground state characterization

The first step in a qubit measurement is to characterize the ground state properties of the qubit as a function of the bias parameters (gate and flux). But before one can carry out any measurements, it is necessary to characterize the JBA readout, the procedure for which was described in chapter 3. We identify an operating frequency and the pulse parameters for the JBA readout. These parameters are often modified later to optimize the signal to noise ratio and the readout fidelity. Once the readout is ready, the only quantity that is monitored is the switching probability of the JBA which is the main output signal of any measurement.

As discussed in the previous chapter, the properties of the quantronium are periodic functions of the gate charge (N_g) and loop flux (ϕ_l). At low enough temperature ($k_B T \ll \hbar\omega_{01}$) and in the absence of any microwave irradiation on the qubit, the qubit stays predominantly in its ground state due to the finite lifetime of the excited state. We monitor the switching probability of the JBA as a function of gate and flux bias and the result (sample A) is shown Fig. 5.3. Each trace is a plot of the switching probability (P_{switch}) as a function of the gate voltage for a given value of flux. The readout bias is adjusted at every value of flux bias to give a mean value of $P_{\text{switch}} = 0.5$. As is expected, the modulations in P_{switch} increase as the flux bias deviates from zero (or integer flux quantum). The modulation magnitude at zero flux depends on the E_J and E_C values of the Cooper-pair transistor. For large ratios of E_J/E_C , this modulation can be quite small and difficult to measure. In that regard,

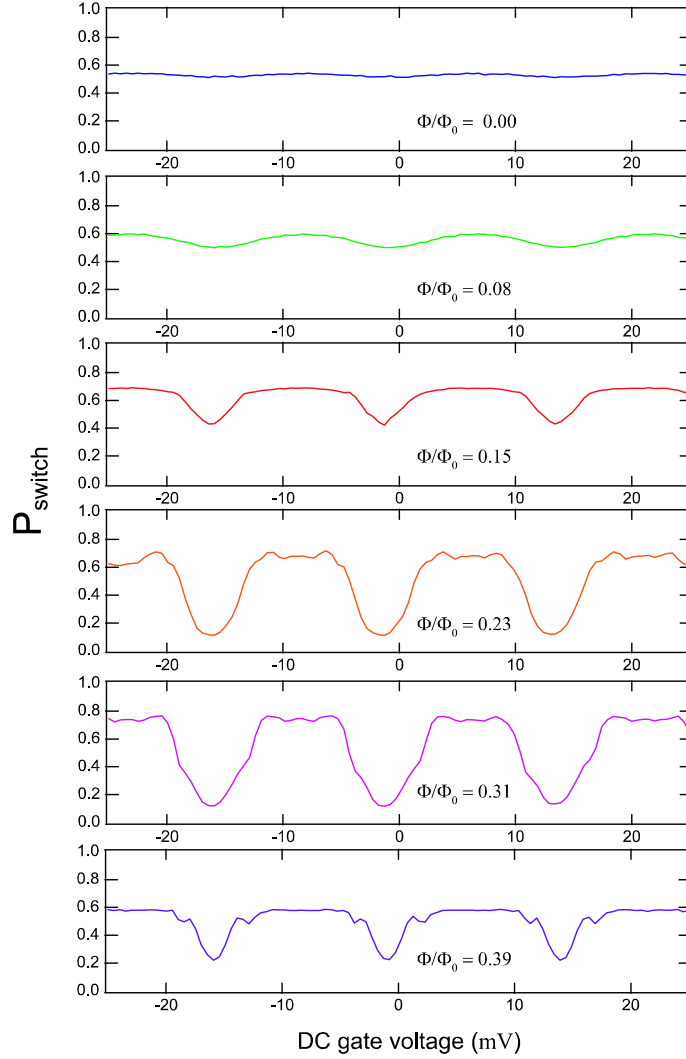


Figure 5.3: Switching probability v.s. DC gate voltage for different values for bias flux. Data (sample A) shows the periodic nature of the ground state properties of the quantronium. As discussed in chapter 4, the JBA probes the effective critical current of the quantronium which varies periodically with gate charge N_g with period 1. By noting that the period in gate voltage is $15 \text{ mV} = 2e/C_g$, we can extract the gate capacitance of this sample $C_g = 21 \text{ aF}$. The magnitude of the modulation also changes with the bias flux as expected for the quantronium.

it is often useful to change the value of flux till you can see a sizable modulation and then slowly bring the value of flux back to zero. These measurements not only provide a basic test of the functioning of the quantronium qubit, but also provide a rough estimate for gate and flux bias which corresponds to the double degeneracy or "sweet spot" of the quantronium qubit. As discussed in the previous chapter, this is the point where the qubit is least sensitive to fluctuations in the bias parameters. For all measurements, unless otherwise indicated, higher switching probability corresponds to lower critical current and vice-versa. The switching probability has the lowest value at the double degeneracy point (highest critical current), and increases as one moves away in either charge or flux direction.

5.3 Spectroscopy

After characterizing the ground state properties, we next determine the qubit energy level splitting. The measurement protocol is identical to the one described in the previous section, except that we now send a weak, continuous microwave signal to the charge port. The energy level separation periodically changes as a function of gate and flux bias and when the frequency of the microwave signal equals to the energy level separation, the qubit has a small probability of being excited to the next higher state. This results in a change in the switching probability. Fig. 5.4 depicts such a trace showing P_{switch} as a function of N_g for a value of $\phi_l \sim 0$. The peaks correspond to the values of N_g where the energy levels are resonant with the incident microwave signal. In this measurement, the spectroscopic probe frequency used, is slightly higher than the qubit level separation at charge degeneracy point. This results in the two closely spaced peaks on either side of the charge degeneracy point as the qubit level

splitting increases as one moves away from the charge degeneracy point.

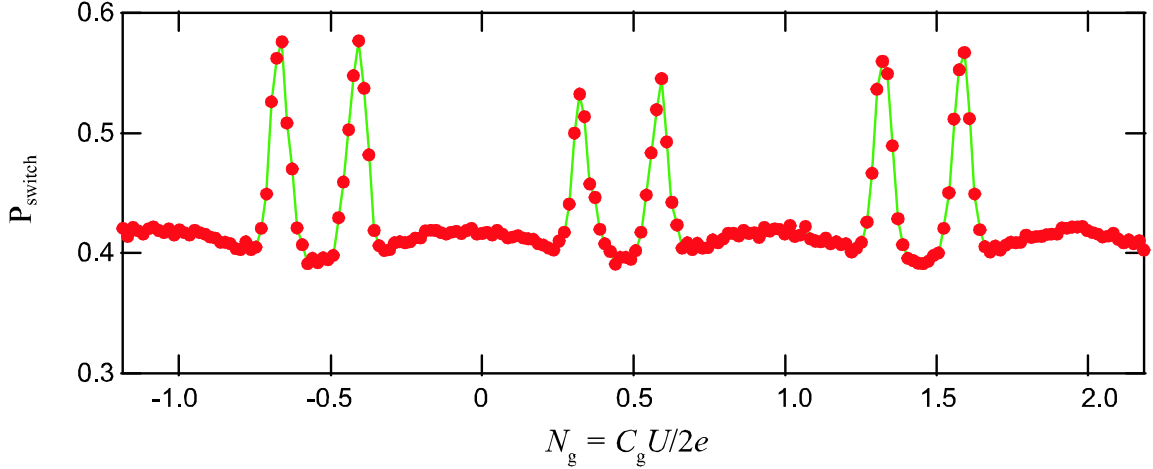


Figure 5.4: Spectroscopic peaks for sample A. The qubit is irradiated with a continuous microwave signal while the gate bias is swept. The switching probably shows the usual gate modulation but now has additional peaks at certain values of gate bias when the qubit level spacing becomes resonant with the incident microwave radiation. The microwave frequency used here is slightly larger than the Larmor frequency at the charge degeneracy point.

We can then map the variation of the qubit level splitting as a function of gate charge by using different probe frequencies. This data for sample A is shown in Fig. 5.5 and allows us to determine the E_J and E_C values for the qubit. The brighter regions correspond to the qubit being excited by the incident microwaves. The light blue curve is the theoretical fit for the variation of qubit transition frequency with gate charge. Sample A had a E_J/E_C ratio of about 6 and the curvature of the energy bands with charge is not too high even at $N_g = 0$. This is evident from the spectroscopy data as shown in Fig. 5.5 We were able to carry out coherent operations on the qubit at both $N_g = 0.5$ and $N_g = 0$ for sample A.

Now we know the approximate value of the Larmor frequency ω_{01} . We then

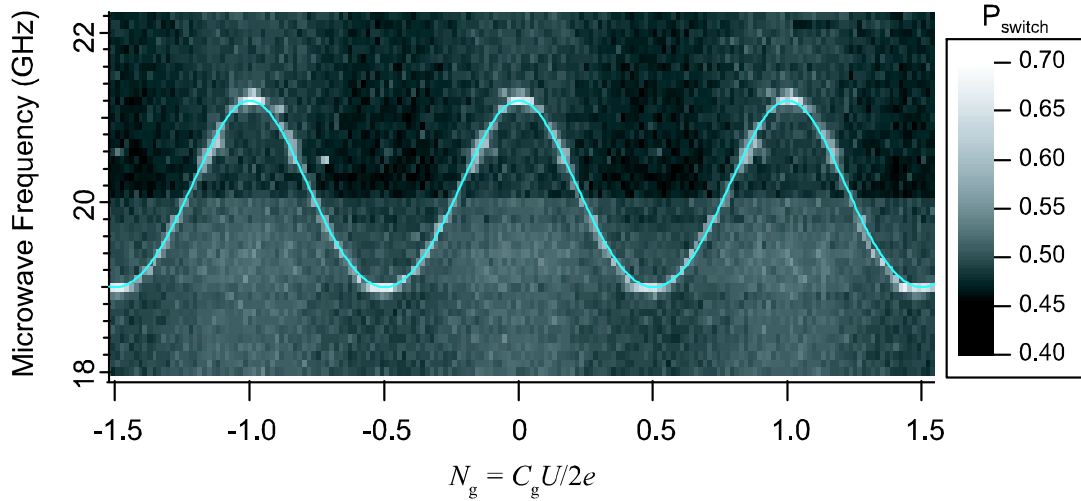


Figure 5.5: Variation of qubit transition frequency with gate charge (sample A). Spectroscopic peaks (bright regions) are observed at different locations for different frequency of microwave irradiation. The light blue line is a theoretical fit which provides the values of E_J and E_C for the qubit.

measured the lineshape of the ground to excited state transition at the "sweet spot". The gate and flux bias was tuned to the "sweet spot" and the switching probability was monitored as a function of the frequency of the microwaves irradiated on the qubit port. The microwave power was slowly reduced till no further reduction in the line width was observed[47]. The gate and flux bias were also finely adjusted to get the smallest possible linewidth. Data for sample A is shown in Fig. 5.6. The red dots are the data points and the solid green line is a Lorentzian fit to the data. The peak in the data corresponds to the Larmor frequency, which is 18.985 GHz in Fig. 5.6. This value is slightly different from the value mentioned in Table 5.1 as the data for Fig. 5.6 was taken earlier in the run and the Larmor frequency often changes slightly over time. The smallest linewidth (FWHM) observed for sample A was about 2 MHz.

In the next section, we present the time domain measurements carried out on sam-

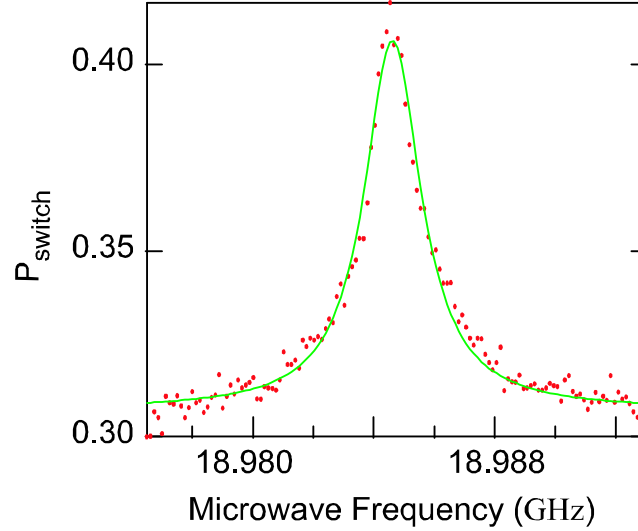


Figure 5.6: Lineshape of the ground to excited state transition of the qubit for Sample A. Data shows a plot of switching probability vs incident microwave frequency on the qubit. Microwave power, gate and flux bias are adjusted till the smallest linewidth is observed which is about 2 MHz here.

ple B. Unless otherwise indicated, all time domain coherent operations were carried out at the double degeneracy point, i.e., $N_g = 0.5$ and $\phi_l = 0$.

5.4 Time domain measurements

The first time domain measurement to be carried out was the Rabi oscillations experiment. We first applied to the charge port a pulse at the Larmor frequency ω_{01} of varying duration τ and amplitude U_{RF}^{\max} , which performs a σ_X rotation of the qubit. This was followed by a readout pulse on the phase port. The resulting Rabi oscillations in the switching probability signal are plotted in Fig. 5.7a for varying τ and fixed U_{RF}^{\max} . Near $\tau = 0$ we observe the P_{switch} corresponding to qubit being in the $|0\rangle$ state. As the pulse length increases, P_{switch} increases, goes through a maximum

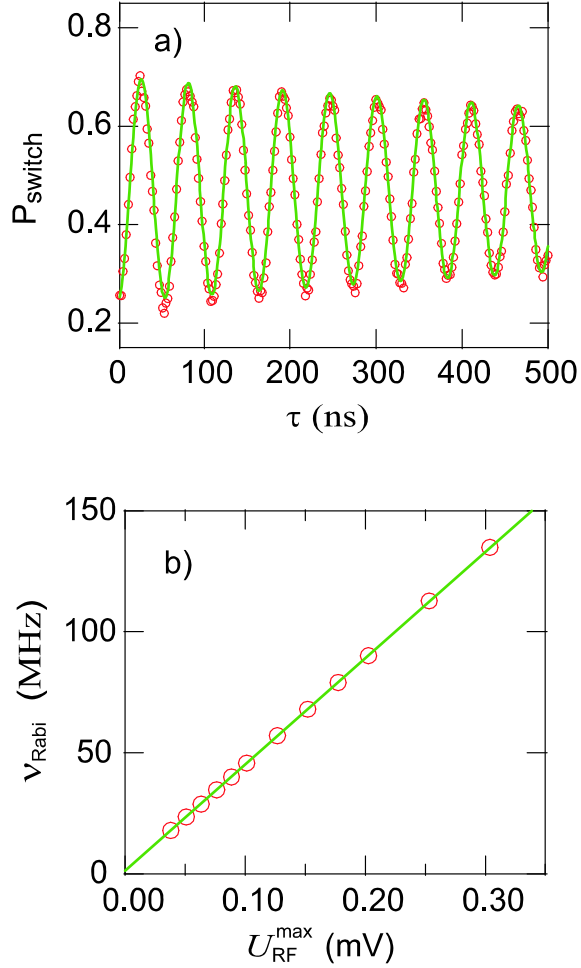


Figure 5.7: a) Rabi oscillations of the switching probability of qubit sample B as a function of the duration τ of a square pulse applied on the gate with maximum amplitude $U_{\text{RF}}^{\text{max}} = 0.12\text{mV}$. Solid green curve is an exponentially decaying sinusoidal fit with $\tilde{T}_2 = 1.6\ \mu\text{s}$. Total acquisition time is 3 minutes and the repetition rate is $16\ \mu\text{s}$, set by T_1 (see below). b) Rabi oscillation frequency (ν_{Rabi}) measured in (a) as a function of $U_{\text{RF}}^{\text{max}}$. Green line represents the expected linear dependence.

where the qubit is purely in the $|1\rangle$ state, defining at this point the length of a π pulse. The switching probability then decreases back to the $|0\rangle$ state value, indicating a full 2π rotation of the Bloch vector. This pattern repeats itself but with diminishing contrast. The decay time \tilde{T}_2 is in the range $0.8 - 1.7 \mu\text{s}$ depending on the sample and precise biasing condition. The Rabi oscillation frequency ν_{Rabi} is plotted as a function of U_{RF}^{max} in Fig. 5.7b. A linear dependence of ν_{Rabi} with U_{RF}^{max} is observed, in agreement with theory. The shortest π pulse we generated was 2 ns long, and was used in the echo experiments described below.

Having calibrated the π pulse, we then performed a qubit energy relaxation measurement by introducing a waiting time t_w between the π pulse and the readout pulse. The decay of P_{switch} with t_w , shown in Fig. 5.8, is well fitted by a single exponential, defining T_1 . For sample A, T_1 was in the range $1.0 - 1.3 \mu\text{s}$, and for sample B, T_1 was between $2.5 - 5 \mu\text{s}$. The values of T_1 obtained with our dispersive readout are comparable with the results of Vion *et al.* [6], and are significantly shorter than the values expected from coupling to a well thermalized 50Ω microwave environment shunting the qubit. The loss mechanisms giving rise to the observed energy relaxation are not understood at this time.

Following measurements of the qubit energy relaxation, we performed a Ramsey fringe experiment to determine the phase coherence of the qubit. In this experiment, two $\pi/2$ pulses were applied to the charge port of the qubit at a frequency $10 - 20 \text{ MHz}$ detuned from ω_{01} followed by a readout pulse on the phase port. A free evolution time Δt was introduced between the two $\pi/2$ pulses. In Fig. 5.9, P_{switch} is plotted as a function of Δt . In the Ramsey sequence, the first $\pi/2$ pulse tips the Bloch vector from the north pole to the equatorial plane. During the time Δt , the Bloch

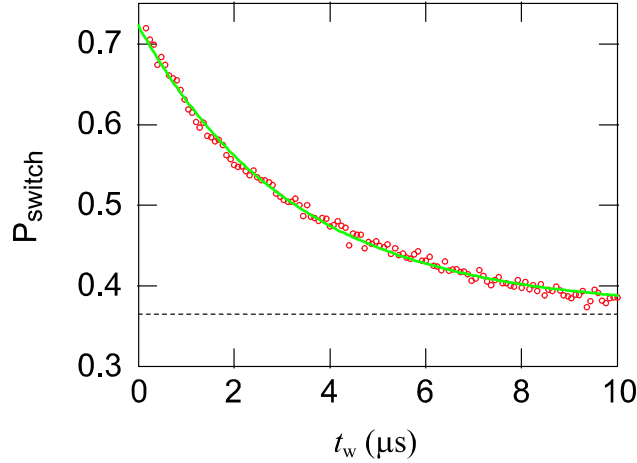


Figure 5.8: Decay of the excited state switching probability (sample B) after preparing the qubit in the excited state by a π pulse, as a function of the waiting time t_w between the preparation pulse and the readout pulse. Data shown illustrates the typical behavior observed with the switching probability decaying exponentially with a single decay constant. Solid green curve is an exponential fit with a $3.2\mu\text{s}$ decay constant. The exponential fit includes an offset and gain factor to account for the fact that $\eta_d < 1$. The dashed line indicates the value of P_{switch} in the absence of a π pulse.

vector precesses around the equatorial plane and is then rotated again by the second $\pi/2$ pulse. For $\Delta t = 0$, the two $\pi/2$ pulses back to back act as a single π pulse and the observed value of P_{switch} corresponds to the qubit being in the $|1\rangle$ state. As Δt increases, P_{switch} decreases until it reaches the value corresponding to the qubit being in the $|0\rangle$ state, corresponding to a free evolution time Δt in which the Bloch vector makes a π rotation in the equatorial plane. The switching probability then continues to increase for larger values of Δt until it reaches a maximum value, corresponding to a time Δt where the Bloch vector makes a full 2π rotation in the equatorial plane. This oscillatory pattern then repeats but with decreasing contrast corresponding to the loss of phase coherence with time. The Ramsey fringes decay in a

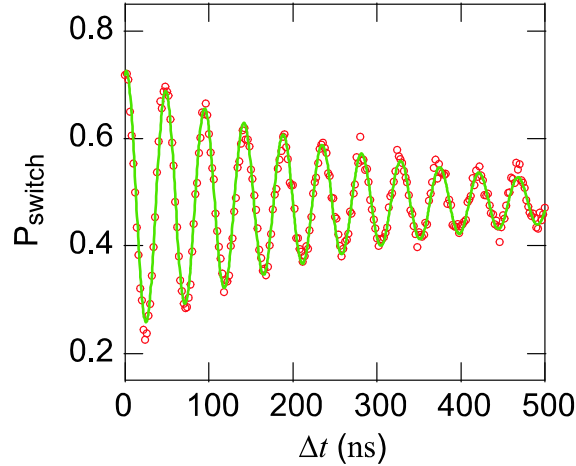


Figure 5.9: Ramsey fringes (sample B) obtained with two $\pi/2$ pulses separated by the time interval Δt . The pulse frequency was detuned from the Larmor frequency by 20MHz. The green curve is a exponentially decaying sinusoid fit. The decay time T_2 is 320ns. Same acquisition conditions as in Fig. 5.7.

time T_2 which has a component due to energy relaxation and one due to pure dephasing: $1/T_2 = 1/(2T_1) + 1/T_\varphi$, where T_φ represents pure dephasing. In our measurements, T_2 is dominated by pure dephasing, except for sample C which had a small $T_1 \simeq 70$ ns and large value of $E_J/E_C = 17.5$. For sample A, $T_2 = 300$ ns while sample B had $T_2 = 320$ ns. The decay of Ramsey fringes in sample C was dominated by energy relaxation with $T_2 \simeq 120$ ns and only slightly smaller than $2T_1$. We then extract a value $T_\varphi = 840$ ns for sample C. Dephasing in charge qubits is usually dominated by $1/f$ offset charge noise and a higher value of E_J/E_C helps in providing immunity against it. This is reflected in the larger value of T_φ for sample C.

In order to correct dephasing of the qubit due to low frequency noise [80], we performed an echo experiment in which we inserted a π pulse in the middle of the two $\pi/2$ pulses of the Ramsey sequence. A set of Ramsey fringes and its corresponding

echo decay are shown in Fig. 5.10 for sample B. For this sample, the decay constant was increased to 400 – 500 ns using the echo technique. For sample A, the echo technique did not increase the phase coherence time. We believe that for sample A, which has a larger ratio of E_J/E_C than sample B, and hence protected from $1/f$ offset charge noise, the dominant source of dephasing is due to broadband noise emanating from residual photons in our readout resonator [81], thus explaining the inefficacy of the echo sequence. It is possible that the $50\ \Omega$ environment shunting the qubit on the phase port side was not fully thermalized to the refrigerator temperature of 10 mK. For sample B, where an improvement was observed with the echo sequence, there are likely two contributing factors. First, the ratio E_J/E_C is much smaller and offset charge noise played a stronger role. The low frequency component of this noise can be corrected using an echo sequence. Second, we added more cryogenic attenuation in the transmission lines directly coupling to the phase port to reduce the resonator temperature, thereby potentially reducing the number of excess photons in the readout resonator and their associated dephasing.

5.5 Readout fidelity

We now come to question of the measurement fidelity of the JBA readout. In all the data shown in earlier sections, we note that the change in switching probability of the JBA when the qubit makes a transition from the ground to the excited state, is about 40 – 60%. An ideal readout would have a 100% change. This was one of the main problems plaguing the quantum qubit with a readout based on the switching of the large Josephson junction from the superconducting state to the finite voltage state [6]. The central motivation for the development of the JBA was to improve

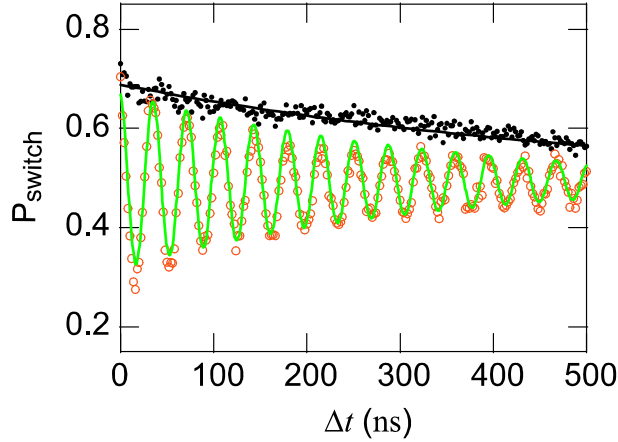


Figure 5.10: Result of an echo experiment (sample B) where a π pulse was kept in the middle of the two $\pi/2$ pulses separated by interval Δt (black dots). The Ramsey fringe data, obtained without the π pulse, is shown with red circles. The thick black curve is an exponentially decaying fit.

the readout contrast (η_c) of the qubit measurement. The JBA readout did achieve a significant improvement (more than a factor of 2) over the original scheme. The best results gave us a readout contrast of about 68% for sample C (Fig. 6.10) where an additional pulse was used to preferentially make the qubit transition from the first to the second excited state. But the ultimate goal of near 100% readout contrast still remains unachieved. We will analyze and discuss this issue in more detail in the next chapter where we try to understand what exactly goes on during a qubit measurement.

We characterized the readout by measuring P_{switch} as a function I_{RF}^{max} and $|\Psi\rangle$, as shown in Fig. 5.11. The blue circles correspond to the qubit in its ground state, obtained by letting the qubit relax spontaneously, while the red circles correspond to the qubit in its first excited state obtained by applying a π pulse, which will be discussed below. An important remark is that only a slight change in shape

of $P_{\text{switch}}(I_{RF}^{\text{max}})$ between the two qubit states is observed, which indicates that the switching process itself does not contribute strongly to the relaxation of the qubit. In cases where the readout is suspected to induce significant relaxation, the switching probability curve for the qubit excited state displays a pronounced kink and can be obtained by a weighted average of the observed curve for the ground state and the prediction for the excited state [82]. The expected discrimination power of the qubit readout is defined as

$$\eta_{dp} = \max_{I_{RF}^{\text{max}}} [P_{\text{switch}}(\langle \sigma_Z \rangle_{\Psi} = 1) - P_{\text{switch}}(\langle \sigma_Z \rangle_{\Psi} = -1)]$$

and its value for various qubit samples are given in Table 5.1 along with the actual contrast (η_c) observed in the experiment. Numerical simulations of the full circuit have been used to compute η_{dp} . Note that several competing factors enter this calculation, yielding similar values for samples A and B. The error bars reflect uncertainties in the values of stray reactances on chip and the precise resonator temperature.

The observed discrimination power is about 15 – 30 % smaller than expected. In a set of experiments described in the next chapter, we used two readout pulses in succession to determine that a 15 – 30 % loss of qubit population occurs, even before the resonator is energized to its operating point. We attribute this loss to spurious on-chip defects[46]. As photons are injected into the resonator, the effective qubit frequency is lowered due to a Stark shift via the phase port (see section 6.2.2). When the Stark shifted frequency coincides with the frequency of an on-chip defect, a relaxation of the qubit can occur. Typically, the qubit frequency spans 200 – 300 MHz (Fig. 6.3) before the state of the qubit is registered by the readout, and 3 – 4 spurious resonances are encountered in this range.

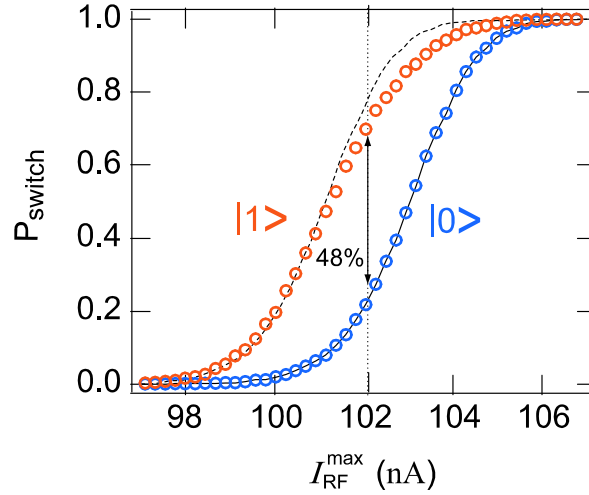


Figure 5.11: Switching probability as a function of maximum drive current and qubit state for sample B. The vertical dotted line represents value of drive current at which maximal discrimination power is observed. The width in current of the curves is in reasonable agreement with numerical simulations (data not shown). The solid line connects the observed data points in the $|0\rangle$ state and the dashed line is a copy of the solid line horizontally shifted to overlap the $|1\rangle$ state data at low values of P_{switch} .

We also note from Table 5.1 that the expected discrimination power for samples A and B was only 0.70. To increase the expected discrimination power, we must use samples with either a larger qubit E_J or a stronger phase coupling between the qubit and readout resonator. We used the latter approach in sample C by replacing the large Josephson junction in the qubit with two Josephson junctions in series. This provided us with an expected discrimination close to unity but the measured discrimination power showed only marginal improvement. Note that a stronger coupling between the qubit and the resonator also leads to a larger shift in effective qubit frequency as the resonator is energized, leading to a possibly larger loss of qubit population. Even the smallest loss in qubit population before the actual measurement will prevent you from achieving 100% readout fidelity.

In conclusion, we have successfully implemented a non-linear dispersive readout of the quantronium qubit using the Josephson Bifurcation Amplifier. The readout speed and discrimination power show a significant improvement when compared with the DC switching readout used in the original quantronium measurements [6]. Perhaps even more important, in the present readout scheme, the total measurement time is much smaller than T_1 , and it is possible to carry out experiments with multiple readout pulses to determine the information flow during a qubit readout and to account for any losses in qubit population. This important aspect can be used to determine the degree to which the measurement is quantum non-demolishing. These ideas are discussed in more detail in the next chapter.

Chapter 6

Qubit readout performance

In this chapter we will discuss the performance of the JBA as a qubit readout. We saw in the previous chapter that it was theoretically possible to choose qubit and JBA parameters to achieve a single shot readout. Experimentally we found that the contrast was smaller than the predicted value. In this chapter, we would like to analyze the possible causes of this reduced performance and provide a possible fix to the problem. Specifically, we would like to separate the intrinsic sensitivity of the JBA from other processes taking place during the readout operation which might lead to reduced performance. We begin by discussing the quantum non-demolition nature of the qubit readout with the JBA which allows successive measurements of the qubit state to be carried out. We will then break down the readout process and describe the evolution of the qubit state during the readout. The AC Stark shift of the qubit Larmor frequency when the JBA is energized will then be described and we will discuss its consequences on the readout process. Finally, we will discuss possible methods by which the goal of a single-shot readout can be achieved.

6.1 Quantum non-demolition readout using a JBA

Quantum non-demolition measurements are basically the ideal, textbook measurements of a quantum system (see ref. [83] for a review). The measurement process yields one of the eigenvalues of the measured observable and the quantum state immediately after the measurement is the eigenstate corresponding that eigenvalue. Since the eigenstate does not evolve under the free evolution of the system, one can then repeatedly measure the eigenstate achieving the same result everytime. This is the most important aspect of a QND measurement. QND measurements were originally discussed in the context of gravitational wave detection using massive metal bars [84]. They can also be useful in optical communication for tapping the signal from an optical fibre without affecting it. QND measurements can also be used for entangling several quantum systems.

A measurement involves coupling a quantum system to a measuring system which we call the "meter". The total Hamiltonian of the combined system can be written as a sum of three terms

$$\hat{H}_{total} = \hat{H}_Q + \hat{H}_M + \hat{H}_I \quad (6.1)$$

where $\hat{H}_Q, \hat{H}_M, \hat{H}_I$ are the Hamiltonians of the the quantum system, the meter and the interaction between them respectively. If we call the measured observable of the quantum system as A_Q , then a QND measurement requires the following two conditions

$$\left[\hat{H}_I, \hat{A}_Q \right] = 0 \quad (6.2a)$$

$$\left[\hat{H}_Q, \hat{A}_Q \right] = 0 \quad (6.2b)$$

The first condition ensures that there is no back-action of the meter on the measured observable¹ while the second condition ensures that the projected state does not evolve after that measurement. In chapter 4, we derived the combined Hamiltonian of the quantrium with the JBA (4.26) which we reproduce below for no gate excitation ($U(t) = 0$)

$$\begin{aligned} \hat{H}_{total} = & -\frac{E_J}{2}\sigma_Z + \lambda\hbar\omega_p\sigma_Z a^\dagger a + \\ & \hbar\omega_p a^\dagger a - \mu \left(1 + \frac{\lambda}{4}\sigma_Z\right) (a + a^\dagger)^4 - f(a + a^\dagger) I(t) \end{aligned} \quad (6.3)$$

The first term is the qubit Hamiltonian (\hat{H}_Q), the second term is the dominant² interaction Hamiltonian (\hat{H}_I) while the rest of the terms constitute the Hamiltonian of the driven, non-linear resonator - our meter (\hat{H}_M). The coefficients λ and μ are defined in equations 4.27b and 4.27c. If we choose σ_Z as our observable, then we note that the QND conditions 6.2a and 6.2b are satisfied. We should point out that equation 6.3 was derived for the case of zero asymmetry ($d = 0$) in the quantrium junctions (see 4.1.3) and only in this limit the QND conditions are fully satisfied. For finite values of d , corrections to the QND fraction of order d^2 exist [79].

With the QND conditions being satisfied for the quantrium with a JBA readout, we can make multiple measurements of the qubit state and determine the extent to which they are QND. The fact that the qubits have a finite lifetime for the excited state is somewhat contradictory to the requirement that the qubit state should not

¹A measurement always involves some backaction but the quantity being affected could be different than the one being observed. In this case, the backaction leads to dephasing of the qubit but does not cause any mixing of the qubit states.

²There is also a coupling term ($\propto \mu$) between the qubit and the non-linear part of the resonator. We neglect that term in this analysis for simplicity as it does not affect the QND nature of the readout.

evolve between measurements. Since any measurement requires a finite amount of time to complete, there is always a finite probability for the qubit to decay to its ground state leading to errors in the subsequent measurements. But we can always factor this out if we know the lifetime of the qubit excited state. In the next section, we will discuss the results of multiple measurements of the qubit state and explore in more detail the evolution of the qubit state during measurement.

6.2 Information flow during qubit measurement

6.2.1 Multiple pulse measurements

The qubit was prepared in its ground state and then multiple readout pulses were used to measure the qubit. This was repeated thousands of times to construct the switching probability for each pulse. We observed that with the qubit in the ground state, the switching probability associated with each pulse was the same, indicating that the qubit remained in the ground state after every measurement. The same procedure when repeated with the qubit prepared in the excited state, led to some interesting results. In Fig. 6.1 we show the result of multiple measurements of the excited state of the qubit for different readout frequencies. Data is shown for sample A with $\omega_{01}/2\pi = 18.989$ GHz (see Table 5.1). The plasma frequency of the JBA readout was $\omega_p/2\pi = 1.81$ GHz.

The switching probability data has been normalized and converted into a probability $P_{|1\rangle}$ of the qubit being in the excited state, by using the result of the first measurement assuming that the first pulse makes a perfect measurement of the qubit state. The time axis indicates the time delay between the π pulse used to prepare

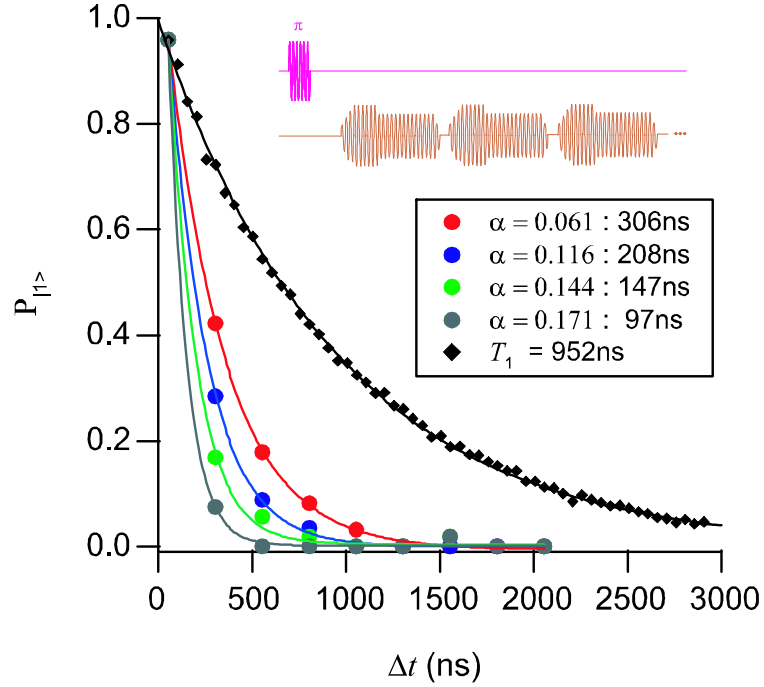


Figure 6.1: Multiple readout of qubit state (Sample A, $\omega_{01}/2\pi = 18.989$ GHz) for four different readout frequencies. The qubit is prepared in the excited state and measured multiple times. The switching probability for each pulse has been normalised by the result of the first measurement. Data is then plotted as the probability $P_{|1\rangle}$ of the qubit being in the excited state after each measurement. Data for four different readout frequencies are shown. The time axis indicates the time delay between the π pulse and the subsequent readout pulses. The solid lines are exponential fit to the data and the decay times are indicated in the legend. The black curve shown for reference is the T_1 decay where the time delay between the π pulse and a single readout pulse is varied. We observe strong relaxation of the qubit with each measurement pulse. The effect is stronger as the readout frequency is lowered. No excitation was observed when the qubit was prepared was the ground state (see Fig. 6.2). Data characterizes the QND capability of the readout. While the ground state is fully preserved after a measurement, the relaxation of the excited state is sped up.

the excited state and the subsequent readout pulses. The black curve is the standard T_1 measurement where the time delay between the π pulse and a single readout pulse is varied. Data clearly indicates that the qubit relaxes after each measurement and the relaxation is much stronger than what one would expect from the T_1 measurement. The exponential fit to each data set (solid lines) provides an effective relaxation rate associated with the different readout frequencies. Another clear trend is that the relaxation rate increases with increasing detuning ($\alpha = 1 - \omega_d/\omega_p$) of the readout frequency. A large readout detuning is associated with stronger drives (Fig. 2.5). Nevertheless, there is clear indication that there is some QND character to the measurement since the ground state is fully preserved after a measurement and the excited state is preserved to some extent.

In order to understand the effect of drive strength on the evolution of the qubit state, we sent two readout pulses to the qubit prepared in the ground/excited state. The switching probability of the second pulse was monitored as a function of the amplitude of the first one. A typical result of such a measurement is shown in the right panel of Fig. 6.2. The left panel shows the pulse protocol used for this measurement. Since we are only interested in variations due to the amplitude of the first pulse, data is normalized by the contrast obtained when the first pulse is of zero amplitude and displayed as the probability $P_{|1\rangle}$ of the qubit being in the excited state:

$$P_{|1\rangle} = \frac{\left[P_{\text{switch}}^{|1\rangle} - P_{\text{switch}}^{|0\rangle} \right]_{A=A_{\text{opt}}}}{\left[P_{\text{switch}}^{|1\rangle} - P_{\text{switch}}^{|0\rangle} \right]_{A=0}} \quad (6.4)$$

This also accounts for the decay due to the finite lifetime of the qubit excited state.

We note that the qubit excited state population starts to decay (red curve) even

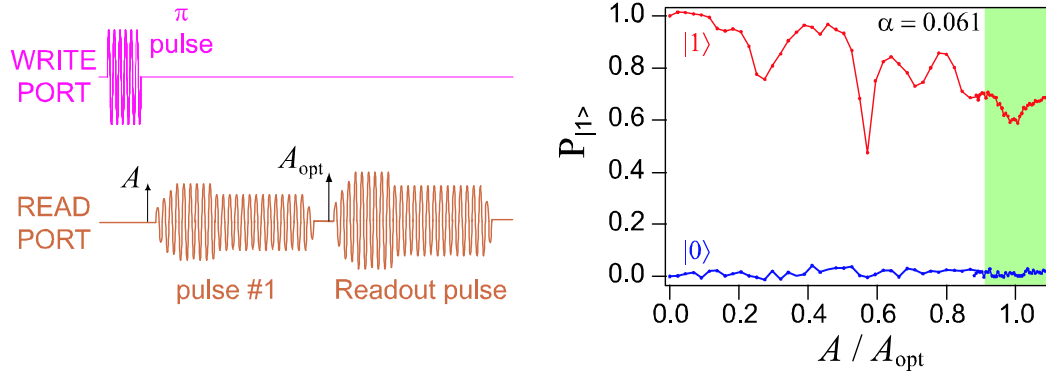


Figure 6.2: Two pulse measurements of the qubit state (Sample A, $\alpha = 0.061$). Pulse protocol is shown in the left panel and data on the right panel. A and A_{opt} are the amplitudes of the first and second pulse respectively. The switching probability of the readout pulse normalised by its value for $A = 0$ is plotted as the probability $P_{|1\rangle}$ of the qubit being in the excited state as function of the normalised first pulse amplitude (A/A_{opt}). No change is observed with the qubit prepared in state $|0\rangle$ (blue) while a steady reduction is observed for the qubit in state $|1\rangle$ (red). We also note some sharp dips at certain amplitudes indicating the presence of some resonant phenomena. Since the JBA starts to measure only when $A/A_{\text{opt}} \simeq 1$, the qubit is decaying due to the excitation of the resonator and not necessarily due to the measurement process. The region shaded in green corresponds to amplitudes where pulse #1 starts to measure strongly.

before the amplitude of the first pulse reaches the optimal value A_{opt} for readout (shaded region). Since the JBA starts to measure only when $A/A_{\text{opt}} \simeq 1$, the qubit is decaying due to the excitation of the resonator and not necessarily due to the measurement process. Clearly some other effect is causing the qubit decay. Apart from the steady decay of the qubit population as a function of amplitude, we also note some sharp dips at certain amplitudes indicating the presence of some resonant phenomena. No excitation is observed when the qubit is prepared in the ground state (blue curve). So the decay of the qubit excited state is related to the drive strength or equivalently the amplitude of oscillations of the resonator. We speculate that these

losses are due to resonances in the qubit environment arising from on-chip defects. As the oscillation amplitude of the resonator increases, the effective qubit frequency is lowered due to a Stark shift [47] via the phase port. When the Stark shifted frequency coincides with the frequency of an on-chip defect, a relaxation of the qubit can occur. We characterize this frequency shift next.

6.2.2 AC Stark shift of qubit

The shifting of the qubit frequency due to the energizing of the oscillator can be understood in two ways. From the discussion in section 4.1.3, we know the qubit Hamiltonian and hence the Larmor frequency is a function of the two control parameters - N_g and δ (4.6). When the resonator coupled to the qubit via the phase port is energized, the phase δ across the qubit oscillates, resulting in a modulation of the qubit Larmor frequency. The frequency modulation which takes place at the resonator drive frequency results in an average shift of the Larmor frequency. The Larmor frequency is maximum at the phase bias point ($\delta = 0$) for the qubit and decreases with increasing δ and this results in the lowering of the Larmor frequency in the presence of driving on the phase port. A similar effect can be achieved if we drive the gate port (N_g) with a frequency far detuned from the Larmor frequency to prevent qubit excitation. But now, the direction of shift is towards higher frequencies because the Larmor frequency is the smallest at the gate bias point ($N_g = 0.5$). We can also understand the AC Stark shift via the phase port in another way by

combining the first two terms in the Hamiltonian in 6.3 and writing it as

$$\begin{aligned} \hat{H}_{total} = & - (E_J - 2\lambda\hbar\omega_p a^\dagger a) \frac{\sigma_Z}{2} + \\ & \hbar\omega_p a^\dagger a - \mu \left(1 + \frac{\lambda}{4}\sigma_Z \right) (a + a^\dagger)^4 - f(a + a^\dagger) I(t) \end{aligned} \quad (6.5)$$

The first term can now be seen as a spin 1/2 with a Larmor frequency which is dependent on the number of photons ($\langle a^\dagger a \rangle$) in the resonator [47]-the frequency shift per photon being $2\lambda\hbar\omega_p$.

In order to calibrate these frequency shifts as a function of the readout amplitude, we carried out the two pulse measurement described above with a small modification. With the qubit prepared in the ground state, we added a probe microwave signal on the gate port overlapping in time with the first pulse which we now call the Stark pulse (see Fig. 6.3). When the amplitude of the Stark pulse is large enough to Stark shift the qubit (prepared in its ground state) into resonance with the probe signal, we observe enhancement in P_{switch} of the readout pulse #2 indicating resonant excitation of the qubit. By repeating this measurement for different probe frequencies ($\omega_{\text{probe}} < \omega_{01}$), we can map out the Stark shifted qubit frequency as a function of the drive amplitude. A similar experiment can be carried out to calibrate the Stark shift from the gate port with both the Stark and the probe pulse being applied to the gate port. The result of such measurements on Sample B is shown in Fig. 6.3.

Panel (a) shows the pulse protocol used for this measurement. Panel (b) plots P_{switch} as a function of drive amplitude for three different probe frequencies. The position of the peak corresponds to the amplitude at which the qubit is Stark shifted into resonance with the probe frequency. Panel (c) maps out this dependence and

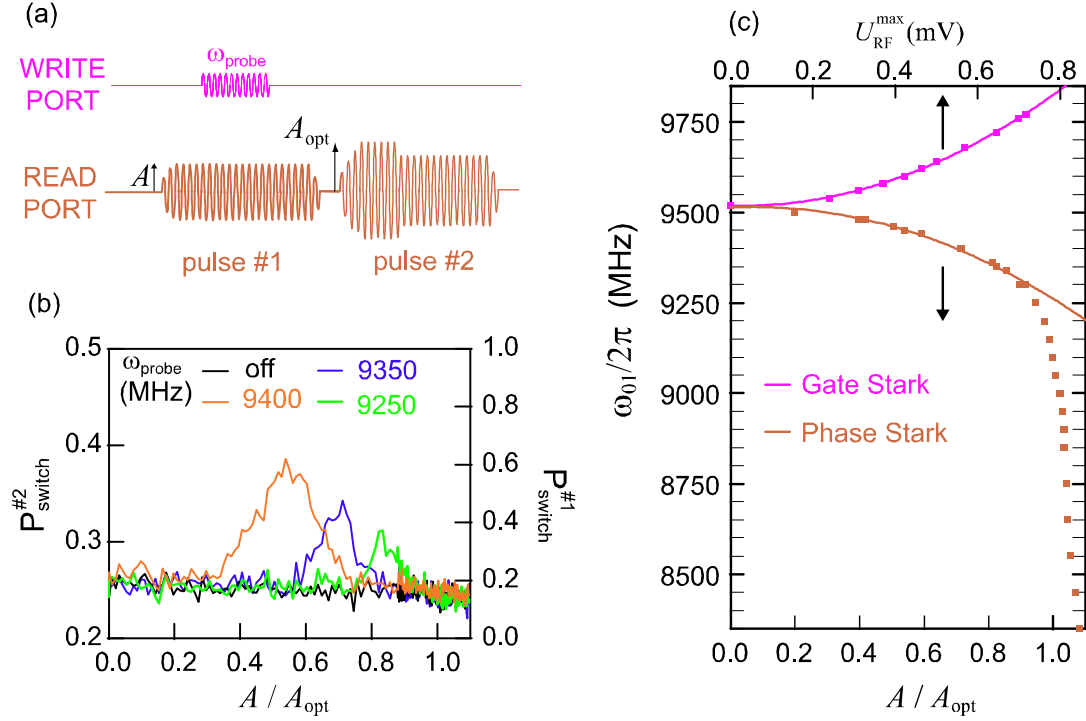


Figure 6.3: Characterizing the AC Stark shift of qubit frequency with driving on phase or gate port. Data shown for Sample B with $\omega_{01}/2\pi = 9.513$ GHz. Panel (a) shows the pulse protocols used. Pulse #1 is the Stark pulse which Stark shifts the qubit (prepared in state $|0\rangle$) into resonance with the probe pulse (ω_{probe}). The switching probability of pulse #2 as a function of the amplitude of pulse #1 is shown for three different probe frequencies in panel (b). By noting the amplitude corresponding to the peaks we can map out the dependence of the Stark shifted qubit frequency and the drive amplitude. The result of Stark shift via the phase port ($\omega_d/2\pi = 1.55$ GHz, brown squares, bottom axis) is shown in panel (c). Stark shift data via the gate port ($\omega_{\text{RF}}/2\pi = 6.90$ GHz, pink squares, top axis) is also shown. The solid lines are the expected quadratic fits. For $A/A_{\text{opt}} \simeq 1$ on the phase port, we observe deviations from the quadratic behaviour due to the non-linearity of the resonator. No such effect is observed for the Stark shift via the gate port as expected.

plots the Stark shifted frequency as a function of drive amplitude for both phase and gate driving. The solid lines are quadratic fits to the data which indicate that the Stark shift is proportional to the drive power and hence photon number in the resonator. For drive amplitudes close to A_{opt} , the non-linearity of the resonator starts coming into play and the frequency starts to change much faster. This is because the oscillation amplitude now grows non-linearly with the drive amplitude. Also, for $A/A_{\text{opt}} \sim 1$, the JBA starts to switch into its high amplitude state resulting in much larger Stark shifts. No such effect is observed for AC Stark shift via the gate port as expected, since the oscillation amplitude of N_g is directly proportional to the drive amplitude U_{RF}^{max} .

6.2.3 Quantifying the losses during readout

In order to quantify the loss in qubit population during readout, we came up with a model to illustrate the evolution of the qubit state during different parts of the readout pulse. Note that this is a very simplistic model and might not account for all scenarios. The model evolved from analyzing typical qubit behavior in experiments. Nevertheless, it provides a simple way to separate the intrinsic discrimination power of the readout from the losses due to qubit decay. This model is illustrated in Fig. 6.4.

The readout pulse is separated into four parts - *ARM*, *PROJECT*, *RECORD* and *DISARM*. The *ARM* phase is when the JBA is energized up to the optimal level for readout. The *PROJECT* phase is when the qubit state is projected and the JBA ends up in its low or high amplitude state. In the *RECORD* phase, the result of measurement is latched and recorded and finally in the *DISARM* phase the readout

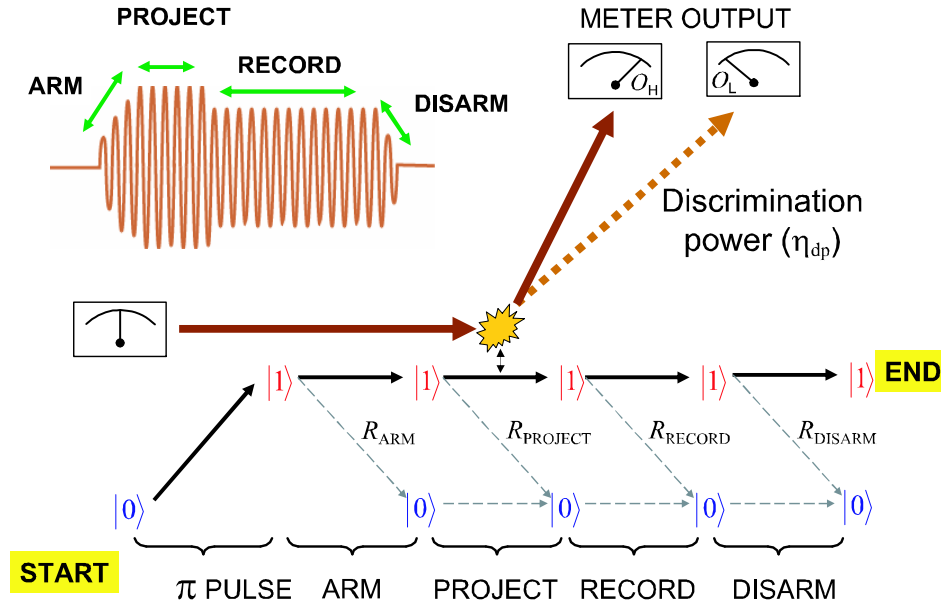


Figure 6.4: Information flow during qubit readout - a model to explain qubit state evolution during readout. The readout pulse is separated into four phases - *ARM*, *PROJECT*, *RECORD* and *DISARM*. The bottom panel shows the evolution of the qubit state during each phase. The qubit goes from $|0\rangle$ to $|1\rangle$ after a π pulse and associated with each phase of the readout is a certain probability R to decay from $|1\rangle$ to $|0\rangle$. By carrying out multiple measurements of the qubit state, one can extract the various decay probabilities and understand the relaxation processes during a readout operation.

is turned off by reducing the amplitude to zero. During each of these parts, the qubit can relax to its ground state with a certain probability. We have neglected the possibility of excitation from the ground state in this analysis since it is not observed in experiments except in marginal cases discussed later in this section.

By using pulses of varying length we found that $R_{ARM} = R_{DISARM}$. The qubit frequency is swept downwards during the *ARM* phase and upwards during the *DISARM* phase. The direction of this sweep does not affect the qubit decay probability and

hence $R_{ARM} = R_{DISARM}$. Also, we found that the decay during the *PROJECT* phase is usually smaller than the *ARM* phase and hence we can set³ that $R_{PROJECT} = 0$. Given these constraints we can analyze the data shown in Fig. 6.5 which shows data for different readout frequencies with the first pulse amplitude close to A_{opt} . The data for smaller amplitudes for the first pulse is similar to Fig. 6.2.

Also shown for reference are the switching probability curves for the ground and excited state obtained from the first measurement pulse. For a single readout, only the *ARM* and *PROJECT* phase is encountered, and we can write

$$\eta_f = (1 - R_{ARM})(1 - R_{PROJECT})\eta_{dp} \quad (6.6)$$

where η_f is the readout fidelity (obtained from the observed contrast after accounting for T_1 losses) and η_{dp} is the actual discrimination power of the readout (see 4.3.5). From the data in Fig. 6.5, if we take the value of the qubit excited state population ($P_{|1\rangle}^A$) at an amplitude just before the S-curves start (indicated by dashed line A), we get the losses associated with the *ARM* and *DISARM* phase of the readout

$$(1 - R_{ARM})(1 - R_{DISARM}) = P_{|1\rangle}^A \quad (6.7)$$

Solving for $R_{ARM} = R_{DISARM} (\leq 1)$, we get

$$R_{ARM} = 1 - \sqrt{P_{|1\rangle}^A} \quad (6.8)$$

³This assumption need not always be true. The decay during the *PROJECT* phase can be accounted for as a modified T_1 effect. Note that the T_1 of the qubit while it is being driven can be different than the undriven T_1 as shown later. It is also possible to combine the *PROJECT* and *ARM* phase together. We usually observed that the dominant relaxation before the actual measurement was due to the *ARM* phase.

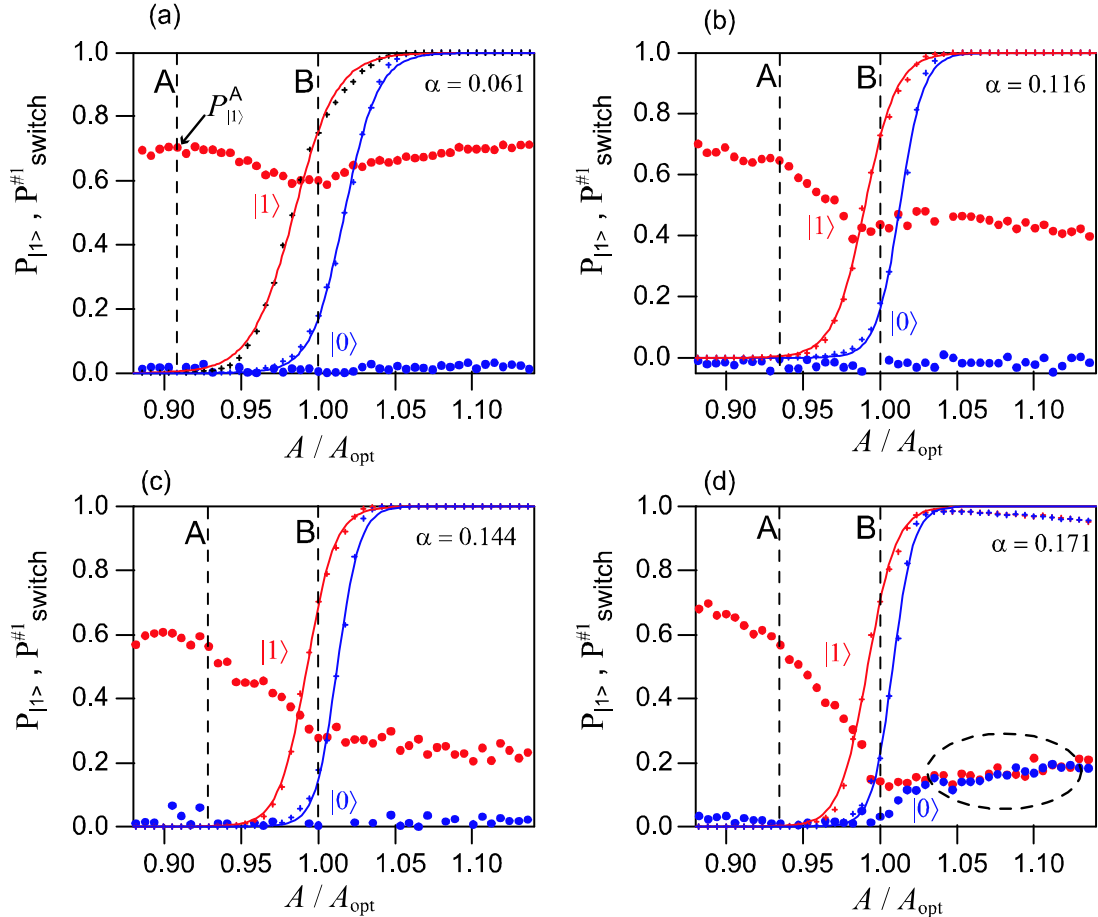


Figure 6.5: Results of two pulse measurements as described in Fig. 6.2 are presented for different readout frequencies with the detuning values α indicated in the plots. Data for Sample A is shown for pulse #1 amplitudes $A \simeq A_{\text{opt}}$. As the data in Fig. 6.1 indicated, we observe an increase in relaxation as the detuning α is increased which is associated with increasing drive strengths. By noting the values of $P_{|1\rangle}$ at positions marked A and B, one can extract the pre-measurement and post-measurement relaxation associated with the readout. As described in the text, this can be used to extract the intrinsic readout discrimination power. As before, the qubit ground state $|0\rangle$ is not affected except for the largest detuning shown in panel (d). Numerical simulations for this detuning indicated that the junction phase was crossing the values $\delta = \pm\pi$ resulting in Landau-Zener tunneling between the qubit states.

Setting $R_{PROJECT} = 0$, we can solve for η_{dp}

$$\eta_{dp} = \frac{\eta_f}{\sqrt{P_{|1\rangle}^A}} \quad (6.9)$$

The value of $P_{|1\rangle}$ at an amplitude equal to the optimal readout amplitude (indicated by dashed line B) tells us about the fraction of qubit excited state population which survives after a full readout operation. We call this the QND fraction F_{QND} given by

$$F_{QND} = (1 - R_{ARM})(1 - R_{DISARM})(1 - R_{RECORD}) = P_{|1\rangle}^B \quad (6.10)$$

where we have set $R_{PROJECT} = 0$. Solving for R_{RECORD} , we get

$$R_{RECORD} = 1 - P_{|1\rangle}^B / P_{|1\rangle}^A \quad (6.11)$$

Processing the data in Fig. 6.5 using the technique described we can compute R_{ARM} and R_{RECORD} for the different readout frequencies. The result is summarized as a function of readout detuning α in Fig. 6.6. The pre-measurement relaxation (R_{ARM}) has a weak dependence on the detuning but the post-measurement relaxation (R_{RECORD}) has a very strong dependence. This implies that the observed contrast doesn't vary much with detuning⁴ as can be seen from the S-curves in Fig. 6.5. The QND fraction which depends on R_{RECORD} must decrease strongly with detuning as we saw in Fig. 6.1.

We note that the data in Fig. 6.5d show some excitation of the qubit state for

⁴This is because the discrimination power η_{dp} also does not vary much with detuning.

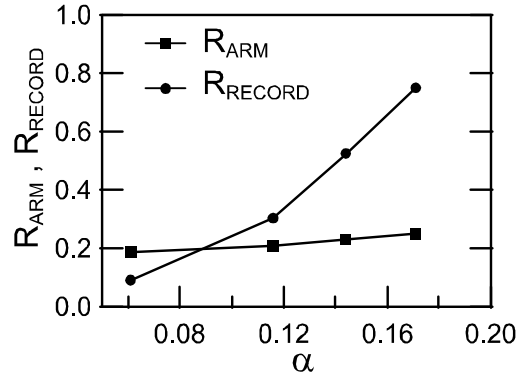


Figure 6.6: Readout induced relaxation as function of drive detuning for Sample A. The pre-measurement (R_{ARM}) and post-measurement (R_{RECORD}) relaxation data as inferred from the data shown in Fig. 6.5 is plotted as a function of the detuning α of the drive frequency. We note that R_{ARM} has a weak dependence on α while R_{RECORD} increases strongly with α .

amplitudes $A \gtrsim A_{opt}$. We verified using numerical simulations that for those readout parameters, the phase of the readout junction was not contained within one well of the cosine potential. This meant that the phase crossed the values $\delta = \pm\pi$ where the qubit spectrum has an avoided crossing. This can cause Landau-Zener tunnelling resulting in the mixing of the qubit states as indicated by the fact that $P_{|1\rangle}$ tends to the same value (circled region in Fig. 6.5d) irrespective of the initial state of the qubit. Apart from this case, we note that the readout operation preferentially affects the qubit excited state.

The numbers extracted for η_{dp} using this technique for the various qubit samples were in good agreement with those obtained from numerical simulations (Table 5.1). This suggests that the above model works well to account for losses during readout.

6.3 Characterizing the qubit environment

It is clear from the data shown in the previous sections that the losses in the environment seen by the qubit have an important role to play in the performance of the qubit and its readout. The T_1 measurements discussed in chapter 5 are not compatible with the values that would be expected from the designed electromagnetic environment [40]. The decoherence in the qubit is set by the properties of an uncontrolled environment coupled to the qubit. It has been conjectured that the losses are due to a collection of two level fluctuators (TLF) which could be present in the substrate, in the oxide layer covering the metallic electrodes or in the oxide barrier of the junction [85]. Such TLFs have been routinely observed as avoided crossings in the spectroscopy of phase qubits which use large area Josephson junctions [46]. They have also been observed in CPB based qubits which typically use small area Josephson junctions, though their occurrence is rarer [40, 86]. This collection of TLFs usually result in an effective, frequency dependent, lossy bath, but coherent coupling between the qubit and the TLF has also been observed.

Fig. 6.7 shows spectroscopy data for sample C. Panel (a) shows the data obtained in the first cooldown. The qubit frequency was varied by applying a magnetic field. Each row is a plot of P_{switch} (mean subtracted) plotted as a color v.s. qubit transition frequency. The red regions correspond to the frequency where the excitation frequency matches the qubit transition frequency. The dashed line is the expected dependence calculated using the E_J and E_C values for this sample (Table 5.1). One can clearly observe a strong avoided crossing (~ 0.2 GHz splitting) around 19.5 GHz along with some weaker cutouts in the spectrum at a few other locations. There is also a cutout in the spectrum at the sweet spot ($\Phi/\Phi_0 = 0$) which explains the extremely low

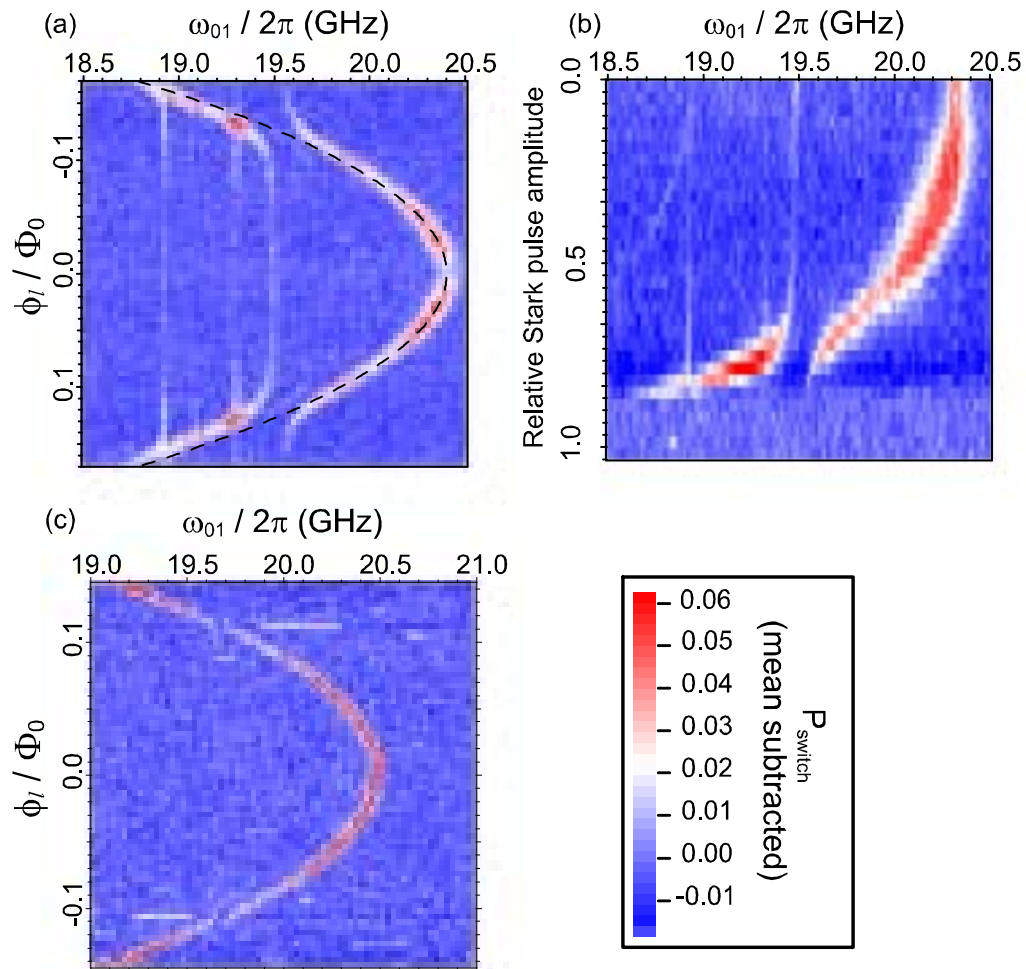


Figure 6.7: Spectroscopy data for Sample C before {panels (a) and (b)} and after {panel (c)} thermal cycling to room temperature. The qubit frequency was varied by applying a flux through the quantum loop in panel (a) while a Stark pulse was used in panel (b). Dashed line in panel (a) is the expected dependence from theory. One can clearly observe a strong avoided crossing (~ 0.2 GHz splitting) around 19.5 GHz indicating that the qubit is coupled to a spurious two-level system in the environment. Other, weaker features in the spectrum are also observed. Panel (c) shows the spectroscopy data after the sample was warmed up to room temperature and then cooled back down to 12 mK. The spectrum is now much cleaner but a remnant of the avoided crossing is still visible (~ 0.05 GHz splitting) at a slightly shifted frequency. Also visible is an improvement in the spectroscopy linewidth.

$T_1 (< 10 \text{ ns})$ which was observed during the first cooldown. Panel (b) shows the same data taken using a Stark pulse to shift the qubit frequency. Sample C had two readout junctions in series for enhanced coupling to the split CPB, resulting in much larger Stark shifts ($\sim 1.6 \text{ GHz}$) as compared to sample B ($\sim 0.2 \text{ GHz}$, 6.3). This is for Stark pulse amplitudes less than those required for the JBA to switch. We can explain the factor of 8 difference observed in the maximum Stark shift between Sample B and Sample C as follows. The two readout junctions double the phase excursion across the split CPB resulting in 4 times the Stark shift (quadratic dependence on amplitude). The remaining factor of 2 is due to the Larmor frequency of Sample C being roughly twice that of Sample B.

Panel (c) shows the spectroscopy performed on sample C after the sample was warmed up to room temperature and cooled back down to 12 mK. The data is now much cleaner with fewer cutouts. There is still a remnant of the avoided crossing at 19.5 GHz which is now slightly shifted in frequency and weaker ($\sim 0.05 \text{ GHz}$ splitting). Also, the cutout at the sweet spot is no longer present, resulting in an improved $T_1 \sim 70 \text{ ns}$. This kind of behavior with temperature cycling is often seen in solid state systems. The temperature cycling can lead to the rearrangement of the microscopic defects leading to a change in the spectrum of the environment.

We also used T_1 measurements as a way to characterize the environment as it is a probe for the available decay modes at the qubit transition frequency. A common feature we observed in all samples is the dependence of T_1 on gate voltage U . Ideally, the qubit properties should be the same as long as $N_g \bmod 1 = 0.5$, the sweet spot in charge. But in practice, we always found that certain values of U were better than others in terms of stability and T_1 values. This variation of T_1 with gate voltage for

Sample B is shown in Fig. 6.8a. We note that variations in T_1 of about a factor of two is observed. The data point with the largest positive gate voltage had a parity jump where one extra electron gets onto the island. Often, the gate voltage at which best results are obtained changes with time. This dependence on gate voltage suggests that the loss mechanism must involve some charged TLFs. Note that the qubit transition frequency is kept the same as we are always biased at the sweet spot. In another set of T_1 measurements shown Fig. 6.8b, we varied the qubit transition frequency by threading a flux through the loop of the quantrium while keeping $N_g = 0.5$. Again, we note variations as large as a factor of two while the expected variation from theory is much smaller. We observe similar behavior when the frequency is varied by changing gate charge. These kind of variations in T_1 have been seen in other superconducting qubit measurements [40].

Qubit properties like T_1 can differ when they are driven by a strong field [40], like during a readout operation. We carried out T_1 measurements on Sample B in the presence of strong driving on the phase and gate port. As discussed in 6.2.2, driving the qubit on the gate or phase port leads to an AC Stark shift of the qubit frequency. This is another way of characterizing the frequency dependence of the qubit environment, though the driving can lead to additional effects. Results of such measurements are shown in Fig. 6.9. The measurement protocol is similar to the one described in 5.4, but now we include a Stark pulse on either the gate or the phase port during the time delay between the π pulse and the readout pulse.

We again see strong variations in T_1 for different Stark shifted qubit frequencies. The dashed line indicates the undriven Larmor frequency of the qubit. We also note an overall reduction in T_1 as the driving strength is increased, though the effect is

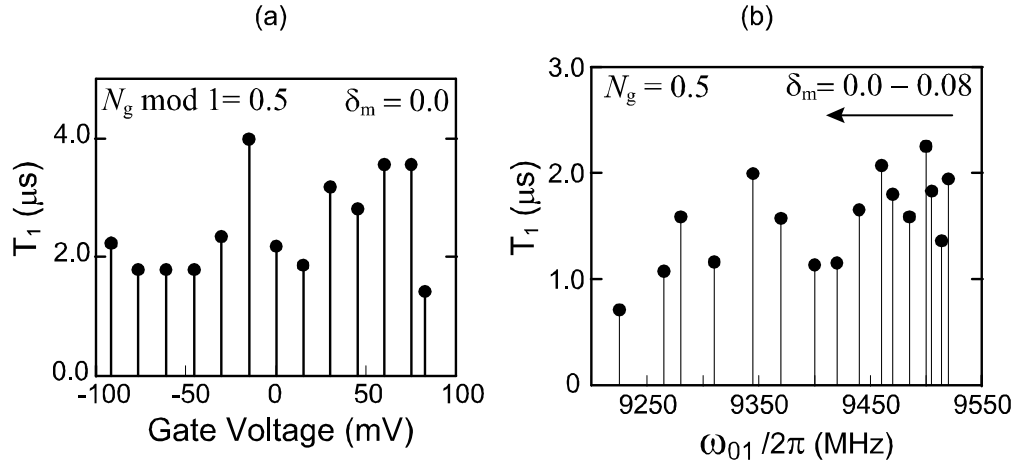


Figure 6.8: T_1 measurements for Sample B are presented. Panel (a) shows the results of T_1 measurements as a function of DC gate voltage. Note that the qubit is always kept at the sweet spot i.e. $N_g \bmod 1 = 0.5$ and $\delta_m = 0.0$. Though the qubit properties should remain the same, we observe significant variation in T_1 as the gate voltage is varied indicating that the gate voltage is affecting the spectrum of the qubit environment. In panel (b), we change the qubit transition frequency by applying flux through the loop and measure T_1 at each position. We again see large changes in T_1 significantly different from the expected smooth dependence from theory. Both data sets indicate that the rate of qubit decay is set by the properties of an uncontrolled environment coupled to the qubit.

much more pronounced (c.f. 6.8b) for driving on the phase/readout port. We can conclude that there are two main effects which explain the above data. The first one is the frequency dependence of the qubit environment resulting in variations in T_1 . The second effect which is just related to the strength of the driving (and not the associated Stark shift) is not fully understood at this time. A new theory being developed for circuit QED systems suggests that noise leading to dephasing can cause mixing of qubit states in the presence of strong driving, with the effect being proportional to the driving strength [87]. The fact that the JBA readout frequency (~ 1.5 GHz) is far detuned from the qubit Larmor frequency ($\gtrsim 10$ GHz) should

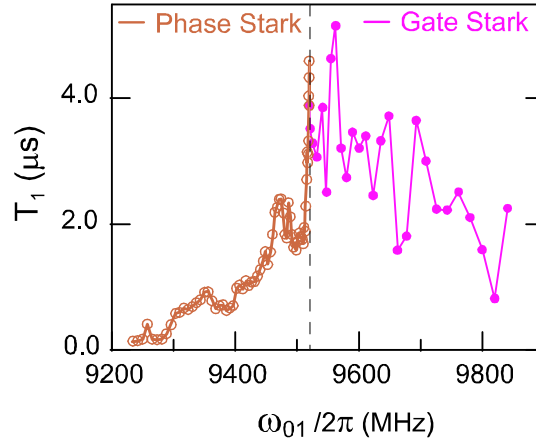


Figure 6.9: T_1 measurements for Sample B in the presence of strong driving on the phase (brown) and gate (pink) port. T_1 values are plotted as a function of Stark shifted frequencies with the dashed line indicating the undriven Larmor frequency. The solid lines are just a guide for the eye. The standard T_1 protocol is modified by incorporating a Stark pulse during the time delay between the π pulse and the readout pulse. On top of the fluctuations in T_1 values, we observe a steady decrease with increasing drive amplitudes (larger Stark shifts). This effect is more pronounced with the driving on the phase port indicating that the variation in T_1 is not just due to a change in the qubit transition frequency (c.f. Fig. 6.8b) but also has something to do with the strength of the driving.

provide protection from such effects. But, the driving strength in the JBA readout is much higher than those used in circuit QED experiments and it is possible that some multi-photon process is involved. A more detailed study of the back-action of the JBA on the qubit is required.

6.4 Approaching a single-shot readout

It is clear from the qubit measurement results that improvements on several fronts are required to achieve the goal of a single-shot readout. In samples A and B, the expected discrimination power was not 100% (Table 5.1) due to insufficient change in the loop

currents between the ground and the excited state. In order to increase this signal, we developed the double junction JBA (DJBA) where the readout junction was replaced by two readout junctions in series. This roughly doubled the coupling between the readout junction and the qubit which was confirmed by numerical simulations (section 4.4). Sample C was made with the DJBA readout and the measured S-curves are shown in Fig. 6.10a.

The measured contrast is about 40% while the calculated discrimination power is 95%. Using the two pulse experiment described above, we found that the qubit relaxation during the ARM+PROJECT phase was much stronger (roughly 3 times) in this sample as compared to samples A and B, resulting in a reduced contrast. We believe that this is due to the much larger Stark shifts observed in the DJBA samples due to the enhanced coupling with the qubit. The larger excursion in frequency space results in a higher probability of encountering environmental resonances and hence relaxation. This sample also had a much smaller T_1 and as is evident from Fig. 6.7, had several environmental resonances near the qubit Larmor frequency. Nevertheless, we were able to improve the contrast further in sample C by using the following technique. Due to the large E_J/E_C ($= 17.5$) ratio, we were able to access the second excited state $|2\rangle$. The transition frequency between the first and second excited state ($\omega_{12} = 18.275$ GHz) is now smaller than $\omega_{01} = 20.344$ GHz. It turns out that for these qubit parameters, the change in the effective critical current of the split CPB is almost double in state $|2\rangle$ as compared to state $|1\rangle$. The measurement protocol now involves applying a π pulse at ω_{12} before the readout operation. If the qubit is initially in state $|0\rangle$, it would remain in that state while if the qubit is in state $|1\rangle$, it would be transformed to $|2\rangle$. In general, a qubit state $\alpha_1|0\rangle + \alpha_2|1\rangle$ would be

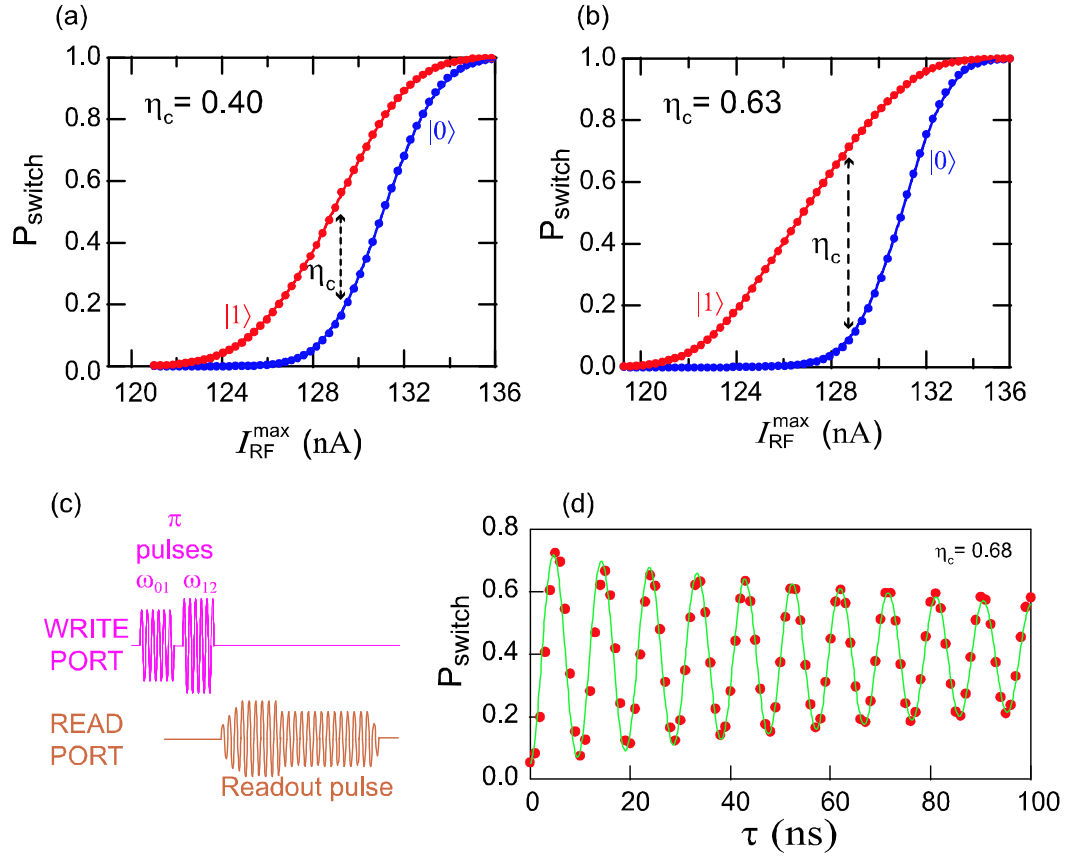


Figure 6.10: Data for Sample C demonstrating enhanced contrast by exploiting the second excited state of the qubit is shown. Panel (c) shows the pulse protocol used. An additional π pulse at transition frequency $\omega_{12} = 18.275$ GHz is used to transform state 1 to 2. This pulse has no effect on state 0 since $\omega_{01} = 20.344$ GHz is significantly different from ω_{12} . For the qubit parameters of sample C, it turns out that state 2 has a much larger change in critical current resulting in a larger shift of the S-curves. Panel (a) shows S-curves without this additional π pulse while panel (b) shows data including the additional π pulse clearly indicating a larger shift and an improved contrast. Panel (d) shows Rabi oscillations with the best contrast obtained ($\eta_c = 0.68$).

transformed to $\alpha_1|0\rangle + \alpha_2|2\rangle$.

The S-curves measured using this new technique are shown in Fig. 6.10c. We note an improved contrast $\eta_c = 0.63$. The excited state S-curve (red) is now shifted more because it now corresponds to the qubit being in state $|2\rangle$ which has a smaller effective critical current. There are still losses associated with the energizing of the oscillator but overall we observe an improvement in the contrast. The excited state S-curve is now a weighted average of the S-curve in state $|2\rangle$, $|1\rangle$ and $|0\rangle$ depending on the probability of decay from state $|2\rangle$ to $|1\rangle$ and from state $|1\rangle$ to $|0\rangle$. There are two effects which result in the improved contrast. As explained above, the first one is the larger change in effective critical current in state $|2\rangle$, though the effective critical current change for state $|1\rangle$ was already large enough to obtain $\eta_{dp} = 0.95$. We believe that a more important effect is the fact that the qubit in state $|2\rangle$ is now sensitive to a different range of frequencies. Due to the selection rules for the qubit transitions, the most probable way for the qubit to relax is from $|2\rangle$ to $|1\rangle$ and then from $|1\rangle$ to $|0\rangle$. For the qubit to decay from $|2\rangle$ to $|1\rangle$, the relevant frequency is $\omega_{12} = 18.275$ GHz. As the oscillator is energized this frequency gets Stark shifted to lower frequencies. It is possible that this frequency range has less environmental resonances resulting in a reduced probability of relaxation during readout. The best contrast obtained using this technique was about 68% as illustrated by the Rabi oscillation data shown in Fig. 6.10d.

In conclusion, getting the qubit readout contrast within a few % of unity is an important problem that needs to be solved for quantum computing applications. This will allow interesting experiments like measuring the entanglement of multiple qubits and testing Bell's inequality [88] with good signal to noise. A single-shot readout

will also enable more stringent tests of the theory of quantum measurements and understanding the evolution of the qubit during a measurement operation [89].

The superconducting qubit community is yet to achieve a readout with near 100% efficiency but steady progress is being made. Phase qubits with about 90% readout contrast are in the front of the race [90]. Flux qubits have demonstrated 87% contrast using a non-linear resonator readout like the JBA [91]. They were able to change the qubit frequency rapidly by applying flux pulses just before the readout operation. This way they were able to minimize the relaxation of the qubit during readout, resulting in a better contrast. Circuit QED systems with charge qubits coupled to superconducting cavities have achieved 100% visibility with weak measurements [86] but the readout contrast is often limited to about 30% [92]. This has been improved recently to about 70% [93]. They are mostly limited due to the noise temperature of their following amplifier but also observe mixing of qubit states when using a large number of photons for measurement. Experiments using a CBA, the distributed element version of the JBA, to measure the quantronium qubit have achieved a readout contrast of 60% [43] though very recent CBA measurements using low Q (~ 100), coplanar stripline resonators indicate a readout contrast of about 85% [94].

All these different systems ultimately suffer from some kind of qubit relaxation during the readout process. The uncontrolled losses in the qubit environment are partly responsible for this relaxation and hence further research in improving the quality of the materials used in fabrication is required. Nevertheless, there is still scope for improvement in readout design which might enable one to achieve 100% readout contrast. A two stage readout process where a weak, yet projective measurement is followed by a stronger amplification stage to improve the signal to noise

ratio seems to be a promising way for solving the problem. An example would be to measure a qubit coupled to a linear resonator with a few photons and following it up with a non-linear system like the JBA or a parametric amplifier for further gain.

Chapter 7

Quantum escape and parametric amplification:

Theory

In this chapter, we will address the problem of transitions between the metastable states of the JBA in the quantum regime. In the classical regime, the transitions are governed by an activation process with thermal noise activating the system over an effective barrier (see section 2.3.2 and ref. [27]). Now, we want to consider the case as $T \rightarrow 0$ [49, 50]. What mechanism governs the transitions as $T \rightarrow 0$? Is there tunneling between the metastable states or does a different mechanism exist? More importantly, what sets the classical to quantum crossover temperature? Borrowing ideas from the theory of macroscopic quantum tunnelling (MQT) in current biased Josephson junctions [95, 48], we can make an educated guess that the crossover temperature must be related to the plasma frequency of the oscillator. We will try to answer these questions in the next few sections.

We will begin by discussing Input-Output theory (see [96] and reference therein) and how we can use it to compute escape rates out of metastable states. We will treat

the prototypical case of a harmonic oscillator coupled to a transmission line and as an example, apply the results to compute escape rates for a DC current biased Josephson junction. Following that, we will compute the transition rates in the JBA. The calculation is based on treating the JBA as a doubly degenerate parametric amplifier [9]. We can then borrow well known techniques from the quantum optics community for analyzing parametric processes and results in a much clearer understanding of the escape dynamics in this non-equilibrium system. We will treat the JBA as a classical system driven by quantum noise. In this treatment, we can calculate the transition rates at any temperature, i.e., we can discuss both classical and quantum behavior in the same formalism. The gain and noise performance of the JBA as a parametric amplifier will then be computed. We will conclude with a discussion on generating squeezed states of light using the JBA.

7.1 Input-Output theory

We will consider a harmonic oscillator coupled to a transmission line to develop the concepts of Input-Output theory (IOT). We can always reduce the problem under consideration to this case. IOT deals with the relationship between the fields entering the oscillator (input field), the fields inside the oscillator (internal field) and the fields exiting the oscillator (output field)¹. It is reminiscent of the scattering theory of microwave circuits where one relates the outgoing and incoming waves from an arbitrary circuit with a scattering matrix. But IOT goes further than that. It allows us to calculate the quantum statistical properties of the internal and the output fields, given the input field. Furthermore, the commutation relations that the field operators

¹The system does not have to be a harmonic oscillator to use IOT.

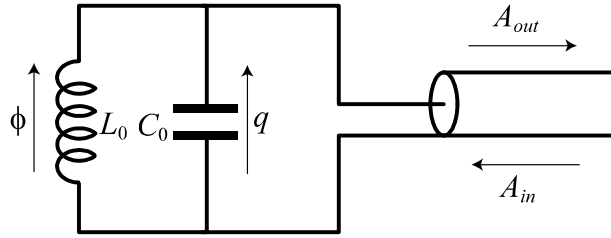


Figure 7.1: The prototypical system considered for analysis in this chapter is a harmonic oscillator couple to a transmission line. The example shown here is an electrical LC oscillator. The flux (ϕ) across the inductor and the charge (q) on the capacitor can be used to describe the dynamics of the oscillator. A_{in} and A_{out} represent incoming and outgoing signals.

must satisfy, place strict constraints on the quantum behavior of the oscillator. This is a very interesting and important aspect of this treatment. We describe our system with classical equations of motion but then subject it to quantum fields (e.g. quantum noise in the transmission line coupled to the harmonic oscillator). This results in the system displaying quantum properties. A very nice review of these ideas is contained in the chapter on IOT in ref. [96].

7.1.1 Harmonic oscillator coupled to a transmission line

Fig. 7.1 shows the prototypical system under consideration. The oscillator is represented as an electrical oscillator consisting of a parallel combination of an inductor (L_0) and a capacitor (C_0). The canonically conjugate variables, flux (ϕ) across the inductor and charge (q) on the capacitor can be used to describe the dynamics of the oscillator. It is coupled to a 1-D transmission line with electromagnetic waves travelling in both directions. The idea of representing signals on a transmission line using incoming and outgoing waves is quite common in microwave engineering.

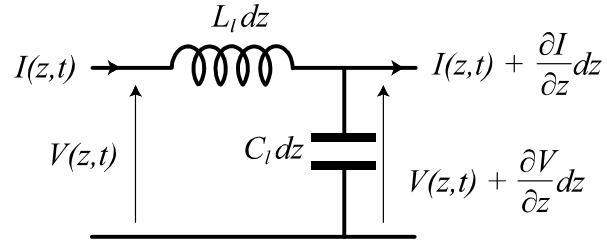


Figure 7.2: A section of a transmission line of length dz is represented as a series inductance $L_l dz$ and a capacitance $C_l dz$ to ground. L_l and C_l are the inductance and capacitance per unit length of the transmission line.

One can derive the wave equation for voltage and current waves by treating the dissipationless transmission line as an infinite sequence of circuits consisting of inductors and capacitors. Fig.7.2 illustrates this idea, where L_l and C_l are the inductance and capacitance per unit length of the transmission line and dz is the length of the section under consideration. The resulting wave equations for the voltage (V) and current (I) are as follows:

$$\frac{\partial V(z, t)}{\partial z} = -L_l \frac{\partial I(z, t)}{\partial t} \quad (7.1a)$$

$$\frac{\partial I(z, t)}{\partial z} = -C_l \frac{\partial V(z, t)}{\partial t} \quad (7.1b)$$

The characteristic impedance of the transmission line is given by $Z_c = \sqrt{L_l/C_l}$ and the velocity of the waves is given by $v = \sqrt{1/L_l C_l}$. The solution to the above wave equations can be written as:

$$V(z, t) = \sqrt{Z_c} \left(A_{out} \left(t - \frac{z}{v} \right) + A_{in} \left(t + \frac{z}{v} \right) \right) \quad (7.2a)$$

$$I(z, t) = \frac{1}{\sqrt{Z_c}} \left(A_{out} \left(t - \frac{z}{v} \right) - A_{in} \left(t + \frac{z}{v} \right) \right) \quad (7.2b)$$

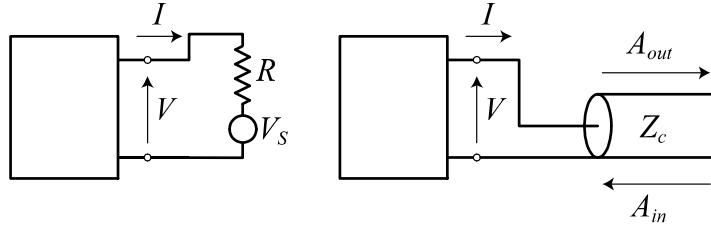


Figure 7.3: The left panel shows a circuit driven by a voltage source V_s with source impedance R . The right panel shows the same circuit now connected to a transmission line with incoming (A_{in}) and outgoing (A_{out}) waves. The two cases depicted represent the same situation if we make the identification $Z_c = R$ and $V_s = 2\sqrt{R}A_{in}(t)$.

The voltage and current along the line can be represented as a linear superposition of waves travelling in opposite directions. This gives now a concrete meaning to what these waves represent. They could represent a signal launched on the transmission line in order to drive the oscillator or they could represent the thermal/quantum fluctuations in the transmission line. Note that the wave amplitudes A_{out} and A_{in} have dimensions of square root of power. The total power crossing a point in the transmission line is given by $(|A_{in}|^2 - |A_{out}|^2) / 2$.

Fig. 7.3 gives an example of an arbitrary circuit driven by a voltage source $V_s(t)$ with internal resistance R . The right panel shows the same circuit connected to a transmission line of characteristic impedance $Z_c = R$ with incoming and outgoing waves.

The two cases depicted are equivalent if we make the identification $Z_c = R$ and $V_s(t) = 2\sqrt{R}A_{in}(t)$. If we set $z = 0$ (the location of the circuit) in equations 7.2a and 7.2b, the outgoing wave computes to:

$$A_{out}(t) = \frac{V(t)}{\sqrt{Z_c}} - A_{in}(t) \quad (7.3)$$

These relations are derived by imposing the appropriate boundary conditions on the solutions given by equations 7.2a and 7.2b. We can now compute the response of the system given the input field. Equation 7.3 is the essence of IOT. It relates the input field A_{in} , the internal field $V(t)$, and the output field A_{out} . In the above example, the voltage source V_s should not only represent the intended drive signal, but also the Nyquist noise of the resistance R , in order to completely describe the problem. In the examples that follow, we will separate any intentional drive signal (classical) from the noise so that A_{in} only represents the noise, which we will describe quantum mechanically from now on.

We introduce quantum mechanics into the picture by quantizing the fields on the transmission line and representing them in terms of creation ($a_{in}^\dagger[\omega]$) and annihilation ($a_{in}[\omega]$) operators of the quantum modes of the transmission line:

$$A_{in}(t) = \frac{1}{2\pi} \left(\int_0^\infty d\omega \sqrt{\frac{\hbar\omega}{2}} \left(a_{in}[\omega] \exp(-i\omega t) + a_{in}^\dagger[\omega] \exp(i\omega t) \right) \right) \quad (7.4)$$

The field operators $a_{in}[\omega]$ and $a_{in}^\dagger[\omega]$ satisfy the standard commutation relations for 1-D scalar fields given below, where we have used the conventions described in [19, 20] but we restrict ω to only have positive values:

$$\begin{aligned} [a_{in}[\omega], a_{in}^\dagger[\omega']] &= 2\pi\delta(\omega - \omega') \\ [a_{in}[\omega], a_{in}[\omega']] &= [a_{in}^\dagger[\omega], a_{in}^\dagger[\omega']] = 0 \\ \langle \{ a_{in}[\omega], a_{in}^\dagger[\omega'] \} \rangle &= S_{aa}(\omega) 2\pi\delta(\omega - \omega') \\ S_{aa}(\omega) &= \coth\left(\frac{\hbar\omega}{2k_B T}\right) \end{aligned} \quad (7.5)$$

where $S_{aa}(\omega)$ is called the symmetrized spectrum and is equal to the sum of the emission and absorption spectrum of $a_{in}[\omega]$. The emission and absorption spectrum are given by $\langle a_{in}[\omega]a_{in}^\dagger[\omega] \rangle$ and $\langle a_{in}^\dagger[\omega]a_{in}[\omega] \rangle$ respectively.

We are now ready to analyze the properties of our system. The equation of motion of a damped harmonic oscillator using the flux (ϕ) as the dynamical variable is:

$$\frac{d^2\phi}{dt^2} + \frac{1}{RC_0} \frac{d\phi}{dt} + \omega_0^2\phi = \frac{2}{C_0\sqrt{R}} A_{in}(t) \quad (7.6)$$

where $\omega_0 = 1/\sqrt{L_0C_0}$ is the plasma frequency of the oscillator and the right hand side of the equation represents the quantum noise field driving the oscillator. We go into the frequency domain by Fourier transforming the above equation which results in the following equations for $\phi[\omega]$ and its Hermitian conjugate $\phi^\dagger[\omega]$:

$$\begin{aligned} \phi[\omega] &= \frac{2}{C_0} \sqrt{\frac{\hbar\omega}{2R}} \frac{a_{in}[\omega]}{(-\omega^2 - i\omega/RC_0 + \omega_0^2)} \\ \phi^\dagger[\omega] &= \frac{2}{C_0} \sqrt{\frac{\hbar\omega}{2R}} \frac{a_{in}^\dagger[\omega]}{(-\omega^2 + i\omega/RC_0 + \omega_0^2)} \end{aligned} \quad (7.7)$$

The above equations are the frequency domain solutions for the oscillator flux subject to quantum noise fields. Using these solutions, it can be shown that the commutation relation between the conjugate variables ϕ and $q = C_0(d\phi/dt)$ is given by

$$[\phi, q] = i\hbar \quad (7.8)$$

We see that the conjugate variables satisfy the correct quantum mechanical relation. We can also compute the zero-point energy in the oscillator at $T = 0$ in the limit of

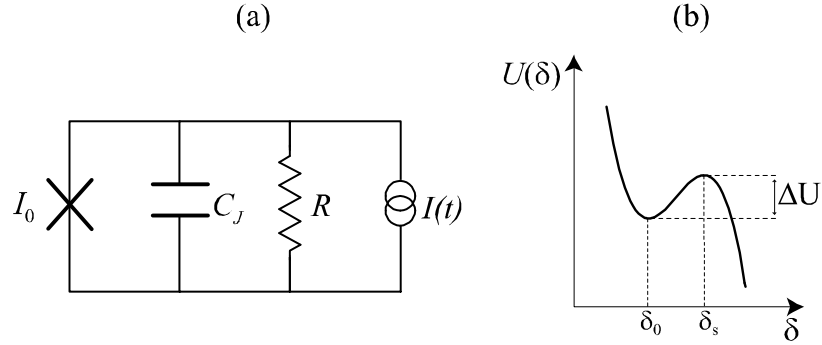


Figure 7.4: Panel (a) shows a Josephson junction with critical current I_0 , capacitance C_J driven by a DC current source with source impedance R . Panel (b) shows the potential energy profile when the circuit is biased with a current slightly less than the critical current.

$Q \rightarrow \infty$:

$$E_0 = \frac{\langle \phi^2 \rangle}{2L_0} + \frac{\langle q^2 \rangle}{2C_0} = \frac{\hbar\omega_0}{2} \quad (7.9)$$

which is the correct quantum mechanical result.

7.1.2 Escape in current-biased Josephson junction

Armed with our new tools, we will now analyze the well known problem of escape from the zero voltage metastable state in a current biased Josephson junction [97]. This example will demonstrate the application of IOT to escape physics. Fig.7.4a shows the familiar schematic of a Josephson junction biased with a current source $I(t)$. I_0 is the critical current of the junction, C_J is the shunting capacitance, R is the source impedance and $I(t) = I_{DC}$ is the DC current bias.

We note that the main difference between this case and the one we analyzed in the previous section, is the non-linearity of the junction and the DC current bias. The current bias tilts the cosine potential of the junction, and the Nyquist noise from

the resistor causes the junction to switch from the zero voltage state. We include the effect of the classical DC current drive in the classical equation of the motion for the system and replace the resistor by a transmission line of characteristic impedance R . Representing the quantum noise as an incoming field as before, we get the following equation:

$$\varphi_0 C_J \frac{d^2 \delta}{dt^2} + \frac{\varphi_0}{R} \frac{d\delta}{dt} + I_0 \sin(\delta) - I_{DC} = \frac{2}{\sqrt{R}} A_{in}(t) \quad (7.10)$$

where $\delta = \phi/\varphi_0$ is the superconducting phase difference across the junction and φ_0 is the reduced flux quantum. In the absence of noise, the junction will develop a phase $\delta = \delta_0 = \sin^{-1}(I_{DC}/I_0)$. This is the metastable state of the junction. The fluctuations in δ induced by the incoming noise cause transitions out of this metastable state. The escape happens when δ fluctuates from the equilibrium point δ_0 and reaches δ_s . This point δ_s , where $U(\delta)$ has a maximum as shown Fig. 7.4b, corresponds to a saddle point in the phase space $(\delta, \dot{\delta})$ and hence is known as the saddle point. In order to compute the fluctuations induced in δ due to the noise, we expand the above equation around the equilibrium point $\delta = \delta_0$, i.e., we write $\delta = \delta_0 + x$, where x is our new dynamical variable. Substituting this in the above equation and retaining only terms up to first order in x , we get:

$$\frac{d^2 x}{dt^2} + \frac{1}{RC_J} \frac{dx}{dt} + \tilde{\omega}_p^2 x = \frac{2\omega_p^2}{I_0 \sqrt{R}} A_{in}(t) \quad (7.11)$$

where $\omega_p = \sqrt{I_0/(\varphi_0 C_J)}$ is the bare plasma frequency of the junction, while $\tilde{\omega}_p = \omega_p(1 - (I/I_{DC})^2)^{1/4}$ is the reduced plasma frequency. This is the step where we have reduced the problem to an effective harmonic oscillator driven by quantum noise, as can be seen by comparing equation (7.11) with equation (7.6) and noting that

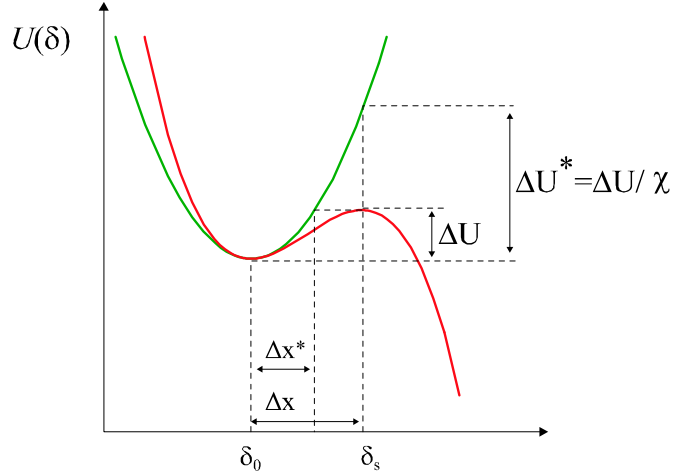


Figure 7.5: The tilted washboard potential of a Josephson junction biased with a DC current $I_{DC} \lesssim I_0$, is shown here in the cubic approximation (red). The potential representing the harmonic approximation is shown in green. δ_0 and δ_s are the equilibrium and the saddle points respectively. Also illustrated is the overestimation of the barrier height (ΔU^* v.s. ΔU) in the harmonic approximation. The correction factor χ can be found by using a value Δx^* at which the harmonic approximation gives the same barrier height as in the cubic case, and computes to $\chi = 1/3$.

$x = \phi/\varphi_0$. The expression for the full potential for the DC biased junction is given by:

$$U(\delta) = -\varphi_0 I_0 [\cos(\delta) + \delta (I_{DC}/I_0)] \quad (7.12)$$

In the limit when $I_{DC}/I_0 \simeq 1$, the tilted potential can be well approximated for $\delta \simeq \delta_0$ by a cubic potential. Fig. 7.5 shows the cubic potential (red) and the harmonic approximation (green).

An important quantity for computing the escape probability is the distance from the equilibrium point (δ_0) to the saddle point (δ_s). This is given by:

$$\Delta x = \delta_s - \delta_0 = 2\sqrt{2}\sqrt{1 - I_{DC}/I_0} \quad (7.13)$$

Using the result of equation (7.7), we can compute the variance of x as:

$$\sigma_x^2 = \frac{1}{2\pi} \int_0^\infty S_{xx}(\omega) d\omega = \left(\frac{2\Gamma\omega_p^2}{E_J} \right) \frac{1}{2\pi} \int_0^\infty \frac{2\hbar\omega S_{aa}(\omega) d\omega}{\left((\tilde{\omega}_p^2 - \omega^2)^2 + \omega^2\Gamma^2 \right)} \quad (7.14a)$$

$$= \left(\frac{k_B T}{E_J} \right) \left(1 - \frac{I^2}{I_{DC}^2} \right)^{-1/2}, \quad k_B T \gg \hbar\tilde{\omega}_p \text{ (classical limit)} \quad (7.14b)$$

$$= \left(\frac{\hbar\tilde{\omega}_p}{2E_J} \right) \left(1 - \frac{I^2}{I_{DC}^2} \right)^{-1/2}, \quad k_B T \ll \hbar\tilde{\omega}_p, \text{ (quantum limit), } Q \gg 1 \quad (7.14c)$$

where $E_J = \varphi_0 I_0$ is the Josephson energy of the junction and $\Gamma = 1/2RC_J$ is the amplitude damping coefficient.

The escape rate in general can be written in the following form

$$\Gamma_{esc} = \frac{\omega_a}{2\pi} \exp\left(-\frac{\Delta U_{esc}}{k_B T_{esc}}\right) \quad (7.15)$$

where ΔU_{esc} is the barrier height, T_{esc} is the escape temperature and characterizes the intensity of fluctuations in the system, and $\omega_a/2\pi$ is the attempt frequency and characterizes the time scale over which escape events occur. Note that changes to the escape rate are dominated by the exponential factor. We will only compute this exponent

$$P_{esc} = \exp\left(-\frac{\Delta U_{esc}}{k_B T_{esc}}\right) \quad (7.16)$$

and call P_{esc} the escape probability. This can be thought of as the probability to escape per attempt while $\omega_a/2\pi$ gives the number of attempts per unit time. We can now define the escape probability for our case as

$$P_{esc}^{DC} = \exp\left(-\chi \frac{\Delta x^2}{2\sigma_x^2}\right) \quad (7.17)$$

which is the probability that x will fluctuate by Δx given the variance σ_x^2 of its distribution. Note how Δx^2 plays the role of ΔU_{esc} and σ_x^2 plays the role of T_{esc} . The factor χ in the exponent is a scaling constant which accounts for the overestimation of the barrier height in the harmonic approximation for the potential. This is illustrated in Fig. 7.5. Instead of using Δx , we can use the value Δx^* for which the harmonic approximation gives the same barrier height as the cubic potential. We compute the value of χ to be

$$\chi = \frac{1}{3}. \quad (7.18)$$

Note that this is a general result for the harmonic approximation of the cubic potential. We will use this value of χ when we compute the escape from the metastable states of the JBA in the next section. Computing P_{esc}^{DC} using equation (7.17), we get in the classical limit ($k_B T \gg \hbar \tilde{\omega}_p$)

$$P_{esc}^{DC} = \exp \left(-\frac{4\sqrt{2}}{3} \frac{E_J}{k_B T} \left(1 - \frac{I_{DC}}{I_0} \right)^{3/2} \right). \quad (7.19)$$

The actual expression for the escape rate for the DC current biased Josephson junction in the classical limit, is given by [97]

$$\Gamma_{esc}^{DC} = \frac{\omega_p}{2\pi} (1 - I^2/I_{DC}^2)^{-1/2} \exp \left(-\frac{4\sqrt{2}}{3} \frac{E_J}{k_B T} \left(1 - \frac{I_{DC}}{I_0} \right)^{3/2} \right). \quad (7.20)$$

Comparing the above two equations, we can see that the exponents are identical. It is important to note that in the harmonic approximation, we are analyzing the system only for small fluctuations around the metastable minimum, while an escape event is essentially a large fluctuation. Even though the average fluctuations are small, there

is always a small probability for the system to make a large fluctuation leading to an escape event. The use of the harmonic approximation is justified because it does not significantly affect the spectrum of the fluctuations as the system is predominantly found near the minimum of the potential. The procedure is valid provided we work with small escape probabilities.

In the quantum regime $k_B T \ll \hbar \tilde{\omega}_p$, the escape out of the metastable state of the DC current biased junction takes place via quantum tunneling. This process is called Macroscopic Quantum Tunnelling (MQT) since it involves the tunneling of a macroscopic quantity - the phase of the Josephson junction. In this regime, the escape rate [95, 48] is given (in the high Q limit) by

$$\Gamma_{esc}^{DC-MQT} = a_p \frac{\omega_p}{2\pi} (1 - I^2/I_{DC}^2)^{-1/2} \exp\left(-\frac{4\sqrt{2}}{3} \frac{E_J}{\hbar \tilde{\omega}_p / 7.2} \left(1 - \frac{I_{DC}}{I_0}\right)^{3/2}\right) \quad (7.21)$$

where a_p is a prefactor of order unity to account for finite damping. We note that the escape rate is now a constant independent of temperature with the effective escape temperature given by $\hbar \tilde{\omega}_p / 7.2 k_B$. We can extend the method outlined in this section to compute this result also. Note that the expression for σ_x^2 in the quantum limit (7.14c) becomes independent of T and related to $\tilde{\omega}_p$. But now these fluctuations in x are arising from "virtual" zero point fluctuations and hence cannot activate over the barrier. For tunneling through the barrier, we could use a different effective Δx in the harmonic approximation to reproduce the result of equation 7.21.

We now have a method for computing exponents in the escape rates. In the next section, we will apply this technique to the case of an RF driven Josephson oscillator. We will be particularly interested in the quantum limit as $T \rightarrow 0$, and we will compare

the results with the MQT case.

7.2 Escape dynamics in the JBA

We will begin by describing the JBA as a parametric amplifier. We then proceed to describe the system in the harmonic approximation so that we can use the techniques developed in the previous section to compute escape rates.

7.2.1 Parametric amplifier description of the JBA

We start with the classical equation of motion describing the driven, non-linear Josephson oscillator. The initial part of this section reproduces some of the calculations done in section 2.2 to keep this chapter self-contained. We will use a slightly different terminology as compared to chapter 2 to simplify calculations. We reproduce equation 2.1 below, the starting point of our calculations:

$$C_S \varphi_0 \frac{d^2 \delta(t)}{dt^2} + \frac{\varphi_0}{R} \frac{d\delta(t)}{dt} + I_0 \sin(\delta(t)) = I(t) \quad (7.22)$$

where C_S is the total capacitance shunting the junction², R is the impedance of the transmission line to which the oscillator is coupled, I_0 is the critical current of the junction, δ is the superconducting phase across the junction, φ_0 is the reduced flux quantum and $I(t)$ is now the RF drive current. Rewriting the above equation for a harmonic drive at frequency ω_d , and retaining only the first non-linear term in the

²We have ignored the junction capacitance C_J since $C_J \ll C_S$.

expansion of the sine term, we get:

$$\frac{d^2\delta(t)}{dt^2} + 2\Gamma\frac{d\delta(t)}{dt} + \omega_p^2\left(\delta(t) - \frac{\delta(t)^3}{6}\right) - \omega_p^2\frac{I_{RF}}{I_0}\cos(\omega_d t) = \frac{2}{C_S\varphi_0\sqrt{R}}A_{in}(t) \quad (7.23)$$

where $\omega_p = (I_0/C_S\varphi_0)^{1/2}$ is the plasma frequency of the oscillator (for small oscillations), $\Gamma = 1/(2RC_S)$ is the damping rate of the oscillation amplitude, and A_{in} is the quantum noise felt by the oscillator written in field representation. As explained in the previous section, we have separated the classical harmonic drive ($I_{RF}\cos(\omega_d t)$) from the input field (A_{in}) which only represents the quantum noise. In order to compute the steady state classical solution, we set A_{in} to zero and use the technique of harmonic balance, i.e., we assume a steady state harmonic solution at frequency ω_d of the form³:

$$\delta_c(t) = \delta_{c\parallel}\cos(\omega_d t) + \delta_{c\perp}\sin(\omega_d t) \quad (7.24)$$

where $\delta_{c\parallel}$ and $\delta_{c\perp}$ are the in-phase and quadrature-phase components of the classical solution. We substitute this solution into the differential equation and equate terms at frequency ω_d . After eliminating terms at frequencies higher than ω_d , we get two algebraic equations for $\delta_{c\parallel}$ and $\delta_{c\perp}$:

$$\begin{aligned} \frac{f_d}{Q}\delta_{c\parallel} + f_d^2\delta_{c\perp} + \delta_{c\perp}\left(\frac{\delta_{c\perp}^2 + \delta_{c\parallel}^2}{8} - 1\right) &= 0 \\ \frac{f_d}{Q}\delta_{c\perp} - f_d^2\delta_{c\parallel} - \delta_{c\parallel}\left(\frac{\delta_{c\perp}^2 + \delta_{c\parallel}^2}{8} - 1\right) - i_{RF} &= 0 \end{aligned} \quad (7.25a)$$

³We use the quadrature amplitude representation as described in 2.2.2 instead of the complex amplitudes of 2.2.1.

where $Q = RC_S\omega_p$ is the quality factor of the oscillator, $f_d = \omega_d/\omega_p$ is the dimensionless drive frequency and $i_{RF} = I_{RF}/I_0$ is the dimensionless drive current. The above equations have three solutions in general. In the bistable regime, there are three real valued solutions. The solution with the smallest (small amplitude state) and the largest (large amplitude state) value of $\delta_{c\parallel}^2 + \delta_{c\perp}^2$ represent the two metastable solutions, while the third solution is the saddle point separating the two metastable states. Fig.7.6 shows the solutions for some typical parameters, where $\delta_c^{\max} = \sqrt{\delta_{\parallel}^2 + \delta_{\perp}^2}$. The different curves correspond to different drive current amplitudes. We note that for small values of drive current, there is only one solution, while above a certain drive amplitude, three solutions are possible for certain drive frequencies.

Now we incorporate the effect of noise and do a perturbation expansion (harmonic approximation) around the classical solution, i.e., we look for solutions of the type:

$$\delta(t) = \delta_c(t) + \delta_q(t) \quad (7.26)$$

where $\delta_c(t)$ is the steady state classical solution in the absence of noise, while $\delta_q(t)$ is the quantum part of the solution in the presence of thermal/quantum noise. By substituting the above solution into differential equation(2.2), and retaining terms only up to first order in $\delta_q(t)$, we get the differential equation describing the dynamics of $\delta_q(t)$ in the harmonic approximation:

$$\frac{d^2\delta_q(t)}{dt^2} + 2\Gamma\frac{d\delta_q(t)}{dt} + \omega_0^2(|\delta_c^{\max}|^2, t)\delta_q(t) = \frac{2}{C_J\varphi_0\sqrt{R}}A_{in}(t) \quad (7.27)$$

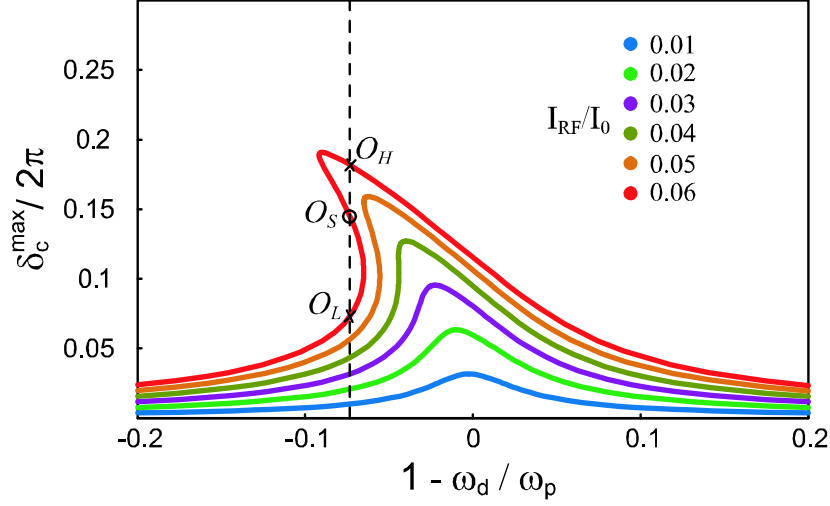


Figure 7.6: Steady state solutions of a driven Josephson oscillator as a function of relative detuning $1 - \omega_d/\omega_p$ and drive amplitude I_{RF}/I_0 . The resonance curves bend over as the drive amplitude is increased and become multi-valued for certain parameters. In this regime, for a given drive frequency and amplitude, there are two stable solutions (\times) separated by an unstable saddle point (\circ). Maximum response for small amplitude oscillations occurs at $\omega_d = \omega_p$. For higher drive amplitudes, maximum response occurs at frequencies below ω_p . The sign of the first non-linear term determines the direction of this shift (which is negative here).

where

$$\omega_0^2(|\delta_c|^2, t) = \omega_p^2 \left(1 - |\delta_c^{\max}|^2/4\right) \left(1 + \frac{|\delta_c^{\max}|^2}{4 - |\delta_c^{\max}|^2} \cos(2\omega_d t - 2\theta)\right) \quad (7.28)$$

$$\tan \theta = \delta_{c\perp}/\delta_{c\parallel}$$

We note that equation 7.27 represents a parametrically driven harmonic oscillator, i.e., a harmonic oscillator with a time varying plasma frequency $\omega_0^2(|\delta_c^{\max}|^2, t)$. The frequency of the parametric drive (7.28) is twice the original drive frequency ω_d , while the magnitude and phase of the parametric drive depends on the magnitude

and phase of the classical solution δ_c . This demonstrates that the system behaves like a parametric amplifier when biased near the bifurcation point, resulting in the amplification of quantum noise (A_{in}) which is feeding the oscillator. It is this amplification of quantum noise we are interested in studying. In the presence of this amplified quantum noise, the steady-state solutions become metastable and the system can make transitions from one steady state to another. By solving the above equation, we can compute the fluctuations felt by the system and hence compute the transition rates between the metastable states. In particular, we are interested in the transition from the low amplitude state to the high amplitude state, the quantity we usually measure in experiments. Also, when implemented as a qubit readout, the JBA is biased near this transition and the width of this transition sets the ultimate sensitivity of the JBA readout. Note that the above equation for the parametrically driven oscillator does not display bistability due to the fact that we have only retained the terms linear in $\delta_q(t)$.

7.2.2 Solutions in the frequency domain

The solutions to the differential equation (7.27) are easily found by going to the frequency domain. We define the Fourier transform of $\delta_q(t)$ as $\delta_q[\omega]$ where the two are related as given below:

$$\delta_q(t) = \frac{1}{2\pi} \int_0^\infty (\delta_q[\omega] \exp(-i\omega t) + \delta_q^\dagger[\omega] \exp(i\omega t)) d\omega$$

Note again that $\omega \geq 0$. Taking the Fourier transform of equation(7.27), we get

$$\begin{aligned} (\omega_p^2(1-\varepsilon) - \omega^2 - i2\Gamma\omega) \delta_q[\omega] - \frac{\omega_p^2\varepsilon}{2} \exp(-2i\theta)\delta_q^\dagger[2\omega_d - \omega] \\ = \frac{4\Gamma\sqrt{R}}{\varphi_0} \sqrt{\frac{\hbar\omega}{2}} a_{in}[\omega] \end{aligned} \quad (7.29)$$

where $\varepsilon = \frac{\delta_c^2}{4}$, and $\sqrt{\hbar\omega/2}a_{in}[\omega]$ is the Fourier representation of $A_{in}[t]$. We have ignored terms at frequencies which are a multiple of ω_d . Note how the above equation couples the creation and annihilation operator for δ_q , a characteristic feature of parametrically driven systems. After making the rotating wave approximation ($\omega_p + \omega \approx 2\omega_p$, $\omega/\omega_p \approx 1$) for the coefficient of $\delta_q[\omega]$ in equation(7.29), and a change of variable $\delta_q[\omega] = \sqrt{\hbar\omega/\Gamma E_J}x[\omega]$, we get after simplifying

$$\left(\frac{\omega_p - \omega}{\Gamma} - \frac{\omega_p\varepsilon}{2\Gamma} - i \right) x[\omega] - \frac{\omega_p\varepsilon}{4\Gamma} \exp(-2i\theta)x^\dagger[2\omega_d - \omega] = a_{in}[\omega] \quad (7.30)$$

We now make the following transformations into dimensionless variables

$$\frac{\omega_p - \omega}{\Gamma} - \frac{\omega_p\varepsilon}{2\Gamma} = \frac{\omega_p - \omega_d}{\Gamma} - \frac{\omega - \omega_d}{\Gamma} - \frac{\omega_p\varepsilon}{2\Gamma} = \Omega - f - 2\epsilon \quad (7.31)$$

where

$$\begin{aligned} \Omega &= \frac{\omega_p - \omega_d}{\Gamma} \\ f &= \frac{\omega - \omega_d}{\Gamma} \\ \epsilon &= \frac{\omega_p\varepsilon}{4\Gamma} \end{aligned} \quad (7.32)$$

Using the above transformation we can now write 7.30 as

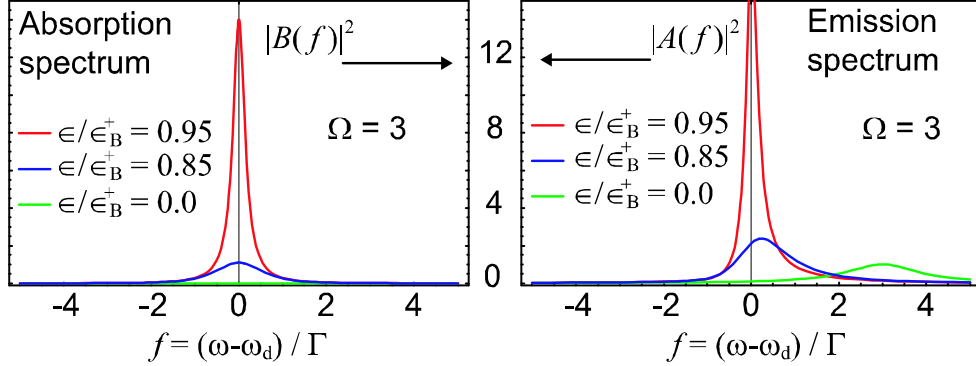


Figure 7.7: Gain functions $|A(f)|^2$ and $|B(f)|^2$ are plotted for $\epsilon/\epsilon_B^+ = 0.0, 0.85, 0.95$ where ϵ_B^+ is the value of ϵ at the upper bifurcation point. The functions $|A(f)|^2$ and $|B(f)|^2$ represent the emission and absorption spectrum of x_q at $T = 0$. The green curve for $\epsilon/\epsilon_B^+ = 0.0$ is the result for a harmonic oscillator subject to quantum noise only which has a finite emission spectrum. As the system is driven to the bifurcation point, the absorption spectrum starts to grow due to parametric amplification of quantum noise. In a sense, the spectrum starts to look classical with equal values for emission and absorption.

$$(\Omega - 2\epsilon \mp f - i) x[\pm f] - \epsilon \exp(-2i\theta) x^\dagger[\mp f] = a_{in}[f] \quad (7.33)$$

where the dimensionless frequency f refers to an offset from the drive frequency ω_d and can have negative values, i.e., $\pm f \leftrightarrow \omega_d \pm \Gamma f$. The above equation along with its Hermitian conjugate forms a set of four coupled algebraic equations. The solution can be written as follows

$$x[\pm f] = A(\pm f) a_{in}[\pm f] + B(\pm f) a_{in}^\dagger[\mp f] \quad (7.34)$$

where the functions $A(f)$ and $B(f)$ are given by

$$A(f) = -\frac{\Omega - 2\epsilon + f + i}{\epsilon^2 + (i + f)^2 - (\Omega - 2\epsilon)^2} \quad (7.35a)$$

$$B(f) = -\frac{\epsilon \exp(2i\theta)}{\epsilon^2 + (i + f)^2 - (\Omega - 2\epsilon)^2} \quad (7.35b)$$

The function $A(f)$ links the annihilation operators of x with the annihilation operators of a_{in} , while $B(f)$ links the annihilation operators of x with the creation operators of a_{in} . This connection between creation and annihilation operators is a characteristic feature of any amplification process. Fig.7.7 shows a plot of the functions $|A(f)|^2$ and $|B(f)|^2$ which represent the emission and absorption spectrum of x_q for $T = 0$. The different curves correspond to different drive strengths approaching the upper bifurcation point. Note how the peak in both functions shifts towards the drive frequency and grows in magnitude as the bifurcation point is approached. This indicates an increase in amplification as one approaches the bifurcation point. The green curve for $\epsilon/\epsilon_B^+ = 0.0$ represents the harmonic oscillator with no parametric driving and hence only the emission spectrum is finite, reflecting the spectrum of quantum noise at $T = 0$. In section 7.3, we will discuss the operation of the JBA as a parametric amplifier and we will see how the functions $A(f)$ and $B(f)$ determine the gain and noise performance of the amplifier.

7.2.3 Quadrature variables

The escape dynamics for this problem can be described best in the quadrature variable space. We will separate $x(t)$ into its two quadrature components as we did for the

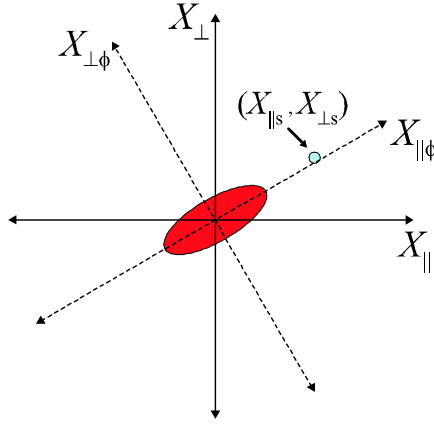


Figure 7.8: The schematic illustrates the noise dynamics in the quadrature variable space. $X_{||}$ and X_{\perp} are the original axes used to describe the classical solutions with $(0, 0)$ being the low amplitude state and $(X_{||s}, X_{\perp s})$ the saddle point. The noise ellipse (red) is drawn with its major and minor axis representing the standard deviation of the amplified and squeezed quadrature respectively. The ellipse is also drawn in a rotated coordinate system $(X_{||\phi}, X_{\perp\phi})$ where the cross-correlations between the two quadratures is imaginary. When biased close to the bifurcation point, the saddle point tends to fall along the major axis of the noise ellipse, allowing us to ignore the other quadrature for computing the escape probability (1-D approximation).

classical solution in equation (7.24):

$$x(t) = X_{||\phi}(t) \cos(\omega_d t + \phi) + X_{\perp\phi}(t) \sin(\omega_d t + \phi) \quad (7.36)$$

The 2D coordinate system for the noise quadratures is rotated by angle ϕ from the one used for the classical solution. This is because we are trying reduce the problem to 1D and for a certain angle ϕ , the motion along one of the quadratures can be ignored as explained below. In Fourier domain, we get:

$$X_{\phi}[f] = \exp(-i\phi) x[f] + \exp(i\phi) x^{\dagger}[-f] \quad (7.37)$$

where X_ϕ is the quadrature rotated by angle ϕ and the other quadrature is found by adding $\pi/2$ to the value of ϕ . We will then find the angle ϕ , along which the fluctuations are maximum (the amplified quadrature). The fluctuations in the other quadrature are de-amplified and the two quadratures have an imaginary correlation function. When one is biased very close to the bifurcation point, this angle will roughly correspond to the direction in which the saddle point lies in the quadrature space. This allows us to neglect the de-amplified quadrature (1D approximation). We can then compute the distance to the saddle point and the variance of fluctuations in $X_\phi[f]$ for this angle, the two quantities needed to compute the escape probability. Fig. 7.8 illustrates these ideas. X_\parallel and X_\perp are the original quadrature axes while $X_{\parallel\phi}$ and $X_{\perp\phi}$ are the rotated axes. The red ellipse is drawn with its major and minor axis given by the standard deviation of the amplified and de-amplified quadratures respectively. The blue circle represents the saddle point which is shown to lie (almost) along the axis corresponding to the amplified quadrature.

7.2.4 Escape rates

We need to compute the variance of X_ϕ and then find the angle ϕ which maximizes it. We reproduce here the commutation relations for the field operators $a_{in}[f]$, but

for dimensionless frequency f

$$\begin{aligned}
[a_{in}[f], a_{in}^\dagger[f']] &= \frac{2\pi}{\Gamma} \delta(f - f') \\
[a_{in}[f], a_{in}[f']] &= [a_{in}^\dagger[f], a_{in}^\dagger[f']] = 0 \\
\langle \{a_{in}[f], a_{in}^\dagger[f']\} \rangle &= S_{aa}(f) \frac{2\pi}{\Gamma} \delta(f - f') \\
S_{aa}(f) &\simeq S_{aa}(\omega = \omega_d) = \coth\left(\frac{\hbar\omega_d}{2k_B T}\right)
\end{aligned} \tag{7.38}$$

Note that we have approximated $\omega = \omega_d$ in $S_{aa}(f)$. This is valid because the spectrum for dynamical variables of the system have a sharp peak at $\omega \sim \omega_d$ but the function $S_{aa}(\omega)$ varies smoothly in this range. This is another manifestation of the rotating wave approximation. The anticommutator in the frequency domain for $X_\phi[f]$ gives us the spectrum $S_{X_\phi X_\phi}(f)$ where

$$S_{X_\phi X_\phi}(f) \frac{2\pi}{\Gamma} \delta(f - f') = \langle \{X_\phi[f], X_\phi^\dagger[f']\} \rangle \tag{7.39}$$

Using the commutation relations for the field operators (7.38), we compute the spectrum of fluctuations to be:

$$S_{X_\phi X_\phi}(f) = S_{aa}(f) \left(\begin{array}{l} (|A(-f)|^2 + |A(f)|^2 + |B(-f)|^2 + |B(f)|^2) + \\ 2 \operatorname{Re}(\exp(-2i\phi) (A(f) B(-f) + A(-f) B(f))) \end{array} \right) \tag{7.40}$$

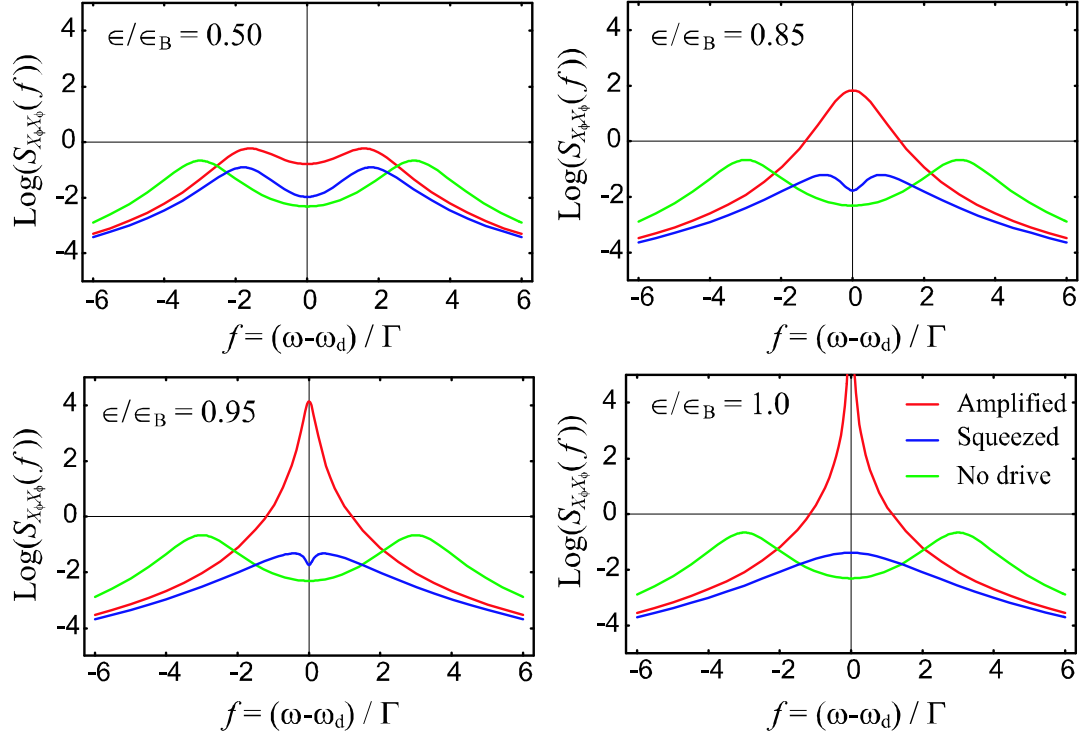


Figure 7.9: The spectrum of the amplified (red) and squeezed (blue) quadrature is shown for $\epsilon/\epsilon_B^+ = 0.5, 0.85, 0.95$ and 1.0 , where ϵ_B^+ is the value of ϵ at the upper bifurcation point. The detuning used is $\Omega = 3$. The green curve for $\epsilon = 0.0$ (no driving) is shown for comparison. We note how the amplified quadrature spectrum grows as we approach the bifurcation while the squeezed spectrum shrinks. At the bifurcation point $\epsilon/\epsilon_B^+ = 1.0$, the amplified spectrum diverges for $f = 0$, while the squeezed spectrum remains finite and does not go to zero.

Substituting for $A(f)$ and $B(f)$, we get

$$S_{X_\phi X_\phi}(f) = S_{aa}(f) \frac{\tilde{\Omega}^2 + 1 + \epsilon^2 + 2\epsilon \left\{ \tilde{\Omega} \cos(2(\theta - \phi)) - \sin(2(\theta - \phi)) \right\} + f^2}{\left(\tilde{\Omega}^2 + 1 - \epsilon^2 \right)^2 - 2f^2 \left(\tilde{\Omega}^2 - 1 - \epsilon^2 \right) + f^4} \quad (7.41)$$

where $\tilde{\Omega} = \Omega - 2\epsilon$. The term in curly brackets changes with the angle ϕ and the two extreme values are $\pm\sqrt{1 + \tilde{\Omega}^2}$ corresponding to the amplified and the de-amplified

quadratures. Fig. 7.9 shows the spectrum of the amplified and de-amplified quadratures for $\Omega = 3$ and four different values of ϵ .

After making a variable change back to $\delta_\phi[f] = \sqrt{\hbar\omega_d/\Gamma E_J} X_\phi[f]$ (again, $\omega = \omega_d$) and integrating over all frequencies, we get the variance for the amplified (+) and de-amplified (-) quadratures

$$\sigma_{\delta_{\phi\pm}}^2 = \frac{1}{2\pi} \frac{\hbar\omega_d}{\Gamma E_J} \int_{-\infty}^{\infty} \Gamma S_{X_\phi X_\phi}(f) df = \frac{k_B T_{eff}}{E_J} \left(\frac{\sqrt{(\Omega - 2\epsilon)^2 + 1}}{\sqrt{(\Omega - 2\epsilon)^2 + 1 \mp \epsilon}} \right) \quad (7.42)$$

where T_{eff} is an effective temperature given by

$$T_{eff} = \frac{\hbar\omega_d}{2k_B} \coth\left(\frac{\hbar\omega_d}{2k_B T}\right) \quad (7.43)$$

Let us evaluate equation 7.42 in a few interesting limits. In the absence of any drive ($\epsilon = 0$), the system is identical to the harmonic oscillator. Setting $\epsilon = 0$, we get $\sigma_{\delta_{\phi\pm}}^2(\epsilon = 0) = \langle \delta_\phi^2 \rangle = k_B T_{eff}/E_J$ which reduces to $k_B T/E_J$ in the classical limit and $\hbar\omega_p/2E_J$ in the quantum limit as expected. Here, we have replaced ω_d with ω_p since in the absence of driving the oscillator responds maximally at ω_p . Note that $\sigma_{\delta_{\phi+}}^2$ goes to infinity when the denominator in equation 7.42 goes to zero. This condition is satisfied when

$$\epsilon = \epsilon_B^\pm = \frac{1}{3} \left(2\Omega \mp \sqrt{\Omega^2 - 3} \right) \quad (7.44)$$

which exactly corresponds to the bifurcation points (for $\Omega > \sqrt{3}$). For the same operating point, $\sigma_{\delta_{\phi-}}^2$ goes to $k_B T_{eff}/2E_J$ which is a factor of two smaller than $\sigma_{\delta_{\phi\pm}}^2(\epsilon = 0)$, the variance in the undriven case. This is a general result for squeezing of the internal field in a cavity. The maximum squeezing one can obtain for the

internal field is a factor of two [98]. Nevertheless, as we will see in section 7.3.3, the output field can be squeezed much more [99]. We will need the variance of the amplified quadrature $\sigma_{\delta_{\phi+}}^2$, and then we can compute the escape probability by knowing the distance to the saddle point which we call $\Delta\delta_{\phi}$. The escape probability is given by:

$$P_{esc}^{RF} = \exp\left(-\chi \frac{\Delta\delta_{\phi}^2}{2\sigma_{\delta_{\phi+}}^2}\right) \quad (7.45)$$

where χ is the same scaling factor introduced in the previous section and corrects for the fact that in the harmonic approximation we overestimate the barrier. In the calculations that follow, we will use $\chi = 1/3$ because the dynamics of this system near the bifurcation point can be understood as that of a particle diffusing in a cubic potential [27].

We expand the expressions for $\Delta\delta_{\phi}^2$ and $\sigma_{\delta_{\phi+}}^2$ around the bifurcation point (7.44), and after keeping only leading order terms in Ω (high detuning limit), we get

$$\sigma_{\delta_{\phi+}}^2 = \frac{1}{2\sqrt{3}} \frac{k_B T_{eff}}{E_J} (1 - I_{RF}^2/I_B^2)^{-1/2} \quad (7.46a)$$

$$\Delta\delta_{\phi}^2 = \frac{32}{9} \frac{\Omega}{Q} (1 - I_{RF}^2/I_B^2) \quad (7.46b)$$

where the relative distance to the bifurcation point is given in terms of the ratio I_{RF}^2/I_B^2 , and I_B is the upper bifurcation current. In general, the escape rate can be written as:

$$\Gamma_{esc}^{RF} = \frac{\omega_a^{RF}}{2\pi} \exp\left(-\frac{\Delta U_{esc}^{RF}}{k_B T_{esc}^{RF}}\right) \quad (7.47)$$

where ω_a^{RF} is the attempt frequency, and the exponent is written as a ratio of a barrier energy divided by an effective temperature. Using the expressions in 7.46, we

can write down the exponent as

$$\frac{\Delta U_{esc}^{RF}}{k_B T_{esc}^{RF}} = \chi \frac{\Delta \delta_\phi^2}{2\sigma_{\delta_\phi+}^2} = \frac{32}{9\sqrt{3}} \frac{\Omega}{Q} \frac{E_J}{k_B T_{eff}} \left(1 - I_{RF}^2/I_B^2\right)^{3/2} \quad (7.48)$$

where we have used $\chi = 1/3$. The expressions for barrier energy and escape temperature then are

$$\Delta U_{esc}^{RF} = \frac{32}{9\sqrt{3}} \frac{\Omega}{Q} E_J \left(1 - I_{RF}^2/I_B^2\right)^{3/2} \quad (7.49a)$$

$$T_{esc}^{RF} = T_{eff} = \frac{\hbar\omega_d}{2k_B} \coth\left(\frac{\hbar\omega_d}{2k_B T}\right) \quad (7.49b)$$

These results for the escape exponent agree with the results derived by other authors using a different technique [49, 50]. The procedure used here has the advantage of clearly highlighting the parametric amplification in the system and its role in the escape process. It also allows us to make the connection with the Dynamical Casimir Effect (DCE) [53] which predicts the creation of thermal photons from zero point fluctuations in a parametrically driven cavity. We note that at high temperatures ($k_B T \gg \hbar\omega_d$), T_{esc}^{RF} tends to T , the bath temperature and hence reproducing the classical result of section 2.3.2. But for $k_B T \ll \hbar\omega_d$, it saturates to a value of $\hbar\omega_d/2$, the full dependence on temperature being given by equation 7.49b. This finite escape temperature, even at $T = 0$, is due to the parametric conversion of zero point fluctuations into thermal noise which results in the activated escape from the metastable state. This activation process dominates over any tunneling from the metastable state, especially near the bifurcation point [50]. The conditions for which tunneling might be observed is discussed in ref. [100]. We will discuss these ideas

in more detail in the next chapter which describes the experiments carried out to measure the escape out the metastable state in the JBA. The main objective of these experiments is to measure T_{esc}^{RF} as function of T .

7.3 Parametric amplification in the JBA

The JBA can be operated in a different mode to exploit the parametric amplification process. Instead of coupling an input signal to the critical current of the junction, we can send a weak signal at frequency ω_s , along with the strong drive (known as the *pump*) at frequency ω_d [9, 101]. Under proper conditions, this additional signal will get reflected from the JBA with gain. Another signal at frequency $\omega_i = 2\omega_d - \omega_s$, called the idler frequency is also created, a typical signature of a parametric amplification process. This mode of operation is called the four-wave or four-photon mixing since four photons are involved (one each at ω_s and ω_i and two at ω_d). Another mode called the three-wave or three photon mixing also exists where $\omega_s + \omega_i = \omega_d$. This requires that the non-linear element have an odd symmetry in the amplitude of the *pump* and is achieved in the Josephson junction by applying a DC bias. When $\omega_s = \omega_i$, it is called a degenerate parametric amplifier and the gain of the amplifier depends on the phase of the input signal with respect to the *pump*. For $\omega_s \neq \omega_i$, it is known as a non-degenerate parametric amplifier with the gain being independent of the phase of the input signal.

In this section, we will only be concerned with the four-photon mode. We will now proceed to compute the gain and noise performance of such a parametric amplifier.

7.3.1 Parametric gain

In order to compute the gain, we need to compute the output field $A_{out}[t]$. Again, we will work in the frequency domain to simplify our calculations. The relation between the input and output field is given by

$$a_{out}[f] = -i2 x[f] - a_{in}[f] \quad (7.50)$$

where we have used the dimensionless frequency f . Using equations 7.34, we can write $a_{out}[f]$ in terms of the gain functions $A(f)$ and $B(f)$ as

$$a_{out}[f] = (-1 - i2A(f)) a_{in}[f] - i2B(f) a_{in}^\dagger[-f] \quad (7.51)$$

We consider the noise free case and set all signals at the idler frequency $(-f)$ to zero, i.e., $a_{in}[f]$ now represents a classical signal at frequency f . We can then define two power gains G_s and G_i which are known as signal and conversion gain respectively

$$G_s(f) = \left| \frac{a_{out}[f]}{a_{in}[f]} \right|^2 = |-1 - i2A(f)|^2 \quad (7.52a)$$

$$G_i(f) = \left| \frac{a_{out}[-f]}{a_{in}^\dagger[f]} \right|^2 = |2B(-f)|^2 \quad (7.52b)$$

The quantity G_s is the power gain you can get for your input signal while G_i tells you how much power is generated at the idler frequency $(-f)$. Using equations 7.35,

we can compute these gains and the result is

$$G_s(f) = 1 + \frac{4\epsilon^2}{((\Omega - 2\epsilon)^2 - \epsilon^2 + 1)^2 - 2f^2((\Omega - 2\epsilon)^2 - \epsilon^2 - 1) + f^4} \quad (7.53a)$$

$$G_i(f) = G_s(f) - 1 \quad (7.53b)$$

The relation between G_s and G_i is again a characteristic feature of the parametric amplification process. Let us analyze the behavior of G_s in various limiting cases. For no driving, i.e., $\epsilon = 0$, we get $G_s = 1$ and $G_i = 0$ as expected. The gain diverges⁴ for $f = 0$ at the bifurcation points (7.44) where the first term in the denominator goes to zero. For $\Omega < \sqrt{3}$, when there is no bistability, the maximum gain is achieved when

$$\epsilon_{\max} = \sqrt{\frac{1 + \Omega^2}{3}} \quad (7.54)$$

and is finite. We also note that the gain is a symmetric function of frequency f . Fig. 7.10 shows a plot of $G_s(f)$ as a function of f and ϵ/ϵ_{\max} for critical detuning $\Omega = \sqrt{3}$.

7.3.2 Noise temperature and the quantum limit

We will now compute the noise performance of the parametric amplifier. Equation 7.51 not only contains information about gain but also about the noise spectrum. If we go back to considering a_{in} and a_{out} as noise fields, we can compute the output noise spectrum

$$\hbar\omega S_{aa}^{out}[f] = G_s(f) \hbar\omega S_{aa}^{in}[f] + (G_s(f) - 1) \hbar\omega S_{aa}^{in}[-f] \quad (7.55)$$

⁴Near points of diverging gain, the theory breaks down and higher order effects start to contribute keeping the gain finite. Nevertheless, maximum gain is achieved at these points.

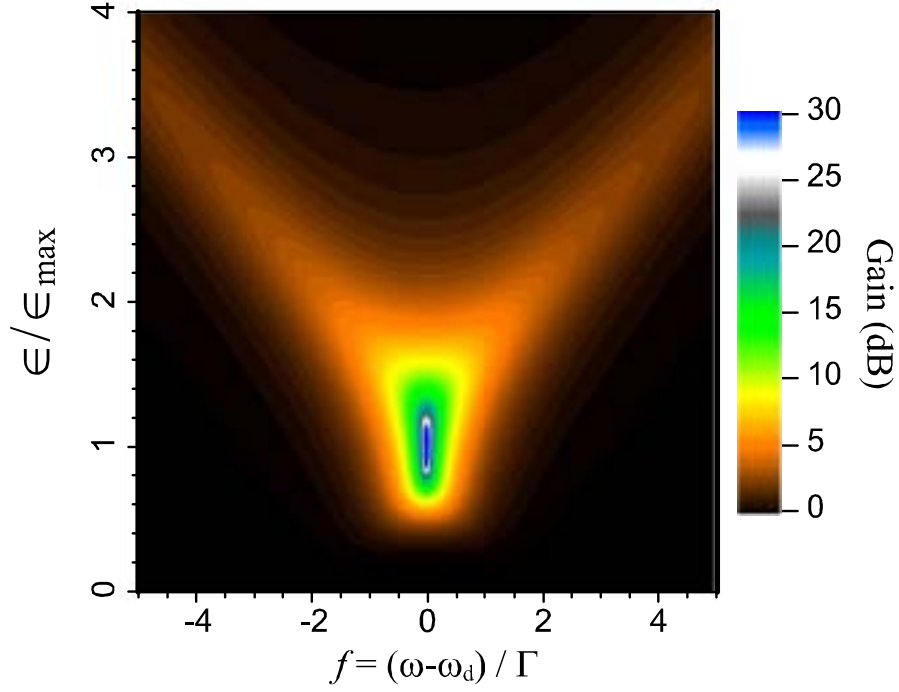


Figure 7.10: The power gain of the JBA operated as a parametric amplifier is plotted (color) as a function of f and ϵ/ϵ_{\max} for critical detuning $\Omega = \sqrt{3}$. The gain has a single maximum at $f = 0$ for $\epsilon/\epsilon_{\max} \leq \sqrt{3}$ but two maxima at other bias points. The gain is also symmetric function of f . At $\epsilon/\epsilon_{\max} = 1.0$ and $f = 0$, the computed gain diverges but higher order effects which have been ignored in this calculation will keep the gain finite.

where $\hbar\omega S_{aa}^{out}[f]$ and $\hbar\omega S_{aa}^{in}[f]$ represent the output and input noise energy respectively. So the system amplifies the noise at signal frequency f by G_s but also adds an amplified component of the noise at idler frequency $(-f)$. The noise at signal frequency f is considered to be a part of the input signal and hence the added noise component is

$$E_N^{out} = (G_s - 1)\hbar\omega S_{aa}^{in}[-f] = (G_s - 1)k_B T_{eff} \quad (7.56)$$

where T_{eff} is defined in equation 7.43 and $\omega = \omega_d + \Gamma f$. We also approximate $S_{aa}[f] = S_{aa}[-f]$ since the function varies slowly around $f = 0$ or $\omega = \omega_d$. We can divide the added noise by the gain G_s to refer it back to the input and compute the noise temperature in the limit $G_s \gg 1$ as

$$T_N = \frac{E_N^{out}}{k_B G_s} = T_{eff} = \frac{\hbar\omega}{2k_B} \coth\left(\frac{\hbar\omega}{2k_B T}\right) \quad (7.57)$$

We note that the noise temperature T_N and the escape temperature T_{esc}^{RF} are given by the same expression T_{eff} . This is not surprising since both quantities are related to the same parametric amplification process which affects the noise properties of the both the internal and the output field. As $T \rightarrow 0$, we get the quantum limit [10] for the noise temperature

$$T_N = \frac{\hbar\omega_d}{2}. \quad (7.58)$$

The amplifier adds half a photon worth of noise to the signal. So an ideal parametric amplifier when operated at a temperature $k_B T \ll \hbar\omega_d$, is always quantum limited. In practice, the noise temperature of a parametric amplifier tends to increase with increasing gain. This has been traditionally known as the "noise rise" problem in parametric amplifiers [26] and has prevented extensive practical applications. Operating points with high gain are typically close to bifurcation points. As the gain starts to increase, higher order effects which have not been treated in the theory described above, can lead to instabilities which can enhance the noise. In the next chapter, we will discuss some experimental results of operating the JBA as a parametric amplifier.

7.3.3 Squeezing

A parametric amplifier can create squeezed states of the output field. The basic idea is that the fields coming out at signal frequency $\omega_d + \Gamma f$ and the idler frequency $\omega_d - \Gamma f$ are correlated. This applies to the noise fields at the two frequencies as well. We can combine the signal at frequencies $\omega_d \pm \Gamma f$ by beating the output field with a signal at ω_d using a mixer. This homodyne spectrum at the output of the mixer (at $\pm \Gamma f$) can go below the vacuum/thermal floor for a properly chosen phase difference between the original drive and the beating signal. This is the essence of squeezing. This mixing operation can be written down in frequency domain as

$$a_{out}^{mix}[f] = \exp(-i\phi) a_{out}[f] + \exp(i\phi) a_{out}[-f] \quad (7.59)$$

where $a_{out}^{mix}[f]$ is the combined signal. Note the similarity between the above equation and equation 7.37 which describes the quadrature components of the internal field. It is not surprising that the expression for the spectrum of $a_{out}^{mix}[f]$ is identical to equation 7.40 but with $A(f)$ and $B(f)$ replaced by $A_{out}(f)$ and $B_{out}(f)$ where

$$\begin{aligned} A_{out}(f) &= -1 - i2A(f) \\ B_{out}(f) &= -i2B(f). \end{aligned} \quad (7.60)$$

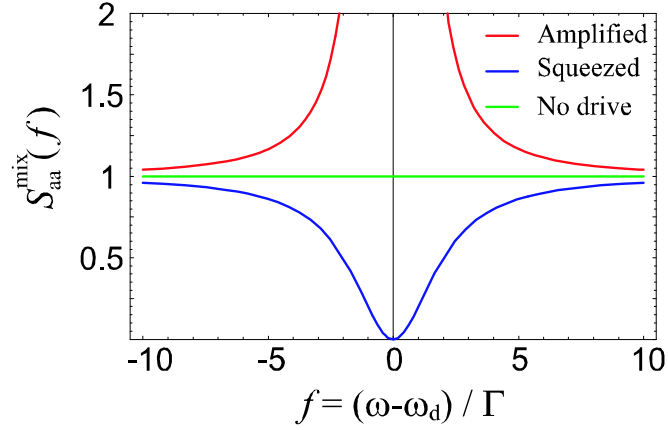


Figure 7.11: The amplified (red) and squeezed (blue) spectrum of the output field of the JBA biased at the critical point $\Omega = \sqrt{3}$ and $\epsilon = \epsilon_{\max}$ is shown for $T = 0$. The green curve is the vacuum noise floor corresponding to the undriven case. We note that the squeezed spectrum goes to zero at $f = 0$, corresponding to perfect squeezing. At the same point, the amplified spectrum diverges but in practice, higher order effects ignored in this calculation will keep it finite.

The spectrum $S_{aa}^{mix}(f)$ computes to

$$S_{aa}^{mix}(f) = 2S_{aa}(f) \left(1 + \frac{8\epsilon^2 - 8\tilde{\Omega}\epsilon \cos(2(\theta - \phi)) + 4\epsilon(1 + f^2 + \epsilon^2 - \tilde{\Omega}^2) \sin(2(\theta - \phi))}{4f^2 + (-1 + f^2 + \epsilon^2 - \tilde{\Omega}^2)^2} \right) \quad (7.61)$$

where $\tilde{\Omega} = \Omega - 2\epsilon$. If we set $\epsilon = 0$ (no driving), we get $S_{aa}^{mix}(f) = 2S_{aa}(f)$ which is the vacuum/thermal floor. If the value of $S_{aa}^{mix}(f)$ goes below $2S_{aa}(f)$, we have squeezing. The point of perfect squeezing is when $S_{aa}^{mix}(f) = 0$ for some f . It can be shown that we get perfect squeezing at the bifurcation points (7.44) at frequency $f = 0$, i.e., the drive frequency. At $f = 0$, $S_{aa}^{mix-}(f) = 0$ while $S_{aa}^{mix+}(f)$ diverges.

Fig. 7.11 shows the squeezed (blue) and amplified (red) spectrum at $T = 0$ for the critical point, i.e., $\Omega = \sqrt{3}$, and $\epsilon = \epsilon_{\max}$. The horizontal line (green) is the vacuum floor. The squeezed spectrum is the same at all bifurcation points. In practice, it is not possible to bias at the bifurcation points since the system will switch to the other metastable state. Hence, it is best to bias near the critical point for observing the maximum amount of squeezing. We will present some preliminary experimental results in the next chapter.

Chapter 8

Quantum escape and parametric amplification:

Experiments

In this chapter, we will discuss the experiments which measure the escape from the low amplitude state of the JBA in the classical ($k_B T \gg \hbar \omega_p$) and quantum regime ($k_B T \ll \hbar \omega_p$). We will compare the results with the quantum escape theory described in the previous chapter. We will begin by discussing the connection of the quantum escape process in the JBA and the Dynamical Casimir Effect (DCE). This will be followed by a discussion of the escape measurements. Finally, we will discuss some preliminary experiments testing the performance of the JBA as a parametric amplifier. We will characterize its gain and noise properties and test its potential for squeezing vacuum noise. These are proof of principle experiments and have not yet been optimized for practical applications. The experiments described in this chapter explore the connection between the four facets of a dynamical bifurcation: parametric amplification, squeezing, quantum escape and the DCE.

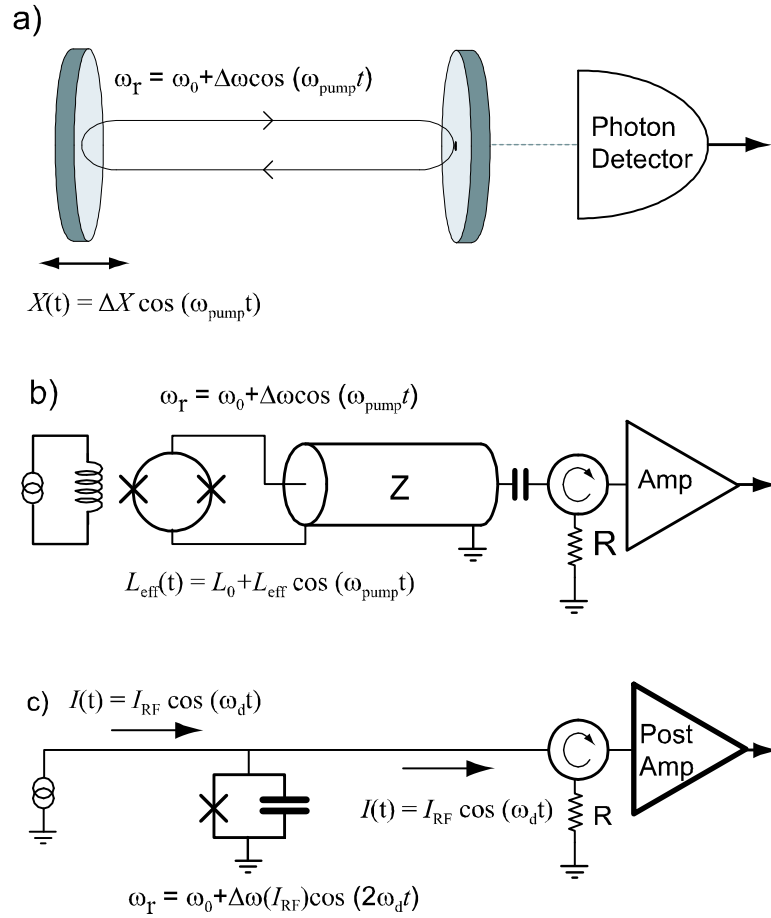


Figure 8.1: Different schemes to implement a parametrically driven oscillator for observing the Dynamical Casimir Effect. (a) The opto-mechanical realization using a cavity with a fixed and a moving mirror. The moving mirror modulates the resonant frequency of the cavity (ω_r) at the driving/pump frequency (ω_p). The thermal photons spontaneously generated from zero point photons leak out of the right mirror and can be detected. (b) An electrical implementation of the cavity with moving mirror. A transmission line cavity with the fixed mirror made from a capacitor and the moving mirror made with a SQUID. The inductively coupled pump signal modulates the SQUID inductance thereby modulating the resonant frequency of the cavity. (c) Our implementation of the parametrically driven oscillator using a non-linear resonator made with a Josephson junction. When biased with a drive at frequency ω_d near a bifurcation point, the system behaves like a resonator whose frequency is modulated at $\omega_{\text{pump}} = 2\omega_d$.

8.1 Dynamical Casimir Effect

The paradoxical nature of quantum fluctuations is particularly well showcased in the Dynamical Casimir Effect (DCE)—an elusively weak phenomenon predicted almost 40 years ago [53] but whose theory remains essentially experimentally unverified (see [102] for a review). In perhaps the most promising opto-mechanical realization of the DCE [55], one of the mirrors of a Fabry-Perot cavity is driven by a force that periodically varies the cavity’s geometric length at a frequency ω_{pump} which is a multiple of the lowest cavity mode frequency ω_0 (see Fig. 8.1a). According to prediction, even when the cavity is at a low temperature T such that it is initially devoid of all photons ($\hbar\omega_0 \gg k_B T$) and contains only virtual zero-point quantum fluctuations, the mirror motion should spontaneously create photons inside the cavity. The effect is surprising for two reasons: i) no free charge is involved in the radiation process and ii) entropy appears to be created from a driven, but perfectly ordered system. These photons obey the statistics of black-body radiation with some effective temperature, i.e., the distribution is thermal. As pointed out by several authors, the DCE is intimately related with the Unruh effect [103] in cosmology which posits that vacuum fluctuations appear to an accelerated observer as a thermal bath with an elevated temperature proportional to the acceleration. The Unruh effect provides a key semi-classical explanation of black-hole evaporation, and, like the DCE, remains to be observed. Present experimental techniques lack the required sensitivity for the unambiguous detection of the DCE by several orders of magnitude, though several proposals exist [55, 104].

Traditionally, the DCE effect has been discussed in the context of mechanical motion of a mirror. The use of resonant cavities was introduced to enhance the

photon production rate, with the cavity frequency being modulated by mechanical means [55]. But if we believe that electrical degrees of freedom are equivalent to mechanical ones, it is possible to construct an experiment to observe the DCE by using an electrical resonator. We can periodically vary the frequency of an electrical resonator not by mechanical means, but through an element whose reactance can be modulated by an electrical signal. Fig. 8.1b shows a possible implementation using a SQUID at the end of an electrical cavity. The SQUID inductance and hence the effective electrical length of the cavity can be varied by coupling a signal inductively. Fig. 8.1a and Fig. 8.1b are essentially parametrically driven oscillators. As we saw in the previous chapter, the JBA (8.1c) biased near the bifurcation point behaves like a parametrically driven oscillator (see section 7.2.1). The JBA converts quantum zero point fluctuations into thermal fluctuations via parametric amplification. This is the link between the JBA and the DCE. The traditional DCE effect in cavities can be thought of as parametric amplification of zero point fluctuations ($T = 0$) with the pump being applied to a mechanical degree of freedom. In the JBA, the pump is applied to an electrical degree of freedom instead. The use of a Josephson junction based non-linear resonator to observe the DCE has two main advantages. The non-linearity enables electrical modulation of the resonator frequency while the absence of dissipation eliminates parasitic channels of heat production.

The DCE predictions and experiments have been mostly concerned with measuring the effective temperature of the output field of the cavity which can be a significant experimental challenge. An unambiguous detection of the effective temperature of the photon field produced by the DCE requires a detector with minimal coupling loss and quantum-noise limited sensitivity. The key feature of our experiment is that

we measure the effective temperature of the internal field of the resonator. This is valid because the output field and the internal field are related to each other (see section 7.1). As we saw in the previous chapter, the thermal noise created from the parametric amplification of zero point fluctuations leads to the switching of the JBA from its low amplitude state to the high amplitude state. By performing a calibration in the high temperature regime where the switching process is dominated solely by ordinary black-body thermal radiation, we can infer the temperature of the spontaneously created noise in the quantum regime and compare it to theory. We now proceed to describe these escape measurements.

8.2 Quantum escape measurements

8.2.1 Switching measurements in the JBA

The main goal of the experiment is to measure the transitions rates from the low amplitude to the high amplitude state of the JBA. By characterizing these rates, we can extract an effective escape temperature T_{esc}^{RF} which is a measure of the intensity of the fluctuations felt by the system. The escape rate from the low amplitude state can be written as

$$\Gamma_{esc}^{RF}(I_{RF}) = \frac{\omega_a^{RF}(I_{RF})}{2\pi} \exp\left(-\frac{U_{esc}^{RF}}{k_B T_{esc}^{RF}} \left(1 - \frac{I_{RF}^2}{I_B^2}\right)^{3/2}\right) \quad (8.1)$$

where $\omega_a^{RF}(I_{RF})$ and U_{esc}^{RF} are defined in equations 2.32a and 2.33b. I have written $\Gamma_{esc}^{RF}(I_{RF})$ as a function of the drive current I_{RF} only since we will be measuring the

variation of escape rate with the drive current. We can rewrite the above equation as

$$\tilde{\Gamma}_{esc}^{RF}(I_{RF}) = \left(\frac{U_{esc}^{RF}}{k_B T_{esc}^{RF}} \right)^{2/3} \left(1 - \frac{I_{RF}^2}{I_B^2} \right) \quad (8.2)$$

where $\tilde{\Gamma}_{esc}^{RF}(I_{RF})$ is a reduced escape rate given by

$$\tilde{\Gamma}_{esc}^{RF}(I_{RF}) = \left(\log \left(\frac{\omega_a^{RF}(I_{RF})}{2\pi\Gamma_{esc}^{RF}(I_{RF})} \right) \right)^{2/3}. \quad (8.3)$$

If we plot $\tilde{\Gamma}_{esc}^{RF}(I_{RF})$ as a function of I_{RF}^2 , we should get a straight line with a slope $\tilde{\Gamma}_{slope}$ and an intercept $\tilde{\Gamma}_{int}$ given by

$$\tilde{\Gamma}_{slope} = - \left(\frac{U_{esc}^{RF}}{k_B T_{esc}^{RF}} \right)^{2/3} \frac{1}{I_B^2} \quad (8.4a)$$

$$\tilde{\Gamma}_{int} = \left(\frac{U_{esc}^{RF}}{k_B T_{esc}^{RF}} \right)^{2/3}. \quad (8.4b)$$

From these two quantities we can determine the bifurcation current I_B and escape temperature T_{esc}^{RF} using the following formulae

$$I_B = \left(-\tilde{\Gamma}_{int} / \tilde{\Gamma}_{slope} \right)^{1/2} \quad (8.5a)$$

$$T_{esc}^{RF} = \frac{U_{esc}^{RF}}{k_B \tilde{\Gamma}_{int}^{3/2}} \quad (8.5b)$$

where U_{esc}^{RF} is computed using equation 2.33b. So the experiment involves measuring $\Gamma_{esc}^{RF}(I_{RF})$ for different operating parameters and extracting the escape temperature T_{esc}^{RF} . From the results of the previous chapter, we expect T_{esc}^{RF} to be given by

$$T_{esc}^{RF} = \frac{\hbar\omega_d}{2k_B} \coth \left(\frac{\hbar\omega_d}{2k_B T} \right). \quad (8.6)$$

We studied the variation of T_{esc}^{RF} with bath temperature T and drive frequency ω_d . Two JBA samples with a plasma frequency of 1.67 GHz (sample LF) and 4.69 GHz (sample HF) were measured to study the scaling of T_{esc}^{RF} with frequency.

In order to get an independent calibration of the intensity of fluctuations at every operating temperature, we measured the escape rates from the superconducting state to the voltage state of the DC current biased Josephson junction. The theory for this experiment is well understood and has been experimentally verified to be quite accurate [48]. The escape rate for this process is given by

$$\Gamma_{esc}^{DC}(I_{DC}) = a_p \frac{\omega_p}{2\pi} (1 - I_{DC}/I_0)^{1/4} \exp\left(-\frac{4\sqrt{2}}{3} \frac{E_J}{k_B T_{esc}^{DC}} \left(1 - \frac{I_{DC}}{I_0}\right)^{3/2}\right)$$

where I_0 is the critical current of the junction, $E_J = \varphi_0 I_0$ is the Josephson energy, ω_p is the plasma frequency and a_p is a prefactor of order unity to account for finite damping. Using the procedure described above, we can extract the escape temperature T_{esc}^{DC} by measuring $\Gamma_{esc}^{DC}(I_{DC})$. In our experiments, we were always in the classical regime ($k_B T \gtrsim \hbar \omega_p (1 - I_{DC}/I_0)^{1/4} / 2\pi$) where $T_{esc}^{DC} = T$, the bath temperature.

8.2.2 Combined RF and DC biasing scheme

One of the main challenges of this experiment was to implement an ultra low noise biasing scheme. We want the JBA to only feel the thermal/quantum fluctuations corresponding to the bath temperature T at which the experiment is carried out. The ability to measure DC and RF switching in the same experimental setup adds to the complication. The best DC biasing schemes are implemented using shielded, twisted-pair wires which are excited differentially. This not only eliminates interaction

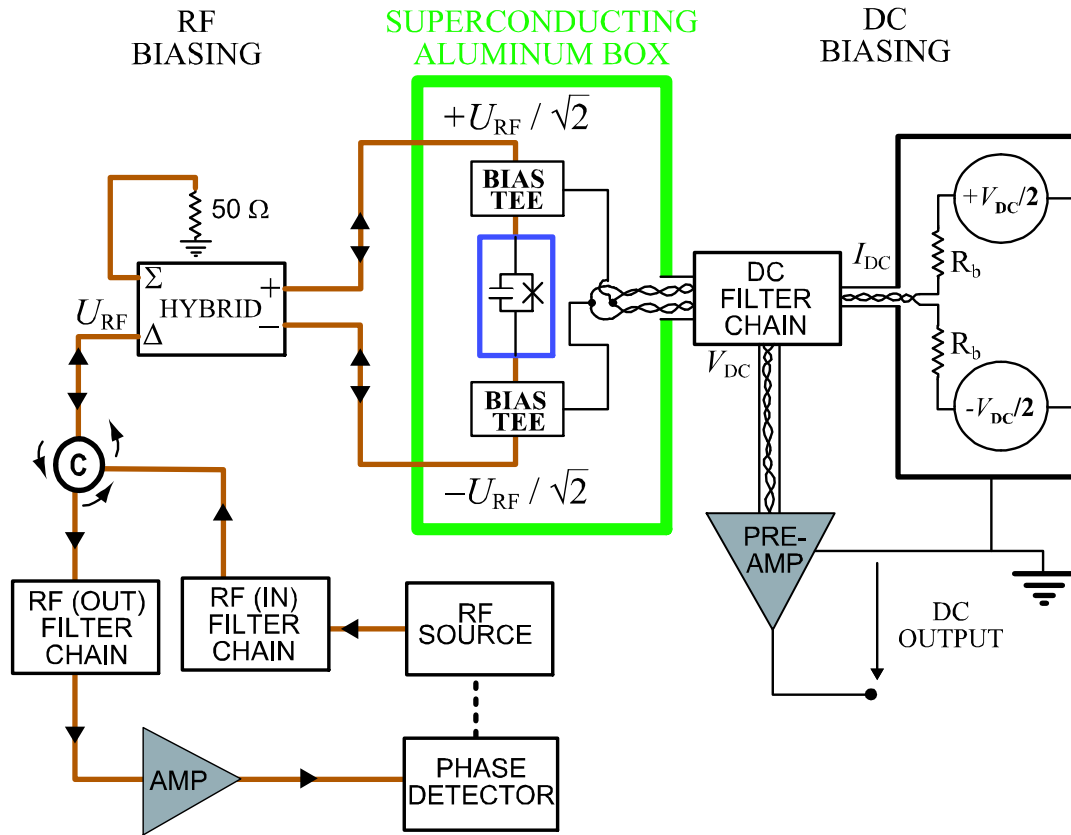


Figure 8.2: A schematic of the biasing scheme for combining singled-ended RF with differential DC signals. Shielded twisted-pair wires are used to carry out a four wire DC $I - V$ measurement. A 180 degree hybrid is used to split the RF signal into two components which are phase shifted by 180 degrees, creating the differential RF drive. The RF and DC signals are combined using a "Bias Tee" before they reach the device (inside blue box). A superconducting (at $T = 12$ mK) aluminum box is used to shield the device from low frequency magnetic fields since the twisted-pairs have to be opened up before they can be combined with the RF signals. This differential biasing scheme allows the creation of an ultra-low noise environment for the device at both low and high frequencies.

with the ground of the electrical system which is often noisy, but also minimizes inductive pickup. RF signals are typically propagated on single ended coaxial lines and since they can be capacitively coupled, grounding problems are usually not an issue. In order to combine the differential DC and single-ended RF bias lines we had to transform the RF signal into a differential one using a device called the 180 degree hybrid. Now we have two single ended RF signals with opposite phase and each part is combined with the DC signal from the two wires of the twisted-pair respectively. This is the most vulnerable part of the biasing circuit since the twisted-pair now opens up into a loop and therefore prone to low frequency inductive pickup. A superconducting (at $T = 12$ mK) aluminum box was used to shield this part of the circuit from low frequency magnetic fields. The combined signals then go to the device enabling differential excitation. The biasing scheme is shown schematically in Fig. 8.2.

The filter chain for the DC path (both current and voltage lines) included several copper powder filters made with twisted-pair wires for filtering high frequency noise ($\gtrsim 1$ GHz). Pi filters made with inductors and capacitors were used to filter the intermediate frequency noise and limit the bandwidth of the DC lines to about 10 kHz. In addition, for the current line, a 100:1 voltage divider at the 4K stage of the fridge and a well thermalized bias resistor at the base temperature stage were used. For the RF lines, the filter chain on the input side included several attenuators (~ 73 dB total) and reflective filters to set a pass band from 1 to 2 GHz for sample LF and 4 to 5 GHz for sample HF. The RF filter chain for the output line was made up of three circulators with two of them anchored at the base temperature and one at the 100 mK stage of the dilution refrigerator. A very important element of the RF output

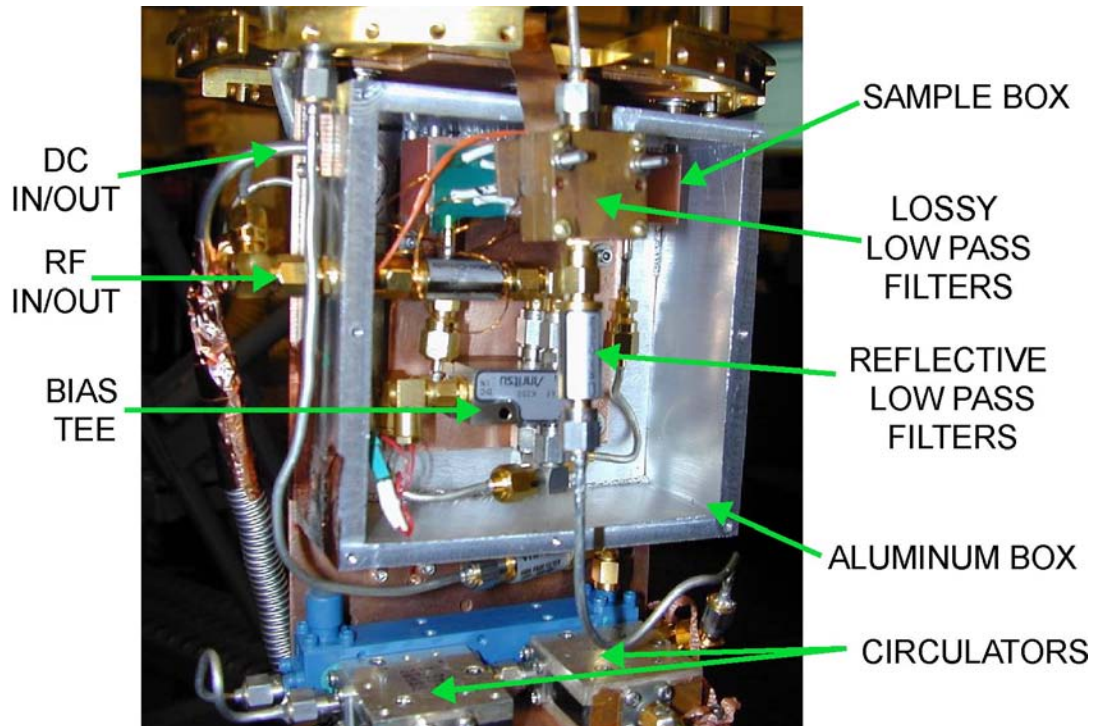


Figure 8.3: A picture of the base temperature stage of the experiment showing the superconducting aluminum box containing the DC and RF circuitry.

line was the lossy low pass filter. This filter is basically a microstrip transmission line where the dielectric has a frequency dependent loss. The main advantage of these filters is that they are well matched to the 50 ohm transmission lines thereby avoiding reflections and the possibility of setting up standing waves. The filtering action comes from a frequency dependent attenuation of the signal passing through. These can be designed to have less than 1 dB attenuation in the pass band (< 2 GHz). The loss outside the pass band can be as large as 60 dB. See [66] for more details. Fig. 8.3 shows an image of the aluminum box with DC and RF circuitry inside.

8.2.3 Measuring escape rates

We will now describe the procedure for measuring the escape rates from the low amplitude state of the JBA. The JBA was biased with a long trapezoidal pulse at frequency ω_d with amplitude I_{RF} . The pulse ramp time used was 40 ns for sample LF and 10 ns for sample HF. The total pulse length was 1 ms. The phase of the reflected pulse is analyzed and the time (τ_i^{switch}) at which the JBA makes a transition from low to high amplitude state is recorded. The experiment is repeated typically for $N = 10^5$ times. We then construct the probability $P_L(\tau)$ of the JBA being the low amplitude state as

$$P_L(\tau) = 1 - \frac{1}{N} \sum_{i=1}^N \Theta(\tau - \tau_i^{\text{switch}}) \quad (8.7)$$

where

$$\begin{aligned} \Theta(\tau) &= 0 & \tau < 0 \\ &= 1 & \tau \geq 0 \end{aligned} \quad (8.8)$$

is the Heaviside unit step function. The probability $P_L(\tau)$ decays exponentially with a decay constant given by the escape rate Γ_{esc}^{RF}

$$P_L(\tau) = \exp(-\Gamma_{esc}^{RF} \tau) \quad (8.9)$$

So by fitting an exponential to $P_L(\tau)$ we can determine $\Gamma_{esc}^{RF}(I_{RF})$ for different bias amplitudes I_{RF} . The results are shown in Fig. 8.4 where we have plotted the reduced escape rate $\tilde{\Gamma}_{esc}^{RF}(I_{RF})$ as a function of I_{RF}^2/I_B^2 for selected values of bath temperatures.

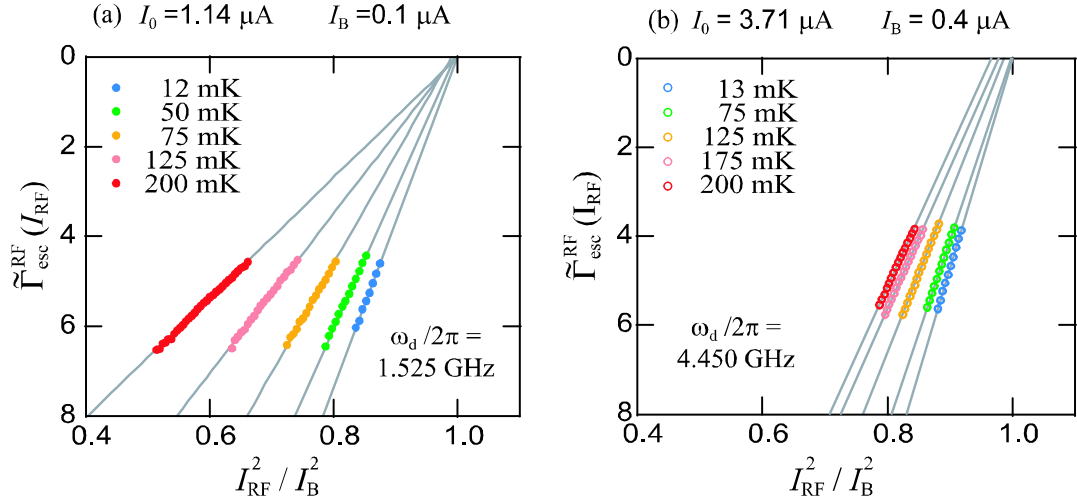


Figure 8.4: A plot of the reduced escape rate $\tilde{\Gamma}_{esc}^{RF}(I_{RF})$ as function of I_{RF}^2/I_B^2 at different bath temperatures. Panel (a) shows data for sample LF with $\omega_p/2\pi = 1.670$ GHz and $\omega_d/2\pi = 1.525$ GHz. Panel (b) shows data for sample HF with $\omega_p/2\pi = 4.690$ GHz and $\omega_d/2\pi = 4.450$ GHz. The solid lines are straight line fits to the data. The slope and intercept of these fits yield information about the escape temperature T_{esc}^{RF} and the bifurcation current I_B .

Panel (a) and (b) show data for sample LF and HF respectively. For both data sets we observe straight lines¹, with different slopes for different bath temperature. This confirms that the escape rate follows the behavior given by equation 8.1. We can then extract the escape temperature T_{esc}^{RF} for each operating point. Note that in the experiment, we control I_{RF} by varying the pulse amplitude (A_{RF}) of the RF generator. Since $I_{RF} \propto A_{RF}$, we can plot $\tilde{\Gamma}_{esc}^{RF}$ as a function of A_{RF}^2 and extract the bifurcation amplitude ($A_B \propto I_B$) using equation 8.5a. Once we have A_B we can plot the data as a function of A_{RF}^2/A_B^2 which is the same as I_{RF}^2/I_B^2 . When plotted this way, the straight lines should intersect $\tilde{\Gamma}_{esc}^{RF} = 0$ at $I_{RF}^2/I_B^2 = 1$ at all temperatures since the bifurcation current I_B (and hence A_B) does not depend on temperature. In

¹Note that the vertical axis is inverted with 0 at the top.

practice, we always observe small differences in the extracted values of A_B at different temperatures. This could imply that the data starts to deviate from the prediction of equation 8.1. But we found that this variation was predominantly due to the slow increase in the attenuation of the input coaxial lines due to slowly decreasing levels of liquid Helium in the dewar of the dilution refrigerator. We observed that the extracted values of A_B always increased with time even when the temperature was kept constant and reverts back when the liquid Helium level is restored. The data shown in Fig. 8.4 takes about 2 days to acquire since one has to wait for the system to thermalize at each operating temperature. During such long periods, the liquid Helium level can change appreciably. We also verified that the extracted values of A_B remained constant when noise was added to the system to artificially elevate the temperature. All these checks were done to ensure that our experiment really follows the prediction of equation 8.1 and we can extract meaningful results for the value of T_{esc}^{RF} . The data for each temperature in Fig. 8.4 has been plotted after normalizing the x -axis with the value of I_B (A_B) extracted at the lowest temperature so that the variations in I_B (A_B) are still visible.

8.2.4 Temperature dependence

In order to extract T_{esc}^{RF} from the data, we need the value of U_{esc}^{RF} . Data from numerical simulations² of the JBA circuit yielded a value for U_{esc}^{RF} which was 10-20% than those obtained from equation 2.33b. This would lead to a 10-20% smaller value for T_{esc}^{RF} and we observed this discrepancy in the experiments. In order to overcome this problem, we used the following procedure. At the highest temperature point, we

²The numerical simulations were used to compute escape rates in the JBA. Since we know the precise temperature (T) used in the simulations, we can extract U_{esc}^{RF} by setting $T_{esc}^{RF} = T$.

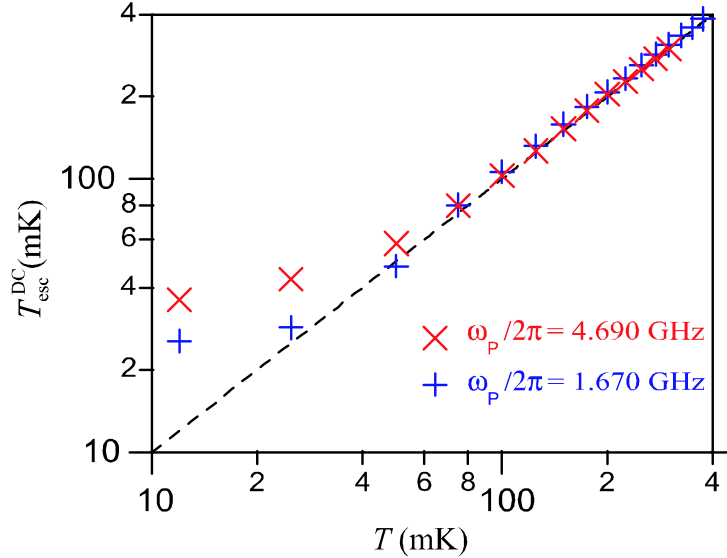


Figure 8.5: A plot of T_{esc}^{DC} vs T in a DC current biased Josephson junction. Data for sample LF with $\omega_p/2\pi = 1.670$ GHz is shown in red while that for sample HF with $\omega_p/2\pi = 4.690$ GHz is shown in blue. The dashed line is expected dependence $T_{esc}^{DC} = T$. The data falls on the dashed line for high temperatures but T_{esc}^{DC} starts to saturate at the low temperature. We believe the small deviations are due to improperly thermalized filters and unfiltered noise in the dual biasing configuration. The high frequency dynamics at the bare plasma frequency (~ 20 GHz) of the junction can also contribute to this effect.

assumed $T_{esc}^{RF} = T$, since that is the expected result in the classical regime. We can then use equation 8.5b to extract $U_{esc}^{RF} = k_B T_{esc}^{RF} \tilde{\Gamma}_{int}^{3/2}$. This extracted value of U_{esc}^{RF} is then used for all the lower temperature points. This is valid provided we can ensure that the intensity of fluctuations felt by the JBA really corresponds to the thermal fluctuations at temperature T . We verified this by biasing the junction with a DC current and measuring the escape rate from the superconducting to the normal state of the junction. We used the procedure³ described in ref. [48] to measure the escape

³The measurement protocol is basically the same as the one for JBA switching but we use a linear ramp instead of a trapezoidal pulse. This slightly changes the procedure for extracting the escape rate from the data.

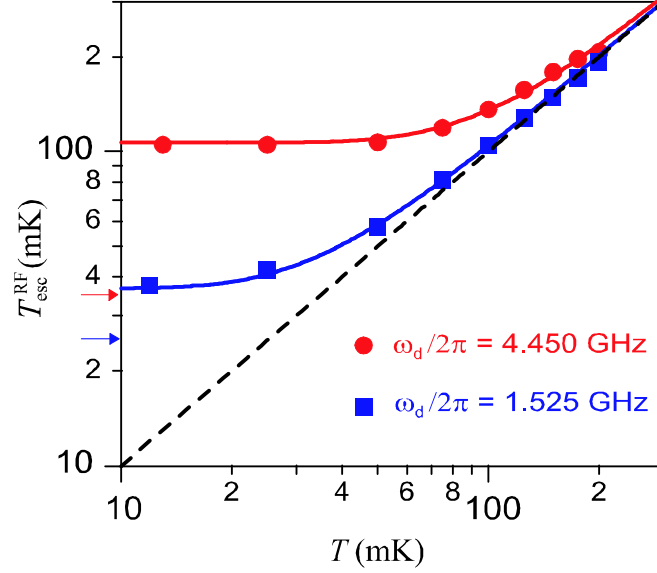


Figure 8.6: A plot of T_{esc}^{RF} vs T in the JBA. Data for sample LF with $\omega_p/2\pi = 1.670$ GHz and $\omega_d/2\pi = 1.525$ GHz is shown as blue squares. Data for sample HF with $\omega_p/2\pi = 4.690$ GHz and $\omega_d/2\pi = 4.450$ GHz is shown as red circles. The solid lines are a plot of equation 8.6 for the corresponding values of ω_d for the two samples. Data shows excellent agreement with the theoretical prediction. The dashed line is the classical dependence $T_{esc}^{RF} = T$. The arrows indicate the lowest escape temperature measured in the DC escape measurements for the corresponding sample. The errors in the measurement of escape temperature are set by the amount of statistics obtained and the stability of the drive power. It is usually less than 5%.

rates $\Gamma_{esc}^{DC}(I_{DC})$ and extract the DC escape temperature T_{esc}^{DC} . The result for samples LF and HF is shown in Fig. 8.5. We note that for both samples $T_{esc}^{DC} = T$ for higher values of T , while at low temperatures, T_{esc}^{DC} tends to saturate. At the lowest bath temperature $T \simeq 12$ mK, $T_{esc}^{DC} = 25$ mK for sample LF and $T_{esc}^{DC} = 35$ mK for sample HF. According to the MQT theory [48], we should have measured $T_{esc}^{DC} = T$ for both samples down to the lowest temperature of 12 mK. We believe that the small residual deviations are due to improperly thermalized filters and unfiltered noise in the dual biasing configuration. Another possibility is the contribution of

high frequency dynamics at the bare plasma frequency of the Josephson junction. This can happen due to the finite stray inductance between the junction and the microfabricated shunting capacitor (see section 3.2.1). Nevertheless, the DC escape temperature data validates our normalization procedure described in the previous paragraph.

Fig. 8.6 plots T_{esc}^{RF} extracted from the data shown in Fig. 8.4 as a function of bath temperature T for both samples. The solid lines are a plot of equation 8.6 with the corresponding values of ω_d used for the two samples. The agreement between theory and experiment is excellent. Note that this is not a fit to the data. The only scaling of data performed, as explained above, is the extraction of U_{esc}^{RF} from the highest temperature data point for each sample. The results for T_{esc}^{RF} not only agree with theory for the lowest temperature point, but the functional dependence on temperature as we cross-over from the classical ($k_B T \gg \hbar\omega_d$) to quantum regime ($k_B T \ll \hbar\omega_d$) is also nicely reproduced.

8.2.5 Detuning dependence

We also studied the variation of T_{esc}^{RF} as function of drive frequency ω_d for each sample separately. Since the range of drive frequencies accessible for a given sample is small ($\omega_d \sim \omega_p$), we expect that the saturation temperature $T_{esc}^{RF}(T \rightarrow 0) = \hbar\omega_d/2k_B$ is roughly constant for each sample. Fig. 8.7 shows a plot of $T_{esc}^{RF}(T \rightarrow 0)$ as a function of $\omega_d/2\pi$ for both samples. Data for sample LF (blue circles) show a fairly constant value of the saturation temperature which is in good agreement with the theoretical prediction (blue dashed line). However, the data for sample HF (red circles) shows a much stronger variation in the saturation temperature. The agreement with theory is

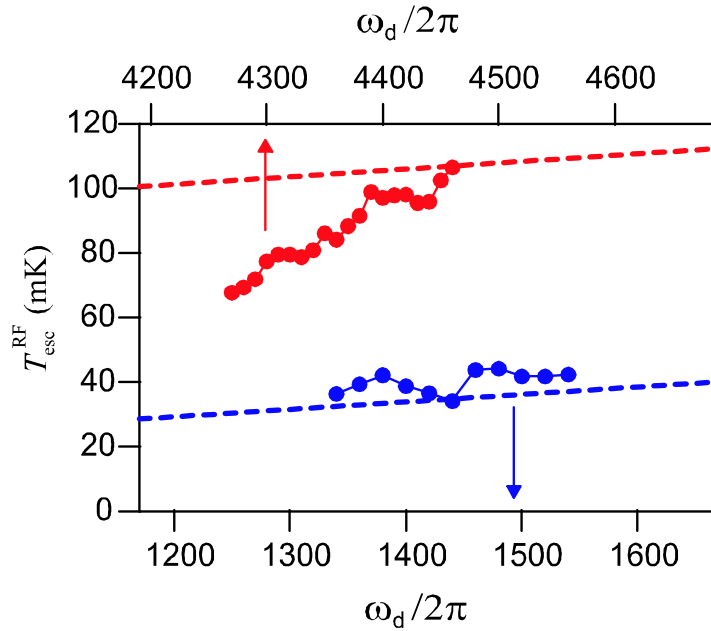


Figure 8.7: A plot of T_{esc}^{RF} vs $\omega_d/2\pi$ measured at a bath temperature $T \simeq 12$ mK for samples LF (blue, bottom axis) and HF (red, top axis). The dashed lines are the expected theoretical dependence $T_{esc}^{RF} = \hbar\omega_d/2k_B$. Data for sample LF shows good agreement with theory but sample HF shows significant deviations as the drive frequency is decreased.

good only for the largest value of ω_d with T_{esc}^{RF} ($T \rightarrow 0$) falling steadily with decreasing frequency. We do not fully understand this behavior at this time but we discuss one possible mechanism below.

The theory described in the previous chapter is derived for operating points very close to the bifurcation point. In practice, we always have to work at a finite distance from the bifurcation point so that the escape rate is small and can be conveniently measured. Since we always work in a constant range of escape rates, the distance to bifurcation increases as we go to higher temperatures (see Fig. 8.4). As we noted in the previous chapter (Fig. 7.9), the position of the peak in the spectrum of the

amplified quadrature in the JBA depends on the distance to the bifurcation. For large distances, the peak is located at $f \simeq \pm |\omega_p - \omega_d| / \Gamma$ while at small distances the peak is located at $f = 0$. In real frequency space, these two positions correspond to ω_p and ω_d respectively, i.e., the peak moves from the plasma frequency to the drive frequency as one approaches the bifurcation point. When we calibrate the barrier height at the highest bath temperature, the relevant frequency is closer to ω_p while for the data at the lowest temperature, this frequency moves to ω_d . This would pose no problem if the impedance shunting the non-linear oscillator was frequency independent as is assumed in the theory discussed in the previous chapter. In practice, this becomes difficult to implement, especially at higher frequencies. If the impedance varies significantly between these two frequencies, the calibration of the barrier height becomes invalid at low temperatures leading to an error in the measured escape temperature. Clearly, this effect will be more pronounced for larger detuning ($\omega_p - \omega_d$) as a larger frequency range is spanned. We now discuss some data which provides evidence that the impedance shunting the junction varies with frequency significantly.

Fig. 8.8 shows the 2D phase plot characterizing the non-linear resonance for sample HF. Each column is a plot of the reflected signal phase (ϕ , in color) as a function of drive power. The different columns correspond to different drive frequencies. In the bistable region, we swept the power in both directions to measure both the upper and lower bifurcation points. Data for forward and reverse power sweeps are shown in alternate columns clearly highlighting the hysteresis. The boundary of the bistable region shows ripples instead of the expected smooth variation. The fact that the upper and lower bifurcation points move in opposite directions suggests that these ripples are due to variations in the shunting impedance and not due to a frequency depen-

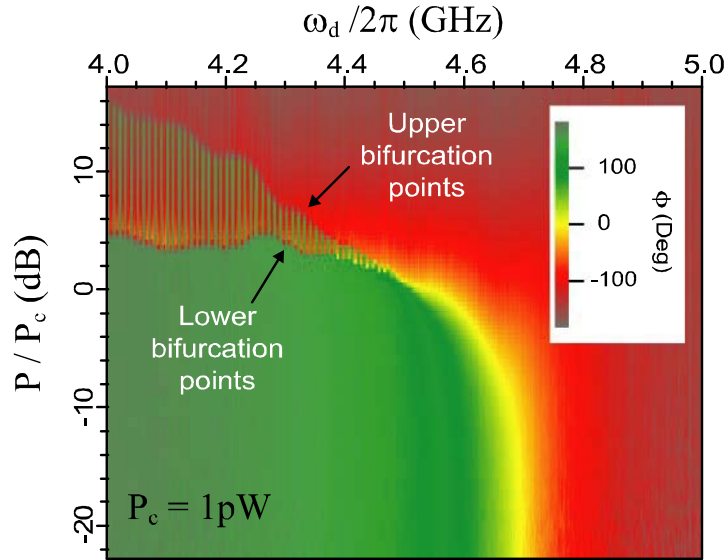


Figure 8.8: A 2D phase plot characterizing the non-linear resonance for sample HF. Each column is a plot of the reflected signal phase (ϕ , in color) as a function of drive power (P/P_c). P_c is the critical drive power. The different columns correspond to different drive frequencies. In the bistable region, we swept the power in both directions to measure both the upper and lower bifurcation points. Data for forward and reverse power sweeps are shown in alternate columns clearly highlighting the hysteresis. Also visible are ripples in the boundary marking the bistable region, indicating variations in the impedance shunting the JBA.

dent power coupling which would have caused them to move in the same direction. The width of the hysteresis is proportional to the real part of the impedance⁴ at that frequency. The use of the hybrid to implement the differential RF biasing scheme can lead to this impedance variation. The electric length of the two paths from the hybrid to the junction have to be kept as identical as possible. Any asymmetry in the two paths can lead to variations in the impedance seen by the junction. This is difficult to implement especially at higher frequencies. The 2D phase plot shown in Fig. 3.6

⁴The width of the hysteresis is proportional to the relative detuning α and the quality factor Q of the resonator. The dependence on α is smooth so any ripples in the hysteresis width has to do with local variations in Q or the real part of the impedance at that frequency. See also ref. [59].

and all other samples we measured without the differential biasing scheme showed no ripples in the width of the hysteresis. Sample LF also showed some variations in the shunting impedance which is reflected in the ripples in the measured T_{esc}^{RF} as seen in Fig. 8.7, though the effect here is much smaller.

At this stage, we believe that the disagreement with theory for sample HF is predominantly due to the impedance variations, though we cannot completely rule out other effects not included in the theory described in the previous chapter. For future experiments, we hope to solve this impedance variation problem by implementing the non-linear oscillator using geometric resonators which would provide a much better control over the impedance shunting the junction.

8.3 Parametric amplification in the JBA

We now describe some preliminary experiments which test the performance of the JBA as a parametric amplifier (PARAMP). These are proof of principle experiments and have not yet been optimized for practical applications.

8.3.1 Measurement protocol

The measurement protocol is as follows. We energize the JBA with a CW signal at frequency ω_d close to the critical point. This signal is known as the *pump*. To this *pump*, we add another input at frequency ω_s which is much weaker than the *pump*. This is called the *signal*. As explained in section 7.3, the reflected output from the PARAMP contains an amplified component of the *signal* at ω_s along with another component called the *idler* at $\omega_i = 2\omega_d - \omega_s$. Fig. 8.9a shows a schematic of the measurement protocol while 8.9b shows the *pump*, *signal* and *idler* components in the

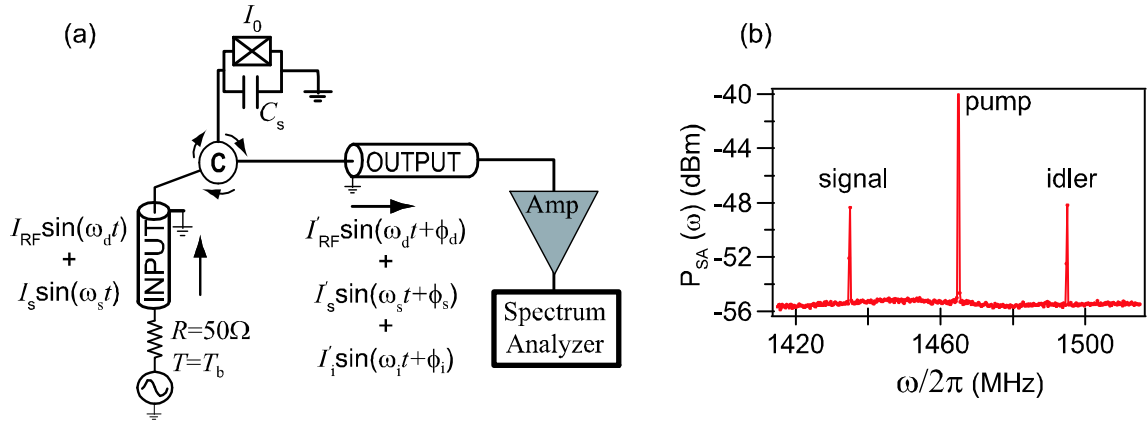


Figure 8.9: Panel (a) shows a schematic of the measurement protocol for parametric amplifier experiments. The non-linear Josephson resonator is driven with strong tone called the *pump* (ω_d). When a weak tone called *signal* (ω_s) is added to the pump, the reflected component at the output contains an amplified version of the signal and an additional tone called the *idler* ($\omega_i = 2\omega_d - \omega_s$). The pump is reflected with a phase shift and only a fractional change in its amplitude. The circulator (C) is used to separate the input from the output. Panel (b) shows the *pump*, *signal* and *idler* components at the output of a PARAMP as measured by a spectrum analyzer. The *signal* is usually kept 40 dB lower in power (before amplification) than the *pump*. Here it is only about 23 dB lower and the gain is about 15 dB.

output from the PARAMP as measured by a spectrum analyzer. The experimental setup for the PARAMP measurements including the filtering is similar to the readout part of the qubit setup shown in Fig. 5.2. The *pump* and the *signal* were combined at room temperature using a directional coupler and the output signal was measured using a spectrum or network analyzer. The spectrum analyzer was used for noise measurements while the network analyzer was to measure the gain of the PARAMP.

8.3.2 Gain and noise temperature

We used the following procedure to measure the gain of the PARAMP. Using a network analyzer, we first measured the transmission through the entire measurement chain but with the *pump* off. In the absence of the *pump*, the JBA behaves like a harmonic oscillator for a weak input. Since the intrinsic dissipation in the JBA is very small, it reflects the entire signal back, i.e., the gain is unity. We then repeat the same measurement with the *pump* on and divide the result by the first measurement. This directly gives us the gain of the PARAMP. We always ensure that the strength of the *signal* is 40 dB lower in power than the *pump* to prevent saturating the PARAMP. We do the same two measurements for determining the noise performance but record the output power spectrum using a spectrum analyzer. The ratio of the two noise spectrums gives us information about the noise added by the PARAMP.

Fig. 8.10 shows the gain as well as the noise spectrum (with *pump* on and off) for an operating point close to the critical point. Note that the gain is maximum at the *pump* frequency (1450 MHz) and is greater than 25 dB. The spurious peak at 1450 MHz in the noise spectrum is the remnant of the *pump* signal which we tried to cancel by adding a coherent tone to the output at the *pump* frequency. The unwanted *pump* signal at the output of the PARAMP within its band is one of the drawbacks of this mode of operation. In the next chapter, we will briefly outline a new, Josephson junction based amplifier which overcomes this problem.

Fig. 8.11 shows a plot of the power gain (color) of the PARAMP as a function of *signal* frequency and *pump* power. The *pump* frequency used was 1450 MHz. This plot qualitatively agrees with the predicted gain shown in Fig. 7.10 with regions of single and double peaks in the gain as a function of frequency. An important difference

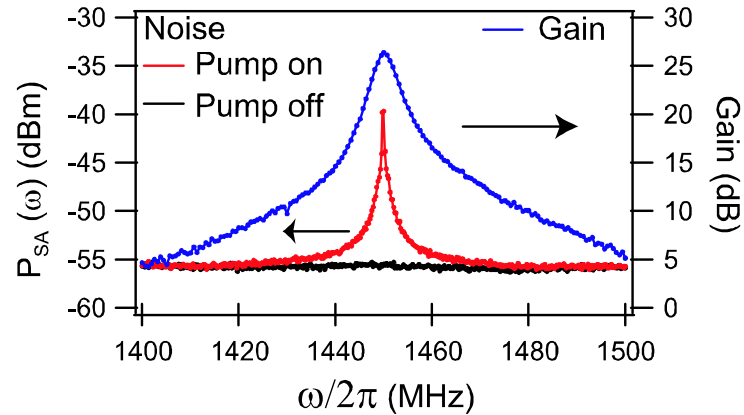


Figure 8.10: Gain (right axis)and noise measurements (left axis) in a PARAMP. Pump frequency is 1450 MHz and the pump power is adjusted for maximum gain. We note a maximum gain of about 27 dB at 1450 MHz which is the pump frequency. Output noise as measured by a spectrum analyzer is plotted in black (pump off) and red (pump on). The increase in noise with the pump on tells us about the noise added in the amplification process. The spurious peak at 1450 MHz in the noise spectrum is the remnant of the pump signal which we tried to cancel by adding a coherent tone to the output at the pump frequency

we note is that the gain is not perfectly symmetric about the *pump* frequency as predicted by theory. This is due to the assumption in the theory that the resonator has no intrinsic dissipation. If we include additional sources of dissipation, the gain becomes asymmetric [101]. Also note how the bandwidth increases with decreasing gain. This is a common feature of PARAMPS. Nevertheless, we can see that it is possible to get about 50 MHz of bandwidth with a gain of about 15 dB.

We will now describe how to extract the noise temperature of the PARAMP. We will call the frequency dependent power gain of the PARAMP as $G_P(\omega)$ and its noise temperature $T_{NP}(\omega)$. In what follows, we will express the noise power as a

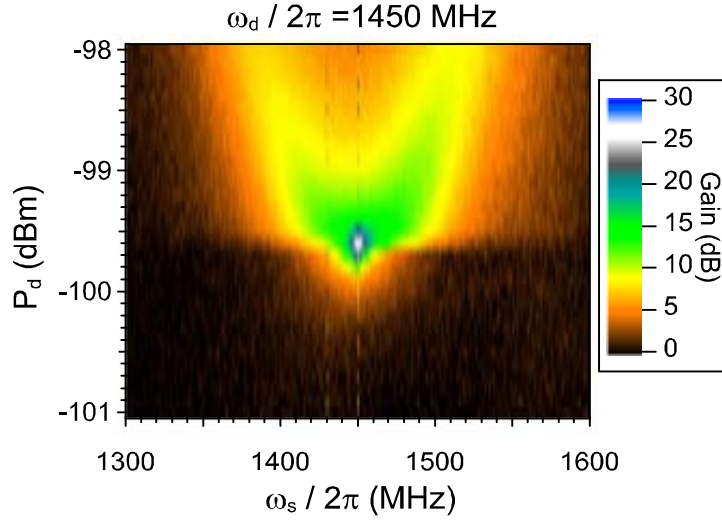


Figure 8.11: Figure shows a plot of the power gain (color) of the PARAMP as a function of signal frequency and pump power. The pump frequency used was 1450 MHz. This plot qualitatively agrees with the predicted gain shown in Fig. 7.10 with regions of single and double peaks in the gain as a function of frequency.

temperature so that the output noise power of the PARAMP can be written as

$$T_{NP}^{out} = G_P(\omega) T_{NP}(\omega) . \quad (8.10)$$

When the *pump* is off, the total output noise power is given by

$$T_{N, \text{pump off}}^{out}(\omega) = G_S(\omega) (T_{NS}(\omega) + T_{\text{vac}}(\omega)) \quad (8.11)$$

where $G_S(\omega)$ and $T_{NS}(\omega)$ are the gain and noise temperature of the measurement chain while $T_{\text{vac}}(\omega) = \hbar\omega/2k_B$ is the effective temperature of the vacuum. In our experiments, $T_{NS}(\omega) \gg T_{\text{vac}}(\omega)$ (see later) and hence we can ignore $T_{\text{vac}}(\omega)$. With

the *pump* on, we get

$$T_{N, \text{pump on}}^{\text{out}}(\omega) = G_S(\omega) T_{NP}^{\text{out}}(\omega) + G_S(\omega) T_{NS}(\omega) . \quad (8.12)$$

Taking the ratio of the two and dividing by the gain of the PARAMP, we get,

$$\frac{T_{N, \text{pump on}}^{\text{out}}(\omega)}{G_P(\omega) T_{N, \text{pump off}}^{\text{out}}(\omega)} = T_{N, \text{ratio}} = 1 + \frac{T_{NP}(\omega)}{T_{NS}(\omega)} . \quad (8.13)$$

Since we can measure $G_P(\omega)$ and the ratio $T_{N, \text{pump on}}^{\text{out}}(\omega) / T_{N, \text{pump off}}^{\text{out}}(\omega)$ as described above, we can compute $T_{N, \text{ratio}}$. We can then determine $T_{NP}(\omega)$ from the above equation if we know $T_{NS}(\omega)$. Accurately determining the system noise temperature of a cryogenic setup is quite challenging and requires a well calibrated variable temperature load or a calibrated noise source which works at cryogenic temperatures. We were only able to make a rough measurement of the system noise temperature by varying the temperature of the base temperature stage of our cryostat, and estimated it to be $T_{NS} \simeq 12 \text{ K} \pm 20\%$ within the frequency band of our experiment (1.3-1.5 GHz). This number agreed with our estimate using the manufacture provided number for the noise temperature of the HEMT amplifier (2.2 K) and about 6 dB of loss in our output line from the sample to the HEMT amplifier. This limits our accuracy to determine the noise temperature of the PARAMP to $\pm 20\%$.

Fig. 8.12 shows plots of the gain and noise temperature (in color) as a function of *signal* frequency and *pump* frequency. The *pump* power at each value of *pump* frequency has been optimized for maximum gain. In panel (b), one should ignore the blue region on either side as it does not represent valid data. Also, the noise temperature data becomes noisy as one moves away from the *pump* frequency due

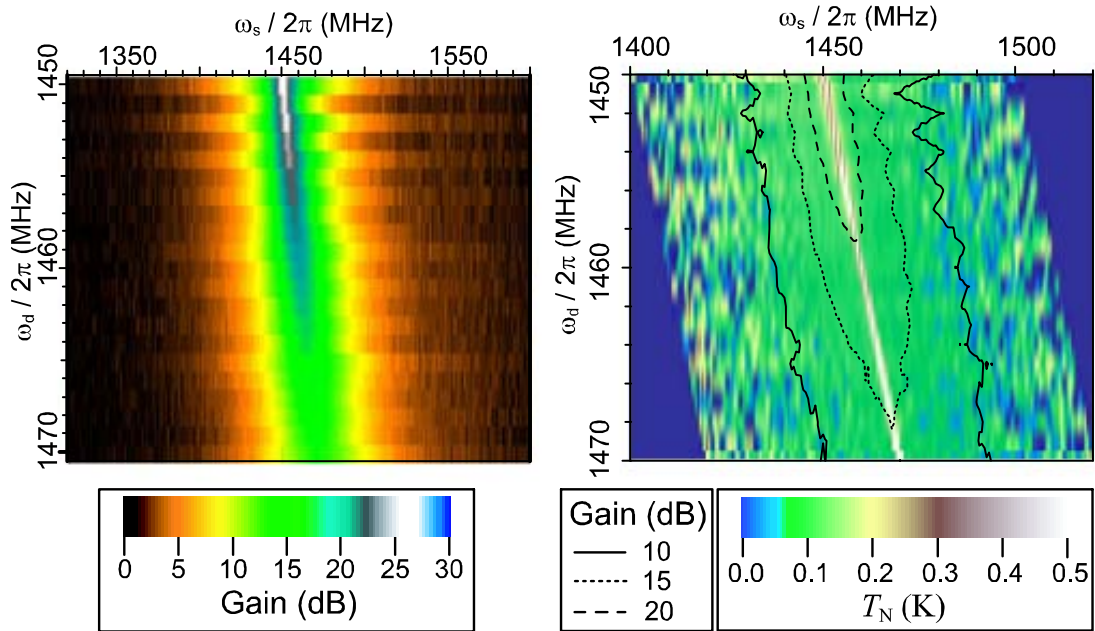


Figure 8.12: Panel (a) and (b) show a plot of gain and noise temperature respectively as a function of signal frequency and pump frequency. The pump power at each value of pump frequency has been optimized for maximum gain. Note the difference in horizontal scales between the two panels. Also in panel (b), one should ignore the blue region on either side as it does not represent valid data. The noise temperature data becomes noisy as one moves away from the pump frequency due to reduced gain. The bright white line at the center of panel (b) is the remnant of the pump. The different black lines are contours of constant gain with the gain increasing as one approaches the pump frequency.

to reduced gain. The bright white line at the center of panel (b) is the remnant of the *pump*. The different black lines are contours of constant gain with the gain increasing as one approaches the center. We note that it is possible to achieve a noise temperature in the range 0.08 - 0.15 K (green areas) with a gain of 15 dB and higher. The quantum limited value for the noise temperature at a frequency $\omega_s/2\pi = 1.5$ GHz is $\hbar\omega_d/k_B = 0.072$ K. So the PARAMP achieves near quantum limited performance with decent gain and is already good enough for practical applications like being the

first stage amplifier for experiments like dispersive qubit measurements. Though the strong pump signal still needs to be isolated from the qubit using isolators. Section 9.3 discusses a modified design to solve this problem.

8.3.3 Squeezing measurements

Squeezing of thermal and vacuum noise has been demonstrated in Josephson junction based parametric amplifiers [105, 25]. We discuss below some preliminary experiments testing the ability of the JBA to squeeze vacuum noise ($T \ll \hbar\omega_d/k_B$). The measurement protocol is similar to the one described in 8.3.1 but now we beat the output signal with another signal at the *pump* frequency ω_d using a mixer. The beating signal is phase locked with the *pump*. The output of the mixer is filtered to remove the high frequency components and fed to a spectrum analyzer. We now look at the spectrum near zero frequency. We first looked at the case when a *signal* tone at ω_s was present along with the *pump* at ω_d . The mixer combines the signals at ω_s and $\omega_i = 2\omega_d - \omega_s$ and outputs them at a frequency $|\omega_d - \omega_s|$. The spectrum at $|\omega_d - \omega_s|$ is monitored as a function of the phase difference (ϕ_{LO}) between the *pump* and the beating signal. The result is shown in Fig. 8.13a. The black curve corresponds to the *pump* being off and shows no dependence on ϕ_{LO} while the red curve taken with the *pump* on shows strong variations. At certain values of ϕ_{LO} , the red curve falls below the black curve implying a destructive interference between the components at ω_s and ω_i . When the same thing happens with the noise, it is called squeezing and is shown in Fig. 8.13b.

Though the effect is small we can clearly see the red curve dipping just below the black curve which corresponds to the vacuum floor. The squeezing effect in the output

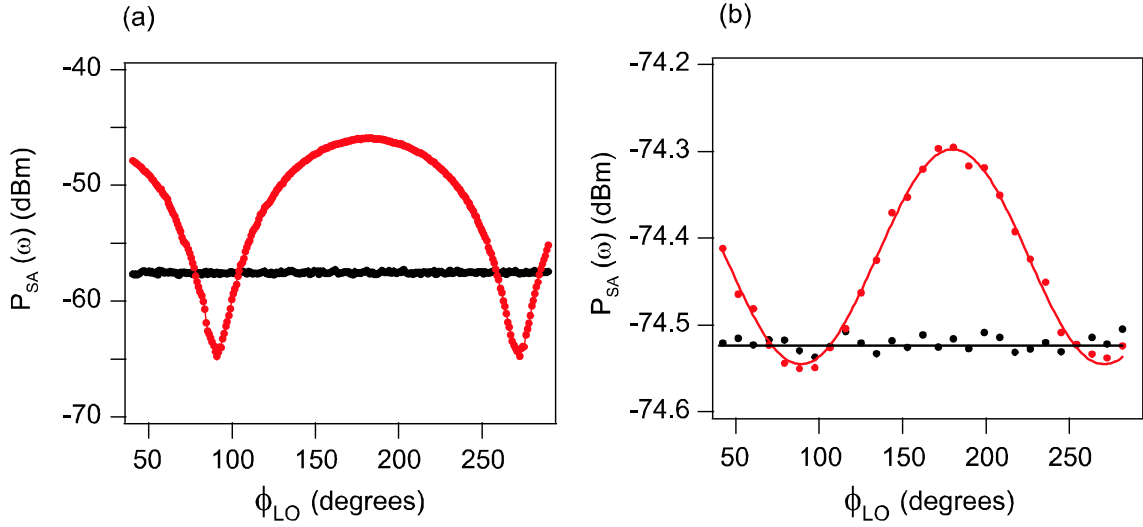


Figure 8.13: Data demonstrating parametric amplification and de-amplification of an input signal is shown in panel (a). The pump frequency used was 1450 MHz while the signal frequency was 1460 MHz. The output of the PARAMP was beat with another tone at 1450 MHz using a mixer. The magnitude of the resulting mixed down signal at the difference frequency 10 MHz is plotted as function of the phase difference (ϕ_{LO}) between the pump and the beating signal. The black curve is with the pump off while the red curve is with the pump. Panel (b) shows the same data but without any signal at 1460 MHz. The output now corresponds to the output noise spectrum of the PARAMP. The solid red curve is a sinusoidal fit to the data. In both cases we see that for certain values of ϕ_{LO} , the red curve dips below the black curve indicating destructive interference of components at the signal (1460 MHz) and idler (1450 MHz) frequencies.

is small because of the high value of our system noise temperature $T_{NS} \gg \hbar\omega_d/2k_B$. When only vacuum noise is feeding the measurement chain (*pump* is off), the output noise expressed as a temperature has a value $G_S(T_{NS} + T_{vac})$ where $T_{vac} = \hbar\omega_d/2k_B$ is the temperature of vacuum noise. When the *pump* is on, we get $G_S(T_{NS} + T_{vac}^{squeeze})$, where $T_{vac}^{squeeze}$ is the temperature of the squeezed vacuum. Even if we assume perfect squeezing ($T_{vac}^{squeeze} = 0$), the output noise is given by $G_S T_{NS}$. The ratio between the two values which is effectively what we measure is $1 + T_{vac}/T_{NS}$. In our experiment,

$T_{\text{vac}}/T_{NS} \simeq 0.003 \ll 1$, and hence the squeezing effect in the output is very small. We now provide a rough estimate of the amount squeezing achieved. From the noise temperature measurements, our best estimate of $T_{\text{vac}}/T_{NS} \sim 0.004$. The red curve dips below the black curve in Fig. 8.13b by about 0.026 ± 0.008 dB. We can then estimate the amount of squeezing $T_{\text{vac}}^{\text{squeeze}}/T_{\text{vac}}$. Unfortunately the error in the noise measurements (estimated from the spread in the black data points) is so large that the estimated amount of squeezing goes all the way from 10% to better than 100% squeezing (which is not possible). At this point, we would just like to say that we observe some evidence of squeezing but further improvements in the system noise temperature and the precision of noise measurements are required to estimate the amount of squeezing more precisely.

Chapter 9

Future directions

In this chapter, we will briefly discuss the future directions and perspectives of experiments related to the work done for this thesis.

9.1 Evolution of the JBA

The non-linear oscillator in the JBA was made by shunting the Josephson junction with a micro-fabricated capacitor. As we learned in chapter 3, fabrication of such a capacitor at microwave frequencies is not easy. The stray elements associated with this capacitance can often lead to the absence of the bifurcation phenomena (section 3.4). Moreover, improvements in the sensitivity and speed of the JBA requires operation at higher frequencies. In order to meet these requirements, it was decided to use geometric resonators instead of lumped element ones.

Geometric resonators can be easily fabricated with much better control of their parameters. They were made by using a section of micro-fabricated transmission line with capacitors at each end playing the role of mirrors in a cavity resonator.

The resonant frequency is now given by the length of the transmission line and the quality factor is controlled by the value of the capacitance. By fabricating them with superconducting materials, the intrinsic dissipation can be made very small. The non-linearity is introduced by placing the Josephson junction at the center of the resonator where there is an antinode in current at resonance. Fig. 9.1 shows an optical image of such a device.

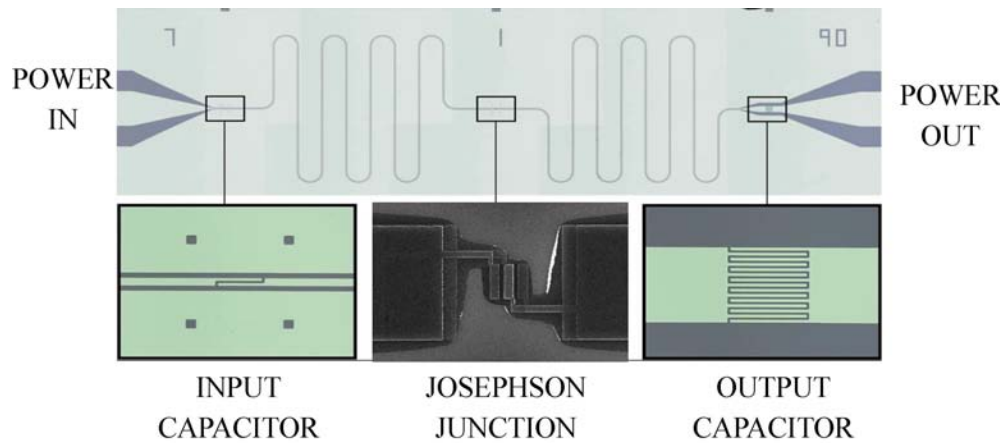


Figure 9.1: Optical image of a Cavity Bifurcation Amplifier. The upper half shows the transmission line cavity. The lower half shows the input coupling capacitor, an SEM image of the Josephson junction which is placed in the center of the resonator, and the output coupling capacitor.

This device has been nicknamed the Cavity Bifurcation Amplifier (CBA) [66]. Note that the physics of operation of the CBA is essentially the same as the JBA since both are non-linear resonators. The CBA offers the advantage of flexibility in design, possibility of multiplexing, operation at higher frequencies and better control over the impedance seen by the junction. The CBA has already been successfully implemented as a qubit readout with similar performance as the JBA [43]. Future qubit experiments in our group will use the new CBA design for the readout.

9.2 Back-action of the bifurcation readout on a qubit

In chapter 6, we saw that the readout operation induced relaxation in the excited state of the qubit, ultimately resulting in a reduced measurement contrast. Coupling to spurious environmental modes due to the AC Stark shift associated with the readout operation was identified as one possible culprit. But this could not completely explain the reduction in contrast observed. The qubit experiments carried out with the CBA also suffered from this reduced contrast. We believe that the highly excited non-linear oscillator has a "cooling" effect on the qubits and hence leads to their relaxation. This would be consistent with the fact that we never observed any excitation of the qubit ground state during the readout. More theoretical analysis is required to compute the effective spectral density of fluctuations seen by the qubit on the phase port, when the readout is energized.

It is also possible that coupling a bifurcation amplifier directly to the qubit is too invasive. We are slowly learning from experience that these quantum two level systems are more delicate than we imagined them to be. To minimize the effect of the readout on the qubit state, the best approach seems to be the one involving a linear resonator coupled to a qubit where the measurement is carried out with a few photons. This approach is used in the circuit QED experiments [33]. The few photons are enough to perform a fully projective measurement, but result in a poor signal to noise due to limitations in the amplifiers used to amplify these photons. This is where the JBA could play a role. The JBA/CBA could be operated as a parametric amplifier to provide a first stage of amplification for these few photons. As we saw in chapter 7, we can achieve a gain of about 20 dB with a near quantum limited noise temperature. This is already good enough to enable single-shot measurements of the

to modes are defined as follows

$$\begin{aligned}
 \delta_X &= (\delta_1 + \delta_2 - \delta_3 - \delta_4) / 4 \\
 \delta_Y &= (-\delta_1 + \delta_2 + \delta_3 - \delta_4) / 4 \\
 \delta_Z &= (\delta_1 - \delta_2 + \delta_3 - \delta_4) / 4
 \end{aligned} \tag{9.1}$$

where δ_1 , δ_2 , δ_3 and δ_4 are the gauge-invariant phases across the four junction. In this representation the Hamiltonian of the four junction system reduces to

$$H_{JPC} = -4E_J \left(\cos \delta_X \cos \delta_Y \cos \delta_Z \cos \frac{\Phi}{4\varphi_0} + \sin \delta_X \sin \delta_Y \sin \delta_Z \sin \frac{\Phi}{4\varphi_0} \right)$$

where E_J is the Josephson energy of each junction and Φ is the flux in the loop. If we work at a flux bias $\Phi = \Phi_0/2$ where Φ_0 is the flux quantum, and for small excitations, the Hamiltonian reduces to

$$H_{JPC}^{mix} = -2\sqrt{2}E_J \left[\delta_X \delta_Y \delta_Z - \frac{(\delta_X^2 + \delta_Y^2 + \delta_Z^2)}{2} \right]. \tag{9.2}$$

The Hamiltonian contains a pure non-linear mixing term $\delta_X \delta_Y \delta_Z$ which allows three mode mixing. The other term only leads to renormalization of the mode frequencies. The implementation of this Hamiltonian is a key feature of the JPC design.

The device can be operated in either the amplification mode with photon number gain ($\omega_{pump} = \omega_s + \omega_i$) or the frequency conversion mode with no photon number gain ($\omega_{pump} = |\omega_s - \omega_i|$). Preliminary experiments have yielded promising results with gain as high 30 dB [106] and we are in the process of investigating the noise performance and the dynamic range of the JPC.

Chapter 10

Conclusions

In this thesis, we have demonstrated that a dynamical bifurcation can be used for amplifying quantum signals. The device which we call the Josephson Bifurcation Amplifier (JBA), exploits a bifurcation in a driven, non-linear oscillator made with a Josephson tunnel junction and a shunting capacitor. The Josephson tunnel junction is the only electronic circuit element which remains non-linear and non-dissipative at arbitrary low temperatures. In this new scheme, all available degrees of freedom in the dynamical system participate in information transfer and none contribute to unnecessary dissipation resulting in excess noise.

We performed a novel, phase-sensitive, microwave experiment demonstrating that the Josephson plasma oscillation can transition between the two dynamical states predicted for a driven non-linear system[28]. Using different samples, we have shown that this dynamical phenomenon is stable, reproducible and can be precisely controlled, thus opening the possibility for practical applications like amplification. Any signal coupled to the critical current of the junction can be detected by monitoring the changes in the dynamical state of the non-linear oscillator[57].

This approach was used to develop a non-linear, dispersive readout for superconducting qubits by coupling a quantronium qubit with the JBA[29]. In order to perform a readout, the resonator is RF-energized to a level where its oscillation state now acts as a sensitive pointer of the qubit state. This technique does not generate any dissipation on chip since the resonator is only damped by circuitry outside the chip, i.e. a 50Ω transmission line with a matched circulator and amplifier, and enables a high-fidelity qubit readout with a MHz repetition rate. We have measured Rabi oscillations and Ramsey fringes in the quantronium qubit with sufficient speed that real time filtering to correct for drifts in the charge and flux bias becomes possible. The coherence properties of the qubit were similar to those of other superconducting qubits. Exploiting the QND nature of the readout, we performed several successive readouts within the energy relaxation time of the qubit (T_1). This provided valuable information on the readout-induced interaction between the qubit and its environment and was useful in understanding the observed contrast. Significant improvement was achieved in the readout contrast (68%) as compared to the original quantronium measurements (10%, [6]).

The JBA was also operated as a parametric amplifier to amplify small signals coupled via the drive port (as opposed to parametric coupling of signals in the qubit readout) achieving signal gain of about 20 dB and near quantum limited noise temperature. We also showed some evidence of squeezing in the JBA. The parametric amplifier model of the JBA also helps us understand its behavior in the quantum regime. The dynamical transition between the metastable states of the JBA takes place via an activation process even in the limit $T \rightarrow 0$ as opposed to a tunneling process observed in static systems. The JBA acts as a parametric amplifier for

the quantum fluctuations and converts them into thermal fluctuations which in turn lead to a transition via activation. The creation of thermal photons from zero point quantum fluctuations is the essence of the Dynamical Casimir Effect which has been traditionally discussed in the context of mechanical modulation of resonant cavities as opposed to the electrical modulation in our case. Theory predicts that the effective temperature of the amplified quantum noise when $T \rightarrow 0$ is given by $\hbar\omega_d/2k_B$ where ω_d is the drive frequency. Experimental data shows good agreement with this prediction. The parametric amplifier model of the JBA brings together four aspects of working with a dynamical bifurcation: parametric amplification, squeezing, quantum activation and the Dynamical Casimir Effect.

In conclusion, we have developed a new amplification principle harnessing the non-linear, non-dissipative inductance of the Josephson junction. The JBA is competitive with other cryogenic amplifiers like the SQUID and the RF-SET, especially when low back-action is required. The JBA principle is already being used by several groups for measuring quantum systems and is well on its way to become a general purpose amplifier/detector for low temperature physics experiments.

Appendix A

JBA formulae

In this appendix, we will provide formulae for computing quantities related to the JBA. These formulae have been computed by retaining higher order terms in detuning α and the inverse of the quality factor $1/Q$ and provide better estimates especially for small Q .

1. Upper bifurcation current

$$I_B^+ = \frac{16}{3\sqrt{3}} I_0 \alpha^{3/2} (1 - \alpha)^{3/2} \left(1 + \frac{9}{4\Omega^2}\right)^{1/2} \quad (\text{A.1})$$

2. Barrier height

$$U_{esc}^{RF} = \frac{64}{9\sqrt{3}} E_J \alpha (1 - \alpha)^3 \left(1 + \frac{9}{4\Omega^2}\right) \quad (\text{A.2})$$

3. Critical detuning

$$\Omega_c = \sqrt{3} - \frac{3}{4Q} \quad (\text{A.3})$$

Note that the critical frequency is no longer universal for small Q . In practice,

the approximation $\Omega_c = \sqrt{3}$ gives less than 5% error for $Q > 5$.

Appendix B

Mathematica formulae

In this Appendix, I provide some useful *Mathematica* formulae to compute various qubit related quantities. Note that the symbols used in the formulae may differ from ones used in the thesis but I describe all symbols used. These formulae were written for *Mathematica* version 5.0.

1. **Energy levels of a split Cooper-pair box:** The function returns the energy levels in units of E_J . Multiply the result by E_J to get the real energy. The function takes five arguments: ng is gate charge in units of single electron, ib is the level number starting from 1 (ground state), $Ej0Ec$ is the ratio E_J/E_C , d is the asymmetry in the two junctions of the split Cooper-pair box and $\delta flux$ is the flux in the loop in units of flux quantum. The function can also be used to compute the transition frequencies

between levels by subtracting the energy of two levels.

$$\begin{aligned}
 \text{EnergyLevels}[ng_ , ib_ , EjoEc_ , d_ , \delta flux_] := \\
 & (ng1 = \text{Abs}[\text{Mod}[ng + 1, 2] - 1]; \text{If}[ng1 == -1, ng1 = 0.999]; \\
 & \frac{1}{EjoEc} \text{MathieuCharacteristicA}[ib - \text{Mod}[ib, 2] - (-1)^{ib} ng1, \\
 & \quad - \left(0.5 EjoEc \sqrt{\frac{1 + d^2 + (1 - d^2) \text{Cos}[2\pi \delta flux]}{2}} \right)]
 \end{aligned}$$

2. Loop currents in the split Cooper-pair box: The function returns the loop currents in the nA. The function arguments are the same as described above except for $EjGHz$ which is the Josephson energy given in GHz, and δ is the phase (divided by 2π) across the split Cooper-pair box. The derivative of this function with respect to δ at $\delta = 0$ gives the effective critical current. The effective inductance is proportional to the inverse of the effective critical current.

$$\begin{aligned}
 \text{iloopnA}[ng_ , ib_ , EjoEc_ , d_ , \delta_ , EjGHz_] := \\
 2.01 \text{EjGHz} D[\text{EnergyLevels}[\text{Mod}[ng, 2, -1], ib, EjoEc, d, y], y] /. \{y \rightarrow \delta\}
 \end{aligned}$$

With these two functions, we can calculate all the relevant numbers concerning the measurement of the quantum qubit with the JBA.

Appendix C

Numerical simulations

Here, I will describe the procedure used to simulate the behaviour of the JBA by numerically solving the differential equations describing its dynamics. The full circuit including the important stray elements is shown in Fig. C.1.

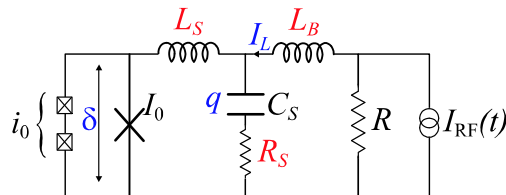


Figure C.1: Full circuit model of the JBA including important stray elements

I_0 is the critical current of the readout junction, i_0 is the effective critical of the qubit, C_S is the on-chip capacitance shunting the junction and R is the impedance of the transmission line bring signals in and out of the device. TheThe stray elements L_S , R_S , and L_B are highlighted in red. The inductance (L_S) is due to the imperfect screening of currents in the capacitor plates by the ground plane and also due the thin leads which connect the capacitor with the junction. The resistance (R_S) is

due to the finite conductivity of the Cu ground planes used in the capacitor. The inductance (L_B) is the inductance of the wire bonds used to connect the JBA sample to the transmission line. Usually, $L_S < 20$ pH, $R_S < 0.05 \Omega$ and $L_B < 1$ nH. The two small junctions represent the qubit and its effect is incorporated by using the state dependent loop currents. The three variables (highlighted in blue) used to describe the dynamics of the system are δ , the phase across the readout junction (and the qubit), q the charge on the capacitor C_S , and I_L , the current through the wire bond inductance.

C.1 Equations of motion

The three coupled differential equations describing the dynamics of the system in terms of these variables are given below:

$$\dot{\delta}(t) = \frac{1}{\varphi_0 \{1 + (L_S/L_J) \cos(\delta(t)) + (L_S/L_J^q) f_d^q(\delta(t))\} \left[\frac{q(t)}{C} + R_S \{I_L(t) - I_0 \sin \delta(t) - i_0 f^q(\delta(t))\} \right]}$$

$$\dot{q}(t) = I_L(t) - I_0 \sin(\delta(t)) - i_0 f^q(\delta(t))$$

$$\dot{I}_L(t) = \frac{R}{L_B} \left[I_{RF}(t) - I_L(t) - \frac{q(t)}{RC_S} - \frac{R_S}{R} \{I_L(t) - I_0 \sin(\delta(t)) - i_0 f^q(\delta(t))\} \right]$$

where $L_J = \varphi_0/I_0$ is the linearised Josephson inductance of the readout junction, $L_J^q = \varphi_0/i_0$ is the linearised inductance of the qubit, $f_q(\delta)$ is the function describing the loop currents of the qubit in a given state and $f_d^q(\delta) = \partial f^q/\partial \delta$ is the function describing the derivative. Before numerically solving these equations, we transform them to reduced units. Since, the typical plasma frequency of the JBA is about 1

GHz and the critical current of the junction is about $1 \mu\text{A}$, we change into a system of units where time is measured in ns, current in μA . So we make the following transformations

$$\begin{aligned} t &= 10^9 \tau \\ \delta(t) &= 2\pi x(\tau) \\ q(t) &= RC_s 10^{-6} y(\tau) \\ I_L(t) &= 10^{-6} z(\tau) \end{aligned}$$

In these new system of variables $x(\tau)$, $y(\tau)$ and $z(\tau)$, the equations become

$$\begin{aligned} \dot{x}(\tau) &= \frac{Q}{\{1 + (L_S/L_J) \cos(2\pi x(\tau)) + (L_S/L_J^q) f_d^q(2\pi x(\tau))\}} \\ &\quad \left(\frac{f_{JGHZ}}{I_{0\mu A}} \right) \left[y(\tau) + \frac{R_S}{R} \{z(\tau) - I_{0\mu A} \sin 2\pi x(\tau) - i_{0\mu A} f^q(2\pi x(\tau))\} \right] \\ \dot{y}(\tau) &= \frac{2\pi}{Q} f_{JGHZ} [z(\tau) - I_{0\mu A} \sin(2\pi x(\tau)) - i_{0\mu A} f^q(2\pi x(\tau))] \end{aligned}$$

$$\begin{aligned} \dot{I}_L(t) &= \frac{2\pi}{Q} f_{JGHZ} \left(\frac{L_J}{L_B} \right) \\ &\quad \left[I_{RF\mu A}(\tau) - z(\tau) - y(\tau) - \frac{R_S}{R} \{z(\tau) - I_{0\mu A} \sin 2\pi x(\tau) - i_{0\mu A} f^q(2\pi x(\tau))\} \right] \end{aligned}$$

The reduced equations are solved using 4th order Runge-Kutta method [107]. The code is written in C++ and the compiled code is imported into the *Labview* software which offers many data processing routines and easy to use graphical interface. The drive and the noise current are generated in Labview. The noise signal is generated

by using a Gaussian distributed random number generator in Labview. In order to correctly mimic thermal noise current at temperature T and resistance R , the random number generator is set to zero mean and a standard deviation I^{rms} given [60] by

$$I^{rms} = \sqrt{\frac{2k_B T}{R \Delta t}}$$

where Δt is the time step used in the numerical simulation. In reduced units defined above this becomes

$$i_{\mu A}^{rms} = \sqrt{\frac{2k_B T}{R \Delta \tau}} 10^{23}$$

where $i_{\mu A}^{rms}$ is the standard deviation of the current noise distribution.

The loop current functions f^q and f_d^q are computed in *Mathematica* and passed on to the C++ code as an array of 1000 values defined for a range of δ going from 0 to π . The code uses linear interpolation compute the functions from these array of values.

Bibliography

- [1] M. Muck, C. Welzel, and J. Clarke, Superconducting quantum interference device amplifiers at gigahertz frequencies, *Appl. Phys. Lett.* **82**(19), 3266–3268 (2003).
- [2] R. J. Schoelkopf, P. Wahlgren, A. A. Kozhevnikov, P. Delsing, and D. E. Prober, The radio-frequency single-electron transistor (RF-SET): A fast and ultrasensitive electrometer, *Science* **280**(5367), 1238–1242 (1998).
- [3] B. D. Josephson, Coupled Superconductors, *Rev. Mod. Phys.* **36**(1P1), 216 (1964).
- [4] Y. Nakamura, Y. A. Pashkin, and J. S. Tsai, Coherent control of macroscopic quantum states in a single-Cooper-pair box, *Nature* **398**(6730), 786–788 (1999).
- [5] J. E. Mooij, T. P. Orlando, L. Levitov, L. Tian, C. H. van der Wal, and S. Lloyd, Josephson persistent-current qubit, *Science* **285**(5430), 1036–1039 (1999).
- [6] D. Vion, A. Aassime, A. Cottet, P. Joyez, H. Pothier, C. Urbina, D. Esteve, and M. H. Devoret, Manipulating the quantum state of an electrical circuit, *Science* **296**(5569), 886–889 (2002).
- [7] J. M. Martinis, S. Nam, J. Aumentado, and C. Urbina, Rabi oscillations in a large Josephson-junction qubit, *Phys. Rev. Lett.* **89**(11), 117901 (2002).
- [8] E. Abraham and S. D. Smith, Optical bistability and related devices, *Reports on Progress in Physics* **45**(8), 815–885 (1982).
- [9] B. Yurke, L. R. Corruccini, P. G. Kaminsky, L. W. Rupp, A. D. Smith, A. H. Silver, R. W. Simon, and E. A. Whittaker, Observation of Parametric Amplification and Deamplification in a Josephson Parametric-Amplifier, *Phys. Rev. A* **39**(5), 2519–2533 (1989).
- [10] C. M. Caves, Quantum Limits on Noise in Linear-Amplifiers, *Phys. Rev. D* **26**(8), 1817–1839 (1982).

- [11] R. Bradley, J. Clarke, D. Kinion, L. J. Rosenberg, K. van Bibber, S. Matsuki, M. Muck, and P. Sikivie, Microwave cavity searches for dark-matter axions, *Rev. Mod. Phys.* **75**(3), 777–817 (2003).
- [12] N. Wadefalk, A. Mellberg, I. Angelov, M. E. Barsky, S. Bui, E. Choumas, R. W. Grundbacher, E. L. Kollberg, R. Lai, N. Rorsman, P. Starski, J. Stenarson, D. C. Streit, and H. Zirath, Cryogenic wide-band ultra-low-noise IF amplifiers operating at ultra-low DC power, *IEEE Transactions on Microwave Theory and Techniques* **51**(6), 1705–1711 (2003).
- [13] P. F. Michelson, J. C. Price, and R. C. Taber, Resonant-Mass Detectors of Gravitational-Radiation, *Science* **237**(4811), 150–157 (1987).
- [14] K. Schwab, Spring constant and damping constant tuning of nanomechanical resonators using a single-electron transistor, *Appl. Phys. Lett.* **80**(7), 1276–1278 (2002).
- [15] M. Muck, J. B. Kycia, and J. Clarke, Superconducting quantum interference device as a near-quantum-limited amplifier at 0.5 GHz, *Appl. Phys. Lett.* **78**(7), 967–969 (2001).
- [16] M. H. Devoret and R. J. Schoelkopf, Amplifying quantum signals with the single-electron transistor, *Nature* **406**(6799), 1039–1046 (2000).
- [17] H. A. Haus and J. A. Mullen, Quantum Noise in Linear Amplifiers, *Physical Review* **128**(5), 2407 (1962).
- [18] C. M. Caves, K. S. Thorne, R. W. P. Drever, V. D. Sandberg, and M. Zimmermann, On the Measurement of a Weak Classical Force Coupled to a Quantum-Mechanical Oscillator .1. Issues of Principle, *Rev. Mod. Phys.* **52**(2), 341–392 (1980).
- [19] J. M. Courty, F. Grassia, and S. Reynaud, Quantum noise in ideal operational amplifiers, *Europhysics Letters* **46**(1), 31–37 (1999).
- [20] J.-M. Courty, F. Grassia, and S. Reynaud, Thermal and quantum noise in active systems, *arXiv:quant-ph/0110021v1* (2000).
- [21] K. Wiesenfeld and B. McNamara, Period-doubling systems as small-signal amplifiers, *Phys. Rev. Lett.* **55**(1), 13–16 (1985).
- [22] K. Wiesenfeld and B. McNamara, Small-signal amplification in bifurcating dynamical systems, *Phys. Rev. A* **33**(1), 629–642 (1986).

- [23] V. M. Eguíluz, M. Ospeck, Y. Choe, A. J. Hudspeth, and M. O. Magnasco, Essential Nonlinearities in Hearing, *Phys. Rev. Lett.* **84**(22), 5232–5235 (2000).
- [24] S. Martignoli, J.-J. van der Vyver, A. Kern, Y. Uwate, and R. Stoop, Analog electronic cochlea with mammalian hearing characteristics, *Appl. Phys. Lett.* **91**(6), 064108 (2007).
- [25] R. Movshovich, B. Yurke, P. G. Kaminsky, A. D. Smith, A. H. Silver, R. W. Simon, and M. V. Schneider, Observation of zero-point noise squeezing via a Josephson-parametric amplifier, *Phys. Rev. Lett.* **65**(12), 1419–1422 (1990).
- [26] P. H. Bryant, R. Movshovich, and B. Yurke, Noise rise in nondegenerate parametric amplifiers, *Phys. Rev. Lett.* **66**(20), 2641–2644 (1991).
- [27] M. I. Dykman and M. A. Krivoglaz, Fluctuations in Non-Linear Systems Near Bifurcations Corresponding to the Appearance of New Stable States, *Physica A* **104**(3), 480–494 (1980).
- [28] I. Siddiqi, R. Vijay, F. Pierre, C. M. Wilson, L. Frunzio, M. Metcalfe, C. Rigetti, R. J. Schoelkopf, M. H. Devoret, D. Vion, and D. Esteve, Direct observation of dynamical bifurcation between two driven oscillation states of a Josephson junction, *Phys. Rev. Lett.* **94**(2), 027005 (2005).
- [29] I. Siddiqi, R. Vijay, M. Metcalfe, E. Boaknin, L. Frunzio, R. J. Schoelkopf, and M. H. Devoret, Dispersive measurements of superconducting qubit coherence with a fast latching readout, *Phys. Rev. B* **73**(5), 054510 (2006).
- [30] M. H. Devoret, A. Wallraff, and J. M. Martinis, Superconducting Qubits: A Short Review, 2004.
- [31] C. Monroe, D. M. Meekhof, B. E. King, W. M. Itano, and D. J. Wineland, Demonstration of a Fundamental Quantum Logic Gate, *Phys. Rev. Lett.* **75**(25), 4714–4717 (1995).
- [32] J. J. García-Ripoll, P. Zoller, and J. I. Cirac, Speed Optimized Two-Qubit Gates with Laser Coherent Control Techniques for Ion Trap Quantum Computing, *Phys. Rev. Lett.* **91**(15), 157901 (2003).
- [33] A. Wallraff, D. I. Schuster, A. Blais, L. Frunzio, R. S. Huang, J. Majer, S. Kumar, S. M. Girvin, and R. J. Schoelkopf, Strong coupling of a single photon to a superconducting qubit using circuit quantum electrodynamics, *Nature* **431**(7005), 162–167 (2004).

- [34] I. Chiorescu, P. Bertet, K. Semba, Y. Nakamura, C. J. P. M. Harmans, and J. E. Mooij, Coherent dynamics of a flux qubit coupled to a harmonic oscillator, *Nature* **431**(7005), 159–162 (2004).
- [35] M. Tinkham, *Introduction to Superconductivity*, Dover, 2004.
- [36] M. Büttiker, Zero-current persistent potential drop across small-capacitance Josephson junctions, *Phys. Rev. B* **36**(7), 3548–3555 (1987).
- [37] V. Bouchiat, D. Vion, P. Joyez, D. Esteve, and M. H. Devoret, Quantum coherence with a single Cooper pair, *Physica Scripta* **T76**, 165–170 (1998).
- [38] A. Cottet, *Implementation of a quantum bit in a superconducting circuit*, PhD thesis, l’Universite Paris VI, 2002.
- [39] J. Mannik and J. E. Lukens, Effect of measurement on the periodicity of the Coulomb staircase of a superconducting box, *Phys. Rev. Lett.* **92**(5), 057004 (2004).
- [40] G. Ithier, E. Collin, P. Joyez, P. J. Meeson, D. Vion, D. Esteve, F. Chiarello, A. Shnirman, Y. Makhlin, J. Schrieffer, and G. Schon, Decoherence in a superconducting quantum bit circuit, *Phys. Rev. B* **72**(13), 134519 (2005).
- [41] J. Mygind, N. F. Pedersen, and O. H. Soerensen, Direct Detection of Parametrically Generated Half-Harmonic Voltage in a Josephson Tunnel Junction, *Appl. Phys. Lett.* **29**(5), 317–319 (1976).
- [42] T. Holst and J. B. Hansen, The Plasma Resonance in Microwave-Driven Small Josephson Tunnel-Junctions, *Physica B* **165**, 1649–1650 (1990).
- [43] M. Metcalfe, E. Boaknin, V. Manucharyan, R. Vijay, I. Siddiqi, C. Rigetti, L. Frunzio, R. J. Schoelkopf, and M. H. Devoret, Measuring the decoherence of a qubit with the cavity bifurcation amplifier, *Phys. Rev. B* **76**(17), 174516 (2007).
- [44] J. Koch, T. M. Yu, J. Gambetta, A. A. Houck, D. I. Schuster, J. Majer, A. Blais, M. H. Devoret, S. M. Girvin, and R. J. Schoelkopf, Charge-insensitive qubit design derived from the Cooper pair box, *Phys. Rev. A* **76**(4), 042319 (2007).
- [45] J. Majer, J. M. Chow, J. M. Gambetta, J. Koch, B. R. Johnson, J. A. Schreier, L. Frunzio, D. I. Schuster, A. A. Houck, A. Wallraff, A. Blais, M. H. Devoret, S. M. Girvin, and R. J. Schoelkopf, Coupling superconducting qubits via a cavity bus, *Nature* **449**(7161), 443–447 (2007).

- [46] R. W. Simmonds, K. M. Lang, D. A. Hite, S. Nam, D. P. Pappas, and J. M. Martinis, Decoherence in Josephson phase qubits from Junction resonators, *Phys. Rev. Lett.* **93**(7), 077003 (2004).
- [47] D. I. Schuster, A. Wallraff, A. Blais, L. Frunzio, R. S. Huang, J. Majer, S. M. Girvin, and R. J. Schoelkopf, AC-Stark shift and dephasing of a superconducting qubit strongly coupled to a cavity field, *Phys. Rev. Lett.* **94**(12), 123602 (2005).
- [48] J. M. Martinis, M. H. Devoret, and J. Clarke, Experimental tests for the quantum behavior of a macroscopic degree of freedom: The phase difference across a Josephson junction, *Phys. Rev. B* **35**(10), 4682–4698 (1987).
- [49] M. I. Dykman and V. N. Smelyansky, Quantum-Theory of Transitions between Stable States of a Nonlinear Oscillator Interacting with the Medium in a Resonant Field, *Zhurnal Eksperimentalnoi i Teoreticheskoi Fiziki* **94**(9), 61–74 (1988).
- [50] M. Marthaler and M. I. Dykman, Switching via quantum activation: A parametrically modulated oscillator, *Phys. Rev. A* **73**(4), 042108 (2006).
- [51] M. I. Dykman, Critical exponents in metastable decay via quantum activation, *Phys. Rev. E* **75**(1), 011101 (2007).
- [52] I. Katz, A. Retzker, R. Straub, and R. Lifshitz, Signatures for a Classical to Quantum Transition of a Driven Nonlinear Nanomechanical Resonator, *Phys. Rev. Lett.* **99**(4), 040404 (2007).
- [53] G. T. Moore, Quantum Theory of Electromagnetic Field in a Variable-Length One-Dimensional Cavity, *Journal of Mathematical Physics* **11**(9), 2679 (1970).
- [54] V. V. Dodonov, Dynamical Casimir effect in a nondegenerate cavity with losses and detuning, *Phys. Rev. A* **58**(5), 4147–4152 (1998).
- [55] A. Lambrecht, M. T. Jaekel, and S. Reynaud, Motion induced radiation from a vibrating cavity, *Phys. Rev. Lett.* **77**(4), 615–618 (1996).
- [56] R. Vijay, I. Siddiqi, P. Hyafil, M. Metcalfe, L. Frunzio, and M. H. Devoret, In preparation.
- [57] I. Siddiqi, R. Vijay, F. Pierre, C. M. Wilson, M. Metcalfe, C. Rigetti, L. Frunzio, and M. H. Devoret, RF-driven Josephson bifurcation amplifier for quantum measurement, *Phys. Rev. Lett.* **93**(20), 207002 (2004).

- [58] L. D. Landau and E. M. Lifshitz, *Small Oscillations*, chapter V, Mechanics, Pergamon Press, 1960.
- [59] V. E. Manucharyan, E. Boaknin, M. Metcalfe, R. Vijay, I. Siddiqi, and M. Devoret, Microwave bifurcation of a Josephson junction: Embedding-circuit requirements, *Phys. Rev. B* **76**(1), 014524 (2007).
- [60] R. L. Kautz, Thermally Induced Escape - the Principle of Minimum Available Noise Energy, *Phys. Rev. A* **38**(4), 2066–2080 (1988).
- [61] M. I. Dykman and M. A. Krivoglaz, Theory of Fluctuational Transitions between the Stable States of a Non-Linear Oscillator, *Zhurnal Eksperimentalnoi i Teoreticheskoi Fiziki* **77**(1), 60–73 (1979).
- [62] M. I. Dykman and V. N. Smelyanski, Fluctuational Transitions between Stable States of a Nonlinear Oscillator Driven by Random Resonant Force, *Phys. Rev. A* **41**(6), 3090–3102 (1990).
- [63] H. A. Kramers, Brownian motion in a field of force and the diffusion model of chemical reactions, *Physica* **7**, 284–304 (1940).
- [64] P. Hänggi, P. Talkner, and M. Borkovec, Reaction-rate theory: fifty years after Kramers, *Rev. Mod. Phys.* **62**(2), 251–341 (1990).
- [65] M. H. Devoret, D. Esteve, J. M. Martinis, A. Cleland, and J. Clarke, Resonant Activation of a Brownian Particle Out of a Potential Well - Microwave-Enhanced Escape from the Zero-Voltage State of a Josephson Junction, *Phys. Rev. B* **36**(1), 58–73 (1987).
- [66] M. Metcalfe, *A new microwave resonator readout scheme for superconducting qubits*, PhD thesis, Yale University, 2008.
- [67] J. Clarke, Principles and Applications of Squids, *Proceedings of the IEEE* **77**(8), 1208–1223 (1989).
- [68] I. Chiorescu, Y. Nakamura, C. J. P. M. Harmans, and J. E. Mooij, Coherent quantum dynamics of a superconducting flux qubit, *Science* **299**(5614), 1869–1871 (2003).
- [69] V. Bouchiat, *Quantum fluctuations of the charge in single electron and single Cooper pair devices*, PhD thesis, l’Universite Paris VI, 1997.
- [70] F. L. Claude Cohen-Tannoudji, Bernard Diu, *Quantum Mechanics*, John Wiley and Sons, Hermann, 1977.

- [71] Abragam, *The principles of nuclear magnetism*, Oxford University Press, 1961.
- [72] I. I. Rabi, Space Quantization in a Gyating Magnetic Field, *Phys. Rev.* **51**(8), 652–654 (1937).
- [73] N. F. Ramsey, A Molecular Beam Resonance Method with Separated Oscillating Fields, *Phys. Rev.* **78**(6), 695–699 (1950).
- [74] K. W. Lehnert, K. Bladh, L. F. Spietz, D. Gunnarsson, D. I. Schuster, P. Delsing, and R. J. Schoelkopf, Measurement of the Excited-State Lifetime of a Microelectronic Circuit, *Phys. Rev. Lett.* **90**(2), 027002 (2003).
- [75] E. Il'ichev, N. Oukhanski, A. Izmailkov, T. Wagner, M. Grajcar, H. G. Meyer, A. Y. Smirnov, A. M. van den Brink, M. H. S. Amin, and A. M. Zagoskin, Continuous monitoring of Rabi oscillations in a Josephson flux qubit, *Phys. Rev. Lett.* **91**(9), 097906 (2003).
- [76] M. Grajcar, A. Izmailkov, E. Il'ichev, T. Wagner, N. Oukhanski, U. Hubner, T. May, I. Zhilyaev, H. E. Hoenig, Y. S. Greenberg, V. I. Shnyrkov, D. Born, W. Krech, H.-G. Meyer, A. M. van den Brink, and M. H. S. Amin, Low-frequency measurement of the tunneling amplitude in a flux qubit, *Phys. Rev. B* **69**(6), 060501 (2004).
- [77] A. Lupascu, C. J. M. Verwijs, R. N. Schouten, C. J. P. M. Harmans, and J. E. Mooij, Nondestructive readout for a superconducting flux qubit, *Phys. Rev. Lett.* **93**(17), 177006 (2004).
- [78] C. M. Wilson, T. Duty, F. Persson, M. Sandberg, G. Johansson, and P. Delsing, Coherence Times of Dressed States of a Superconducting Qubit under Extreme Driving, *Phys. Rev. Lett.* **98**(25), 257003 (2007).
- [79] N. Boulant, G. Ithier, P. Meeson, F. Nguyen, D. Vion, D. Esteve, I. Siddiqi, R. Vijay, C. Rigetti, F. Pierre, and M. Devoret, Quantum nondemolition readout using a Josephson bifurcation amplifier, *Phys. Rev. B* **76**(1), 014525 (2007).
- [80] D. Vion, A. Aassime, A. Cottet, P. Joyez, H. Pothier, C. Urbina, D. Esteve, and M. H. Devoret, Rabi oscillations, Ramsey fringes and spin echoes in an electrical circuit, *Fortschritte Der Physik-Progress of Physics* **51**(4-5), 462–468 (2003).
- [81] P. Bertet, I. Chiorescu, G. Burkard, K. Semba, C. J. P. M. Harmans, D. P. DiVincenzo, and J. E. Mooij, Dephasing of a superconducting qubit induced by photon noise, *Phys. Rev. Lett.* **95**(25), 257002 (2005).

- [82] P. Bertet, I. Chiorescu, K. Semba, C. J. P. M. Harmans, and J. E. Mooij, Detection of a persistent-current qubit by resonant activation, *Phys. Rev. B* **70**(1), 100501 (2004).
- [83] V. B. Braginsky and F. Y. Khalili, Quantum nondemolition measurements: the route from toys to tools, *Rev. Mod. Phys.* **68**(1), 1–11 (1996).
- [84] V. B. Braginsky, Y. I. Vorontsov, and K. S. Thorne, Quantum Nondemolition Measurements, *Science* **209**, 547–557 (1980).
- [85] A. B. Zorin, F.-J. Ahlers, J. Niemeyer, T. Weimann, H. Wolf, V. A. Krupenin, and S. V. Lotkhov, Background charge noise in metallic single-electron tunneling devices, *Phys. Rev. B* **53**(20), 13682–13687 (1996).
- [86] J. A. Schreier, A. A. Houck, J. Koch, D. I. Schuster, B. R. Johnson, J. M. Chow, J. M. Gambetta, J. Majer, L. Frunzio, M. H. Devoret, S. M. Girvin, and R. J. Schoelkopf, Suppressing Charge Noise Decoherence in Superconducting Charge Qubits, 2007.
- [87] M. Boissonneault, J. Gambetta, and A. Blais, In preparation, (2008).
- [88] M. Steffen, M. Ansmann, R. C. Bialczak, N. Katz, E. Lucero, R. McDermott, M. Neeley, E. M. Weig, A. N. Cleland, and J. M. Martinis, Measurement of the Entanglement of Two Superconducting Qubits via State Tomography, *Science* **313**(5792), 1423–1425 (2006).
- [89] N. Katz, M. Ansmann, R. C. Bialczak, E. Lucero, R. McDermott, M. Neeley, M. Steffen, E. M. Weig, A. N. Cleland, J. M. Martinis, and A. N. Korotkov, Coherent State Evolution in a Superconducting Qubit from Partial-Collapse Measurement, *Science* **312**(5779), 1498–1500 (2006).
- [90] M. Steffen, M. Ansmann, R. McDermott, N. Katz, R. C. Bialczak, E. Lucero, M. Neeley, E. M. Weig, A. N. Cleland, and J. M. Martinis, State Tomography of Capacitively Shunted Phase Qubits with High Fidelity, *Phys. Rev. Lett.* **97**(5), 050502 (2006).
- [91] A. Lupascu, E. F. C. Driessen, L. Roschier, C. J. P. M. Harmans, and J. E. Mooij, High-contrast dispersive readout of a superconducting flux qubit using a nonlinear resonator, *Phys. Rev. Lett.* **96**(12), 127003 (2006).
- [92] A. Wallraff, D. I. Schuster, A. Blais, L. Frunzio, J. Majer, M. H. Devoret, S. M. Girvin, and R. J. Schoelkopf, Approaching unit visibility for control of a superconducting qubit with dispersive readout, *Phys. Rev. Lett.* **95**(6), 060501 (2005).

- [93] R. J. Schoelkopf, Private communication.
- [94] C. Rigetti, Private communication.
- [95] A. O. Caldeira and A. J. Leggett, Quantum tunnelling in a dissipative system, *Annals of Physics* **149**(2), 374–456 (1983).
- [96] B. Yurke, *Input-Output theory*, chapter 3, page 53, *Quantum Squeezing*, Springer, 2004.
- [97] T. A. Fulton and L. N. Dunkleberger, Lifetime of the zero-voltage state in Josephson tunnel junctions, *Phys. Rev. B* **9**(11), 4760–4768 (1974).
- [98] G. Milburn and D. F. Walls, Production of squeezed states in a degenerate parametric amplifier, *Optics Communications*, **39**(6), 401–404 (1981).
- [99] B. Yurke, Use of cavities in squeezed-state generation, *Phys. Rev. A* **29**(1), 408–410 (1984).
- [100] I. Serban and F. K. Wilhelm, Dynamical tunneling in macroscopic systems, [arXiv.org:0706.3022](https://arxiv.org/abs/0706.3022) (2007).
- [101] B. Yurke and E. Buks, Performance of Cavity-Parametric Amplifiers, Employing Kerr Nonlinearities, in the Presence of Two-Photon Loss, *Journal of Lightwave Technology* **24**(12), 5054–5066 (2006).
- [102] V. V. Dodonov and A. V. Dodonov, Quantum harmonic oscillator and non-stationary Casimir effect, *Journal of Russian Laser Research* **26**(6), 445–483 (2005).
- [103] W. G. Unruh, Notes on Black-Hole Evaporation, *Phys. Rev. D* **14**(4), 870–892 (1976).
- [104] E. Segev, B. Abdo, O. Shtempluck, E. Buks, and B. Yurke, Prospects of employing superconducting stripline resonators for studying the dynamical Casimir effect experimentally, *Physics Letters A*, **370**(3-4), 202–206 (2007).
- [105] B. Yurke, P. G. Kaminsky, R. E. Miller, E. A. Whittaker, A. D. Smith, A. H. Silver, and R. W. Simon, Observation of 4.2-K equilibrium-noise squeezing via a Josephson-parametric amplifier, *Phys. Rev. Lett.* **60**(9), 764–767 (1988).
- [106] N. Bergeal, R. Vijay, V. Manucharyan, I. Siddiqi, R. J. Schoelkopf, S. M. Girvin, and M. H. Devoret, In preparation, (2008).

- [107] H. Press, S. Teukolsky, W. Vetterling, and B. Flannery, *Numerical Recipes in C++. The Art of Scientific Computing, second edition*, Cambridge University Press, 2002.